UNIVERSITEIT VAN PRETORIA
UNIVERSITY OF PRETORIA
YUNIBESITHI YA PRETORIA

The effect of stabilizing elements, specifically titanium and niobium, on the susceptibility of ferritic stainless steels to solidification cracking

By

David Sasu Konadu

Supervised by

Prof. P. G. H. Pistorius

Submitted in fulfillment of the requirement for the degree

Doctor of Philosophy (Metallurgy)

In the

Department of Materials Science and Metallurgical Engineering

Faculty of Engineering, Built Environment and Information Technology

University of Pretoria

Republic of South Africa

October 2018

ABSTRACT

The susceptibility to solidification cracking of unstabilized and stabilized ferritic stainless steels was investigated using self-restrained Houldcroft, Modified Varestraint-Transvarestraint (MVT), and hot tensile testing. Five experimental steel grades comprising an unstabilized, two mono stabilized (Ti or Nb), and two dual stabilized (Ti + Nb), and two commercial unstabilized and a dual stabilized (Ti + Nb), and another dual stabilized containing-Mo alloy (nine different alloys in total) were used in this study.

Seven steel grades comprising an unstabilized, two mono stabilized (Ti and Nb) respectively, three dual stabilized (Ti + Nb) and a dual stabilized containing Mo were used for the self-restrained Houldcroft method. Autogenous gas tungsten arc welding at a speed of 6 mm/s, 3 mm/s, and 1 mm/s was done. The unstabilized ferritic stainless steel was resistant to solidification cracking. Ti addition to ferritic stainless steel resulted in a minor increase to susceptibility to solidification cracking. Nb in ferritic stainless steel increased solidification cracking. The addition of Ti and Nb resulted in a decreased susceptibility to solidification cracking compared to an alloy containing only Nb. The weld metal microstructures were a mixture of columnar and equiaxed grains. The interdendritic crack surfaces were enriched in Nb, Ti, Mn, Si, Al, Mn, and Mo.

The MVT test was used for the test of an unstabilized, a Nb stabilized and two (Ti + Nb) dual stabilized ferritic stainless steels. Two different welding speeds of 6 mm/s and 3 mm/s using autogenous gas tungsten arc welding were employed. The high content (Ti + Nb) steel at a welding speed of 3 mm/s had the greatest sensitivity to solidification cracking. The Nb stabilized steel at both welding speeds (6 mm/s and 3 mm/s) and high content (Ti + Nb) steel at a welding speed of 6 mm/s showed intermediate sensitivity to solidification cracking. The unstabilized and low content (Ti + Nb) grades were the least sensitive to solidification cracking. The weld metal microstructures transverse to the welding direction revealed columnar grains in all the samples for both welding speeds.

Three experimental Ti-, Nb-, and dual Ti + Nb stabilized ferritic stainless steels were used for hot tensile testing using a Gleeble-1500D thermo-mechanical machine at testing temperatures of 1200°C, 1250°C, and 1300°C. The dual stabilized ferritic stainless steel showed a high and fairly constant hot ductility with an increasing testing temperature. The Ti stabilized alloy revealed a slightly lower ductility compared to the dual stabilized steel but much higher ductility than the Nb stabilized ferritic stainless steel. The SEM images of the intergranular cracking showed interdendritic morphologies. EDX analysis showed the elements Al, Mn, Ti, Si, Ni, S, Nb, and Ni to be associated with the fractured surfaces. The hot tensile test results were inconclusive, due to the small number of samples and an acquisition frequency that was too low.

The MVT test was better than the self-restrained Houldcroft, and the self-restrained Houldcroft was better than the hot tensile tests in quantifying the susceptibility of a specific ferritic stainless steel alloy to solidification cracking. The cracking response of Houldcroft seemed to be dominated by welding speed. Cracking response of MVT test seemed to be dominated by the Nb content.

The effect of Nb and Ti on the susceptibility cracking could be explained in terms of the effect of these two alloying elements on the difference between the liquidus and the solidus. Nb was found to segregate strongly to the grain boundaries (low k value) which resulted in a significant increase in the difference between the liquidus and the solidus. This difference increased BTR which results in a high susceptibility to solidification cracking. Ti has a higher k value and segregates less than Nb during solidification.

Keywords: Ferritic stainless steel, solidification cracking, Houldcroft, Modified Varestraint-Transvarestraint, hot tensile testing, microstructure, welding.

DEDICATION

This thesis is dedicated to my wonderful wife, Mrs Cynthia Konadu, for her patience whilst I was studying and my beloved daughter, Emmanuella Akosua Adepa Konadu, my source of hard work and reason for coming this far.

ACKNOWLEDGEMENTS

I give thanks to the Most High God for His love, protection, wisdom and understanding. I humbly express my deepest appreciation to the following persons for their immense contributions towards the completion of my study.

Professor PGH Pistorius for your supervision of the work. I am grateful to you for the patience when the going was tough, encouragement, fatherly advice, mentoring me to be a good researcher and financial support.

Professor M Du Toit, whom God used for me to undertake this study at University of Pretoria, I am highly indebted to you. I cannot forget Dr Axel Griesche of BAM Federal Institute for Materials Research and Testing, Germany, who performed the MVT-test for me.

Sibusiso Mahlalela and Mr Joel Matea of Materials Science and Metallurgical Engineering Department as well as Mr Peet Kruger and Sehlomola Edwin Mohale of the Mechanical Engineering department, I am grateful to you for the help received and providing the laboratory materials for the project work.

I will not forget the welding group for their immense sharing of ideas for every step of the way. To Lwazi Magwentshu and Kristian Kruger, I appreciate you all.

My parents; Mr. and Mrs. Konadu, brothers and sisters, and all friends in the departments of University of Pretoria, Pretoria and University of Ghana, Legon-Accra, for your prayers and moral support.

Finally, I want to thank Office of Research, Innovation, and Development (ORID), University of Ghana, Department of Research and Innovation Support (DRIS), and the South African Institute of Welding Centre for Welding Engineering in the Department of Materials Science and Metallurgical Engineering at the University of Pretoria for financial assistance in funding my studies in South Africa.

TABLE OF CONTENTS

LIST OF TABLES

LIST OF FIGURES

LIST OF ABBREVIATIONS

AISI	American Iron and Steel Institute
BAM	Bundesanstalt für Materialforschung und –prüfung
HAZ	Heat affected zone
MVT	Modified Varestraint - Transvarestraint
SEM	Scanning electron microscope
EDX	Energy dispersive X-ray
UP	University of Pretoria
MCL	Maximum crack length
MCD	Maximum crack distance
TCL	Total crack length
NDT	Nil ductility temperature
BTR	Brittle temperature range
NST	Nil strength temperature
DRT	Ductility recovery temperature
SCTR	Solidification cracking temperature range
MCD	Maximum crack distance
DSC	Differential scanning calorimetry
HTE	High temperature embrittlement
DBTT	Ductile to brittle transition temperature
HTHAZ	High temperature heat affected zone
LTHAZ	Low temperature heat affected zone

SMAW	Shielded metal arc welding
GTAW	Gas tungsten metal arc welding
GMAW	Gas metal arc welding
PAW	Plasma arc welding
EBW	Electron beam welding
LBW	Laser beam welding
SAMS	Small Alloys and Metallurgical Services
DRX	Dynamic recrystallization
SRX	Static recrystallization
MDRX	Metadynamic recrystallization
PVR	Program Controlled Deformation Cracking Test

CHAPTER ONE - BACKGROUND

1.1 Introduction

Welding is formally defined as a localized coalescence of metals or nonmetals made plastic or liquid by heat or pressure or both to the welding temperature and with or without a filler material [1]. After welding, it is expected that the joint will be sound and reasonably free from defects. Potential weld metal defects include slag inclusions, cracks, lack of penetration, and porosity [2]. One crack-like defect is solidification cracking [3-4]. Weld solidification cracking occurs during the final stages of weld solidification due to the combined effects of impurity and alloying element segregation, liquid film formation at grain boundaries, and imposed thermo-mechanical strains. The impurities and alloying elements result in the lowest solidification temperature at the grain boundaries in the microstructure. It can be a serious defect when welding many alloys. Solidification cracking is mostly observed in the centreline of the weld [3–5].

A group of high-alloy steels based on the iron-chromium (Fe-Cr), iron-chromium-carbon (Fe-Cr-C), and iron-chromium-nickel (Fe-Cr-Ni) systems constitute stainless steels. About 10.5 wt% chromium in iron allows formation of a passive surface oxide that prevents oxidation, even at high temperatures, and corrosion of the underlying metal [3-4, 6]. Stainless steels are classified by the dominant metallurgical phase. The three possible phases are ferrite, martensite and austenite. There are five types of stainless steels based on the phases present and these are austenitic, ferritic, martensitic, duplex and precipitation-hardenable grades [3-4, 6].

Among the ferritic stainless steels, type AISI 444 is a dual stabilized (Ti + Nb) steel containing Mo, 441 is dual stabilized (Ti and Nb), AISI 436 and 439 are Nb and Ti mono stabilized respectively, and 430 is unstabilized. The stabilizing alloying elements form carbides or nitrides or carbonitrides to prevent sensitization.

1.2 Motivation for the current study

Most stainless steels are weldable. Welding may require special procedures which can result in significant changes in the microstructure of the weld metal and the heat affected zone (HAZ) [4]. Such microstructural changes may include a change in the phase balance, formation of undesired intermetallic constituents, grain growth and segregation of alloy and impurity elements, which affects the properties and performance of the material [4].

Research on the solidification cracking of stainless steels has been largely limited to duplex and austenitic stainless steels [7–9]. Investigations on the welding of ferritic stainless steels have focused on the mechanical properties and the microstructure of the welded joint [10-11]. The ferritic stainless steels are generally regarded as not susceptible to solidification cracking, but there are reports in the literature that suggest that Ti, Nb, and high impurity levels increase the risk of solidification cracking [4, 12].

A modified E430 electrode employing shielded metal arc welding and a submerged arc welding using a flux were used to weld type AISI 430 ferritic stainless steel. A sound weld was attainable due to a fine ferrite weld structure. On the other hand, coarse ferrite grains which resulted from 17 % Cr-Nb weld metal, induced hot cracking [13].

1.3 Problem statement

A South African stainless steel processor reported weld metal cracking of Type 441 ferritic stainless steel during fabrication. Preliminary studies suggested that the failures might have been caused by solidification cracking. Type 441 is a dual-stabilized (Ti and Nb) ferritic stainless steel with a nominal chromium content of 18%. A literature search on solidification cracking of ferritic stainless steels yielded a small number of papers on the solidification cracking of an unstabilized ferritic stainless steel [12] and fully ferritic weld metals that contain Nb, Ti and Al [13]. A limited amount of published results on the effect of alloying content on the susceptibility of ferritic stainless steels to solidification cracking could be found.

Kah and Dickinson [12] reported on the weldability of ferritic stainless steels using type AISI 430, E-Brite 26-1, and AISI 430 and 444L ferritic stainless steels employing a modified subscale Varestraint test. It was concluded that the hot cracking susceptibility of these materials was at least partially dependent on the composition. Susceptibility to hot cracking increased with an increase in sulphur, carbon, nitrogen, niobium, titanium, phosphorus, and manganese. Similarly, it has been stated that titanium and niobium with other alloying elements in ferritic stainless steels can cause solidification cracking [4].

Expanding on the work by Kah and Dickinson [12], the weldability of ferritic stainless steels using type AISI 430 and E-Brite 26-1 materials was investigated. It was found that the hot cracking susceptibility of these materials was at least partially dependent on the composition and was promoted by sulphur, carbon, nitrogen, niobium, titanium, phosphorus, and manganese. In explaining the mechanism for the elements aiding solidification cracking, plots were constructed for the total crack length and percentage alloying addition for each set of alloying additions. It was not clear why these plots were made and a figure comprising all the alloying elements with a 0.1% change in alloy addition revealed which elements contributed to solidification cracking susceptibility (Figure 1.1). The susceptibility to solidification cracking was also dependent on the shape of the weld bead. By visual inspection, wider weld beads showing teardrop shaped pools produced the highest total crack length compared to elliptical weld shaped pools. The weld bead shape depended on the chemical composition and welding parameters.

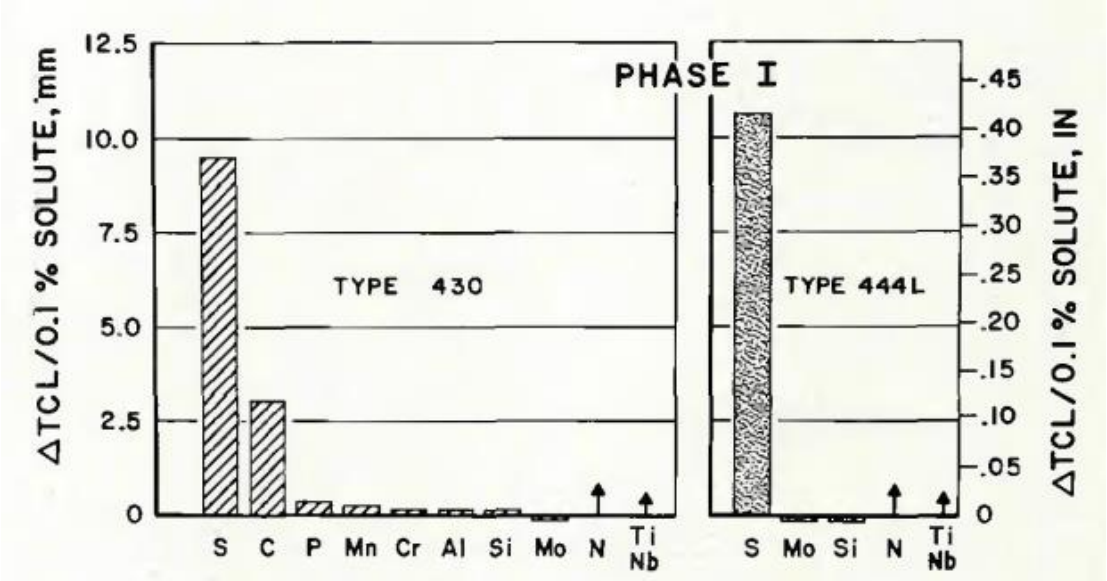

Figure 1.1: Summary of the change in total crack length for Type 430 and 444L as a function of a 0.1% increase in solute content [12].

Furthermore, acceptable resistance to hot cracking could be achieved by using titanium, tantalum, and niobium as stabilizers in AISI 430 and 444L ferritic stainless steels with a (C + N) content less than 0.04%. Resistance to hot cracking could be obtained using low (C + N) levels with titanium, tantalum, or dual stabilization but not niobium alone [12]. A modified E430 electrode containing 0.78Nb, 0.07Ti, and 0.06Al was used with shielded metal arc welding and a submerged arc welding using a flux containing 1.88Nb, 2.22Ti, and 1.10Al was used to weld type AISI 430 ferritic stainless steels. The authors did not state the heat input. A sound weld was attainable if the weld metal contained niobium and nitrogen or niobium, titanium and aluminum. This was attributed to the ferrite weld structure and the refining effect of niobium, titanium and aluminium containing nitrides and oxides that act as nuclei, resulting in a fine grain structure in the weld. The low melting points are distributed uniformly on the fine crystal grains and prevents hot cracking. On the other hand, coarse ferrite grains which resulted from 17 % Cr-Nb weld metal induced hot cracking [13].

As the steel is now becoming popular as a high temperature corrosion-resistant alloy that is more often welded, there is the need for proper understanding of the mechanism

of solidification cracking in ferritic stainless steels with varying amounts of stabilization additions. In this project, the conflicting reports on the susceptibility of ferritic stainless steels to solidification cracking were investigated. This was done by evaluation of a reference steel with no stabilizing element, mono stabilized steels (containing either Ti or Nb), and dual stabilized (Ti + Nb) steels.

1.4 Aim

The main aim of the project work was to understand the mechanism of solidification cracking and the effects of stabilization during welding of ferritic stainless steels using type AISI 430, 436, 439, 441, and 444 materials.

1.5 Research questions

- What will be the susceptibility to solidification cracking of an unstabilized ferritic stainless steel?
- Will Ti addition to ferritic stainless steels have any effect on the susceptibility to solidification cracking?
- Will Nb addition in ferritic stainless steels increase the susceptibility to solidification cracking?
- Will the addition of Ti to a Nb stabilized ferritic stainless steel counteract the negative effects of Nb, if any?

1.6 Outline of experimental work

The following techniques were used:

1.6.1 A self-restrained Houldcroft technique

1. The base metal were laboratory heats of type AISI 430, 436, 439, and 441 ferritic stainless steels and an industrially produced material of types AISI 441 and 444 ferritic stainless steels.

2. The characterisation methods were optical microscopy and SEM with EDX.

1.6.2 Modified Varestraint-Transvarestraint (MVT) test

1. The base metal were laboratory heats of type AISI 430, 436 and 441 ferritic stainless steels were used.
2. The characterisation method was optical microscopy.

1.6.3 Hot tensile testing

1. The base metal were laboratory heats of type AISI 436, 439 and 441 ferritic stainless steels.
2. The characterisation methods were optical microscopy and SEM with EDX.

1.7 Scope

This chapter has introduced the material to be used in this study and described the motivation for the study. Chapters Two and Three will review the available literature on the solidification cracking, microstructure, and carbides in ferritic stainless steel welded joints. The experimental procedures will be outlined in Chapter Four. The results and discussion of the self-restraint Houldcroft, the MVT and the hot tensile tests will be reported in Chapters Five, Six and Seven respectively. A general discussion of the results of the different experimental techniques, conclusions and recommendations for further work will be given in Chapter Eight.

CHAPTER TWO –SOLIDIFICATION CRACKING

2.1 Introduction

One of the defects potentially associated with welding is solidification cracking. A brief survey of weld solidification, solidification cracking mechanisms and the methods used for measuring solidification cracking susceptibility of a material will be presented. The focus of the discussion on the experimental techniques will be the modified Houldcroft method, the modified Varestraint-Transvarestraint method and hot tensile testing, as these techniques were used during the current study.

2.2 Solidification cracking

Solidification cracking occurs in the fusion zone during the last stage of weld solidification, when the strength of the almost completely solidified weld metal is lower than the tensile stresses developed across the adjacent grains leading to cracking in the weld metal [3, 5, 14-15]. Solidification shrinkage and thermal contraction (of the weld metal and the heat affected zone) cause the solidifying weld metal to shrink. The solidifying weld metal may be restrained from contraction by the base metal and cannot shrink freely. This results in tensile stresses developing in the weld metal. The magnitude of these stresses depends on the degree of constraint and material thickness [5]. Cracks may form to relieve the strain accumulated due to the failure of the semisolid weld metal to absorb strain [15].

The risk of solidification cracking is increased if low melting point phases are present between the dendrites [3, 5, 14]. Liquid films along solidification grain boundaries give rise to weld solidification cracking. As a consequence, the cracks are mostly intergranular [16]. Depending on the specific stainless steel, these phases may contain phosphorus and sulphur which segregate to the grain boundaries or interdendritic regions [5, 12]. Micro-fissures can occur when these low melting phases are subjected to shrinkage strains during cooling. Restraint during cooling, the weld metal shape and crystallization structure play a role during solidification cracking [3, 14].

For ferritic stainless steels, cracking normally occurs when alloying elements segregate to the solidification grain boundaries, resulting in local regions with a lower solidification temperature. The solidification cracking susceptibility is normally low since these grades of stainless steel solidify as primary ferrite. However, additions of Ti and Nb, and high impurity levels will increase solidification cracking susceptibility. These impurities which segregate to grain boundaries, can form low melting liquid films during freezing [4].

2.3 Metallurgical factors influencing susceptibility to solidification cracking

Solidification cracking involves interactions between metallurgical, mechanical, and thermal factors which are complex in nature, making direct correlation between theory and observation difficult. Phase transformations are related to the chemical composition and temperature, which constitute metallurgical factors. Stress and strain properties depend on mechanical factors.

The solidification temperature range, also known as the brittle temperature range (BTR), can be approximated by the difference between the liquidus and solidus temperatures of a material. The solidus in non-equilibrium conditions is the lowest melting eutectic temperature [5, 17].

During solidification, liquid can be drawn back by capillary flow through the dendrite network to heal or fill the crack. The movement of liquid by capillary flow is known as back-filling. This is observed metallographically as solute pool material found in crack-shaped defects. This theory was derived from foundry technology with risers that are used to feed hot spots to avoid shrinkage porosity and hot tearing. In weld metal, the weld pool material takes the place of risers (Figure 2.1) [16-17].

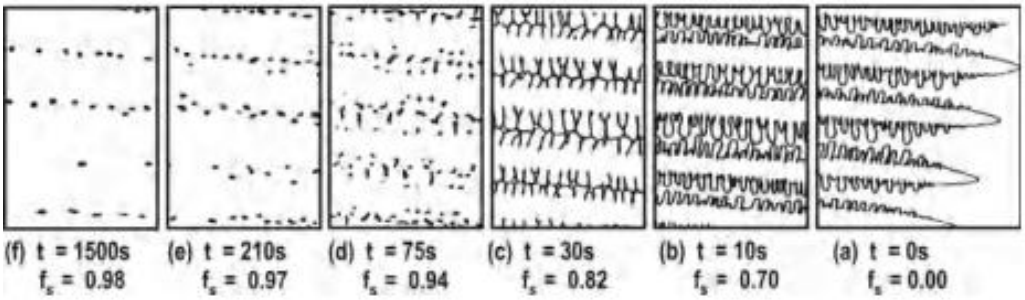

Figure 2.1: Schematic diagram revealing progressive stages of dendritic solidification, a-b: back filling, c: thin liquid film, d-f: dendrite coherency [17].

The region where liquid and solid coexist during solidification is the two-phase mushy zone. The size of the mushy zone can be estimated by the solidification temperature range (in °C or in K) divided by the temperature gradient (in °C/m or in K/m). In the mushy zone, the grains (cells or dendrites) are surrounded by a liquid phase, so weld solidification cracking is not possible [17]. As temperature decreases, interaction between the solids starts and a rigid network is formed. It has been postulated that an extended mushy zone is prone to solidification cracking because it experiences more shrinkage strain. Solid-solid bridging occurs to accumulate strain, leading to cracking in regions where sufficient liquid is not available to back-fill the susceptible crack. This is known as the shrinkage-brittleness theory [16]. There are other various theories based on a coherent interlocking solid network which is separated by continuous thin liquid films and are torn apart by tensile stresses [5, 16, 18].

At the last stage of weld solidification, should the last liquid to solidify wet the dendrites (low $\gamma_{L/S}$, the surface energy between the liquid and the solid interface), the probability for back filling is high due to the presence of a continuous liquid network. Where there is no wetting (high $\gamma_{L/S}$), dendrite arms bridging is enhanced, strain is resisted, and cracking is avoided. At intermediate values of $\gamma_{L/S}$, cracking may occur [17].

Porosity is observed as a form of liquid rupture which involves the formation of a liquid/vapour interface and is usually round in shape rather than planar. Interdendritic

porosity near weld solidification cracks has been observed in steel using real-time radiography [17]. These pores can act as a nucleus for a solidification crack as they flatten and elongate similar to the gathering of micro-pores. On the other hand, porosity has been known to counter solidification shrinkage as they reduce the need for back-filling as seen in killed steel versus rimmed steel during autogenous welding [17].

When an intergranular liquid film is strained above some critical value, cracking is found. Pellini, Prokhorov, and Senda, cited by Böllinghaus & Herold [17], established ductility curves where a maximum strain is reached before cracking. Figure 2.2 shows the lower and upper temperature boundaries for the solidification range and by experimentally determining the critical ductility curve, cracking occurs when the deformation curve (strain across the mushy zone) intersects the ductility curve [17].

From Figure 2.2, the thermal contraction which is represented by line AD will not result in solidification cracking. Line AC which is the critical strain, may result in cracking. Line AB describes the condition when the thermal strain exceeds the ductility curve to cause solidification cracking of the material in the BTR [17].

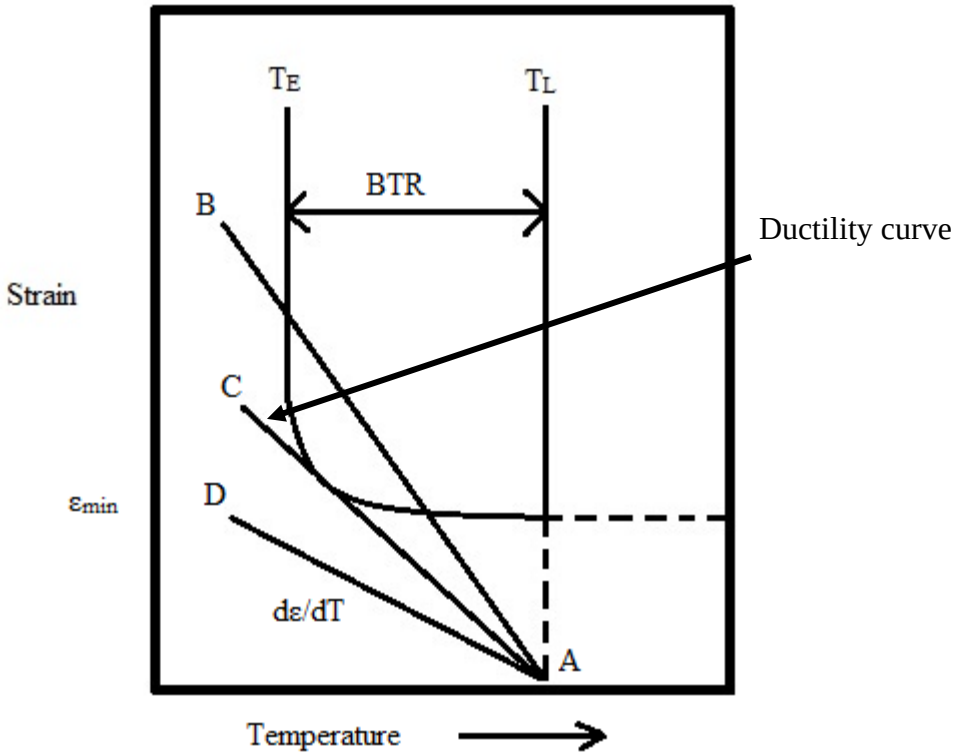

Figure 2.2: Schematic ductility curve and brittle temperature range (BTR) [17].

A critical strain must be reached before cracking is achieved as has been established by Prokhorov and Senda [17] and from Figure 2.2, the slope of the deformation curve is related to the cooling rate (dT/dt) and strain rate (dε/dt) by

$$d\varepsilon/dT = (d\varepsilon/dt) / (dT/dt) \qquad (2.1)$$

It has been assumed that a high level of weld restraint results in a high susceptibility to solidification. The assumed relationship between restraint and an increased susceptibility to solidification cracking, is the basis for self-restrained tests (like the Houldcroft test, which will be described later). It has been recently found that high restraint does not always give high susceptibility to cracking, for reasons that were not noted [17].

With an increase in temperature from ambient (T_S) to melting point (T_L), the hot ductility of a weldable alloy increases gradually till melting occurs. The ductility drops

abruptly from its maximum value to near zero at a temperature called the nil ductility temperature (NDT) just before reaching the melting point. Nil strength temperature (NST) follows the NDT at which the alloy loses its strength as a result of liquid phases forming along the grain boundaries. Recovery of ductility is not exactly at NDT as cooling occurs from NST, but at a lower temperature than the NDT which is known as ductility recovery temperature (DRT). The brittleness temperature range (BTR) or nil ductility range (NDR) is the temperature range between NST to DRT which shows how fast ductility recovers on cooling, Figure 2.3 [19-20]. This shows that the definition of BTR is not consistent as it was previously defined as the difference between the liquidus and solidus temperatures of a material [5, 17] which is different from the temperature range between NST to DRT [19-20].

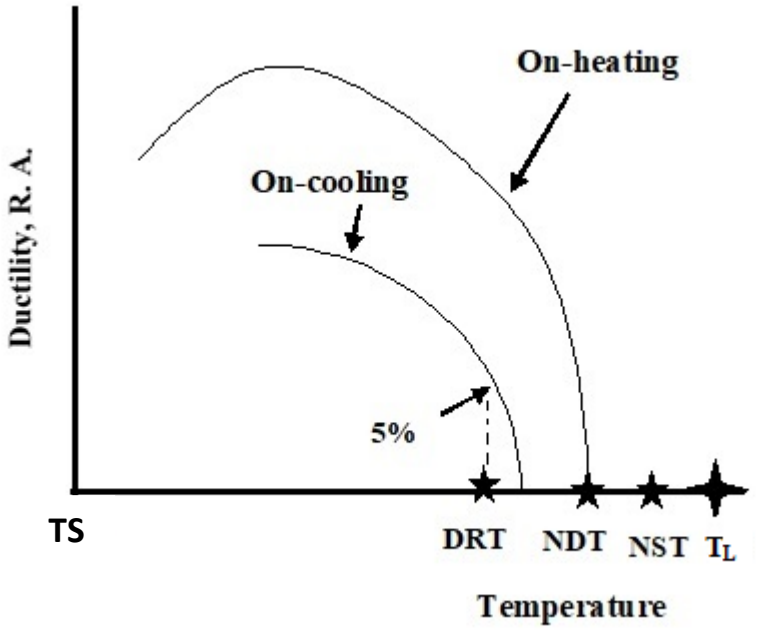

Figure 2.3: Hot ductility curve showing T_S: the ambient temperature, DRT: ductility recovery temperature, NDT: the nil ductility temperature, NST: nil strength temperature, and T_L: melting point [20].

It has been suggested that a liquid film has a critical strength which relies on its surface tension and thickness. It is expected that the degree of solid-solid bonding in the dendrite arms should give additional resistance to fracture. This may give some inherent strength in the weld mushy zone. Gleeble simulation, among other experimental methods have been used to measure the strength of the liquid-solid mushy zones. A cylindrical sample placed in a quartz jacket to contain the molten sample is used while applying a uni-axial tensile stress. The results have been inconclusive, probably due to the complexity of deformation in the liquid-solid zone [21]. Gleeble testing is a simulation of the real welding process that cannot reproduce the exact conditions of temperature, cooling rate, restraint, and externally applied strains present in an actual welded joint. A large number of samples are required for the hot tensile test and the various strains should represent the welding methods (heat input) using the Gleeble [19].

Weld metal grain boundaries play a role in solidification cracking as the cracking normally occurs in the intergranular position. The grain size, shape, and structure contribute to solidification cracking. Columnar grains growing normal to the welding direction impinge at the centre resulting in cracking. This normally occurs when the welding speed is high which results in tear-drop weld pool shapes and may cause impurities to segregate along the weld, which can result in a low solidus temperature [5, 17, 22].

It has been shown by Brooks that a different grain boundary structure might account for the weldability difference between austenite and δ-ferrite primary solidification in stainless steels. The weld metal grain boundaries are seen to be well defined as primary austenite which solidifies, resulting in easy crack propagation [17].

More grain boundaries per unit volume exist for smaller grains resulting in smaller strains on each grain since the strain is partitioned to each individual grain boundary [17]. This increases resistance to solidification cracking as researchers have proven the effect of grain refinement on the risk of solidification cracking in ferrous and non-ferrous alloys [17, 22].

In conclusion, weld hot cracking occurs when the solidifying weld metal contracts and the shrinkage cannot be healed by back-filling of the molten material and the strain accumulated at the welded joint is greater than the resistance of the material. Impurities in the form of solute contents, the presence of susceptible grain boundaries, and welding parameters play significant roles in solidification cracking.

2.4 Residual stresses

Solidification shrinkage and thermal contraction can lead to solidification cracking, residual stresses and distortion. During welding, the weld zone and the surrounding base meal are restrained from expansion and contraction during heating and cooling by areas farther away from the weld metal respectively. The weld metal and the adjacent base metal are seen to be under residual tensile stresses while the areas farther away from the weld metal are under residual compressive stresses. Transverse residual stresses distributed along the length of the weld is shown in Figure 2.4. The middle part of the weld shows relatively low tensile stresses. The much cooler base metal farther away restrains thermal contraction in the transverse direction. In effect, compressive stresses developed at the end of the weld are balanced by tensile stresses in the middle of the weld. Hydrogen induced cracking and stress corrosion cracking can be induced by residual stresses. Solidification shrinkage and thermal contraction can distort the workpiece during welding. Shrinking in the welded workpiece can occur in both the transverse and longitudinal directions [5].

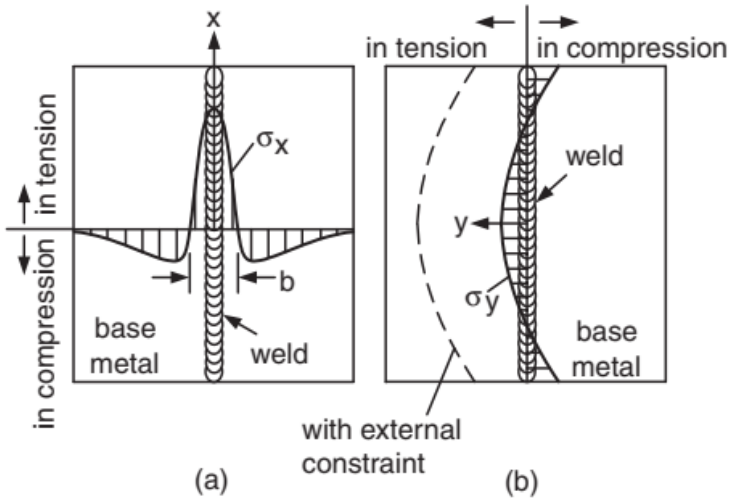

Figure 2.4: Typical distributions of longitudinal (σx) and transverse (σy) residual stresses in butt weld [5].

The profile of the weld bead can influence its susceptibility to solidification cracking. For a simple V-groove joint, concave welds produce more restraint than convex beads. As a result, concave welds are more susceptible to solidification cracking [16].

2.5 Solidification cracking susceptibility tests

Most of the weldability tests used to evaluate the susceptibility of the specimen to weld solidification cracking are laboratory based. It has been stated that a welding test should be economical, simple to conduct and evaluate, repeatable, and be able to show a direct relation between fabrication and service conditions. The test methods can be grouped as self-stressing (self – restraint), that is the method that uses restraint or stress within the sample to cause cracking, and methods where external strains or loads are applied [3, 20, 23-24].

2.5.1 Self-restraint tests

Self-restraint tests use stress or restraint in the sample to make the weld metal crack. Differing restraint arises from the design of the samples which causes cracking without applying external load [23]. Selected self-restraint tests are explained below.

2.5.1.1 The Keyhole Restraint Test

This uses a simplified version of the Lehigh restraint which involves welding along a groove beginning at an open end and progressing toward a hole. Varying degree of restraint is imposed along the weld with the maximum at the hole and minimum at the edge where welding started. The crack develops at the hole and extends outward to a point where the restraint is low enough to arrest the crack growth. The crack length is regarded as a quantitative measure of the crack susceptibility (Figure 2.5) [23].

2.5.1.2 Lehigh test

In the Lehigh test, slots are machined into the sides and ends of a plate sample. A single weld pass is made along a groove which is machined along the centreline of the plate. Restraint from the plate and slots produce a weld with cracks of varying lengths. The crack length is used to quantify the susceptibility to solidification cracking (Figure 2.6) [23].

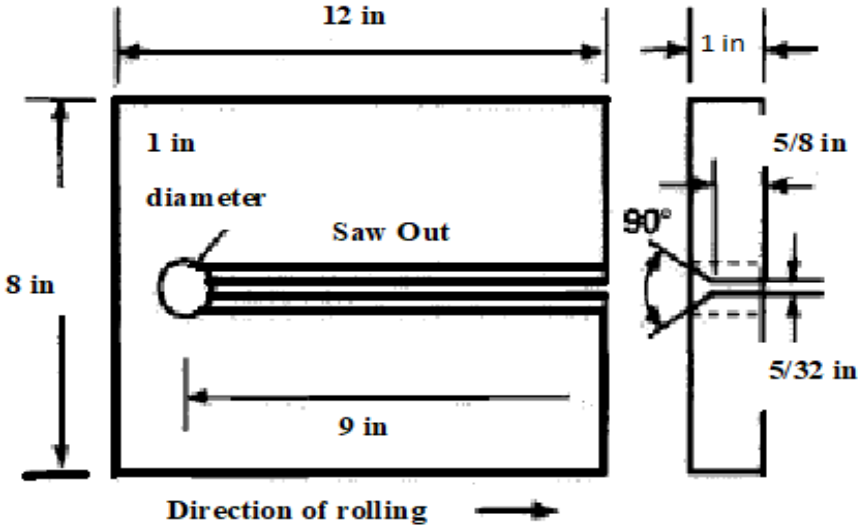

Figure 2.5: Keyhole Restraint Cracking Test [23]

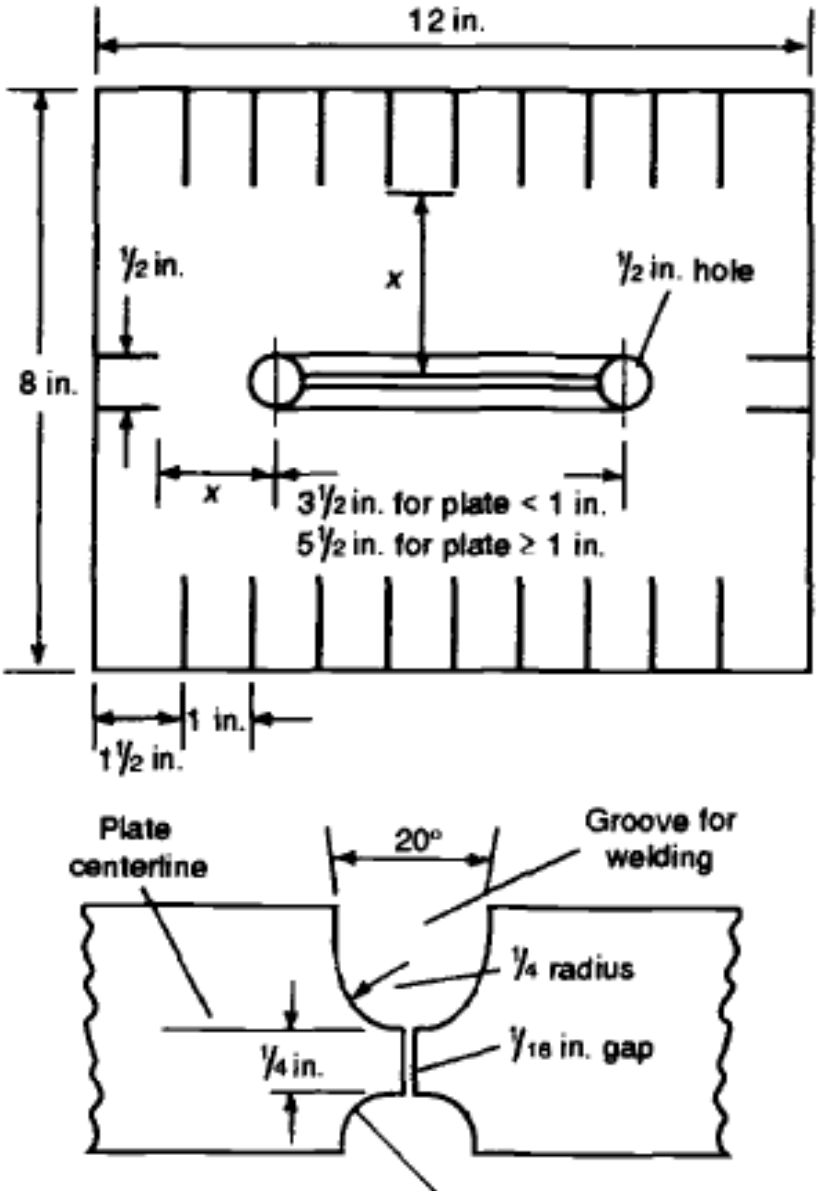

Figure 2.6: The Lehigh restraint test [23].

2.5.1.3 Keyhole Slotted-Plate Restraint Test

The Keyhole Slotted-Plate Restraint Test is shown in Figure 2.7. This test is a variant of the Houldcroft test described later. The uncut width of the specimen at which the crack propagation stops is used to measure crack sensitivity, similar to the Lehigh test [23].

2.5.1.4 Navy circular patch test

The Navy circular patch test is used for evaluating different electrodes on various base metals and has a much larger specimen which is shown in Figure 2.8. A patch is placed into a circular hole cut into a plate. A back up ring is used to hold the patch and the plate together. One quadrant of a multipass weld is made one at a time and cracking measurement is by visual, radiography and/or liquid penetrant inspection [23].

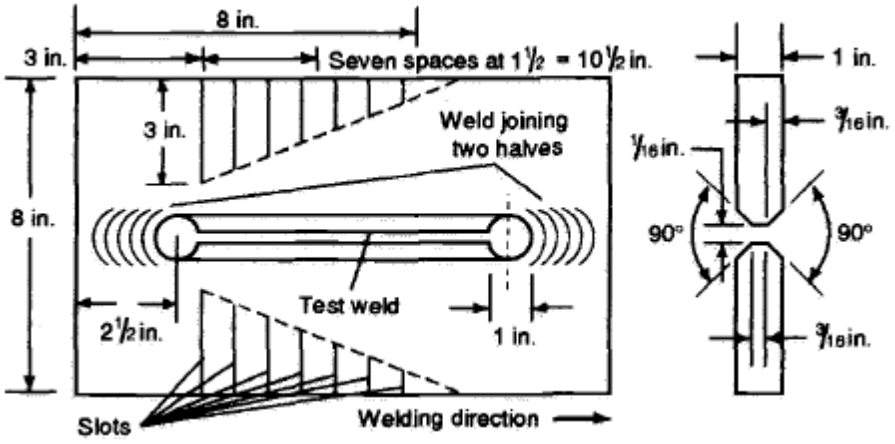

Figure 2.7: Keyhole Slotted-Plate Restraint Test [23].

2.5.1.5 Houldcroft

The Houldcroft test (also known as the fishbone test) uses a specimen with slots of different depths in a progressive manner (Figure 2.9). The gas tungsten arc welding (GTAW) process is used to deposit a weld bead. Complete penetration is necessary. Solidification begins as the heat source starts to move inwards from the starting edge of the test sample. Solidification cracking starts from the starting edge and propagates along the centreline. The weld metal is strained in a direction transverse to the welding direction. Cracking of the weld metal occurs because of expansion from the starting edge due to continued heat input to the specimen. The stress along the length of the specimen can be decreased by reducing the width. The susceptibility to cracking is quantified by the crack length from the starting edge [5, 22, 23, 25].

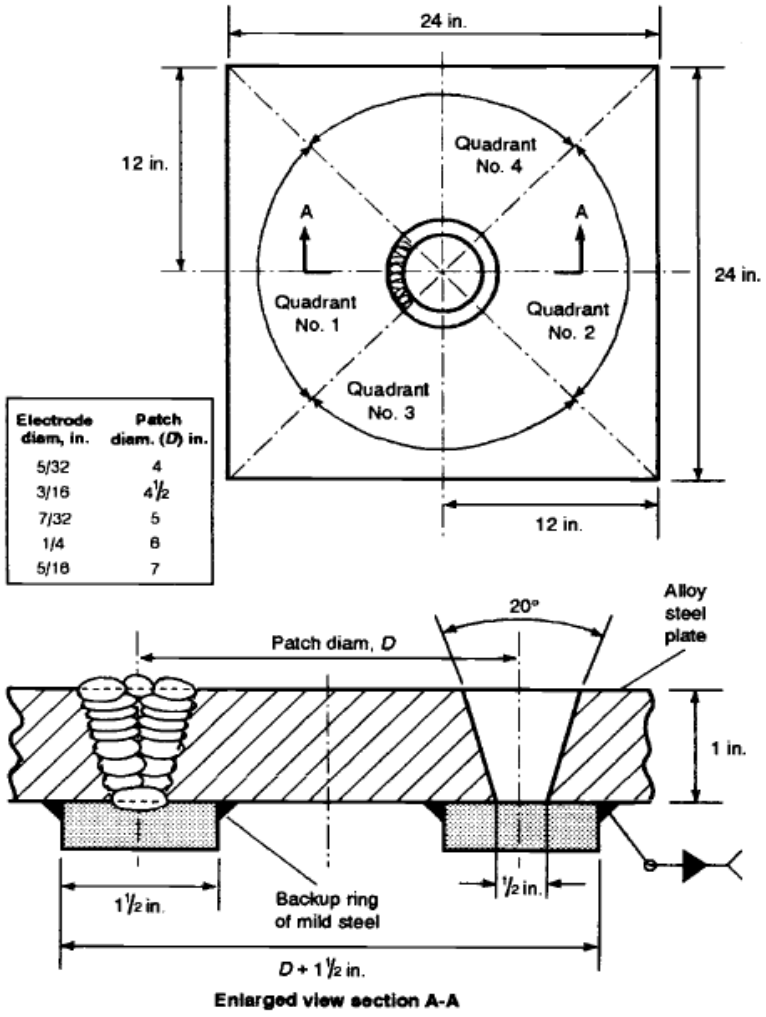

Figure 2.8: Navy Circular Patch Test [23].

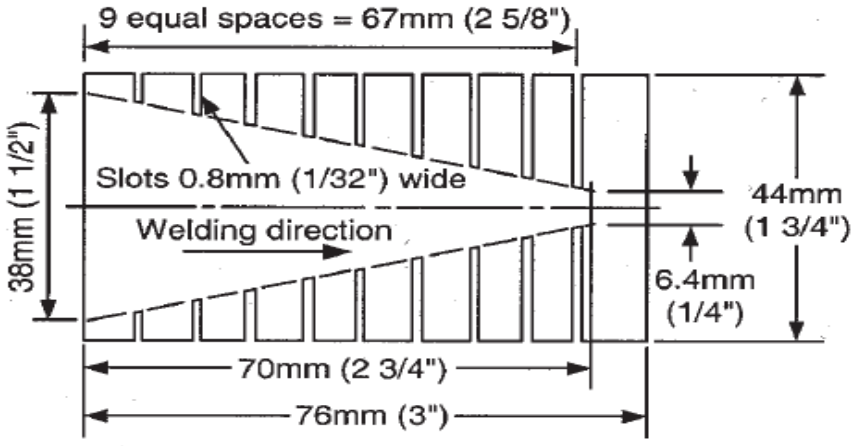

Figure 2.9: The Houldcroft or fishbone test [5, 22-23].

2.5.1.6 Circular Patch Test

The Circular Patch Test has a circular hole cut out from a plate and replaced by a patch. A weld joint is machined into both the plate and the patch. Cracking is detected in the circular groove by welding one or more passes, which is detected by visual, radiographic, and/or liquid penetrant inspection (Figure 2.10) [23].

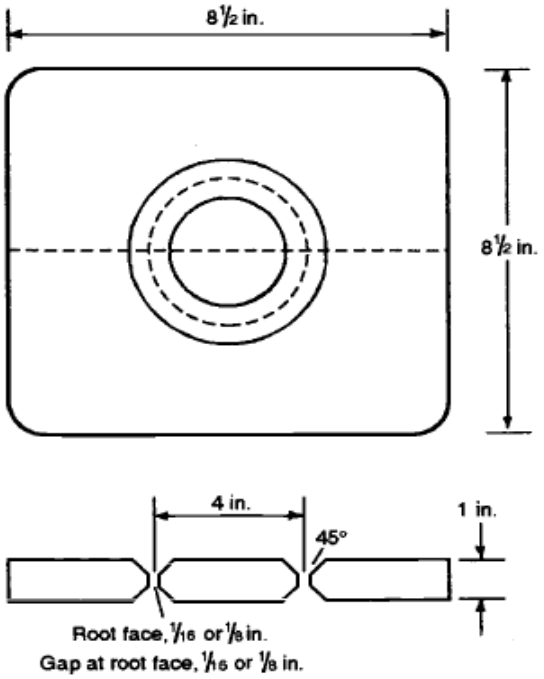

Figure 2.10: Circular Patch Test [23].

These self-restraint tests either crack or do not. The cracking temperature range or stress-strain data cannot be obtained. Comparison of different materials is difficult to make. There are examples of materials that were crack resistant under self-restraint tests, but during actual fabrication conditions were found to be crack susceptible [3].

From the self-restraint tests noted in section 2.5.1, all the dimensions for the set up are quite large and also may need some modifications on the specimen. Except the Houldcroft test which has slots, some in addition to the slots need either a groove or a circular hole which is cut in the specimen. The Houldcroft test can be varied in dimension, shape and the number of slots, making it easier to design. Moreover, the

Houldcroft method uses an autogenous GTAW welding process, similar to the industry welding process that motivated the current investigation. For these reasons for the current study, a self-restrained test based on the Houldcroft test was developed.

2.5.2 Modifications to the Houldcroft test for the project

Many researchers have used the self-restraint Houldcroft method but with different shapes, dimensions and number of slots. All the Houldcroft-type tests used autogenous GTAW. A different dimension with the same shape was proposed by Lancaster [22] and shown in Figure 2.11. The slots were seven instead of nine and dimensions are different.

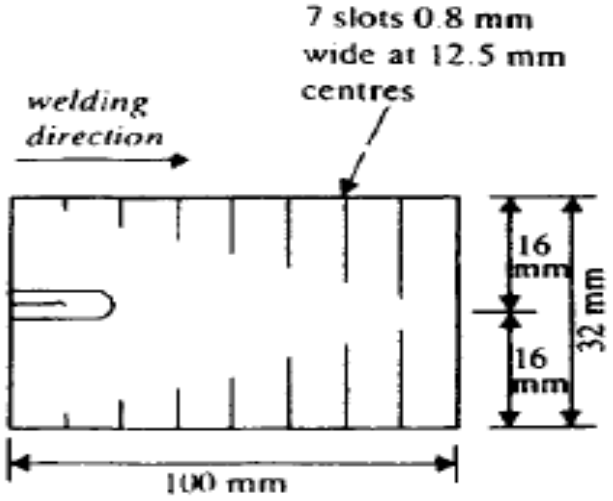

Figure 2.11: Dimensions of sample geometry, as reported by Lancaster, for the study of the susceptibility to solidification cracking in an aluminium alloy [22].

The effect of grain refinement on Al alloys using vibration or stirring the weld pool through an ultrasonic vibrator or by electromagnetic stirring was studied. The electromagnetic stirring resulted in optimum reduction of the amount of solidification cracking; as demonstrated by using a Houldcroft test which had nineteen slots and different dimensions (Figure 2.12) [22].

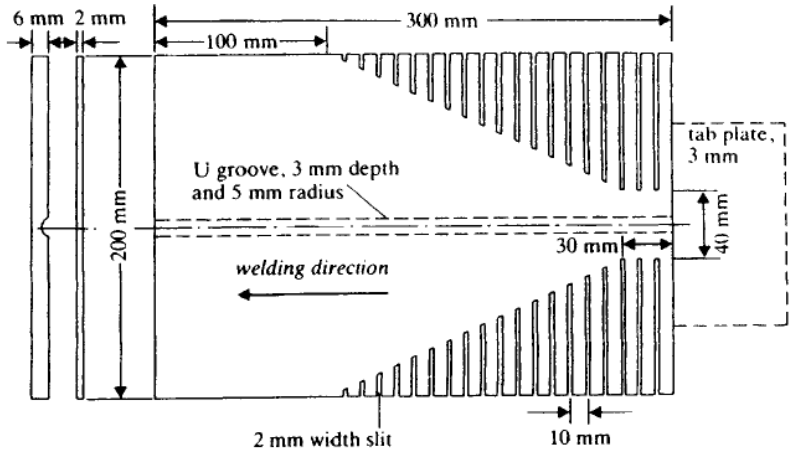

Figure 2.12: Houldcroft sample geometry dimensions of grain refinement of aluminium alloy by Matsuda et al., [26], [22].

Kou [5] reporting on this method showed an image (Figure 2.13) by Liptax and Baysinger (1968) that showed eight slots. Dimensions were not indicated. All attempts at tracing the article proved futile.

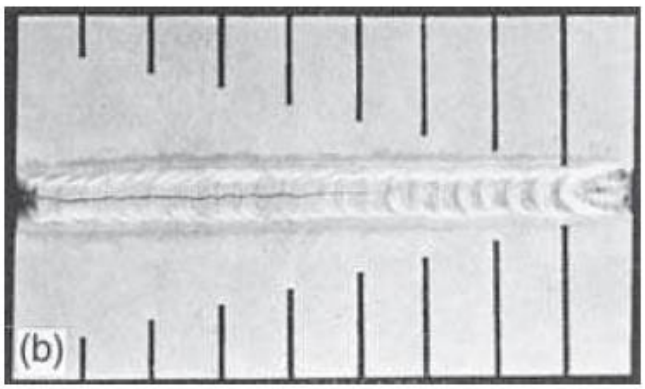

Figure 2.13: Houldcroft specimen with eight slots of aluminium by Liptax and Baysinger [5].

Madhusudhan [27] reported on the use of the Houldcroft test for evaluating the influence of scandium on the weldability of 7010 aluminium alloy. Ten slots were used and the recommended shape and dimensions were different. In determining the susceptibility to hot cracking, a premachined crack initiation slot was used as shown in Figure 2.14. A longitudinal crack propagates along the weld centreline and gradually

comes to a stop due to the slots. The distance to which the crack propagates is used as the index of the hot cracking susceptibility of the weld.

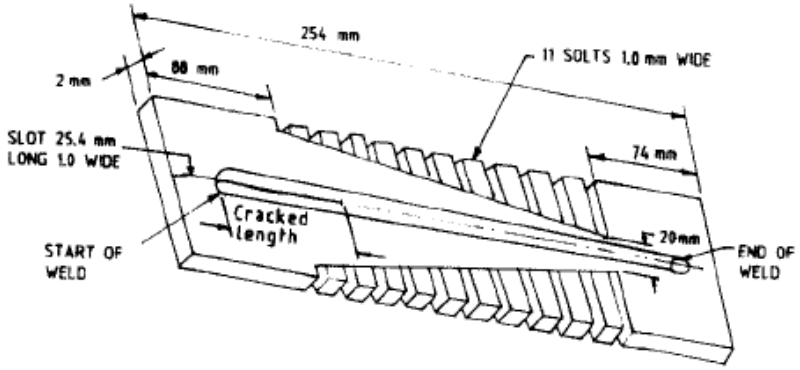

Figure 2.14: Houldcroft dimensions for evaluating the weldability of scandium in aluminium alloy used by Madhusudham [27].

The susceptibility of magnesium alloys to hot cracking has been ascertained using the Houldcroft test as shown in Figure 2.15 [28].

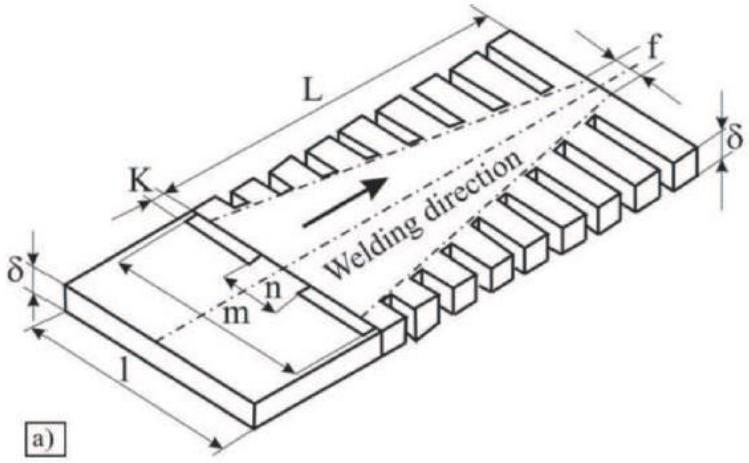

Figure 2.15: Dimensions of the Houldcroft sample of magnesium alloy used by Ademaic [28].

It can be seen that the shape was similar to that in Figure 2.9 in section 2.5.1 but the dimensions and number of slots were different. In measuring the susceptibility to cracking, the ratio of the crack length to the length of the sample was taken [28].

Safari et al. [29] simulated hot cracking using Houldcroft plate dimensions without slots as shown in Figures 2.16 & 2.17 with a trapezoidal sample.

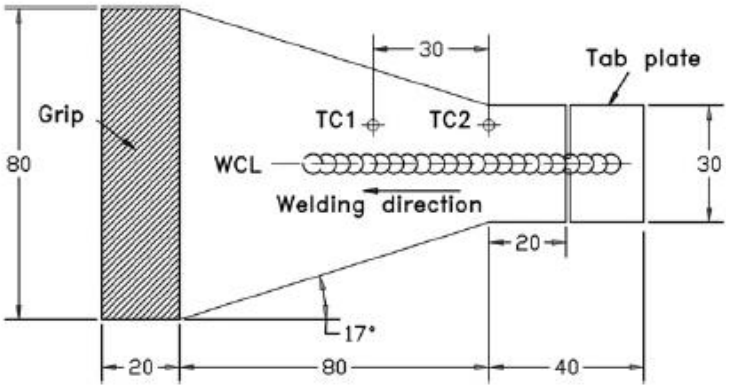

Figure 2.16: Schematic dimensions of a sample used to evaluate the cracking susceptibility of AISI 310 material by Safari et al [29].

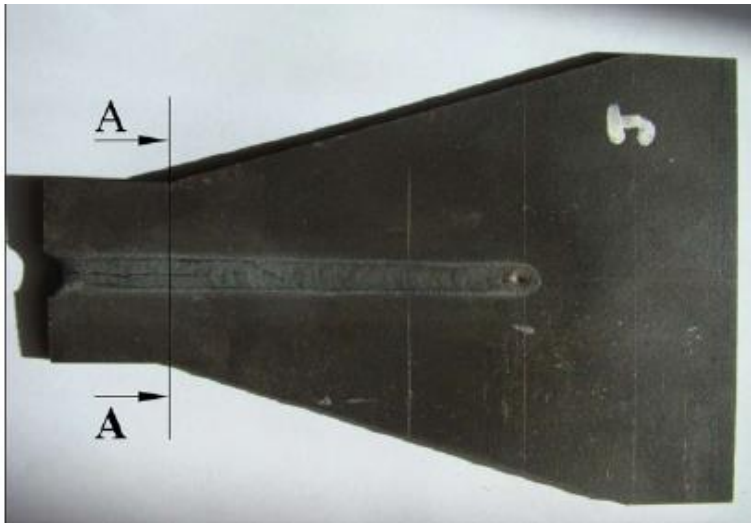

Figure 2.17: Actual sample of AISI 310 material (image shows no dimensions) by Safari et al [29].

Table 2.1 presents the different dimensions of self-restraint Houldcroft samples. It is seen that the materials tested using the Houldcroft method have different lengths, widths and number of slots.

Table 2.1: Tabulation of dimensions of self-restrained samples used to evaluate susceptibility to hot cracking

Reference	Figure number	Alloy type	Thickness (mm)	Length of sample (L) (mm)	Width of sample (W) (mm)	W/L ratio	No. of slots	Width of slots (mm)	Weld direction
Campbell & Walsh, 1993	2.9	No stated	N/K (1)	76.2	44.5	0.58	9	0.8	Normal (2)
Lancaster 1999	2.11	Al	N/K	100	32	0.32	7	0.8	Normal
Lancaster 1999	2.12	Al	N/K	300	200	0.67	19	2	Opposite
Kou 2003b	2.13	Al	N/K	N/K	N/K		8	N/K	Normal
Madhusudham 2005	2.14	Al	2	254	Not given		11	1	Normal
Adamiec 2011	2.15	Mg	4	131	78	0.60	8	1	Normal
Safari et al. 2012	2.16 & 2.17	AISI 310	N/K	120	80	0.67	N/K	N/K	Opposite
Summary			2 - 4	76.2 - 300	32 - 200	0.32 – 0.67	7 - 19	0.8 - 2	Various
This study	2.18	FSS	2	90	36	0.40	8	1	Normal

(1) N/K - value not known. (2) Normal: the usual welding direction was from position of high restraint to position of low restraint. (3) FSS = ferritic stainless steel.

From Table 2.1, there was a wide variety of geometries used for the Houldcroft test. The dimensions for the Houldcroft experiment in this project were chosen and calculated as seen in Figure 2.18. The width and length were chosen based on the as received experimental samples which had dimensions of 40 × 100 mm. The ratio of width (36 mm) to length (90 mm) was 0.4, which was within the range of 0.32 and 0.67 [Table 2.1] [5, 22, 25, 27-28]. The dimensional values were calculated based on the ratios in Figure 2.9 and the other modifications done as shown in Table 2.2.

Table 2.2: Houldcroft dimensions used in the current study

Theoretical sample dimensions in Figure 2.7 (mm)		**Actual sample dimensions (mm)**
Width (CD)	44.5	36
Length (AC)	76	90
Slot width	0.8	1
High restraint dimension (IJ)	38	$\frac{IJ}{CD} = \frac{38}{44.5} = 0.854 \times 36 = 30.74 \approx 30$
Low restraint dimension (KL)	6.4	$\frac{KL}{CD} = \frac{6.4}{44.5} = 0.144 \times 36 = 5.178 \approx 5$
Slotted length (AB)	67	$\frac{AB}{AC} = \frac{67}{76} = 0.882 \times 90 = 79.34$
Number of slots	9	8

The following observations could be made from Table 2.2:

- The theoretical/original slot distances were 0.8 mm each but it was approximated to 1 mm in the current study.
- The length of the specimen was ninety (90) mm and the ratio of length AC to the slot's length AB as noted in Table 2.2, was 0.882 in the current study. Using eight (8) slots of nine (9) mm equalled seventy-two (72) mm which was less than the slotted length of 79.34 mm. Nine (9) slots would require a greater length of 81 mm (Figure 2.18). Therefore, eight (8) slots were used.

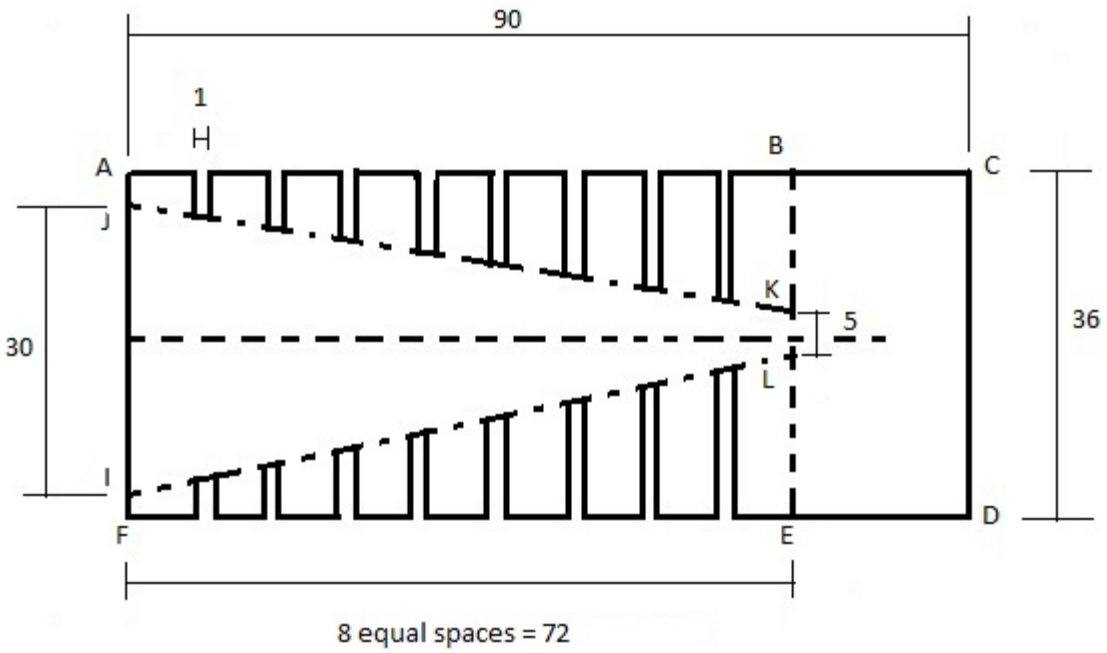

Figure 2.18: Schematic dimensions of the modified Houldcroft sample used in the current study.

2.5.3 Hot tensile tests

Hot tensile tests can be used to simulate the welding operation in which the specimen is quickly heated to just below the melting temperature and quickly cooled again, similar to temperature gradients experienced during welding [3]. The Gleeble (Figure 2.19) has a readily programmed computer interface system which gives reference signals for closed loop control of both thermal and mechanical operations. Heating is by flow of low-frequency alternating current in the specimen. Heating rates of up to 20,000°C/s can be obtained [25, 30]. The material, usually a round tensile specimen, is held in a pair of water-cooled copper grips, one fixed and the other movable and heated by its own resistance to the passage of a preprogrammed cycle of current from a power transformer [16, 31].

Solidification cracking susceptibility using a Gleeble involves controlled melting and solidification of a rod-like specimen. The central portion of the specimen is protected by a quartz sleeve and heated above the solidus temperature of the specimen to melt or

partially melt. The molten metal is kept from flowing out of the crucible by the quartz tube. The thermal gradient between the molten metal and the mounting jaws are controlled by the thermal cycle to simulate real welding. The hot ductility is measured after solidification using a tensile test [19].

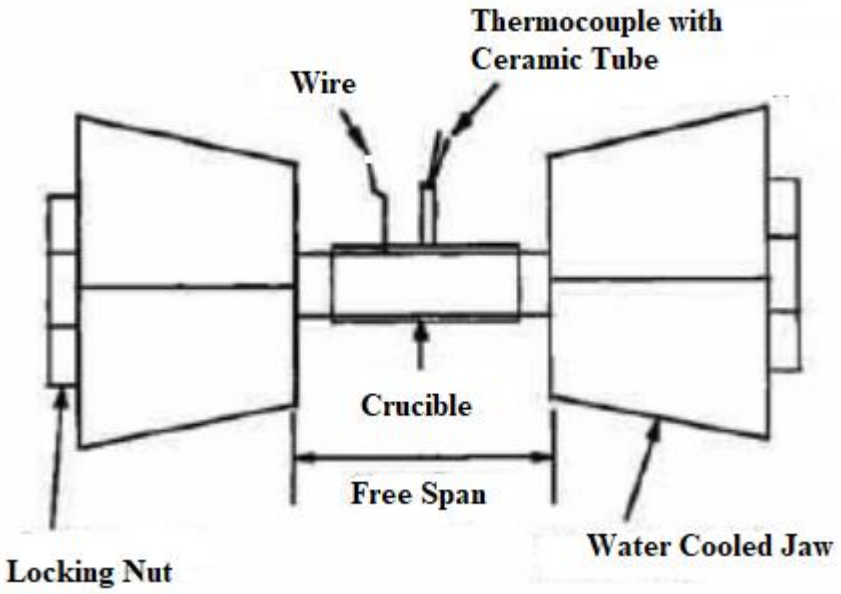

Figure 2.19: Schematic Gleeble set up for controlled melting and solidification study [19].

During simulation using the Gleeble, the specimen may be subjected to high temperature deformation which affects the mechanical properties. The steel undergoes a softening process after being subjected to strain and time. Recrystallization and dynamic recovery are the two main softening processes. Recrystallization includes static (SRX), metadynamic (MDRX), and dynamic (DRX) recrystallization. Static recrystallization occurs after deformation while recrystallization under stress is dynamic recrystallization. Recrystallization might start during deformation and is completed through the growth of dynamically nucleated grains [32-33].

Dynamic recovery is the reorganization of dislocations into a lower energy configuration. This is observed in the early stages of deformation and this continuous

throughout the deformation. The ease of cross-slip in high stacking fault energy materials, like ferritic stainless steels, produces dynamic recovery. The rapid rearrangement of the dislocations in ferritic stainless steels results in work hardening, which is balanced with softening at high temperatures, and this leads to a steady state. After reaching the maximum attainable level during dynamic recovery, the remaining stored energy (which is lower than the amount of energy input by deformation) is used during dynamic recrystallization. The energy input in most steel systems in the austenitic region is higher than that given off during dynamic recovery. Nucleation of new strain-free grains occur during the deformation when the energy level reaches a critical point and this is known as dynamic recrystallization. However, in most high stacking fault energy materials, the critical energy is not reached due to the high softening achieved by dynamic recovery, making dynamic recrystallization difficult to observe. In such materials, the flow curve is the most common method used to determine dynamic recrystallization. Such flow curves are characterized by the presence of a peak (or peaks) stress-strain curve, followed by a steady state (Figure 2.20) [34].

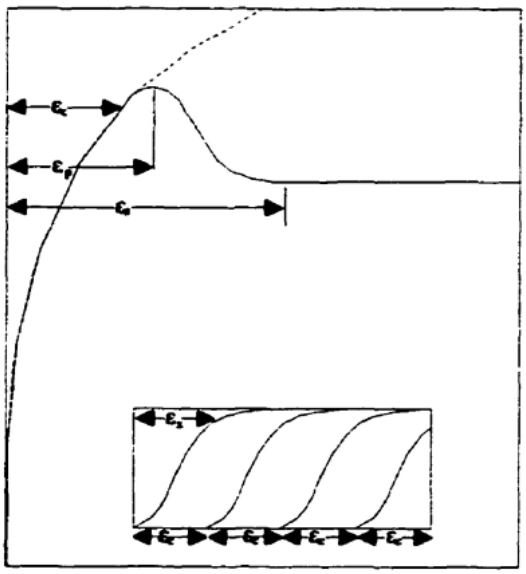

Figure 2.20: Stress-strain curve illustrating salient points of dynamic recrystallization [34].

2.5.4 Externally applied load tests

In this method, a load is applied whilst welding the specimen and the load is varied to change the stress state to reveal the extent of cracking [23]. Savage & Lundin [35] developed the Varestraint (VAriable-Restraint) testing (Figures 2.21 & 2.22). A weld is deposited on the test specimen which is bent during welding. The bending line is either parallel to or transverse to the welding direction. The measure of crack sensitivity is the amount of applied strain and the maximum crack length, the number of cracks and the accumulated total crack length [3, 5, 14]. Lundin et al. [24] reported that the Varestraint test is reproducible when using autogenous GTAW. The modified Varestraint-Transvarestraint (MVT) test has specific dimensions as reported in section 2.4.5 whilst the other Varestraint tests do not have specific dimensions. The Varestraint method has been used by many researchers to evaluate susceptibility to solidification cracking. Materials evaluated using the Varestraint method include Haynes HR-160 alloy, carbon steels, various grades of austenitic stainless steels, alloy C-22, aluminium alloys, Si & Al-Si killed steels, duplex stainless steels, ferritic stainless steels and alloy 800 Ni-Cr [7–9, 12, 14, 20, 29, 36–39].

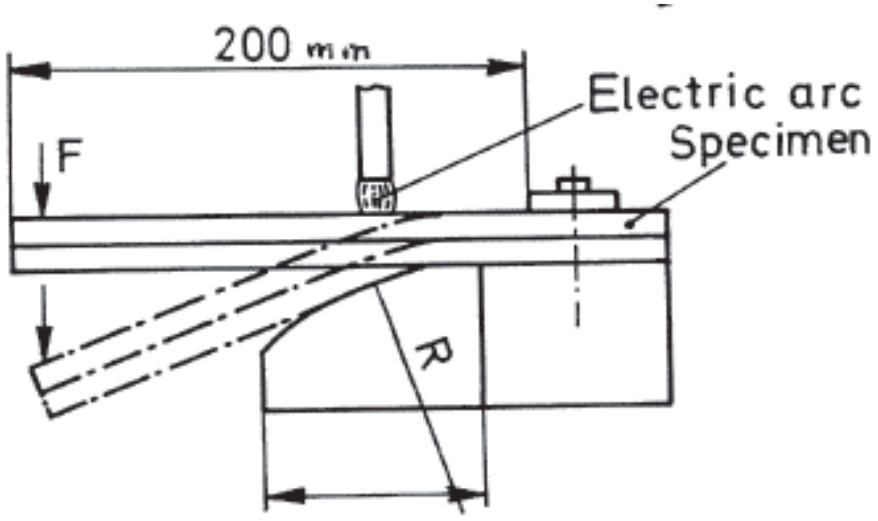

Figure 2.21: Varestraint test [3].

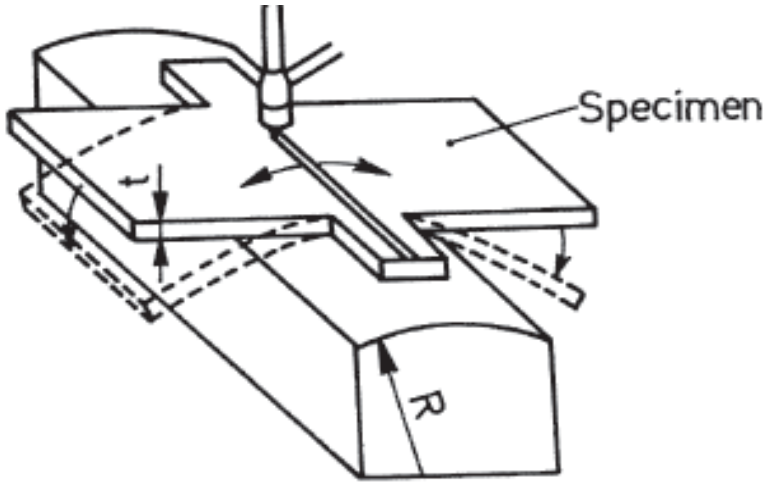

Figure 2.22: Trans-Varestraint [3].

The Program Controlled Deformation Cracking Test (PVR Test) consists of a flat tensile material clamped into a horizontal tensile testing machine and loaded to the yield point as shown in Figure 2.23. A weld is deposited in the flat position and is subjected to plastic deformation with a certain programmed rate of elongation. It is programmed to keep the elongation rate either constant or varied. After welding, the specimen is air cooled to ambient temperature. The rate of elongation present at the point where hot cracking appeared is determined and is used as a measure of the hot cracking susceptibility of the material [3]. Nickel base alloys, austenitic stainless steels, ferritic stainless steels, and TWIP steels are some materials examined for weld solidification cracking by using the PVR test [39].

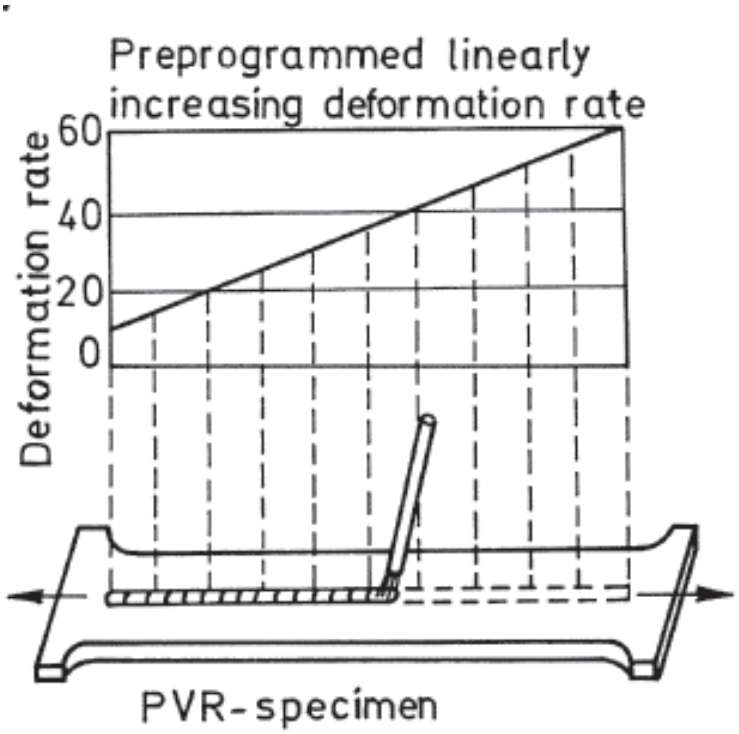

Figure 2.23: PVR test with programmable rate of deformation [3].

Figure 2.24 shows a Sigmajig test which uses a 50 × 50 mm sheet specimen in which a transverse normal stress is applied. The stress is increased with each specimen for centreline cracking to occur as an autogenous GTAW weld is made along the longitudinal centreline. The hot cracking susceptibility is quantified by reaching a threshold stress level necessary to cause 100% crack. The Sigmajig test is particularly useful when thin sheets of 2 mm must be evaluated [23].

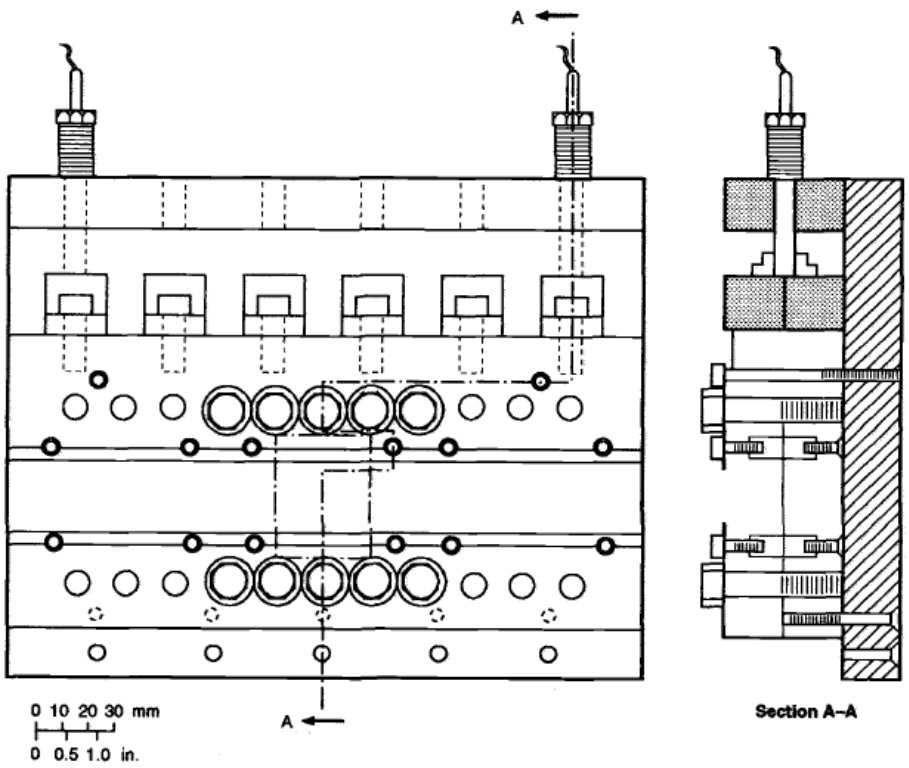

Figure 2.24: Relationship of 50 by 50 mm sheet specimen to apparatus used in the Sigmajig test [23].

In the Murex test, two test pieces are welded and five seconds later, the weld is twisted with a variable rotational/angular speed (Figure 2.25). The crack length produced at a certain twisting rate is defined as a quantitative measure of the susceptibility of the material to solidification cracking as the weld metal is deformed during solidification and cooling [3].

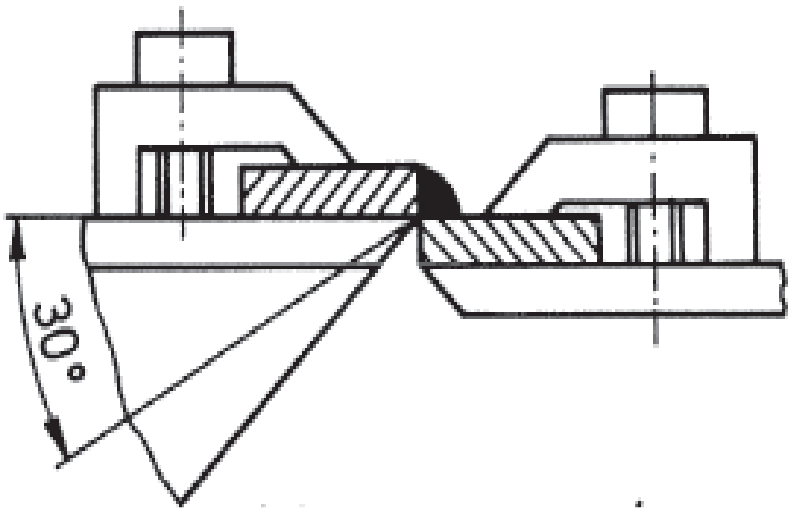

Figure 2.25: Murex test [3].

2.5.5 Modified Varestraint-Transvarestraint (MVT) Test

As reported in section 2.5.2, a self-restraint test is used for evaluation of weld solidification cracking susceptibility for this study. Most researchers use the Varestraint test for solidification cracking. For this study, one of the Varestraint methods was used and since the University of Pretoria, South Africa, does not have the equipment, BAM was contacted. Access to MVT equipment was made available by BAM, the Federal Institute of Material Testing, Germany.

In certain weldability tests where strain is used, the maximum crack length measured corresponds to a certain temperature range which may be equal or less than the solidification range [21]. In the Varestraint testing method, the presence of tensile stresses and a susceptible microstructure in the weld metal or HAZ affect cracking of weldments [39-40].

In the trans-Varestraint test, the solidification cracking temperature range (SCTR) is a subset of BTR and is a measure of the strain and the maximum crack length [40]. At a certain saturated strain level, the maximum crack distance (MCD) becomes independent of the applied strain. The typical strain range over which samples are

tested is 0 - 7%. Threshold strain levels range from 0.5 to 2% and saturated strain levels for most fully austenitic and Ni-base alloys are between 5 and 7%. A thermocouple is plunged into the weld pool to determine the cooling rate through the solidification temperature range and the SCTR is calculated as follows,

$$SCTR = [Cooling\ Rate] \times [\frac{MCD}{V}] \quad (2.2)$$

where V is the solidification velocity,

MCD = maximum crack distance.

The higher the SCTR value, the more susceptible that material is to solidification cracking [16].

In the Modified Varestraint-Transvarestraint (MVT) test, specimens of 10 × 40 × 100 mm dimensions are cut and gas tungsten arc welding (GTAW) is used to remelt a machined surface. The sample is bent at a constant rate around a die by a constant strain of well-defined level and rate as the arc passes a predefined point. Hot cracks form during bending at or near the sample surface. Cracks, if present, are detected during visual examination at a magnification of ×25. A plot of total crack length versus bending strain is used to determine the solidification cracking susceptibility of the material [3, 41]. In MVT, the SCTR is not evaluated. Some materials tested for susceptibility to solidification cracking under this method are austenitic stainless steels, Ni base alloys, railway steels, and duplex stainless steels [41-42].

CHAPTER THREE - WELDING METALLURGY OF FERRITIC STAINLESS STEELS

3.1 Introduction

This chapter introduces welding and weld metal solidification. The literature on some ferritic stainless steel materials, the phases that precipitate and welding of ferritic stainless steels are also reviewed.

3.2 Welding processes and welding parameters

A heat source sufficiently intense enough to melt the filler metal, if used, and the metal pieces to be joined, comprise the welding processes. In autogenous welding, after locally melting the pieces together and removing the heat source, solidification takes place to join the components without the addition of further material. The addition of a filler material which is metallurgically compatible with the workpieces is used preferably in the case of thicker sections or where gaps may exist [31]. The self-restrained Houldcroft and MVT methods use the GTAW process for investigations and this welding process will be reviewed in the next paragraph.

The gas tungsten arc welding (GTAW) process also known as Tungsten Inert Gas (TIG) in Europe or Wulfram Inert Gas (WIG) in Germany was used for this project, as the industrial process that led to this study used this welding process. GTAW is a process that melts and fuses metals by heating them with an arc established between a non-consumable tungsten electrode and the workpiece. A torch holds the tungsten electrode which is connected to a shielding gas cylinder and a power source terminal. To protect the weld pool and the electrode from the atmosphere, an inert gas is used to shield the arc which can be either argon or helium. GTAW is limited in deposition rates and joint completion rates which are low but has good joint quality, good control, and high arc intensities [5, 31, 43-44].

3.3 Welding speed

The welding speed changes the weld pool shape and the corresponding microstructure. At low welding speeds, the weld pool is elliptical. The weld pool becomes teardrop shaped at high welding speeds. Columnar grains, which are mostly straight at high speeds, result from the teardrop weld pool shape which is also almost straight and the grains grow perpendicular to the pool boundary. The trailing boundary of an elliptical weld pool is curved and since the columnar grains grow perpendicular to the pool boundary, the columnar grains are also curved. Axial grains can also be found in the fusion region. These axial grains start from the fusion boundary and grow along the length of the weld and block the columnar grains growing from the pool boundary inwards towards the centre [5, 16, 22]. Figure 3.1 shows a schematic representation of the welding speed of a macroscopic weld pool shape.

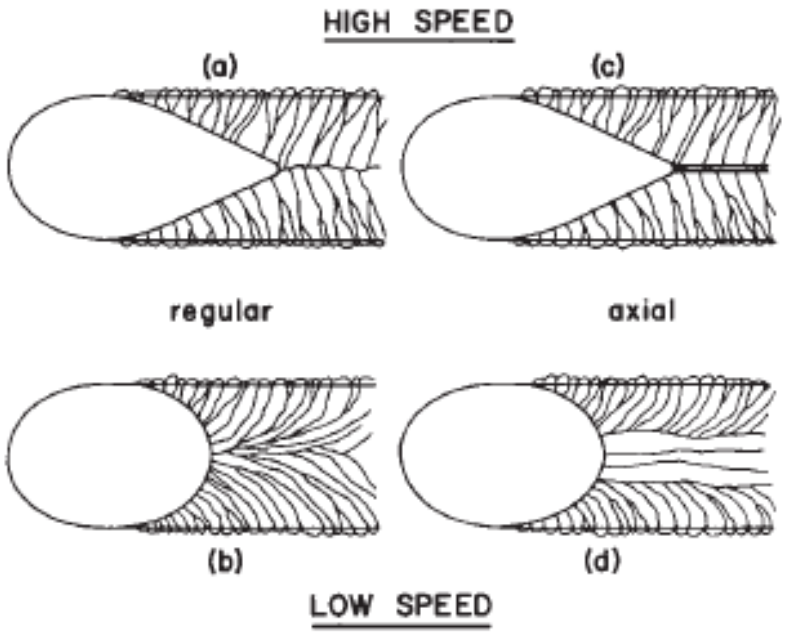

Figure 3.1: Effect of welding speed on columnar grain structure [5].

3.4 Weld metal solidification

The welding pool can be seen as a moving solid-liquid interface whereby solid metal is consumed in the front half and solidifies in the rear half. The microstructure of the

weld pool depends on the chemistry and cooling rate conditions during welding whereas the macrostructure depends on the crystallographic direction of the grains subject to the thermal gradients of the weld pool [16].

When a molten liquid cools, solid nuclei in the melt form and grow into crystals which eventually form the grain structure. Two main mechanisms of solidification are homogeneous and heterogeneous. In homogeneous solidification, there is formation of nuclei of the new phase uniformly throughout the liquid whereas in heterogeneous solidification, the nuclei form at structural inhomogeneities, like container surfaces, insoluble impurities, grain boundaries, dislocations, and so on [16]. During autogenous welding, the atoms arrange on the substrate grains without changing the existing crystallographic orientation from the liquid metal during solidification of weld metal. This is termed epitaxial growth and is shown schematically in Figure 3.2. The growth direction of the cells or dendrites is <100> for face centered cubic or body centered cubic like ferritic stainless steels. These are the "easy growth" directions [5, 16]. The crystals join together and meet at grain boundaries to complete solidification [16, 45].

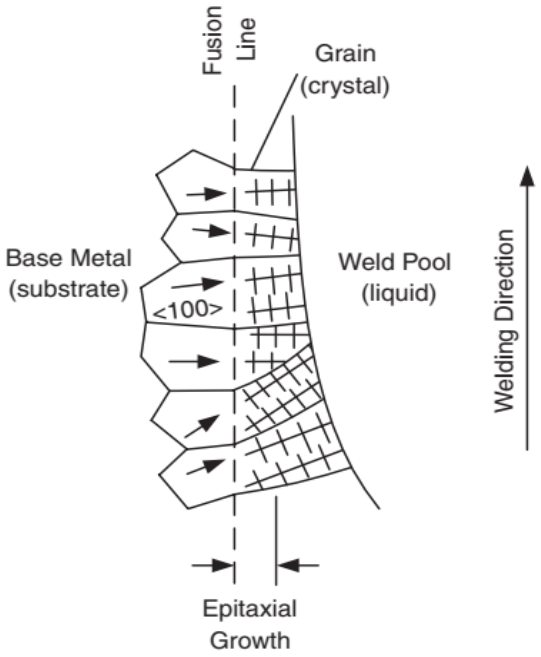

Figure 3.2: Epitaxial growth of weld metal near fusion line [5].

The solidification front determines the type of substructure that appears in the weld metal. The solute content of the liquid weld metal has an influence on the solidification front and solidification parameter. This parameter is equal to the temperature gradient *G* in the direction of solidification divided by the rate of advance *R* of the solidification front (Figure 3.3). The microstructure becomes more dendritic as the G/R ratio decreases for a given solute content. The increase in freezing time $(GR)^{-1/2}$ increases the dendrite spacings. At high values of $(GR)^{-1/2}$, the structures becomes equiaxed as the dendrites nucleate at a point [5, 22].

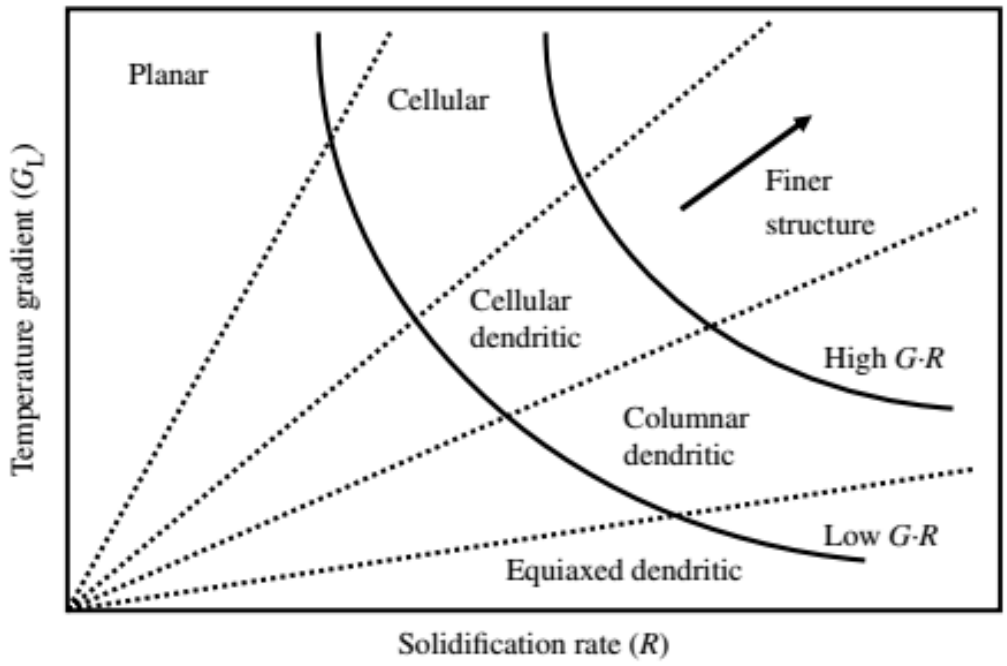

Figure 3.3: Effect of temperature gradient in the liquid, GL, and solidification growth rate, R, on solidification mode [16].

During solidification, a cellular front grows from a planar solidification front. This cellular front may break into either cellular, cellular dendritic, columnar dendritic modes, or a combination of these depending on the solidification conditions (Figure 3.4). In fusion welds, cellular or cellular dendritic growth occurs because the planar front is not stable [16].

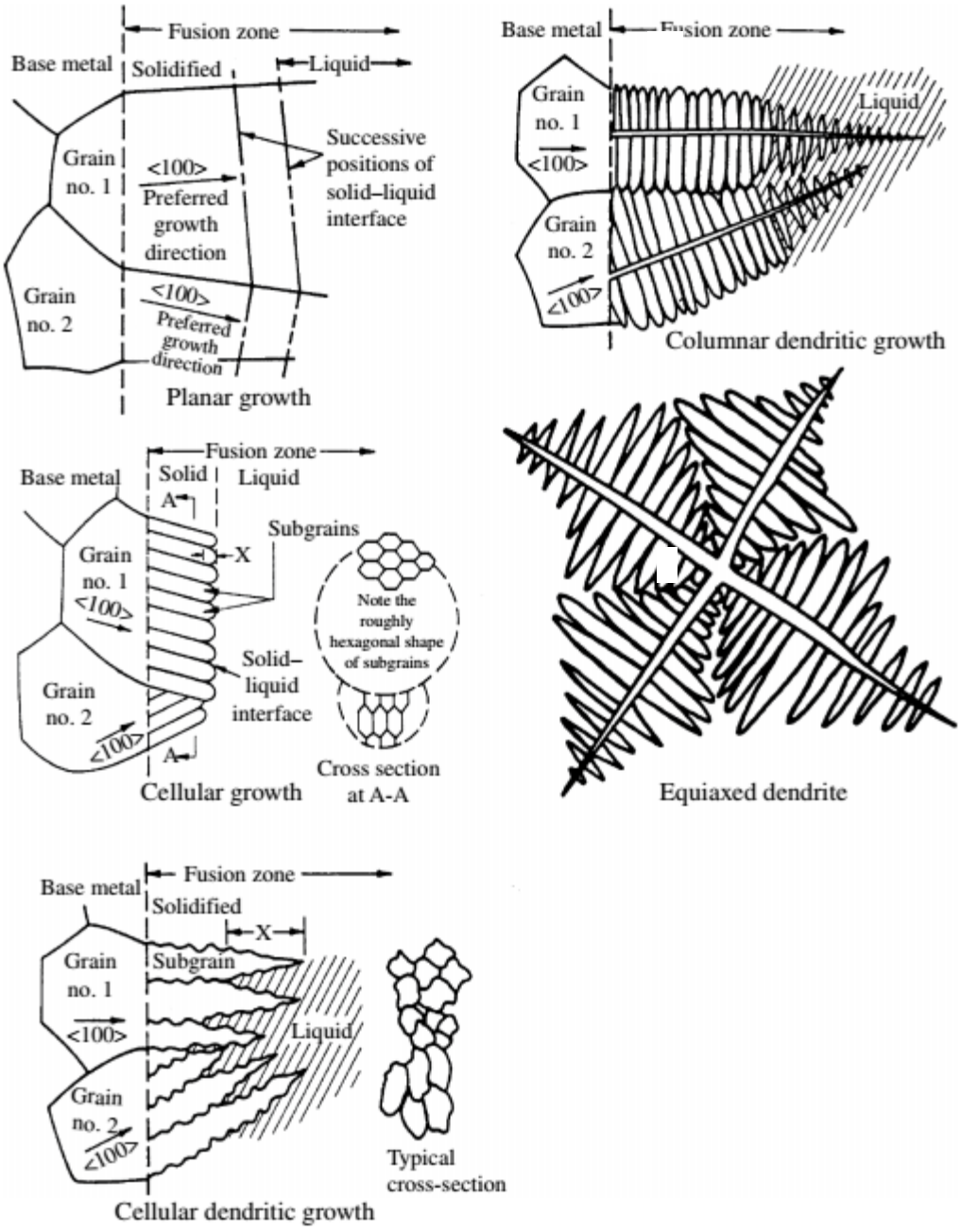

Figure 3.4: Solidification modes that occur in metals [16].

The grain structure of the final solid metal depends on the number of nucleation sites available to the freezing metal. Relatively few solidification sites result in a coarse grained structure and many sites produce a fine grained structure. These grains either

grow approximately equal in all directions, i.e. equiaxed, or long thin grains form in the presence of a steep temperature gradient, i.e. columnar grains [16].

Macroscopic aspects of weld metal solidification

On a macroscopic scale, solidification is dominated, initially, by a planar solidification front. The shape of the weld pool is affected by the heat flow, heat input and welding speed. Epitaxial growth from the surrounding base metal dominates nucleation of autogenous fusion welds and there is no undercooling required. Grain boundaries are continuous as the newly formed grains maintain the same crystal orientation. Nonepitaxial nucleation and growth may occur due to direct introduction of heterogenous nuclei ahead of the solid-liquid (S/L) interface in the fusion zone. The advancing liquid may contain some heterogenous nuclei formed in the liquid which cannot be swept into hotter regions to cause nonepitaxial growth. Different crystal structures of base metal and weld metal produces nonepitaxial nucleation [16].

The composition, local temperature gradient and solidification rate affect the solidification mode. A planar front results from high temperature gradient and low solidification rate. A decrease in the temperature gradient and an increase in solidification rate breaks down the planar front into cellular and dendritic modes. The solidification rate is the same as the welding velocity at the weld centreline, progressively decreases along the S/L interface and approaches zero at the fusion boundary as shown schematically in Figure 3.5 [16].

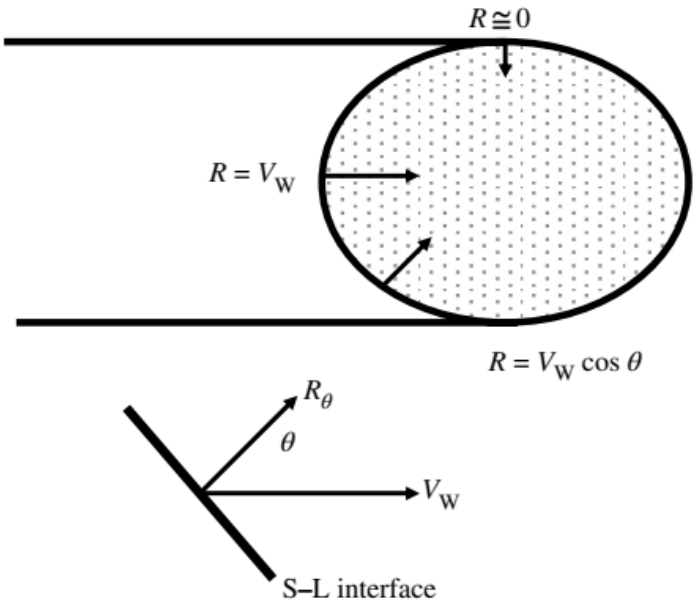

Figure 3.5: Relationship between weld travel speed, VW, and local solidification rate, R [16].

Microscopic aspects of weld solidification

The formation of cells and dendrites and solute redistribution make up the solidification subgrain boundary (SSGB) with a composition different from the bulk structure. SSGBs have low-angle boundaries due to small crystallographic misorientation across these boundaries. Packets of subgrains intersect which result in crystallographic misorientation and are called solidification grain boundaries (SGBs). There are different growth direction and orientation for these packets of subgrains which intersect to produce "high-angle" grain boundaries. Solute redistribution also occurs in SGBs which can form low melting liquids to promote solidification cracking. There is both a compositional and crystallographic component of SGBs that forms at the end of solidification. At times, the crystallographic component of the SGBs migrates away from the compositional component and this is called migrated grain boundary (MGB). The MGBs are characterized by misorientations typically greater than 30° high angle boundary [16]. Figure 3.6 shows the schematic representation of SSGB, SGB and MGB.

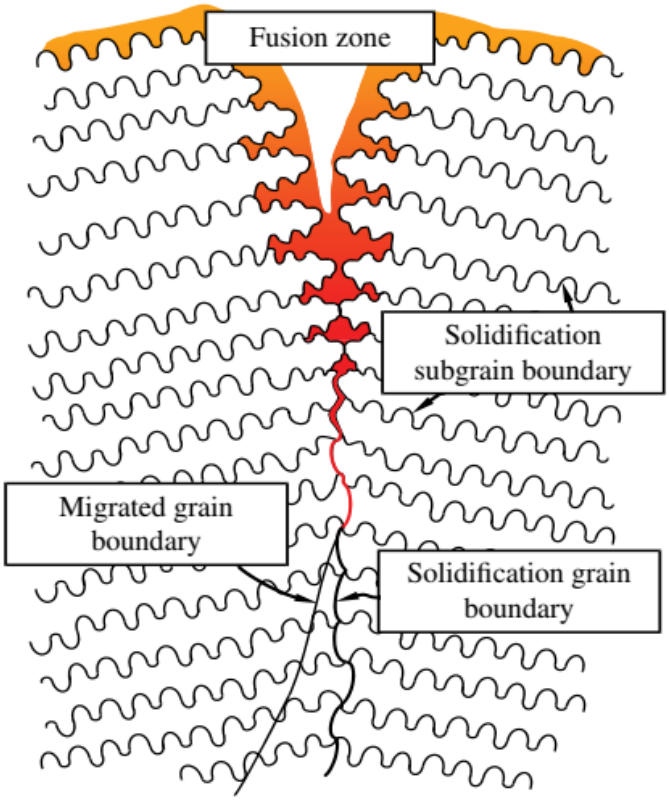

Figure 3.6: Schematic representation of the boundaries in single-phase weld metals [16].

Solute redistribution

The partitioning coefficient ($k = C_S/C_L$), liquidus temperature gradient ($G_L = dT_L/dx$), solidification rate ($R = dx/dt$) and cooling rate ($G_L.R = dT/dx$) are the solidification parameters for describing microstructural development and solute redistribution. The partitioning coefficient is the solid/liquid (S/L) composition ratio in contact with each other. The S/L interface movement is dictated by the solidification rate and the temperature field in advance of the S/L interface, this is the temperature gradient. The product of the solidification rate and temperature gradient ($G_L \cdot R$) influences the dendrite arm spacing [5, 16].

Solidification of molten metals starts with a planar front that becomes unstable as solidification progresses. The planar instability has been attributed to constitutional

supercooling, as proposed by Chalmers. This involves undercooling of the liquid in the S/L interface [5, 16]. The Chalmers theory proposes that solute partitioning takes place in advance of the solidification front. Considering a planar front of an alloy with composition C_0, if the temperature of the liquid is above the liquidus line, then the liquid boundary layer is thermodynamically stable (Figure 3.7). The planar front breaks down to cellular or dendritic if the layer is below the liquidus temperature and solid and liquid coexist [5, 16]. Figure 3.3 shows the region of constitutional supercooling where the actual liquid temperature is below the liquidus temperature.

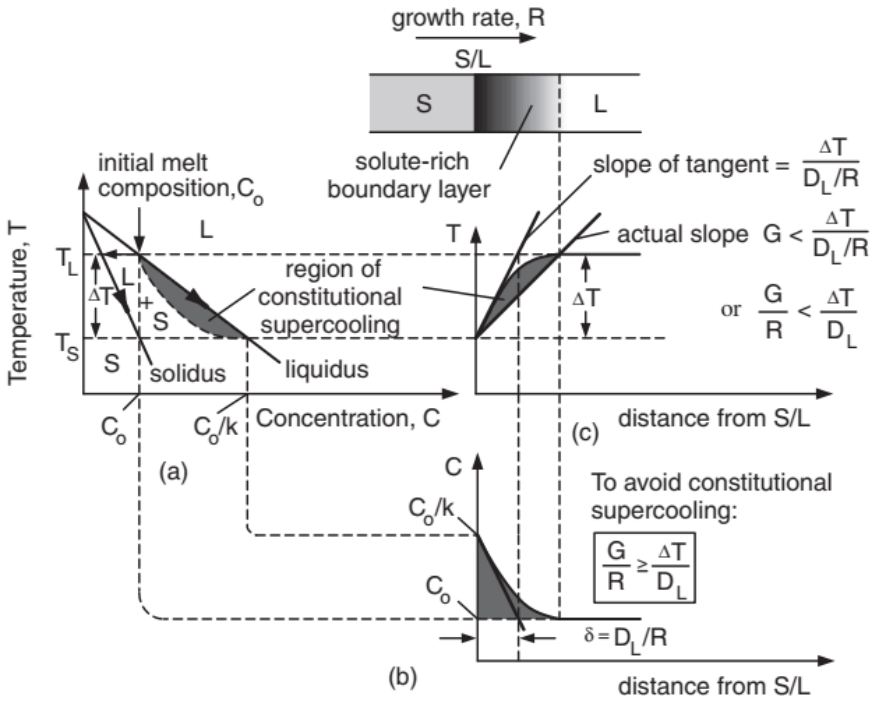

Figure 3.7: Constitutional supercooling: (a) phase diagram; (b) composition profile in liquid; (c) liquidus temperature profile in liquid [5].

During solidification of an alloy, solute redistribution occurs between liquid and solid as temperature decreases. Mass transport of solute atoms to maintain equilibrium at the solidification interface occurs between the liquid and solid. The mass transport of solute occurs in the liquid through mixing and in the solid through diffusion. For non-equilibrium cooling as in welding, diffusion of solute in the solid is negligible and mixing in the liquid is considered to be diffusion due to the small distances (microns)

solute travel. Under equilibrium cooling, there is no restriction of mass transport of solute in the liquid and solid. When there is restriction in mass transport in both liquid and solid or both, nonequilibrium weld solidification occurs [5, 16].

Three distinct regions of solute redistribution during macroscopic weld solidification are an initial transient, a steady-state region and a final transient. These were mathematically modelled by Smith *et al*. to reveal solute redistribution during macroscopic weld solidification. The composition of the initial solid in contact with the liquid of nominal composition C_0 is kC_0. The solid composition reaches C_0 when the initial transient ends. Flemings modelled the solute profiles for the solid in the initial transient and the liquid in the steady state region as

$$C_s = C_0\left[1-(1-k)exp\left(\frac{-kRx_c}{D_L}\right)\right] \quad \text{3.1}$$

$$C_s = C_0\left[1+\left(\frac{1-k}{k}\right)exp\left(\frac{-Rx_c'}{D_L}\right)\right] \quad \text{3.2}$$

Where D_L is the diffusion distance, R, the solidification rate and χ_c represents a "characteristic distance." Steady state solidification dominates the solidification process under macroscopic solidification. This is due to solid of composition C_0 forming from liquid composition C_0/k using microscopic equilibrium at the S/L interface. The solid composition again rises (for $k < 1$) as the final liquid is consumed and this is known as "dumping" of solute. The dimension of the final transient region is a few microns or less (Figure 3.8). There is depletion of solute in the initial transient and this must equal the solute enrichment in the final transient. Along SGBs and trailing edge of the weld pool, there is solute redistribution under macroscopic weld solidification. In the final transient, the segregation in the liquid results in an increase in alloying content of the last-to-solidify liquid, and an associated increase in the alloying content of the solid. Thus, the liquid and solid are enriched in solute for alloy systems with decrease in temperature within the solidification temperature range. This can form low-melting liquid films along the boundaries to potentially cause weld solidification cracking [16].

For microscopic solidification, there is complete mixing in the liquid considering solute redistribution. In this process, the liquid composition is constant while there is no diffusion in the solid. There is no solute gradient as diffusion in the liquid is rapid. The Scheil equation, also known as the nonequilibrium lever law, is used to model microscopic solute redistribution. The solidification front is considered to be planar on a microscopic scale since the solid does not change its composition by diffusion once formed. The Scheil equation is

$$C_s = kC_0(1 - f_s)^{k-1} \quad \text{.....3.3}$$

Where f_s is the fraction solidified and k is the solute distribution coefficient. For $k < 1$, the composition of the liquid is uniform and that of the initial solid is kC_0. There is an increase in the solid composition from the outward cell core and rises rapidly at the end of solidification [16].

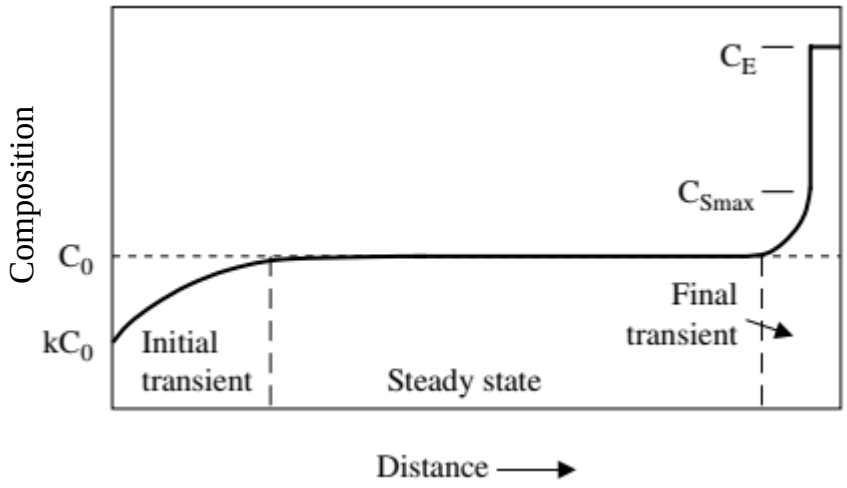

Figure 3.8: Solute profiles for macroscopic weld solidification showing the initial transient, steady state region and final transient [16].

3.5 Stainless steels

The chromium content in stainless steels results in the formation of a very stable passive surface oxide film, chromium (III) oxide (Cr_2O_3), which prevents oxidation and corrosion of the metal underneath in oxidizing conditions when alloyed with iron. This happens as some of the chromium reacts to form carbides or other compounds, reducing

the amount needed to support a continuous protective oxide. Nickel, molybdenum, copper, titanium, aluminium, silicon, niobium, nitrogen, sulphur, and selenium can be added to improve mechanical properties and corrosion resistance or to control the microstructure [3-4, 6]. It is reported that all stainless steels with a carbon content above 0.001% are susceptible to carbide precipitation [3, 5].

The focus of this project is on ferritic stainless steels and this stainless steel type is considered in more detail.

3.6 Ferritic stainless steels

Ferritic stainless steels are iron-chromium alloys containing about 12 – 30 wt% Cr with a carbon content of 0.25% maximum. Chromium as a powerful ferrite former suppresses the austenite phase and expands the α-ferrite phase field. Ferritic stainless steels usually do not undergo the γ-austenite – α-ferrite transformation. Ferritic stainless steels are magnetic and find applications in chemical plants, pulp and paper mills, refineries, automobile trim, catalytic converters and decorative purposes [4]. Ferritic stainless steels are a cheaper alternative to austenitic stainless steels because Ni is not added as an alloying element [3-5, 46-47].

There are low - (10.5-12.5 wt% Cr), medium - (16-18 wt% Cr), high - (>25 wt% Cr), and super-ferritic grades. Ferritic stainless steels are classified as Group I, II and III with the group I being standard, group II being modified versions of the standard, and group III have very low interstitial elements. The group I are the medium chromium steels with relatively high carbon contents and are used primarily for their resistance to corrosion and oxidation at elevated temperatures. These wrought alloys when welded, have a lower toughness, corrosion resistance, and ductility due to grain growth and martensite formation. The group II steels have lower levels of chromium and carbon with ferrite stabilizers (Ti or Nb) added to ‘tie up’ carbon and nitrogen to promote ferrite stability. High chromium, low interstitial (C + N) contents, and low impurity levels constitute group III and are for specific applications with different trade names [4, 25].

3.6.1 Composition and physical properties of ferritic stainless steels

The compositions of type AISI 430, 436, 439, 441, and 444 ferritic stainless steels are presented in Table 3.1.

Table 3.1: Composition of type AISI 430, 436, 439, 441, and 444 ferritic stainless steels [6]

Type	UNS designation	Composition (mass %)							
		C	Mn	Si	Cr	Ni	P	S	Other
430	S43000	0.12	1.00	1.00	16.0 – 18.0	-	0.04	0.03	
436	S43600	0.12	1.00	1.00	16.0 – 18.0	-	0.04	0.03	0.75-1.25 Mo; 5 × %C min - 0.70 max Nb
439	S43035	0.07	1.00	1.00	17.0 - 19.0	0.50	0.04	0.03	0.15 Al; 12 × %C min - 1.10 Ti
441	S44100	0.03	1.00	1.00	17.5 - 19.5	1.00	0.04	0.04	0.3 + 9 × (%C) min to 0.90 max Nb; 0.1-0.5 Ti; 0.03 N
444	S44400	0.025	1.00	1.00	17.5 - 19.5	1.00	0.04	0.03	1.75 – 2.50 Mo; 0.025N; 0.2+4 (%C+%N) min – 0.8 max (Ti+Nb)

From Table 3.1, the unstabilized ferritic stainless steel (Type 430) has neither titanium nor niobium additions. The type AISI 436 has Nb as a stabilizing element and 439 has

Ti for stabilization. Type 441 has both Ti and Nb as stabilizing elements and so is referred to as a dual stabilized grade. The type 444 is Ti and Nb, stabilized and contains Mo. Ti addition to ferritic stainless steel improves pitting resistance, pins the grain boundaries of the heat affected zones, and results in fine grained equiaxed structure. Excess Ti strengthens the ferritic stainless steels by solid solution strengthening. Ti addition can produce a poor surface finish of the steel sheet. Nb addition in ferritic stainless steels forms small spherical precipitates which toughens the steel, do not show poor surface finish, and result in low ductility of welded joints [47]. Nb is a high temperature solid solution strengthener in ferritic stainless steels [48-50].

3.6.2 Metallurgical characteristics of ferritic stainless steels

The iron-chromium phase diagram is shown in Figure 3.9. A gamma loop exists at lower concentrations where austenite is present in the temperature range of 912 to 1394°C. A fully ferritic microstructure is obtained at elevated temperatures for alloys with greater than 12.7 wt% Cr. If the steel contains less than 12.7 wt% Cr, some austenite forms at elevated temperatures. Alloys less than 12 wt% Cr will be fully austenitic and rapid cooling can transform the austenite to martensite [4].

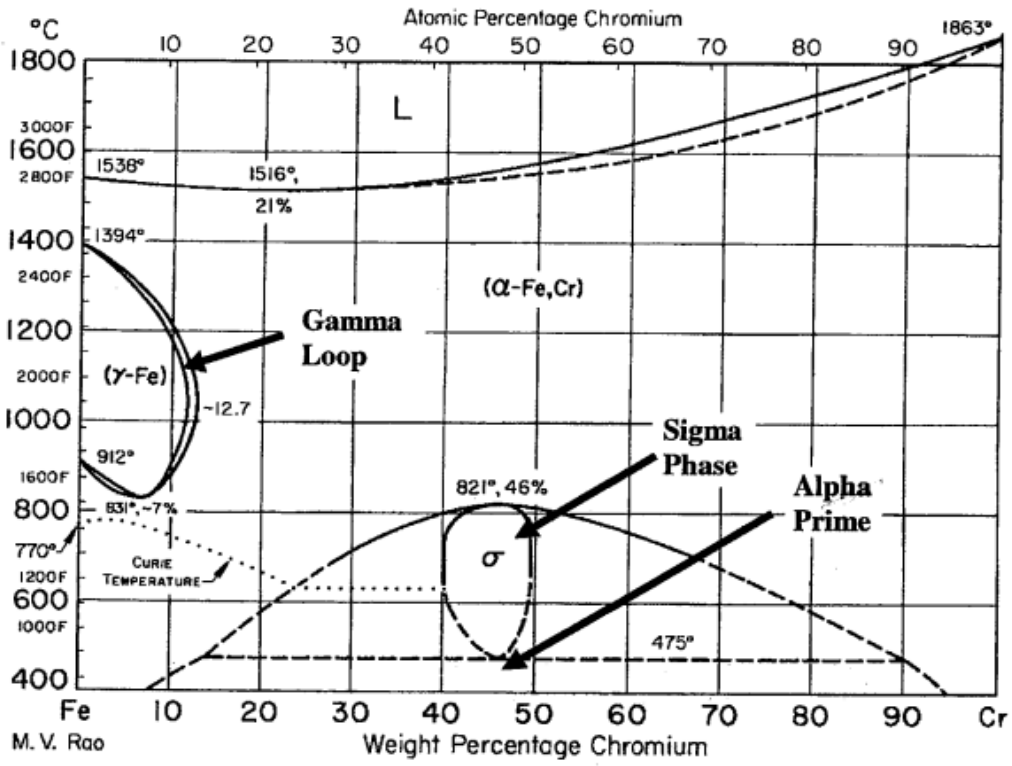

Figure 3.9: The iron-chromium phase diagram [4].

Ferritic stainless steels are prone to the precipitation of undesirable intermetallic phases at certain temperatures. Tetragonal sigma (σ) phase based on the compound FeCr can precipitate for the higher Cr contents at about 440°C which embrittles the steel but it is very slow to form. Mo increases the temperature of formation of σ phase to 1000°C but forms the complex chi (χ) phase which has a nominal composition of $Fe_{36}Cr_{12}Mo_{10}$. The ferritic stainless steels can be cooled rapidly to suppress the formation of intermetallic phases. Welded ferritic stainless steels containing high Cr contents and Mo should not be used at about 850°C [16, 25].

With Cr levels higher than 12%, the ferritic stainless steel is prone to "475°C embrittlement" due to the decomposition of the Fe-Cr system into a mixture of iron-rich alpha (α) and chromium-rich alpha-prime (α') phases from the iron-chromium ferrite phase through a spinodal transformation, which is often called "alpha prime

embrittlement". There is the additional precipitation of chromium carbides and nitrides which play significant roles in 475°C embrittlement [16, 25].

High temperature embrittlement (HTE) is the lack of ductility at high temperatures when no molten phase is present. This occurs when the steel is exposed to above 0.7 T_m (melting point) with metallurgical changes taking place, which can result in severe loss in corrosion resistance. HTE occurs during thermo-mechanical operations or welding. The susceptibility of ferritic stainless steels to HTE depends on the composition, particularly chromium and interstitial concentration, and grain size but low chromium and stabilized grades are relatively insensitive [4].

Rapid grain growth occurs for ferritic stainless steels that are held above 1100°C in the δ-ferrite region. The grain boundaries become enriched with impurities and the ductile-to-brittle transition temperature (DBTT) increases. A related phenomenon is the joining of coarse ferrite grains meeting at the weld centreline, leading to solidification cracking [4]. The ferritic stainless steels are sensitive to cooling rate and this causes precipitation of carbides and nitrides in the matrix to be distributed randomly or aligned along grain boundaries [25].

In general, ferritic stainless steels have low solubility for carbon at ambient temperatures. Chromium-rich carbides precipitate as $M_{23}C_6$ and in rare instances also at high carbon contents as M_7C_3 or with Mo present in the steel as M_6C. These carbides have a rich chromium content typically in the range of 42 to 65%, resulting in chromium depleted zones adjacent to the grain boundary precipitates. If the depletion is below 12 wt%, intergranular corrosion attack progresses along the chromium depleted grain boundaries since the corrosion resistance is significantly reduced. The grain boundaries are destroyed and may lead to grain dropping and this is known as sensitization. These can be prevented by reducing either the carbon and nitrogen amounts below certain levels or using titanium, niobium or tantalum as stabilizers [4, 5, 16]. Titanium and niobium have a high affinity for carbon and nitrogen. As such, they are used as stabilizers to arrest carbon and nitrogen in stainless steels by forming stable carbides, nitrides or carbonitrides to prevent sensitization [3, 47].

3.6.3 Ti and Nb iron phase diagrams

Equilibrium phase diagrams are used to study the phase transformations and precipitates that occur in systems. The binary phase diagram of iron-titanium resembles that of iron-niobium. Both Ti and Nb constricts the area of the gamma phase because they are ferrite formers [3]. The iron-titanium binary phase diagram forms an eutectic at 14% titanium at 1289°C, an iron titanide ($FeTi_2$) with approximately 14% Ti (Figure 3.10, Table 3.2). Nb forms a eutectic with Fe at 18.6% Nb with the melting point at 1373°C. The Laves (ε) phase $FeNb_2$ forms between 38 to 51% Nb (Figure 3.11) [3, 51]. The solvus composition of Fe-Ti system is 8.7%Ti and that of Nb is 5.2%Nb (Table 3.2). The Fe-Nb binary phase diagram is characterized by a lower distribution coefficient k, a lower liquidus slope m, and a larger difference the liquidus and the solidus temperature than the Fe-Ti phase diagram (Table 3.2). Stabilised ferritic stainless steels are not binary alloys, and the effect of Nb of Ti on the liquidus and solidus temperature will be more complex than that illustrated in the binary phase diagram and summarised in Table 3.2.

Table 3.2: Eutectic formation of Fe-Ti and Fe-Nb binary alloys

Alloy system	Fe-Ti	Fe-Nb
Solubility of alloying element in BCC phase	8.7%Ti	5.2%Nb
Eutectic composition	14%Ti	18.6%Nb
Eutectic temperature	1289°C	1373°C
Phase in equilibrium with BCC phase at eutectic point	$TiFe_2$	$FeNb_2$ (ε)
Distribution coefficient	k = 8.7/14 = 0.62	k = 5.2/18.6 = 0.28
Slope of liquidus	$m = \frac{1289-1538}{14} = -18°C/\%Ti$	$m = \frac{1373-1538}{18.6} = -8.9°C/\%Nb$
Difference between liquidus and solidus at 1% alloying addition	$\Delta T = mC_0\frac{k-i}{k} = -18.1.\frac{0.62-1}{0.62}$ =11°C	$\Delta T = mC_0\frac{k-i}{k} = -8.9.1.\frac{0.28-1}{0.28}$ = 23°C

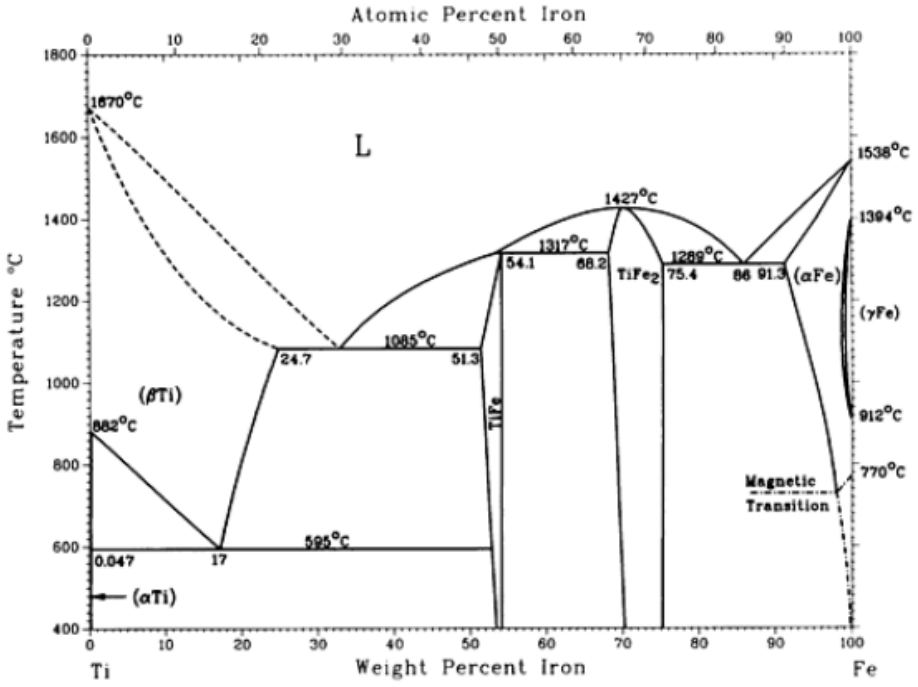

Figure 3.10: The iron-titanium binary phase diagram [51].

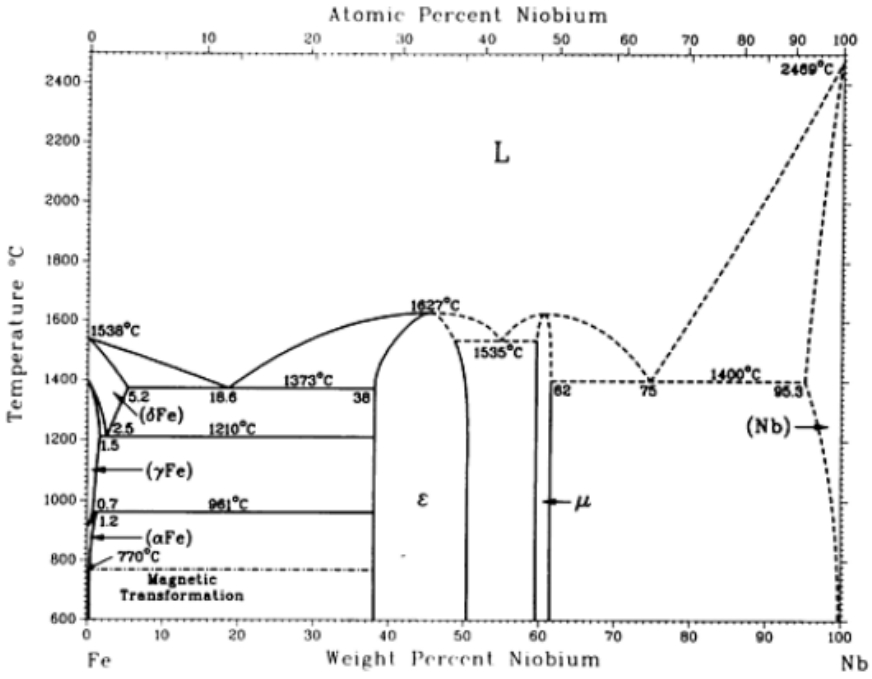

Figure 3.11: The iron-niobium binary phase diagram [51].

3.6.4 Precipitates in ferritic stainless steels

When Ti was added to Nb-bearing ferritic stainless steel, it was observed that fine precipitates of Nb(CN) and TiN were formed. Comparing the two steels, it was reported that the dual stabilized steel had finer grains than a ferritic stainless steel containing only Nb, and no Ti [52].

Nb has been found to form a variety of precipitates, including Nb(C,N) (carbonitride), Fe_2Nb (Laves phase) and Fe_3Nb_3C (M_6C carbide) during service. Thermo-Calc revealed the formation of TiN, Nb(C,N) and Fe_2Nb precipitates after isothermal aging at 800°C of Nb-modified ferritic stainless steel. SEM with EDX showed the precipitation of (Ti,Nb)(C,N) with the TiN that was tetragonal. A greater amount of epitaxial precipitation of NbC on the TiN occurred and a greater amount of Fe_2Nb precipitated at the grain boundaries [53]. Fujita et al. [49] investigated microstructural changes at high temperature of Nb containing ferritic stainless steels. It was observed that more than 0.2 wt% Nb had strength degradations at high temperatures due to Nb

being in solid solution. At a Nb content less than 0.2 wt%, Nb was found in precipitates. The precipitates Nb(C,N), Fe_2Nb and Fe_3Nb_3C were detected after annealing and aging for a short time. For longer aging times, Fe_3Nb_3C had clearer diffraction patterns and Nb(C,N) and Fe_2Nb got weaker during X-ray diffraction patterns measurements.

It is agreed that the coarsening rate of Fe_2Nb is much faster than that of NbC or Nb(C,N) [50, 53]. This is due to the incoherent interface between Fe_2Nb and the Fe matrix, which is in contrast to the semi-coherent interface between NbC and the Fe matrix [50]. Kuzucu et al. [54] noted that $M_{23}C_6$, NbC and sigma phase formed in ferritic stainless steels containing 17–18 wt.% Cr and with an increase in Nb concentration, the micro-hardness of the matrix and the amount of $M_{23}C_6$ decreased and the toughness of the specimen increased.

Yan et al. [55] reported on the addition of Nb and Ti as dual stabilizers in ferritic stainless steels. Thermo-Calc and experimental results showed TiN, Nb(CN) and Laves phase (Fe_2Nb) precipitates were formed. The observation from the experimental results was confirmed by SEM and TEM with EDX. In a research in which Nb + Ti were used to stabilize high purity ferritic stainless steel, it was noted that TiN acted as a particle in a heterogenous nucleation which promoted the formation of equiaxed grain zone. Fine NbC precipitates precipitated at the grain boundaries and in the matrix, as found by TEM with EDX analysis which was confirmed by Thermo-Calc [56].

3.7 Differential scanning calorimetry (DSC)

Differential scanning calorimetry (DSC) can be used to study the phase transformations that occur upon heating and cooling of various alloys, including ferritic stainless steels by heating or cooling at a steady rate without mass exchange with its surroundings [57], [58]. Two widely used DSC systems are heat flux DSC and power-compensated DSC. With heat flux DSC, also called quantitative differential thermal analysis, the temperature difference between the sample and an inert reference body is measured directly. The temperature difference is converted to a heat flow. On the other hand, the enthalpy of the sample during a thermal event is measured by the power-compensated DSC (Figure 3.12). In the power compensated DSC, two separate chambers contain the

sample and the reference, and each chamber has its individual heating element for temperature control. A thermal null state is always maintained in the instrument. A change of the power to the heating element occurs to maintain the temperature difference between reference and sample bodies at zero. An increase in power to heat the sample occurs during an endothermic event and a reduction in power to cool the sample occurs in an exothermic event. The compensation for heat release or gain of the sample is measured by the amount of power change [58]. A plot of the electrical power needed for this temperature equalization is plotted against temperature. Peaks may be characterized by calculating the energy per unit mass [57].

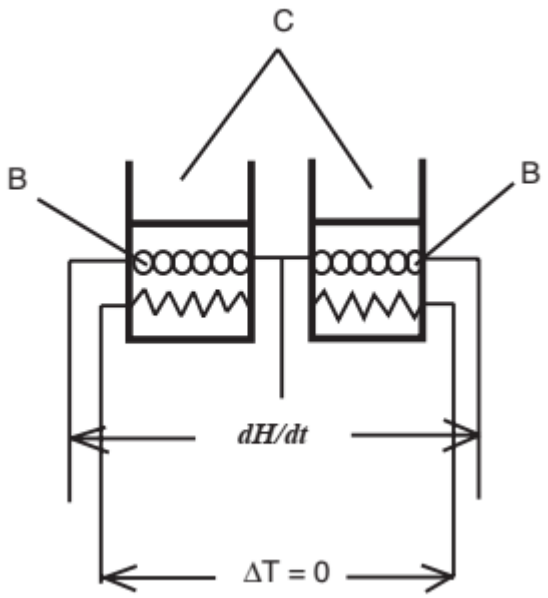

Figure 3.12: Power compensation DSC, where B is the separate heaters and C is sample and reference holders [58].

Ganesh et al. [58] reported on the use of differential scanning calorimetry to determine the phase transformations and the phase transformation temperatures in a range of 9%Cr creep resistant martensitic stainless steels. A heating rate of 1 to 3 $K.min^{-1}$ to a peak temperature of 1833 K (1560°C) was used. The authors claimed that the heating rate was low enough that equilibrium conditions were reached, and that the solidus and liquidus temperatures could be determined reliably.

Petrovič et al. [60] determined the liquidus and solidus temperature of a nitrogen-containing Type 304LN austenitic stainless steel using differential scanning calorimetry on cooling from 1550°C at a cooling rate of either 5, 10 or 25 $K.min^{-1}$. A higher cooling rate resulted in a lower measured liquidus, a lower measured solidus, and an increase in the difference between the measured liquidus and solidus temperature.

3.8 Welding metallurgy of ferritic stainless steels

During welding, various microstructural changes occur in the welded joint. Melting takes place in the fusion zone. The weld metal and its surrounding area are usually chemically heterogeneous composites which consist of six metallurgically distinct zones. These are the composite zone, unmixed zone, weld interface, partially melted zone, true heat-affected zone (HAZ), and unaffected base metal [16].

Ferritic stainless steels solidify directly from the liquid to the ferrite phase without any intermediate phase transformation [3, 46, 61-62]. In the fusion zone, initial solidification of ferritic stainless steel is always primary ferrite [4]. Ferritic stainless steel welds undergo three solidification and transformation sequences. The first and simplest is the fully ferritic structure;

$$L \rightarrow L + F \rightarrow F \qquad 3.4$$

Where L = liquid metal and F = ferrite phase.

The full suppression of austenite formation at elevated temperatures by alloying elements promoting ferrite, makes ferrite dominant in the weld. This is found in low-chromium alloys with low carbon content, medium-chromium alloys with Ti and Nb stabilizers, and high-chromium alloys [4]. This solidification path ($L \rightarrow L + F \rightarrow F$) is likely to represent the solidification and transformation of the steels used in this study.

There are two transformation paths in the fusion zone when martensite is present. Solidification proceeds as only ferrite which is stable over some temperature range in the solid state [4].

$$L \rightarrow L + F \rightarrow F \rightarrow F + A \rightarrow F + M \quad 3.5$$

Where L = liquid metal, F = ferrite phase, A = austenite phase, and M = martensite phase.

At elevated temperatures, some austenite is formed along the ferrite grain boundaries. When the fusion zone cools to room temperature, the austenite transforms to martensite. This transformation occurs for carbon contents in the range of 0.05 to 0.15 wt% [4].

Another transformation path results in the formation of austenite (Eqn 3.6)

$$L \rightarrow L + F \rightarrow L + F + A \rightarrow F + A \rightarrow F + M \quad 3.6$$

From Equation 3.3, solidification begins as primary ferrite but a peritectic-eutectic reaction results in austenite formation. If the carbon level is above 0.15 wt%, ferrite, austenite and a three phase liquid region exists below the primary ferrite and liquid phase zone. The cooling of the alloy continues in the two phase ferrite + austenite region and then rapid cooling transforms the austenite to martensite at room temperature [4].

3.9 The effect of Ti and Nb on the welding behavior of ferritic stainless steels

Different welding methods, microstructural evolution, and the effect of stabilizers on various ferritic stainless steel joints in general, are discussed in this section. Welding of ferritic stainless steels reduces toughness, ductility, and corrosion resistance because of grain coarsening in the weld metal and the heat affected zone [3, 46, 61-62].

Single pass autogenous welding of type AISI 409M ferritic stainless steel was investigated using a laser beam welding process. It was revealed that there was a virtual absence of grain growth. The absence of grain growth was due to the relatively low heat input associated with laser beam welding [63]. The welding of AISI 430 ferritic stainless steel with the GTAW process was compared to the SMAW process. Columnar

fusion zone grains were observed using SMAW whilst for GTAW, equiaxed grains were found. The SMAW welds contained austenite due to nitrogen pick-up from the atmosphere [46].

Gas tungsten arc welding (GTAW), friction stir welding (FSW), laser beam welding (LBM) and electron beam welding (EBW) were used to fabricate 409M ferritic stainless steels joints. TEM images of the fusion zone for EBW and LBW joints showed the presence of prior δ-ferrite grain boundaries, subgrain structures, chromium carbides and grain boundary martensite (Figure 3.13) [63]. Continuous current gas tungsten arc welding (CCGTAW), pulsed current gas tungsten arc welding (PCGTAW), and plasma arc welding (PAW) methods were used to prepare single pass butt weld joints of 409M ferritic stainless steels. The CCGTAW process produced coarser grains in the fusion zone compared to PCGTAW and PAW processes due to the relatively higher heat input [11].

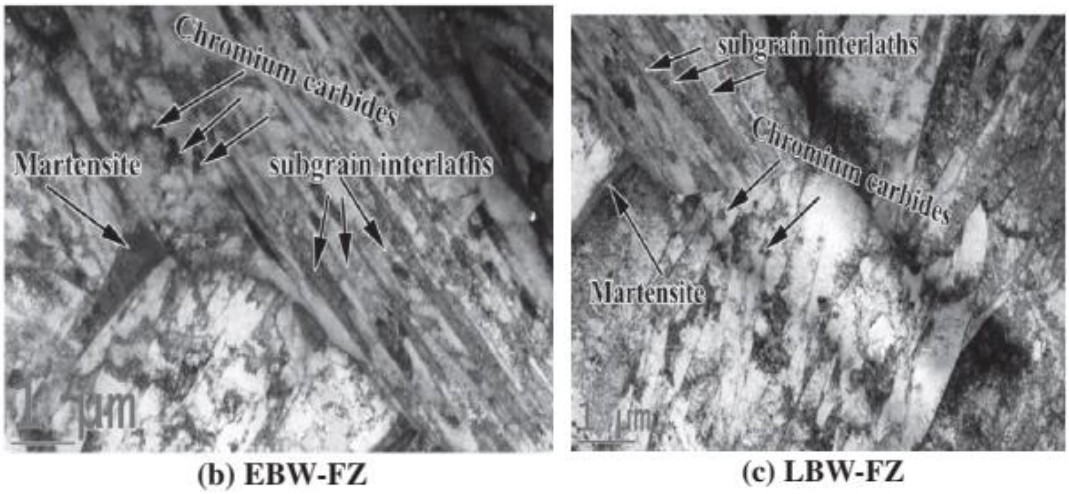

Figure 3.13: Transmission electron micrographs of weld metal region for EBW and LBW [63].

Villaret et al. [64] reported on using GMAW to weld modified AISI 444 ferritic stainless steels for exhaust manifold applications using different filler wires. The Ti content changed the structure of the grains from completely columnar for low Ti contents and to finer and equiaxed grains above 0.15% wt Ti. Between 0.1% and 0.15%

Ti, a transition from columnar to equiaxed grain structure occurred. Very fine Ti precipitates were found at above 0.15% wt Ti and these promoted fine equiaxed grains by forming refractory compounds in the weld pool which acted as heterogeneous nucleation sites before solidification. There was no improvement in the structure with an increase in Ti content above 0.15% (Figure 3.14). The addition of Nb seemed to have no effect on the fusion zone grain structure [64].

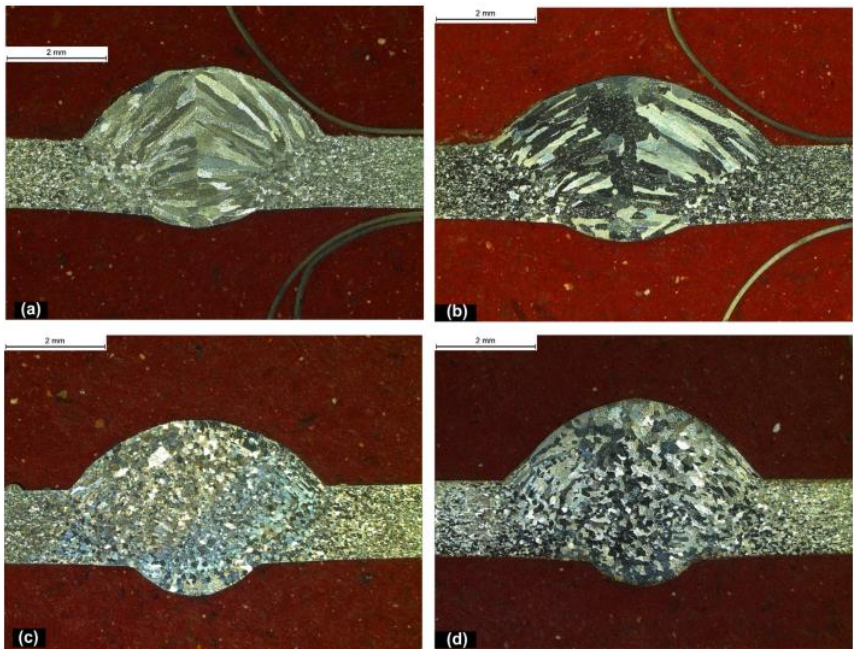

Figure 3.14: Influence of Ti content on the grain structure in the fusion zone of a Type 444 ferritic stainless steel, (a) 0.05% Ti, (b) 0.10% Ti, (c) 0.15% Ti, and (d) 0.25% Ti [64].

It has been revealed that the addition of Nb to ferritic stainless steels promote hot cracking in the weldment. A titanium content in excess of 0.5 pct significantly reduces the room temperature ductility. The dual stabilization of Nb + Ti is expected to reduce the detrimental effect of the individual Ti and Nb elements respectively. Coarse angular TiN particles were about two thirds of the inclusions in the base metal volume. The authors assumed that the smaller particles were NbC or Nb(C,N). The same volume fraction of very fine precipitates was observed in the weld metal which may be attributed to the higher solubility of TiN in the liquid phase than in the solid phase [65].

Alloying elements Nb, W, and V were incorporated in ferritic stainless steels. Rod-shaped Laves phase and rectangular (Nb,Ti)(C,N) precipitates were observed in the base metal. HAZ simulation revealed the average size of the Laves phase became smaller than the (Nb,Ti)(C,N) precipitate, but the carbonitride did not change. This was due to the difference of high temperature stability of (Nb,Ti)(C,N) and Laves phase since the dissolution temperatures of (Nb,Ti)(C,N) and Laves phase are over 1400 and 860°C respectively. The dissolution temperature of Laves phase was increased by the addition of tungsten. More (Nb,Ti)(C,N) carbides were formed but the volume fractions of both precipitates were not severely changed in relation to the Laves phase. Moreover, grain growth was inhibited by (Nb,Ti)(C,N) precipitates on the grain boundaries [66].

A new ferritic stainless steel (designated as K44X) for exhaust systems was developed and welded with GMAW process using ferritic filler materials containing same Cr and Mo as base metals but different Ti and Nb contents. Pulsed or short-circuit transfer mode which corresponded to two sets of welding parameters were determined for each filler wire. Most columnar grains grew epitaxially and were oriented in the direction of the heat flux. When the liquid located just in front of the solidification front was undercooled, transition from columnar to equiaxed grains (CET) could occur. Maintaining the Ti content of about 0.05% and varying Nb contents from 0.15 to 0.7% of some filler wires, the fusion zone exhibited similar grain morphologies, with a columnar structure in most of the zone [67].

Furthermore, the fraction of equiaxed grains in the fusion zone of this K44X ferritic stainless steel seemed to increase with an increase in Ti content (Figure 3.15). Low Ti contents resulted in columnar structure in the fusion zone whereas equiaxed structure was obtained with higher Ti contents. The CET was observed with about 0.1–0.15% Ti in the fusion zone, revealing equiaxed grains in the centre and columnar grains in the peripheral zone. The CET was seen at the start of the weld pool solidification, which effectively stopped the columnar grains from growing for higher Ti contents. Using the pulsed and short-circuit modes with the same Ti content, the transition from columnar to equiaxed was the same [67].

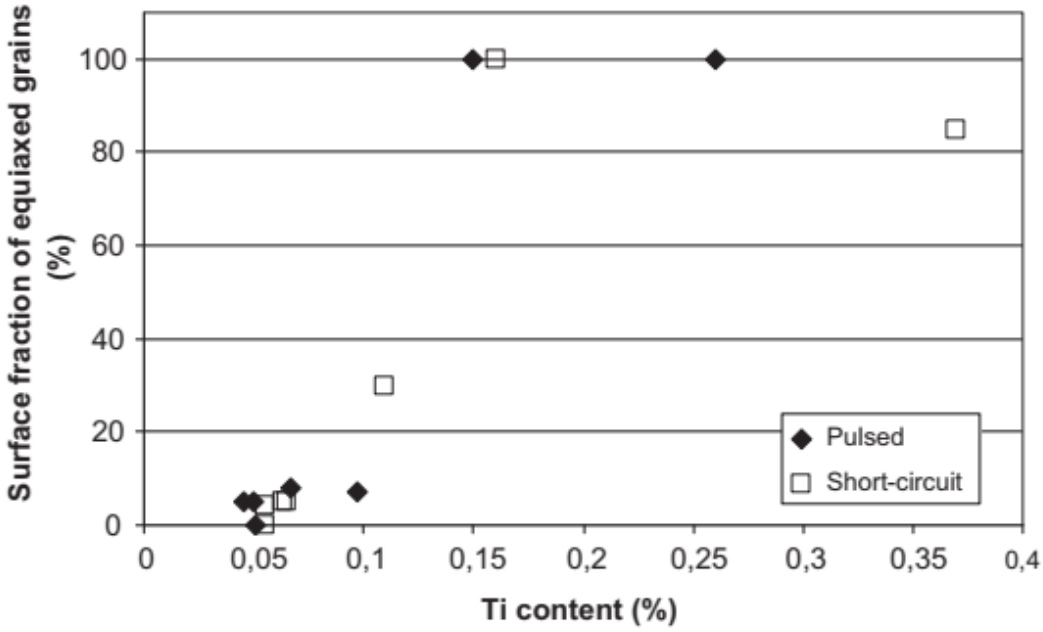

Figure 3.15: Fraction of equiaxed grains in the fusion zone versus titanium content [67].

It is more desirable to have equiaxed grain structures in castings and welds than columnar structures, for several reasons: segregation of alloying elements to the central plane or region is reduced, there are more isotropic structures, and toughness is improved by a smaller grain size in materials subject to brittle fracture. A technique for quenching moving weld puddles using Sn was developed. Most steels containing titanium showed a columnar-to-equiaxed transition (CET) when TiN particles were added to the static weld pool, an increased fraction of equiaxed grains resulted. The amount of TiN particles added was not reported. Equiaxed grains did not form when only Ti was added [68].

A ferritic stainless steel with a Cr content of 40% with 0.14%wt Nb was welded using laser and electronic beam (EB) processes. Coarser columnar grains formed by epitaxial growth. Along the centreline of the laser welds, a relatively narrow zone of finer equiaxed grains were found. The weld metal grains were free of grain boundary precipitates and virtually no grain growth was observed in the HAZ region. This was

related to the low heat input of the laser welding process and the finely dispersed niobium-carbonitrides in the alloy probably pinned the grain boundaries. This same phenomenon was observed for the EB welding process [69].

Reporting on grain refinement in ferritic stainless steel joints, it was found that irrespective of alloying element additions of Ti and Al, the equiaxed grain size generally decreased with increasing welding speed. This was attributed to heterogenous nucleation by particles rich in Ti. It had been discussed that cuboidal particles at the centre of dendrites supported heterogenous nucleation, promoting columnar to equiaxed transition. Moreover, increasing the welding speed promoted columnar to equiaxed transition in alloys having Ti-rich nucleating particles. At high Ti additions, the welding speed had less effect on the size and fraction of the equiaxed grains than at low Ti contents. Figure 3.16 shows the fraction of equiaxed grains were high during the high welding speeds compared to the low welding speed [70-71].

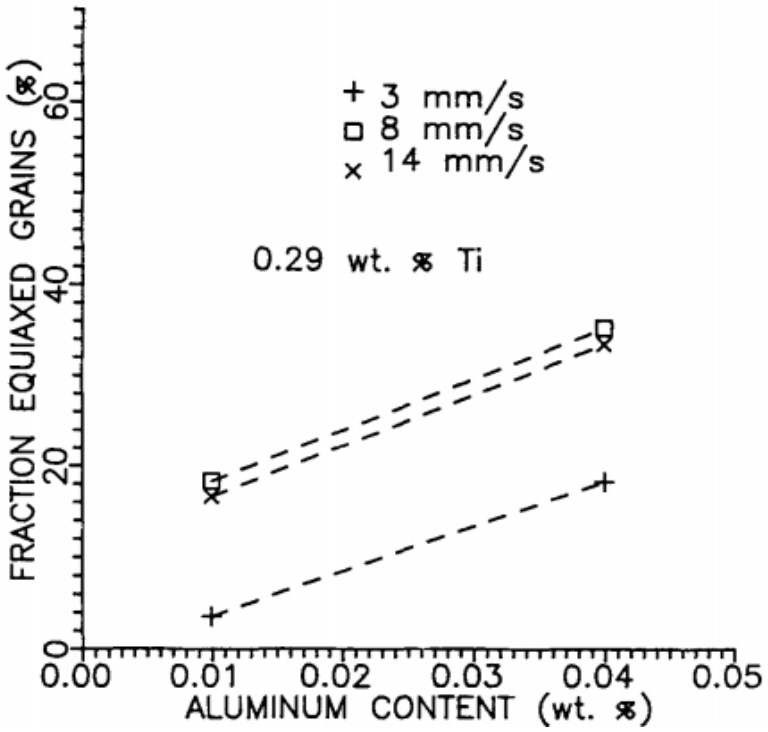

Figure 3.16: Average fraction equiaxed grains observed at the surface of ferritic stainless steel weld metal containing 0.29 wt pct Ti vs aluminum content [71].

Villafuerte et al. [71] observed that the fraction of equiaxed grains depended on the welding speed and the Ti and Al contents. A high Ti contents produced finer grain sizes during GTA welding of ferritic stainless steels. Also, at a given Ti content, an increase in Al content resulted in a significant increase in the equiaxed fraction. These equiaxed grains were due to the number of Ti-rich carbo-nitride particles which increased with an increase in Al. The presence of Al increased the Al-rich or other phases in the Ti-rich phases. Higher welding speeds generated greater equiaxed grain fractions compared to low welding speeds (Figure 3.17). Higher welding speeds affected some critical thermal conditions which in turn affects the local solidification (the liquid thermal gradient, G, and the solidification velocity, R). The equiaxed grains grew where there was a lower G and a higher R region, and this region increased with high welding speed. Carbo-nitride Ti-rich particles were found at the centre of equiaxed ferrite dendrites which provided direct support for heterogeneous nucleation for the formation of the grains. However, not all the Ti-rich particles were found at the equiaxed dendrite centre, which negatively affects the effectiveness of the nucleants.

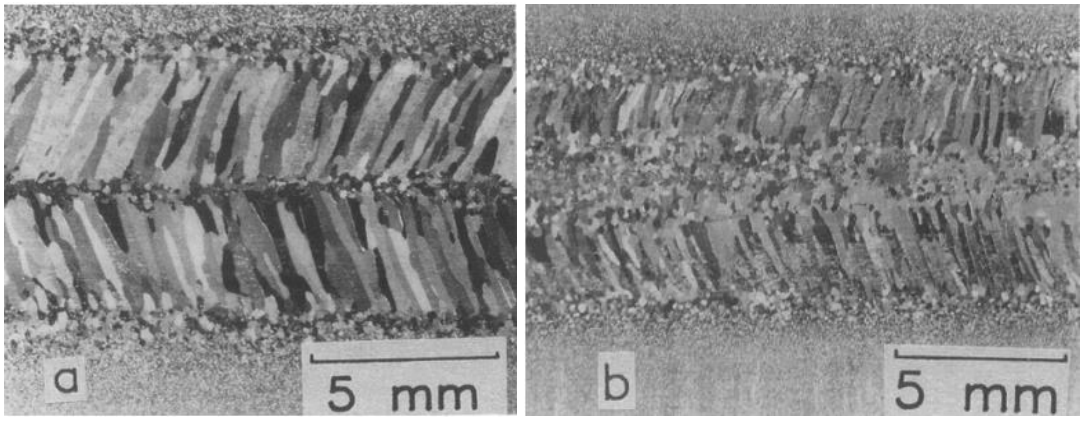

Figure 3.17: Grain structures observed at the surfaces of welds containing 0.32 wt pct titanium welded at (a) 3 mm/s and (b) 14 mm/s [71].

It is suggested that grain refinement for ferritic stainless steels welds is possible through pulsed direct current as well as by pulse alternating current techniques. This is due to better convective currents in the weld pool resulting in dendrite fragmentation and grain detachment which refines the grains [72].

From the discussion under the welding of ferritic stainless steels, it can be seen that Ti acts as a grain refiner when present as Ti(C,N) or TiN particles. The TiN particles also inhibit grain growth in the HAZ. Nb was found to have no or less effect on the fusion zone grain structure. Ti + Nb dual stabilization produced (Nb,Ti)(C,N) precipitates which also inhibited grain growth in the HAZ.

The use of stabilizers Ti and Nb on ferritic stainless steel will affect the weld metal microstructure. It is expected that the equiaxed grains might reduce solidification cracking of ferritic stainless steels, due to the increased amount of grain boundary surface area.

CHAPTER FOUR – EXPERIMENTAL PROCEDURE

4.1 Introduction

The various experimental procedures employed to determine the solidification cracking susceptibility using self-restraint Houldcroft, Modified Varestraint -Transvarestraint (MVT) and the welding parameters on the influence of Ti and Nb content on ferritic stainless steel materials are set out in this section. In addition to the evaluation techniques based on welding, the hot tensile testing of some ferritic stainless steel grades was done to simulate the susceptibility to solidification cracking. The experimental procedures are described in detail below.

4.2 Experimental materials

Five experimental alloys produced by Small Alloys and Metallurgical Services (SAMS) and four commercial alloys from Columbus Stainless were used for the solidification cracking tests. Table 4.1 presents the actual composition of all the ferritic stainless steels used for this study. There were two unstabilized (experimental and commercial), two experimental mono (Ti & Nb) stabilized, four dual (Ti + Nb) stabilized (experimental and commercial), and a commercial dual stabilized containing Mo ferritic stainless steels. The S and P were below the maximum amounts specified, for all experimental and industrial heats (Table 3.1). In this document, a specific alloy was identified by a letter (A to I) that was randomly assigned, with the nominal Ti and Nb content indicated. For example, alloy B:0Ti;0Nb did not contain any stabilization elements.

Table 4.1: Actual chemical composition of type AISI 430, 436, 439, 441 and 444 ferritic stainless steels

Element	Composition (mass %)								
	A:0Ti;0Nb	B:0Ti;0Nb	C:0.7Ti	D:0.6Nb	E:0.4Ti;0.6Nb	F:0.4Ti;0.9Nb	G:0.1Ti;0.4Nb	H:0.1Ti;0.4Nb	I:0.1Ti;0.5Nb;2Mo
C	0.006	0.046	0.006	0.012	0.017	0.011	0.013	0.011	0.015
Si	0.600	0.450	0.610	0.420	0.400	0.440	0.510	0.490	0.530
Mn	0.510	0.360	0.500	0.330	0.370	0.370	0.440	0.430	0.440
P	0.019	0.020	0.018	0.024	0.022	0.025	0.024	0.025	0.033
S	0.008	0.002	0.007	0.007	0.001	0.004	0.013	0.002	0.003
N	0.069	0.055	0.069	0.070	0.069	0.067	0.013	0.015	0.018
Cr	18.030	16.070	17.940	18.810	18.120	18.170	17.660	17.500	18.100
Nb	0.010	0.001	0.003	0.580	0.620	0.920	0.422	0.396	0.535
Ti	0.001	0.001	0.680	0.030	0.410	0.360	0.146	0.112	0.096
Ni	0.230	0.270	0.240	0.230	0.350	0.370	0.150	0.150	0.160
V	0.007	0.100	0.040	0.050	0.110	0.110	0.130	0.120	0.130
Cu	0.010	0.070	0.020	0.060	0.060	0.070	0.050	0.070	0.080
Al	0.200	0.009	0.180	0.030	0.020	0.020	0.012	0.010	0.014
Mo	0.020	0.005	0.020	0.020	0.020	0.020	0.014	0.011	2.000
Fe	Bal	Bal	Bal	Bal	Bal	Bal	Bal	Bal	Bal

4.3 Determination of precipitates using Thermo-Calc software

Thermo-Calc version 2015b (TCFE6 database) software was used to identity of precipitates present at a range of temperatures, through thermodynamic equilibrium and phase diagram calculations using the full chemical compositions as shown in Table 4.1. Table 4.2 notes the liquidus and solidus temperatures and the probable solid phases present at equilibrium with liquid metal for the steel grades used. It can be seen that the addition of Nb to the unstabilized alloy decreased the solidus temperature from 1433 to 1387°C. The addition of Ti increased the solidus temperature to 1448°C. The dual stabilized steels had an estimated solidus temperature similar to that of the steels that contained only Ti. From Table 4.2, the possible precipitates that will be expected within the liquidus and solidus temperatures for all the ferritic stainless steels are MnS, TiN, $Ti_4C_2S_2$, NbC, and Ti(C,N). The Thermo-Calc stable phases are presented in Tables A.1 to A.22 in Appendix A. Figures B.1 to B.9 (Appendix B) show the amounts of phases present in the steel grades from temperatures 1350 to 1500°C. It can be seen that the predicted phase fractions are all very low (Figures B.1b – B.9b) except ferrite which decreases with increase in temperature from 1400°C (Figures B.1a – B.9a). Shan et al. [72] reported that with Ti or Nb content increasing in ferritic stainless steels, the solidus temperature is reduced more, for the same increase in Ti or Nb, than the liquidus temperature using Thermo-Calc simulations. It was also stated that Nb contributed more than Ti in the solidification temperature range for the ferritic stainless steels [73]. This behavior was generally observed though the unstabilized steels showed high $T_L - T_S$ values.

Table 4.2: Results of Thermo-Calc modelling of the experimental matrix showing nominal Ti and Nb content

Steel ID	Grade	Ti	Nb	Liquidus temperature (T_L) (°C)	Solid state phases in equilibrium with liquid metal	Solidus temperature (T_S) (°C)	$T_L - T_S$ (°C)
A:0Ti;0Nb	430	0.0	0.0	1500	Ferrite and MnS	1433	67
B:0Ti;0Nb	430	0.0	0.0	1500	Ferrite and MnS	1411	89
C:0.7Ti	439	0.7	0.0	1500	Ferrite, TiN, and $Ti_4C_2S_2$	1448	52
D:0.6Nb	436	0.0	0.6	1497	Ferrite, NbC, and MnS	1387	110
E:0.4Ti;0.6Nb	441	0.4	0.6	1500	Ferrite, Ti(C,N), and $Ti_4C_2S_2$	1448	52
F:0.4Ti;0.9Nb	441	0.4	0.9	1500	Ferrite, TiN, and $Ti_4C_2S_2$	1433	67
G:0.1Ti;0.4Nb	441	0.1	0.4	1500	Ferrite, Ti(C,N), and $Ti_4C_2S_2$	1470	30
H:0.1Ti;0.4Nb	441	0.1	0.4	1500	Ferrite, Ti(C,N), and $Ti_4C_2S_2$	1464	36
I:0.1Ti;0.5Nb;2Mo	444	0.1	0.5	1490	Ferrite, Ti(C,N), and $Ti_4C_2S_2$	1450	40

Table 4.3 is a presentation of the experimental matrix showing the various steel grades used for the experimental work. It can be seen that the three different methods for the study were performed on only D:0.6Nb ferritic stainless steel. This was due to the high mass of castings produced which could meet the number of samples needed for the experiments. Moreover, the MVT-test required a specific thickness of 10 mm and only the commercial unstabilized B:0Ti;0Nb and H:0.1Ti;0.4Nb, and the experimental D:0.6Nb and F:0.4Ti;0.9Nb ferritic stainless steels could be sourced in an adequate thickness for these tests. The hot tensile testing also required a dimension of about 15 mm × 170 mm, which was machined along the rolling direction to 10 mm × 120 mm cylindrical rods. The C:0.7Ti, D:0.6Nb, and E:0.4Ti;0.6Nb ferritic stainless steels were selected due to the availability of such dimensions. Not enough material of the other alloys was available for all three tests. All the types of stabilization for ferritic stainless steels were represented in the self-restrained Houldcroft and the MVT tests – see Table 4.3. Hot tensile tests were only done on samples that contained Ti, Nb, or Ti and Nb.

Table 4.3: Experimental matrix, showing nominal Nb and Ti content, and experimental work done

Type of stabilization	Steel ID	Type of heat	Ti	Nb	Self-restrained Houldcroft	MVT	Hot tensile testing
None	A:0Ti;0Nb	Laboratory	0.0	0.0	x		
	B:0Ti;0Nb	Industrial	0.0	0.0		x	
Ti only	C:0.7Ti	Laboratory	0.7	0.0	x		x
Nb only	D:0.6Nb	Laboratory	0.0	0.6	x	x	x
Ti + Nb	E:0.4Ti;0.6Nb	Laboratory	0.4	0.6	x		x
	F:0.4Ti;0.9Nb	Laboratory	0.4	0.9	x	x	
	G:0.1Ti;0.4Nb	Industrial	0.1	0.4	x		
	H:0.1Ti;0.4Nb	Industrial	0.1	0.4		x	
	I:0.1Ti;0.5Nb;2Mo	Industrial	0.1	0.5	x		

4.4 Determination of temperature range and solidification mechanism of the ferritic stainless steels using DSC

The samples were machined to approximate dimensions of 5 mm diameter and 2 – 3 mm height. Sample A had a mass of about 293 mg. The other samples had a mass between 393 and 395 mg. Power compensated DSC thermal analysis was executed with Netszch STA409 instrument. The furnace was heated to 1500°C. The maximum sample temperature (about 1500°C) was very close to the liquidus temperature (estimated using Thermo-Calc simulations at 1490 to 1500°C [Table 4.2]). The DSC experiments were performed in a static atmosphere of 99.99% purity argon gas to prevent contamination and minimize oxidation of the sample. An argon pressure of about 1000 mbar was maintained in the graphite furnace chamber to avoid oxidation at high temperatures. An alumina crucible was used as the reference. A heating and cooling rate of 5 K/min was used. There was a holding time of 5 minutes before cooling started to ensure that the sample was fully melted. From the work by Ganesh et al. [59] and Petrovic et al. [60], it can be assumed that equilibrium conditions were reached.

Solidification mechanism and solidification temperature range

A typical DSC thermogram recorded during slow heating to the liquidus temperature and followed by slow cooling to room temperature of the sample A:0Ti;0Nb is presented in Figure 4.1. The DSC melting thermogram was characterized by one endothermic peak by heating from 500°C till melting and the cooling curve by one exothermic peak. These peaks represents the melting of the δ-ferrite phase and solidification to δ-ferrite [74]. It could be seen that there was no change in the curves till when solidification started. Figure 4.1 was difficult to use to estimate the solidus and liquidus temperatures. The high temperature behavior was replotted using the data to give the exploded view (Figure 4.2). Not all the parameters (solidus and liquidus temperatures) could be determined (Table 4.4). The rest of the thermograms can be found in Appendix D.

It has been stated that weld solidification cracking occurs during the last stage of weld solidification where stresses developed across adjacent grains can lead to cracking in

the weld metal [3, 5, 14]. Moreover, the solidification temperature range (BTR) is the cooling of the weld metal which has been approximated by the difference between the liquidus and solidus temperatures of a material [5, 17]. Tripathy et al. [72] used the beginning of solidification of an austenitic stainless steel during cooling of a DSC experiment as the liquidus temperature of the alloy. Based on these statements, the cooling curve was used to estimate the liquidus and solidus temperatures of the alloys which corresponded to solidification start and finish respectively (Figure 4.2).

The cooling curve can be used to explain the mechanism of solidification of the ferritic stainless steels which represents the phase changes occurring in the alloy when it is solidifying/cooling [5, 59, 74]. It can be seen that after melting, the first solid to form during cooling, which was after the 5 minutes hold time and the beginning of the exothermic peak could not be approximately estimated and the solidification ended at 1483°C (Figure 4.2 & Table 4.4). After the solidification, there was no phase change till room temperature. All the DSC thermograms for the alloys followed similar behavior by showing straight lines from the start of melting to completion and the on-cooling curves followed similar behavior.

The solidification mechanism of all the ferritic stainless steels of above 16 wt% Cr showed a solidification temperature range during melting from on-heating and cooled through δ and α ferrite phases to room temperature without passing through austenite phase field. The amount of Cr, a ferrite former, was able to enlarge the ferrite phase field at the expense of the austenite phase region [4]. The effect of Ti and Nb was not observed on the solidification mechanism as the DSC spectra showed the same phase changes of δ and α ferrite during the on-heating and on-cooling cycles. A plot of DSC solidus temperature values was made with the Nb content (based on the amount of Nb content in the alloy and neglecting the Ti content). It was observed that, with no Nb content, the solidus values were high and this decreased with increasing Nb content (Figure 4.3). The decrease in solidus temperature with increasing Nb content agrees with the behavior that Nb content increasing in ferritic stainless steels reduced solidus temperature using Thermo-Calc simulations [73].

Table 4.4 shows the solidus, liquidus and the solidification temperature range for the alloys used in the DSC experiment for the on-heating and on-cooling cycles. The solidification temperature range values of the unstabilized steels A:0Ti;0Nb and B:0Ti;0Nb could not be estimated. The highest solidification temperature range was F:0.4Ti;0.9Nb (50°C). This was contrary to Thermo-Calc results, which showed alloy D:0.6Nb as having the highest BTR value (Table 4.2). This could be attributed to the high Nb content in the alloy. This was followed by E:0.4Ti;0.6Nb (39°C), both C:0.7Ti (32°C) and I:0.1Ti;0.5Nb;2Mo (32°C), D:0.6Nb (27°C) and H:0.1Ti;0.4Nb (16°C) [Table 4.4]. Comparing the on-cooling with the Thermo-Calc values (Table 4.2), it can be seen that there were differences in values and this could be due to the probable exact equilibrium condition of the Thermo-Calc simulation compared to the 5°C/min scan rate. Petrovič et al. [59] reported that different scan rates produced non-identical liquidus temperatures for the same austenitic stainless steel. Generally, the liquidus temperature values of the DSC experiment were between 1486°C and 1497°C and that of the Thermo-Calc values were around 1500°C on average (Figure 4.4). The solidus temperature values of the on-cooling DSC experiment were similar compared to that of the Thermo-Calc values, though some differences were found of same alloys (Table 4.2). It has been shown that selected empirical equations for the liquidus and solidus temperatures were often not particularly accurate, though some predictions correlated well. Reasons for the differences between estimated and actual liquidus and solidus temperatures were given as the equipment arrangement, sample mass and sensitivity of sensors [75]. Also, the solidification temperature range was high for Thermo-Calc simulation compared to DSC experiment (Tables 4.2 and 4.4). This might be due to the scan rate which has been found to give changes in such values [60].

Sample E:0.4Ti;0.6Nb

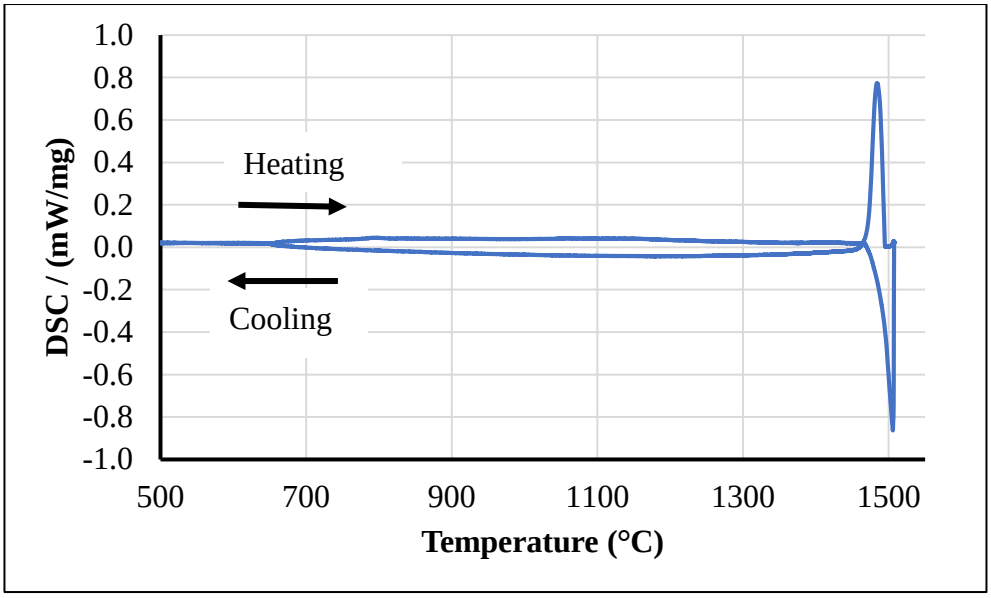

Figure 4.1: DSC thermogram for the sample E:0.4Ti;0.6Nb during heating and cooling.

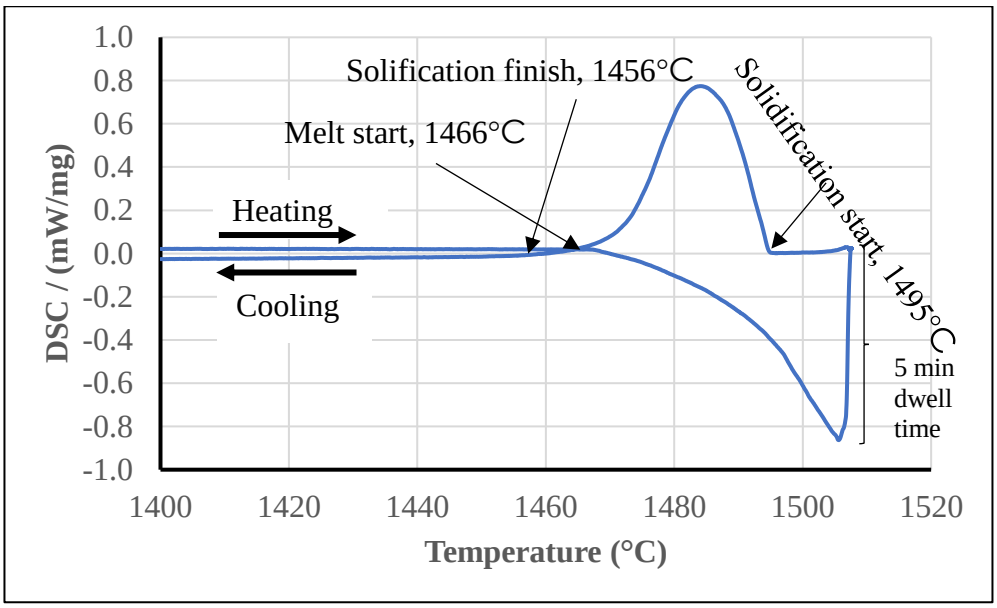

Figure 4.2: Expanded thermogram for alloy E:0.4Ti;0.6Nb showing the solidus and liquidus temperatures.

Table 4.4: DSC measurement (on cooling) results of the solidus and liquidus temperatures of the tested samples

	On heating			On cooling		
Sample ID	Liquidus temperature (°C)	Solidus temperature (°C)	Solidification range (°C)	Liquidus temperature (°C)	Solidus temperature (°C)	Solidification range (°C)
A:0Ti;0Nb	--	1497	--	--	1483	--
B:0Ti;0Nb	--	1498	--	--	1482	--
C:0.7Ti	--	1478	--	1497	1465	32
D:0.6Nb	--	1480	--	1494	1467	27
E:0.4Ti;0.6Nb	--	1466	--	1495	1456	39
F:0.4Ti;0.9Nb	1505	1452	53	1490	1440	50
H:0.1Ti;0.4Nb	--	1482	--	1486	1470	16
I:0.1Ti;0.5Nb;2 Mo	--	1466	--	1486	1454	32

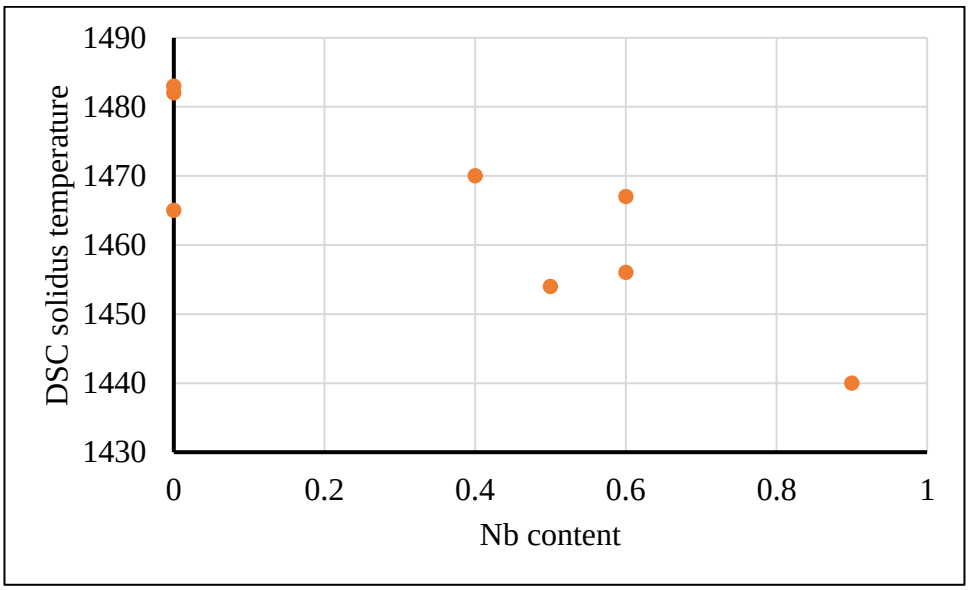

Figure 4.3: DSC solidus temperature measurement (on cooling) as a function of Nb content as determined on cooling at 5 K/min.

The relationship between the DSC liquidus and solidus temperatures and that of the Thermo-Calc simulations were plotted and shown in Figure 4.4. It could be seen that the DSC temperature liquidus values were found on the 1500°C of the Thermo-Calc

values except one (Figure 4.4). With the solidus temperature values, the values were scattered (Figure 4.4), signifying that there was no relationship between the DSC and Thermo-Calc liquidus and solidus temperatures. Three of the solidus values were seen to be separated from the ideal line. These solidus values corresponded to the alloys A:0Ti;0Nb, B:0.7Ti and D:0.6Nb. At zero Nb, the solidification temperature range was above 30°C. This decreased to 16°C and then increased with increasing Nb content (Figure 4.4). This reveals the harmful effect of Nb as it forms low melting eutectics to increase the BTR, which eventually increases the susceptibility to solidification cracking of ferritic stainless steels. For the steels that contained Nb, the estimated difference between the liquidus and the solidus temperature as a function of Nb content increases quite strongly with Nb content (Figure 4.5). The results for the Thermo-Calc simulation and for the DSC for the solidification range differed by about 15°C. From the limited amount of data available, it seems that an increase in the Nb content of 1% results in an increase in the solidification range around 67 to 69°C. Although the results for the Thermo-Calc estimate and the DSC measurement for the solidification range differ by about 15°C (Figure 4.4), these two techniques result in a similar estimate for the effect of 1% Nb on the change in solidification range, i.e., between 67 and 69°C / 1% Nb.

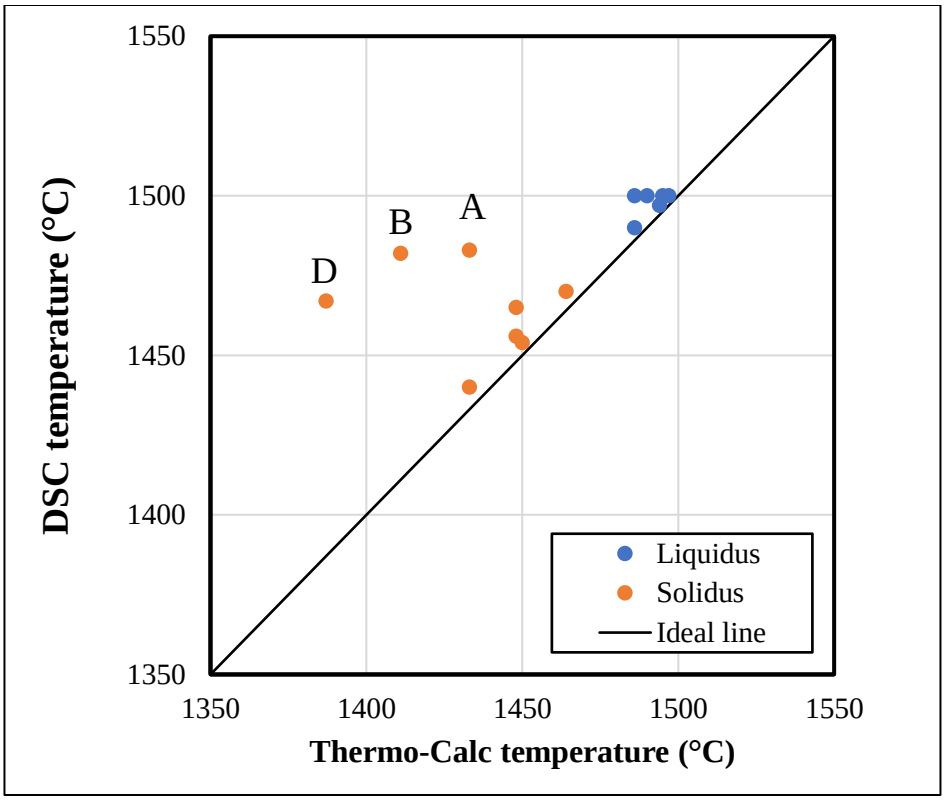

Figure 4.4: The relationship between DSC measurement (on cooling) and Thermo-Calc for the solidus and liquidus temperature values.

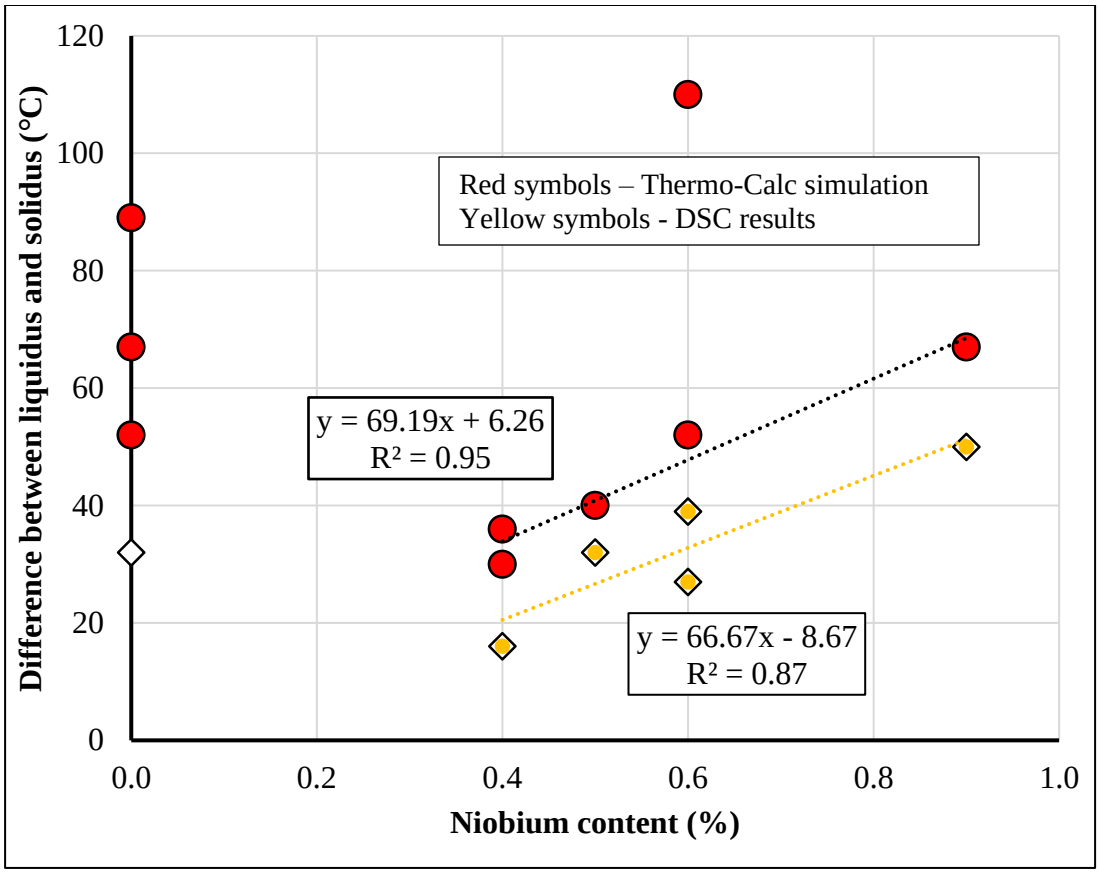

Figure 4.5: The difference between liquidus and solidus of DSC and Thermo-Calc against Nb content.

4.5 Self-restrained Houldcroft solidification method

Figure 4.7 is an image of the self-restraint sample before welding. The steel grades that were characterized included experimental unstabilized (A:0Ti;0Nb), mono stabilized Ti and Nb containing grades (C:0.7Ti & D:0.6Nb), three dual stabilized (Ti + Nb) grades (E:0.4Ti;0.6Nb, F:0.4Ti:0.9Nb, & G:0.1Ti;0.4Nb) (commercial and experimental) and a commercial dual stabilized grade containing Mo (I:0.1Ti;0.5Nb;2Mo). These Houldcroft samples were the as received steel grades which were 100 × 40 × 10 mm and fulfilled the required geometry. The samples were wire cut to dimensions of 90 × 36 × 2 mm with each having eight slots of 1 mm as shown in Figure 2.18 of Chapter Two. Autogenous gas tungsten arc welding was performed on the self-restraint Houldcroft-type samples using a welding speed of 6 mm/s, 3 mm/s, and 1 mm/s. Duplicate samples were welded to ascertain repeatability.

A Lincoln Electric Square Wave TIG – 355 power source was used. All samples were degreased with ethanol before welding and all the welds were made on a graphite backing plate. There was no visual evidence of any interaction between the graphite plate and the weld metal. Direct current electrode negative polarity was used. The arc was started on a run-on tab of the same ferritic stainless steel before continuing on the Houldcroft sample. Care was taken to ensure that welding was done in the centre of the Houldcroft specimen. Since complete penetration was to be complied with, it was impossible to use the same heat inputs (Table 4.5) for welding speeds of 3 mm/s and 1 mm/s. After welding, the samples that cracked were examined using a SMZ – 10A stereomicroscope to locate the crack tip. A Vernier caliper was used to measure the crack length. A Cyber-shot 7.2 megapixels Sony camera was used to take the photographs of the cracked and uncracked samples. The weld bead sizes were measured using a vernier caliper.

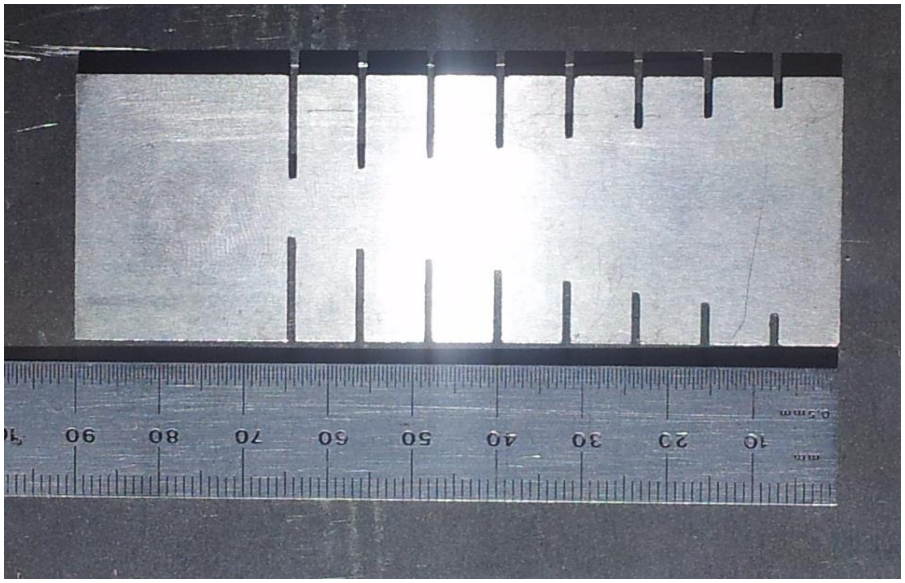

Figure 4.6: A Houldcroft sample before welding.

The welding parameters used for the Houldcroft solidification cracking method are presented in Table 4.5. The average arc efficiency (η) of 0.48 was used to calculate the heat input from equation 3.1 [76].

$$\text{Heat input} = \frac{\eta VI}{v} \qquad 4.1$$

where η is the arc efficiency,

V is the welding voltage,

I is the current and

v is the welding speed.

Table 4.5: Houldcroft welding parameters

Speed (mm/s)	**6**	**3**	**1**
Current (A)	250	180 - 190	90 - 120
Voltage (V)	18	15 – 16	12 - 13
Arc length (mm)	2	2	2
Gas flow rate (l/min)	15	15	15
Electrode diameter (mm)	3.2	2.4	2.4
Gas	99.999 % Argon		
Heat input (kJ/mm)	0.3	0.4 - 0.5	0.5 - 0.8

4.6 Modified Varestraint-Transvarestraint (MVT) test

This experiment was executed in the varestraint mode according to the DIN EN ISO 17641-3:2005 (E) standard. The results of the MVT-test are plotted on a graph showing the total crack length visible on the top surface of the weld against the bending strain. The graph of total crack length against strain is divided into three sectors or regions, consistent with DIN EN ISO 17641-3:2005 with sector 1 being hot crack-resistant, sector 2 shows increasing hot crack susceptibility, and sector 3 being prone to hot cracking. The borders of these sectors were developed based on a large body of experimental work by Bundesanstalt für Materialforschung und – prüfung, Berlin (BAM), combined with practical knowledge [21].

The MVT-test was conducted in BAM (the Federal Institute for Materials Research and Testing, Germany). Four steel grades were used for the experiment, which included two experimental and two commercial alloys. A mono stabilized D:0.6Nb and dual stabilized F:0.4Ti;0.9Nb grades were the experimental alloys. Commercial grades included an unstabilized B:0Ti;0Nb and a dual stabilized H:0.1Ti;0.4Nb ferritic stainless steels. The samples were prepared with the dimensions 100 × 40 × 10 mm. These specimens were subjected to dye penetrant and ultrasonic testing and was found

that there was no crack in them [77]. Table 4.6 shows generic welding parameters used. Table 4.7 shows welding current, voltage and bending strain for individual specimens. Two different welding speeds of 6 mm/s and 3 mm/s were used. For testing in the MVT machine, the samples were clamped and laid on a mandrel die with the required radius based on the strain. The mandrel die geometries were 125 mm, 250 mm and 500 mm for 4%, 2%, and 1% bending strain respectively. The sample surfaces were cleaned with ethyl alcohol immediately before welding. Stereoscopic photography was taken to observe the cracks at ×25 for standard morphology after treating the weld with Antox 71 E (etchant based on HNO_3 and HF) for crack evaluation. The hot cracks were measured in BAM, Germany and again in the University of Pretoria laboratory. The total crack lengths were plotted against the bending strain to quantify the susceptibility to solidification cracking.

Table 4.6: Welding process specifications for MVT specimens welded at BAM

Item	**Specification**
Welding process	141 WIG-DC (DIN EN 287)
Electrode	WC 20 (DIN EN 26848)
Shielding gas:	Argon 5.0-I1 (DIN EN ISO 14175) Air Liquide
Welding power source	Cloos GLW 450 I-H-P-R
Electrode diameter	2.4 mm, angle at electrode tip**:** 30°
Flow rate	15 l/min

Table 4.7: Welding parameters for the MVT test and the bending strain in %

Steel	Current (A)	Voltage (V)	Heat input (kJ/mm)	Bending Strain (%)
B:0Ti;0Nb (1)	218.5	12.3	0.43	1
B:0Ti;0Nb (2)	218.4	13.1	0.46	2
B:0Ti;0Nb (3)	218.4	12.1	0.42	4
D:0.6Nb (1)	218.4	13.1	0.46	1
D:0.6Nb (2)	218.9	13.6	0.48	2
D:0.6Nb (3)	218.4	12.7	0.44	4
F:0.4Ti;0.9Nb (1)	218.4	12.6	0.44	1
F:0.4Ti;0.9Nb (2)	218.9	13.1	0.46	2
F:0.4Ti;0.9Nb (3)	218.4	12.4	0.43	4
H:0.1Ti;0.4Nb (1)	218.6	12.1	0.42	1
H:0.1Ti;0.4Nb (2)	218.4	12.5	0.44	2
H:0.1Ti;0.4Nb (3)	218.4	12.2	0.43	4
D:0.6Nb (4)	255.9	13.8	0.28	1
D:0.6Nb (5)	255.8	14.4	0.29	2
D:0.6Nb (6)	255.5	14.0	0.29	4
F:0.4Ti;0.9Nb (4)	255.8	13.4	0.27	1
F:0.4Ti;0.9Nb (5)	255.6	14.1	0.29	2
F:0.4Ti;0.9Nb (6)	255.5	13.5	0.28	4

4.7 Hot tensile testing

Hot tensile testing was used to evaluate the solidification cracking susceptibility of ferritic stainless steels using a thermo-mechanical Gleeble-1500D. Two mono stabilized (C:0.7Ti & D:0.6Nb) and one dual stabilized (E:0.4Ti;0.6Nb) ferritic stainless steels were used. A cylindrical sample which was machined along the rolling direction was employed (Figure 4.8). The sample was contained in a silica glass tube. The quartz tube had a narrow longitudinal opening which permitted a Pt/Rh – Pt thermocouple to be welded onto the sample surface for temperature measurements. The heating was programmed to 1320°C. Manual adjustments were made from 1320°C till

some liquid metal could be seen. The sample temperature was increased by an additional 10°C to ensure complete melting. The samples were soaked for about 50 seconds and cooled to the testing temperature that ranged from 1200 to 1300°C. The testing temperatures were chosen because testing at 1100°C did not produce a solidification cracked fracture surface but 1200°C to 1300°C did. Testing at 1350°C was very close to the melting point of the samples and was difficult to program this testing temperature. The sample temperature was maintained at the testing temperature for about 20 seconds before tensile loading started. The samples were fractured at a cross-head rate of 5 mm/s. This hot tensile test was performed according to Sun [8] who used only the reduction in area and the tensile strength of the material against the testing temperatures. The only difference was the heating rate of 200°C/s in Sun's [8] work whilst the authors used 23.3°C/s and 5.1°C/s till melting (Figure 7.1). Lundin et al. [78] reported on only reduction in area with the on-heating and on-cooling temperatures.

The fracture of the sample typically occurred within three seconds of the onset of strain. The time, force, temperature and the stroke/displacement data were extracted and the flow curves were plotted. Due to the measurement interval (1 measurement per second), the flow curve and the temperature-time record were poorly defined and it was not possible to determine the tensile strength accurately. Measurement of the diameter of the specimen at the point of failure made calculation of the reduction in area, the engineering fracture stress, and the true fracture stress possible.

The testing temperatures were found below the estimated solidus temperatures using Thermo-Calc simulations, but fracture surfaces showed solidification cracking. The testing temperatures and the estimated solidification temperature of the different steels are noted in Table 4.8. There was a consistent discrepancy between the liquidus and solidus temperatures (as estimated using Thermo-Calc, Table 4.2) and the temperatures measured during hot tensile testing (Table 4.8). These discrepancies were due to the two different solidification conditions. Thermo-Calc is an equilibrium simulation and the Gleeble is a non-equilibrium condition. The discrepancy might also be due to the fact that the peak temperatures were missed as a result of poor choice of measurement interval and low acquisition frequency. Figure 4.9 is an example of the data for force,

temperature and crosshead displacement recorded during the testing of a sample (for C:0.7Ti ferritic stainless steel). The ductility recovery temperature (DRT), the nil ductility temperature range (DTR), and the nil strength temperature (NST) could not be determined.

Figure 4.7: A hot tensile test sample before the thermo-mechanical simulation in the Gleeble – 1500D.

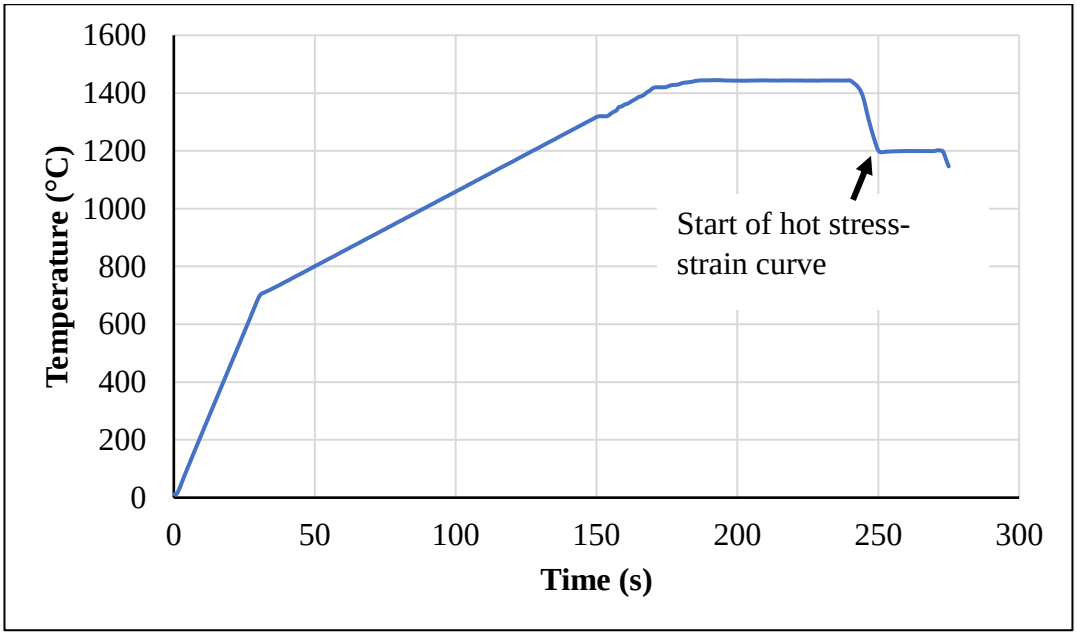

Figure 4.8: Temperature - time heating and cooling during hot tensile testing of a sample from 0.7Ti – stabilized ferritic stainless steel (Alloy C:0.7Ti) at 1200°C.

Table 4.8: The peak temperature extracted from the flow curves for every sample, and the nominal testing temperatures. The liquidus and solidus temperature (as estimated using Thermo-Calc) are also shown

Sample ID	Estimated liquidus temperature (°C)	Estimated solidus temperature (°C)	Average peak temperature during the soaking period (°C)	Testing temperature (°C)
C:0.7Ti	1500	1448	1443	1200
			1435	1250
			1429	1300
D:0.6Nb	1497	1387	1425	1200
			1403	1250
			1410	1300
E:0.4Ti;0.6Nb	1500	1448	1443	1200
			1429	1250
			1441	1300

4.8 Microstructure

(a) Houldcroft test

The samples were characterized after welding by sectioning close to the cracked part (Figure 4.10) and where there was no crack, near to the starting point of the weld. The samples were sectioned for optical and SEM analysis in two planes, one with the polished surface parallel to the plate surface and the second transverse to the welding direction. These sections were used to analyze the solidification structure in the welding direction and transverse to the welding direction. In addition, the polished surface parallel to the plate surface was used to measure the crack length.

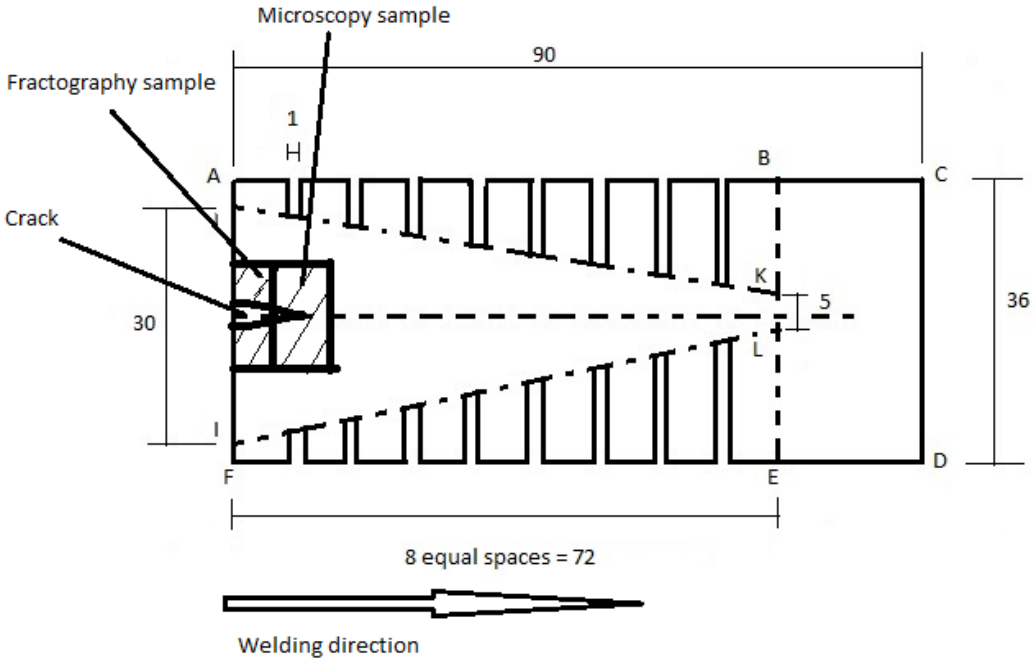

Figure 4.9: Schematic diagram showing sectioning for fractography and microscopy samples.

The cut pieces were hot mounted in bakelite after which the mounted samples were mechanically ground on 240, 320, 600, 800, and 1200/4000 grade silicon carbide papers. The samples were further polished to a 1 µm surface finish using diamond spray and diamond extender (lubricant). The polished samples were etched with an etchant containing three parts hydrochloric acid (HCL) and one part nitric acid (HNO_3) at room temperature to reveal grain boundaries and carbides [79]. An XM–15 optical microscope mounted with an Olympus U-TV0.5XC-3 camera was used for microstructural analysis of the etched samples with Stream Essentials software.

A JEOL JSM-IT 300 scanning electron microscope (SEM) with EDX at a voltage of 15 kV which uses Aztec software, was used for fractography studies. A gold sputter coating of the etched samples was done to prevent charging. The microstructure of the etched samples was imaged using the SEM while a secondary electron detector was used to acquire the images. The fraction of columnar and equiaxed grains were counted on the cross-sectional weld microstructures using point counting.

(b) Details of the MVT-test

Optical microscopy of the plane transverse to the welding direction was done using the XM–15 optical microscope. The polished surface was etched with 1.5 g potassium disulphite, 5 ml HCl and 100 ml distilled water [79].

(c) Hot tensile test

The hot tensile testing samples were sectioned lengthwise into two equal halves for microstructural examination and for fractography analysis. The sectioned half was mounted, ground and polished in accordance with the procedure used in the Houldcroft test. The hot tensile testing samples were etched with mixed acids of one part each of acetic acid, hydrochloric acid and nitric acid at room temperature. Fractography was done as stated earlier.

CHAPTER FIVE - RESULTS AND DISCUSSION FOR SELF-RESTRAINT HOULDCROFT TESTS

The self-restraint Houldcroft tests were done on seven different steels, and three welding speeds (6, 3 and 1 mm/s). Two samples were welded at the same welding speed. The resultant crack length was measured on the top and the bottom surfaces and the average was calculated. For the measurement of solidification cracks using Houldcroft method, the crack starts from the starting edge and propagates along the centreline of the weld [5, 22-23, 25]. All the cracks were observed to have started from the starting edge of the samples.

Generally, the length of the crack on the top and bottom surfaces were not the same. The bottom surface cracks were usually longer than the top surface cracks (Table 5.1). The average crack length on the top and bottom surfaces are presented in Table 5.2. The variation in crack length of the top and bottom surfaces was much pronounced in the I:0.1Ti;0.5Nb;2Mo grade than the rest which were mostly insignificant (Table 5.1). The degree of restraint played a role in the difference between the top and bottom surface crack lengths. The longer lengths might have been caused by greater restraints at the bottom surface, where the bead was narrower (Table 5.3) [5]. The properties of the surrounding HAZ and base metal, and the weld bead shape affect the internal restraint [16]. The magnitude of the difference was, in most cases, significantly smaller than the average crack length (Table 5.2). The difference in the crack length on the top and the bottom surface did not affect the results of this investigation. More so, from the micrographs of the cross sections, the morphology of the grains was different through the thickness, with some being columnar and others equiaxed for the same section thickness, and this might have contributed to the different crack lengths of the top and bottom surfaces (Figure 5.17).

The results showed that all the ferritic stainless steels cracked with a welding speed of 6 mm/s (Tables 5.1-5.2 & Figure 5.1). For the A:0Ti;0Nb grade, there was a crack in the first test but not in the second test (Table 5.1). For a welding speed of 3 mm/s, both mono stabilized and the dual stabilized steels cracked, and only the unstabilized steel

did not crack (Tables 5.1-5.2 & Figure 5.1). As there were two experiments to find repeatability of the alloys, Table 5.1 showed that the F:0.4Ti;0.9Nb and G:0.1Ti;0.4Nb grades did not crack in the second test. At a welding speed of 1 mm/s, the Nb stabilized and the dual stabilized steel containing Mo cracked whilst the other alloys did not (Tables 5.1-5.2 & Figure 5.1). It was observed that the I:0.1Ti;0.5Nb;2Mo grade cracked in all the welding speeds (Tables 5.1-5.2). For the Mo containing steel, the change in crack length with change in welding speed was not typical, as there was an increase and then a decrease in crack length with increasing welding speed (Tables 5.1-5.2). On the other hand, the crack length of the D:0.6Nb, which also cracked in all welding speeds, increased with increasing welding speed (Tables 5.1-5.2). This showed the detrimental effect of Nb mono stabilization in ferritic stainless steels.

The strain theory can be used to explain the crack formation. At the mushy stage of solidification, there was uniform distribution of strain in the solid-liquid mixture. Strains accumulated extremely high locally during the film stage, resulting in separation of the solid grains along the boundaries with continuous liquid films present. The cracking was a solid-liquid separation as the fracture surfaces of the dendrites were smooth (Figures 5.20, 5.22 & 5.25)

Table 5.3 shows the weld bead sizes of the top and bottom surface of the alloys. Comparing Tables 5.1 and 5.3, there was no relationship between the crack length, welding speed and the weld bead sizes. Literature has showed that it is the weld pool geometry that has been used to estimate solidification cracking [5, 80]. The effect of weld bead shape, concave or convex, can affect solidification cracking in a multipass weld [5]. From Table 4.5, the heat input decreased significantly as the welding speed increased (1 mm/s: 0.5 to 0.8 kJ/mm; 3 mm/s: 0.4 to 0.5 kJ/mm; 6 mm/s: 0.3 kJ/mm). This showed that the risk of solidification cracking increased with a lower heat input. This is in agreement with Ankara and Ari [42].

A plot of the stabilization content of Ti + Nb was made to investigate the effect of Ti and Nb on the cracking behavior of ferritic stainless steels (Figure 5.1), based on the average surface crack lengths (Table 5.2). In plotting either the Nb or Ti content, the

total amount of that stabilization was taken into account. For the steels characterized, the crack length increased with Ti + Nb content and with welding speed (Figure 5.1). Standard deviation of the stabilization contents could not be determined by the two (2) test data points. The welding speed was more influential in determining the crack length than the chemistry of the alloys. This was revealed in the circled marker points in Figure 5.1 which showed that, welding speed was more prominent than the stabilization content. Figures 5.3 and 5.5 showed the effect of Nb and Ti on the crack length respectively. It can be said that the dual stabilization contributed to the solidification cracking as the range of the average crack length values was a function of (Ti + Nb) content, similar to the two graphs plotting the crack length against the Ti or the Nb content (Figures 5.3 & 5.5).

In general, there were more columnar grains than equiaxed grains. The fraction of equiaxed grains are shown in Figures 5.2, 5.4 & 5.6. The fraction equiaxed grains points were a bit scattered for the Nb stabilization content (Figure 5.4) and further scattered for the Ti stabilization content (Figure 5.6) relatively. A plot of crack length and fraction equiaxed grains was made and it was found that there was no correlation between the two parameters (Figure 5.7). It was therefore concluded that, under the thermal conditions prevalent during the Houldcroft test, the susceptibility to solidification cracking was not sensitive to the solidification grain structure.

Table 5.1: The average top and bottom crack lengths measured for the self-restraint Houldcroft method

Steel grade	Welding speed (mm/s)	Test number	Crack length on top surface (mm)	Crack length on bottom surface (mm)	Average crack length (mm)	Crack length on bottom surface – crack length on top surface (mm)
A:0Ti;0Nb	1	1	0.0	0.0	0.0	0.0
		2	0.0	0.0	0.0	0.0
	3	1	0.0	0.0	0.0	0.0
		2	0.0	0.0	0.0	0.0
	6	1	10.5	12.3	11.4	1.8
		2	0.0	0.0	0.0	0.0
C:0.7Ti	1	1	0.0	0.0	0.0	0.0
		2	0.0	0.0	0.0	0.0
	3	1	26.5	27.8	27.2	1.3
		2	7.9	9.1	8.5	1.2
	6	1	29.4	31.1	30.3	1.7
		2	19.5	19.8	19.7	0.3
D:0.6Nb	1	1	5.0	4.2	4.6	-0.8
		2	4.8	4.4	4.6	-0.4
	3	1	12.0	11.5	11.8	-0.5
		2	11.5	14.0	12.8	2.5
	6	1	36.2	38.2	37.2	2.0
		2	31.5	31.5	31.5	0.0
E:0.4Ti;0.6Nb	1	1	0.0	0.0	0.0	0.0
		2	0.0	0.0	0.0	0.0
	3	1	15.2	19.0	17.1	3.8
		2	11.8	14.0	12.9	2.2
	6	1	31.1	31.8	31.5	0.7
		2	30.3	31.0	30.7	0.7
F:0.4Ti;0.9Nb	1	1	0.0	0.0	0.0	0.0
		2	0.0	0.0	0.0	0.0
	3	1	23.0	22.2	22.6	-0.8
		2	0.0	0.0	0.0	0.0
	6	1	34.0	32.1	33.1	-1.9
		2	32.5	29.6	31.1	-2.9
G:0.1Ti;0.4Nb	1	1	0.0	0.0	0.0	0.0
		2	0.0	0.0	0.0	0.0
	3	1	16.0	17.8	16.9	1.8
		2	0.0	0.0	0.0	0.0
	6	1	31.9	34.2	33.1	2.3
		2	20.0	18.0	19.0	-2.0
I:0.1Ti;0.5Nb;2Mo	1	1	6.2	10.9	8.6	4.7
		2	3.0	9.9	6.5	6.9
	3	1	7.2	14.1	10.7	6.9
		2	12.9	14.5	13.7	1.6
	6	1	10.0	0.0	5.0	-10.0
		2	5.8	0.0	2.9	-5.8

Table 5.2: The average top and bottom crack lengths (in mm), as measured using the self-restraint Houldcroft method, as a function of welding speed and steel grade

Steel grade	Welding speed		
	6 mm/s	3 mm/s	1 mm/s
A:0Ti;0Nb	5.7	0.0	0.0
C:0.7Ti	25.0	17.8	0.0
D:0.6Nb	34.4	12.3	4.6
E:0.4Ti;0.6Nb	31.1	15.0	0.0
F:0.4Ti;0.9Nb	32.1	11.3	0.0
G:0.1Ti;0.4Nb	26.0	8.5	0.0
I:0.1Ti;0.5Nb;2Mo	4.0	12.2	7.5

Table 5.3: The weld bead size of the top and bottom surface of the alloys

Alloy	Top (mm)	Bottom (mm)	Top (mm)	Bottom (mm)	Top (mm)	Bottom (mm)
	6 mm/s		3 mm/s		1 mm/s	
A:0Ti;0Nb	6.6	5.2	8.4	6.4	9.6	9.4
C:0.7Ti	6.5	6.1	7.7	7.1	9.0	7.2
D:0.6Nb	9.3	6.5	12.2	10.6	9.0	8.5
E:0.4Ti;0.6Nb	8.6	6.8	9.1	6.7	8.1	7.7
F:0.4Ti;0.9Nb	9.7	6.1	8.5	7.3	8.3	6.8
G:0.1Ti;0.4Nb	7.8	5.2	8.6	6.5	6.2	4.7
I:0.1Ti;0.5Nb;2Mo	8.8	7.4	12.7	9.1	11.0	8.0

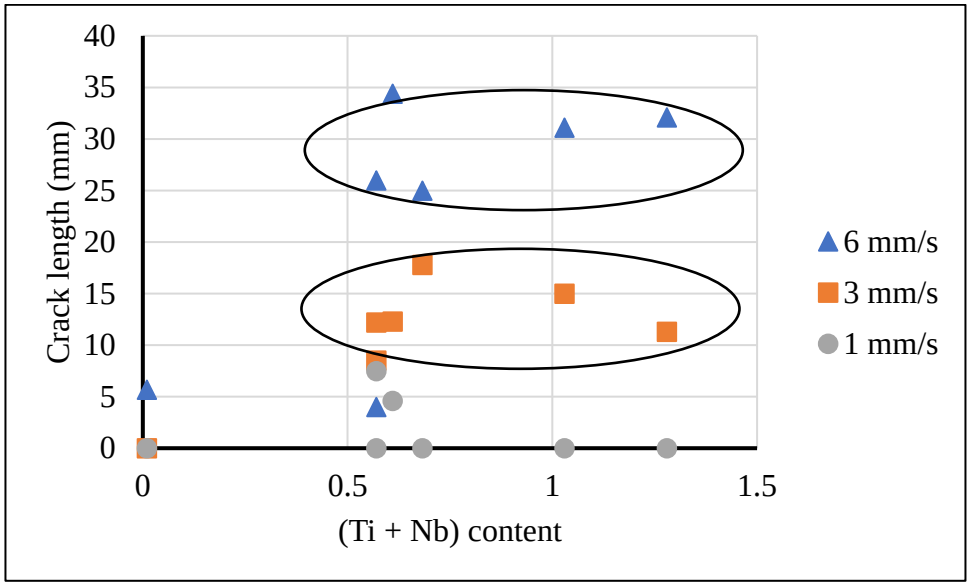

Figure 5.1: Average crack length against (Ti + Nb) content for a welding speed of 6, 3 and 1 mm/s.

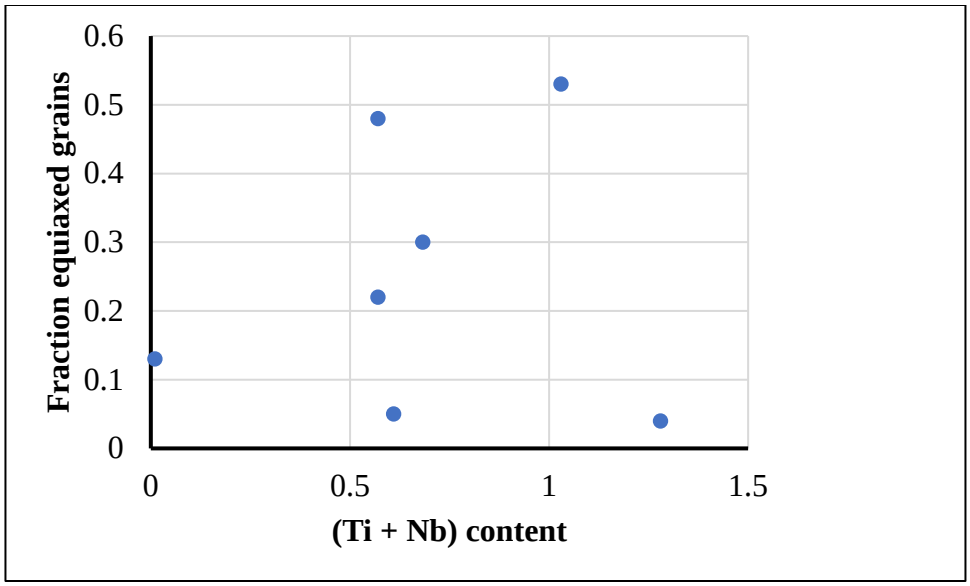

Figure 5.2: The fraction equiaxed grains, as measured on a metallographic section transverse to the welding direction was determined for the Ti + Nb content using a Houldcroft-type self-restraint sample.

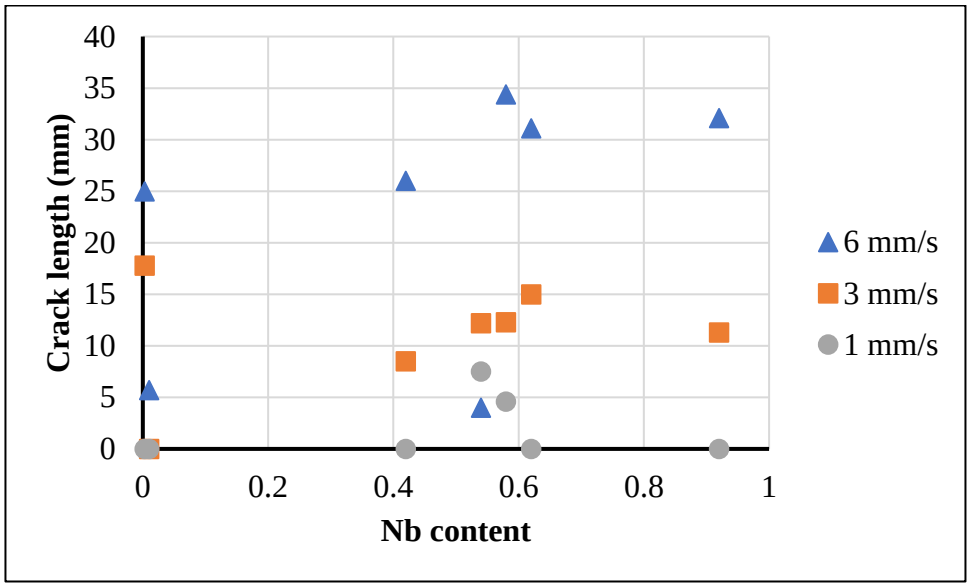

Figure 5.3: Average crack length against Nb content for a welding speed of 6, 3 and 1 mm/s.

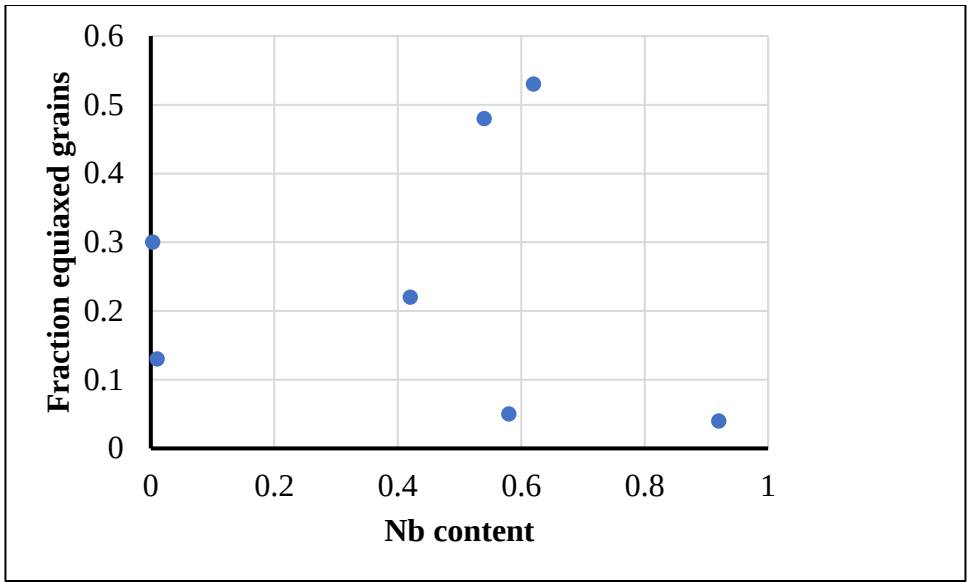

Figure 5.4: The equiaxed grains, as measured on a metallographic section transverse to the welding direction was determined for the Nb content using a Houldcroft-type self-restraint sample.

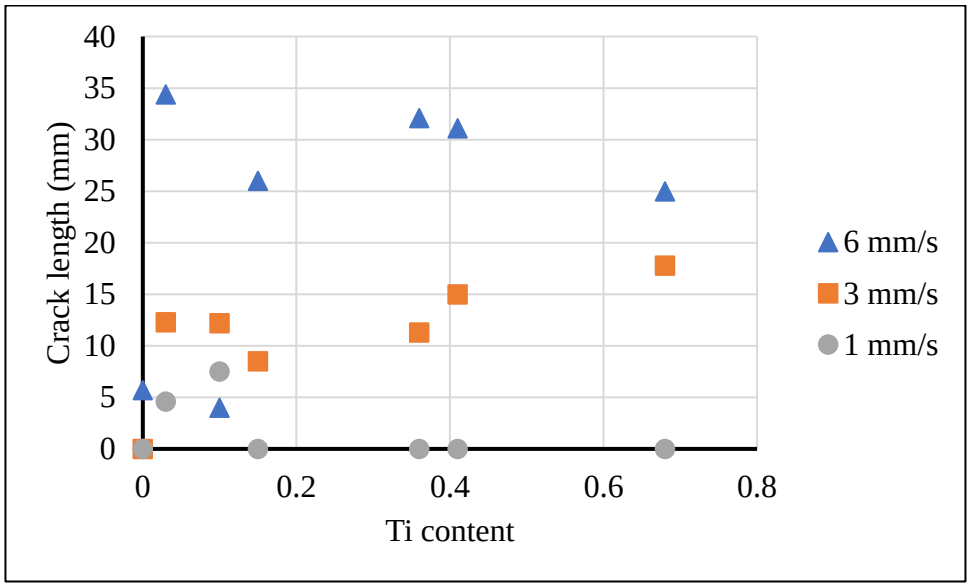

Figure 5.5: Average crack length against Ti content for a welding speed of 6, 3 and 1 mm/s.

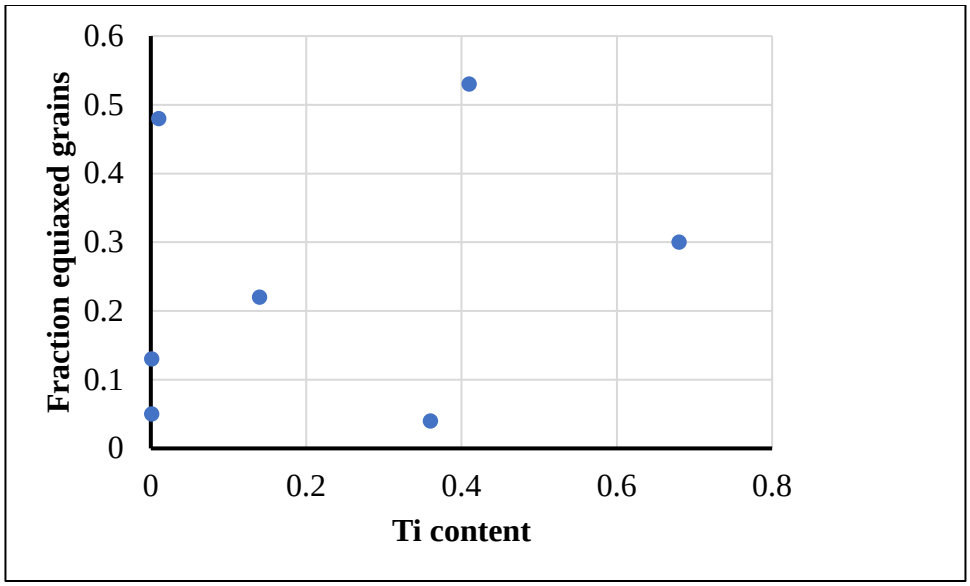

Figure 5.6: The equiaxed grains, as measured on a metallographic section transverse to the welding direction was determined for the Ti content using a Houldcroft-type self-restraint sample.

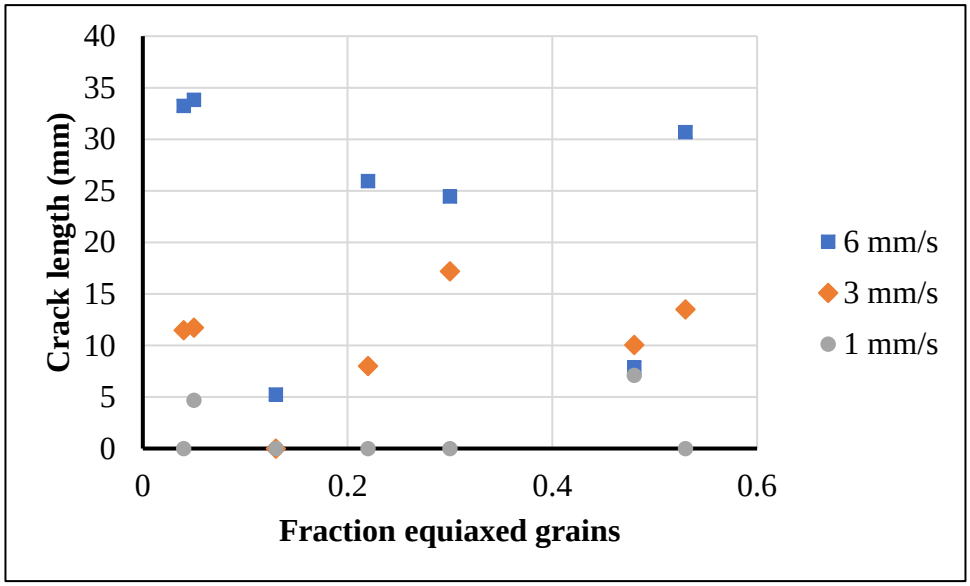

Figure 5.7: Crack length as a function of equiaxed grains using the self-restraint Houldcroft method.

The weld metal solidification structure was expected to affect the susceptibility to weld solidification cracking. When columnar grains impinge at the weld centreline, the risk

of solidification cracking increased with other factors like low melting eutectic liquids. For columnar grains that do not impinge at the centre due to a low welding speed or the presence of equiaxed grains, solidification cracking susceptibility is reduced [5, 16-17, 25, 78]. These statements were not observed in the current study as revealed in Figure 5.7.

The SEM morphology of the microstructures revealed:

Two of the solidification cracks were found to be transgranular at the end of the crack (Figures 5.9 & 5.12) and the rest intergranular (Figures 5.14 – 5.16). The transgranular cracks were not solidification cracks as solidification cracks are intergranular [5, 16, 81]. The transgranular cracks were not representative of the microstructures, given that the SEM images (Figures 5.17, 5.19 & 5.22) showed the crack path to be intergranular. The transgranular cracks were observed at the tip of the whole crack length. From Figure 4.7, the experimental diagram for analysis for fractography was such that, such investigations were not conducted at the crack tip to confirm this fracture through the grains. Research shows that hydrogen induced cracking is intragranular and it occurs within 72 hours after welding [16]. All the specimens were investigated after this waiting period. It has also been stated that residual stresses can cause hydrogen induced cracking [5]. The possibility of transgranular hydrogen induced cracking was considered beyond the scope of this research.

For a metallographic plane parallel to the plate surface, the samples had the following microstructures:

At a welding speed of 6 mm/s, these structures were observed:

- All the welds showed epitaxial growth for all the welding speeds (Figure 5.8). The existing base metal at the fusion line acted as the substrate for nucleation of new grains. Crystals nucleate from the liquid metal in contact with the base metal substrate grains and there is little or no nucleation barrier. It is observed as the atoms of the liquid metal arranging on the substrate grains without changing their crystallographic orientations. Grain boundaries become continuous across the fusion boundary [5, 16, 22, 82].

- The unstabilized (A:0Ti;0Nb) (Figure 5.10), the mono-stabilized (C:0.7Ti & D:0.6Nb) (Figures 5.9 & 5.11) and the commercial dual stabilized (G:0.1Ti;0.4Nb) (Figure 5.15) ferritic stainless steels showed columnar grains which impinged at the weld centre. A high heat input of 250 A × 18 V and a high welding speed of 6 mm/s without nucleation by refractory particles in the bulk weld metal resulted in the columnar grains of the A:0Ti;0Nb, C:0.7Ti, D:0.6Nb and G:0.1Ti;0.4Nb [5, 16, 22, 83]. Tear drop shaped weld pools are associated with high welding speeds. The favourably oriented grains to the solid-liquid interface, which are straight, grow from the fusion boundary to the centreline. This prevents competitive growth of the grains and they continuously grow till they impinge on those from the other side of the weld along the weld centreline [5, 16].
- The commercial G:0.1Ti;0.4Nb steel revealed columnar grains with the crack adjacent to the weld centreline (Figure 5.15). The columnar grains might be due to the low Ti + Nb content as the high content produced equiaxed grains. As noted previously, Villaret et al. [64] reported that columnar grains of ferritic stainless steel changed their structure to equiaxed grains for contents above 0.15 wt% Ti. Not all the grades with Ti contents above 0.15 wt% showed equiaxed grains since the E:0.4Ti;0.6Nb alloy revealed columnar grains on one side of the crack during a welding speed of 6 mm/s (Figure 5.13).
- The experimental dual stabilized steels (E:0.4Ti;0.6Nb & F:0.4Ti;0.9Nb) (Figure 5.13) revealed different microstructures on either side of the weld centreline. The steel containing E:0.4Ti;0.6Nb alloy showed columnar grains at one side and fine equiaxed grains on the other side (Figure 5.12). As the work was based on solidification cracking, these cracks were assumed to be exactly in the weld centreline. The cracks were probably not really in the centre, but rather within the weld zone. This might have resulted in the different structures on either side of the crack. The high heat input of 250 A × 18 V and a high welding speed of 6 mm/s with nucleation in the weld resulted in the equiaxed grains in the weld zone [22, 83]. The columnar grains on the other side of the

crack can be attributed to no nucleation in the weld zone [5, 16, 22, 83]. The effect of residual stresses on either side of the crack might have contributed to the different grains formation. The measurement of strain is not possible with self-restrained tests which includes the Houldcroft method. The steel containing F:0.4Ti;0.9Nb showed very fine equiaxed grains on one side of the crack. These fine equiaxed grains might be due to more nucleation sites in this side of the crack, which produced more numerous new grains [83]. The other side had a structure consisting of coarse equiaxed grains. The coarse equiaxed grains can be seen to be fewer nucleation particles being present at that side of the crack, which produced fewer new grains. As discussed earlier, thermal strains might have played a role in the different microstructures at either side of the crack.

- The commercial dual stabilized steel containing Mo (I:0.1Ti;0.5Nb;2Mo) showed equiaxed grains.
- The crack in the dual stabilized steels without Mo (E:0.4Ti;0.6Nb & G:0.1Ti;0.4Nb) was apparently discontinuous (Figures 5.13 & 5.15). The probably discontinuous crack might be from the plane of sectioning for microstructural examination, which portrayed a discontinuous crack.

The samples that were welded at 3 mm/s showed the following features:

- An axial grain which was perpendicular to the weld pool boundary grew between columnar grains in the unstabilized steel (A:0Ti;0Nb). This sample did not crack. The axial grains grew from the start of the fusion boundary and along the length of the weld. This axial grain blocked the columnar grains from the weld pool boundary from impinging at the weld centre and might have helped in making A:0Ti;0Nb being resistant to solidification cracking [5, 16, 22]. The zero stabilization of Ti and Nb in ferritic stainless steels also contributed to the resistance of steel A:0Ti;0Nb to solidification cracking [4].
- The mono stabilized steels (C:0.7Ti & D:0.6Nb) and dual stabilized steel containing E:0.4Ti;0.6Nb showed columnar grains adjacent to the centreline crack. This could be due to the heat input of 180 – 190 A × 15 – 16 V and a welding speed of 3 mm/s with the absence of nucleation in the bulk weld metal

producing columnar grains [5, 16, 22, 83] which impinged at the weld centre to produce solidification cracks.

- The dual stabilized steels containing F:0.4Ti;0.9Nb, G:0.1Ti;0.4Nb, and I:0.1Ti;0.5Nb;2Mo grades showed equiaxed grains next to the crack. This is also explained as the heat input of 180 – 190 A × 15 – 16 V and a welding speed of 3 mm/s producing new grains from nucleation on precipitation particles within the weld zone. These equiaxed grains could not prevent solidification cracking and is contrary to literature [5, 16, 81, 83]. This will be explained further.
- The crack in the dual stabilized steels containing E:0.4Ti;0.9Nb, F:0.4Ti:0.9Nb (Figure 5.15), G:0.1Ti;0.4Nb, and I:0.1Ti;0.5Nb;2Mo alloys were probably discontinuous.
- The effect of the residual stress was more severe in the welding speed of 6 mm/s than the welding speed of 3 mm/s. The different grains of fine equiaxed and equiaxed in the same alloys were much pronounced in the welding speed of 6 mm/s. This could be due to the different heat inputs which generated thermal contraction and volumetric shrinkage on the specimens [82-83, 85]. The photography of the unsectioned samples during a welding speed of 6 mm/s was much strained in the slotted length compared to the same sample during a welding speed of 3 mm/s (Figure 5.18).

At a welding speed of 1 mm/s, the weld metal microstructure consisted of columnar grains. The columnar grains were due to low heat input of 90 – 120 A and 12 – 13 V and a low welding speed of 1 mm/s producing these columnar grains. Low welding speeds are known to produce elliptical weld pool which results in columnar grains and do not impinge at the weld centre [5, 16, 22, 83].

The presence of equiaxed grains of the experimental dual stabilized grades in the weld metal was consistent with the observations by Villaret et al. [64]. On the other hand, the solidification crack associated with equiaxed grains is contrary to some published literature [5, 16-17, 81]. The crack in the weld metal dominated by equiaxed grains

indicated that neither equiaxed nor columnar grains could resist the propagation of solidification cracks, in the Houldcroft samples used during the current study.

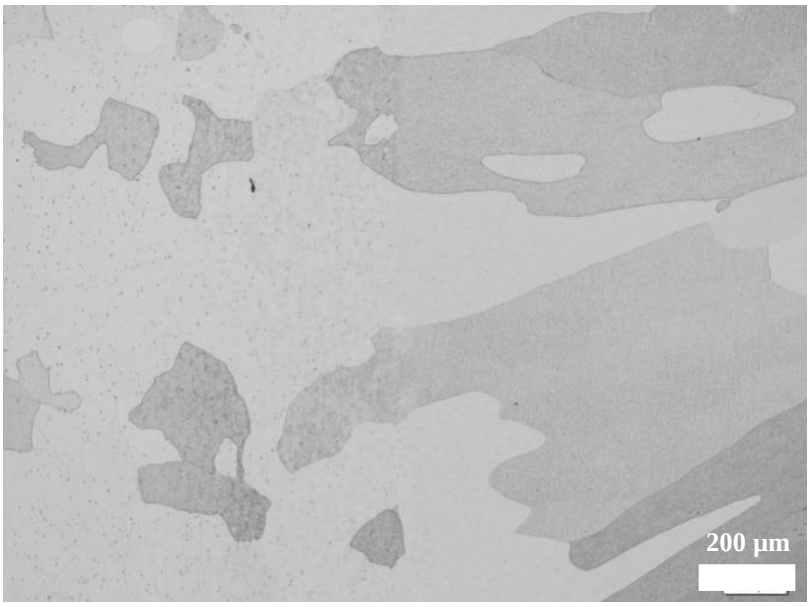

Figure 5.8: Epitaxial growth of the 0.6Nb - stabilized ferritic stainless steel (D:0.6Nb) during a welding speed of 6 mm/s.

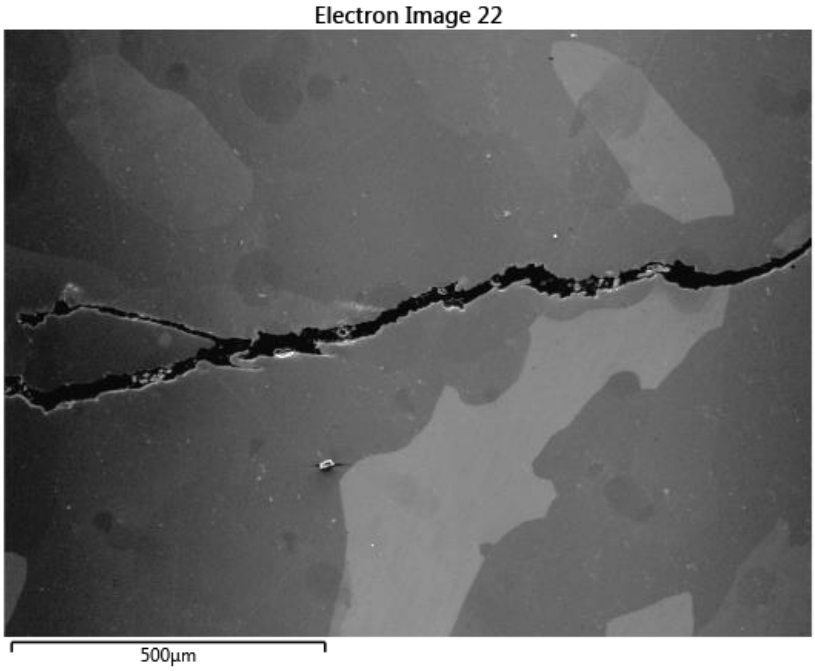

Figure 5.9: Secondary electron micrograph of the 0.7Ti - stabilized ferritic stainless steel (C:0.7Ti) showing a transgranular crack in the grain during the welding speed 6 mm/s in the polished surface parallel to the plane surface.

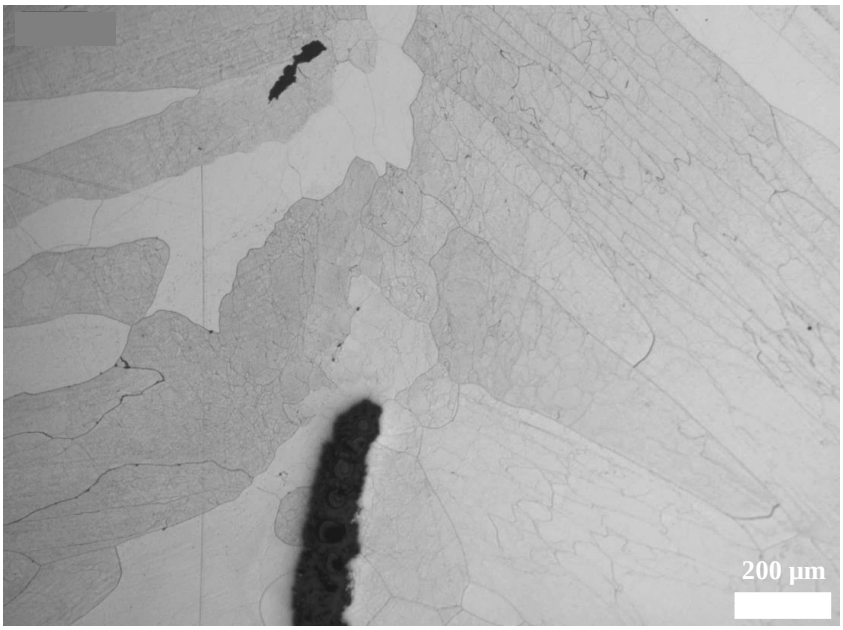

Figure 5.10: The crack at the weld centre of the unstabilized ferritic stainless steel (A:0Ti;0Nb) during a welding speed 6 mm/s.

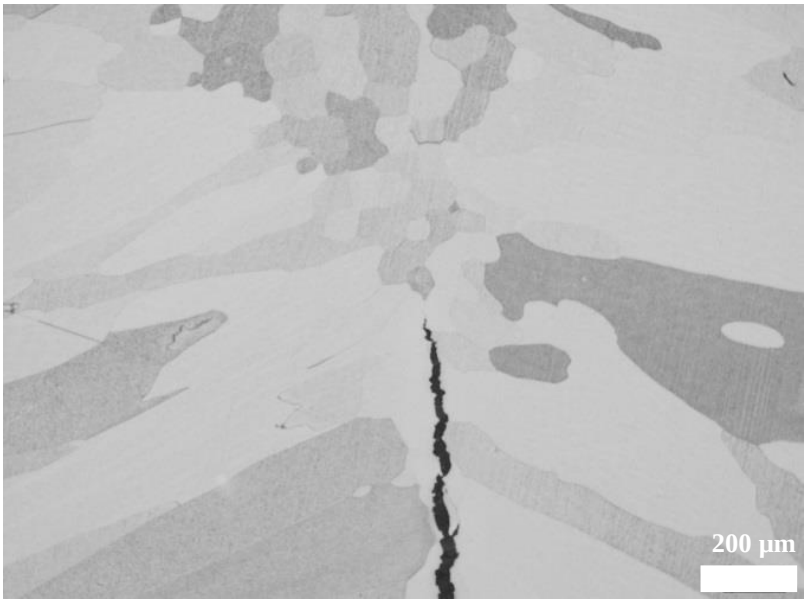

Figure 5.11: The centre of the weld metal showing the crack of the 0.6Nb stabilized ferritic stainless steel (D:0.6Nb) during the welding speed 6 mm/s.

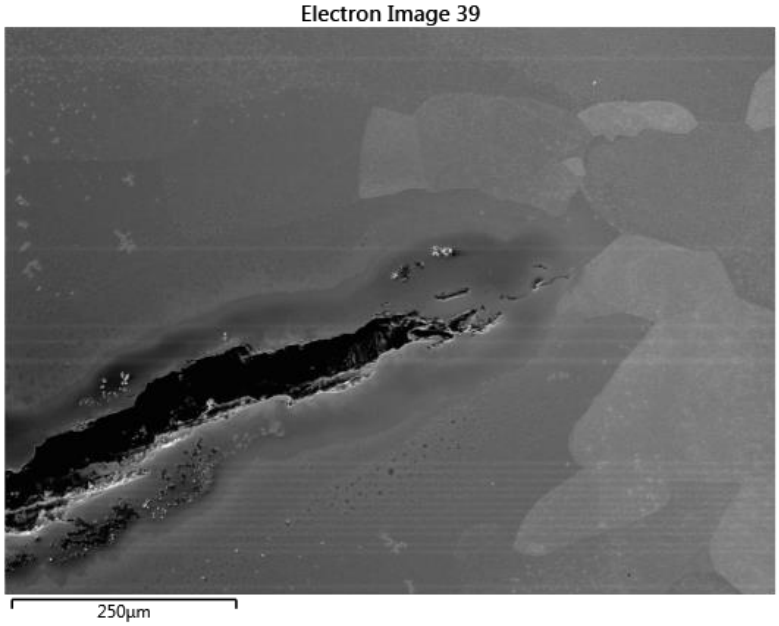

Figure 5.12: Secondary electron micrograph of the 0.6Nb - stabilized ferritic stainless steel (D:0.6Nb) with the crack in the grain during the welding speed 3 mm/s.

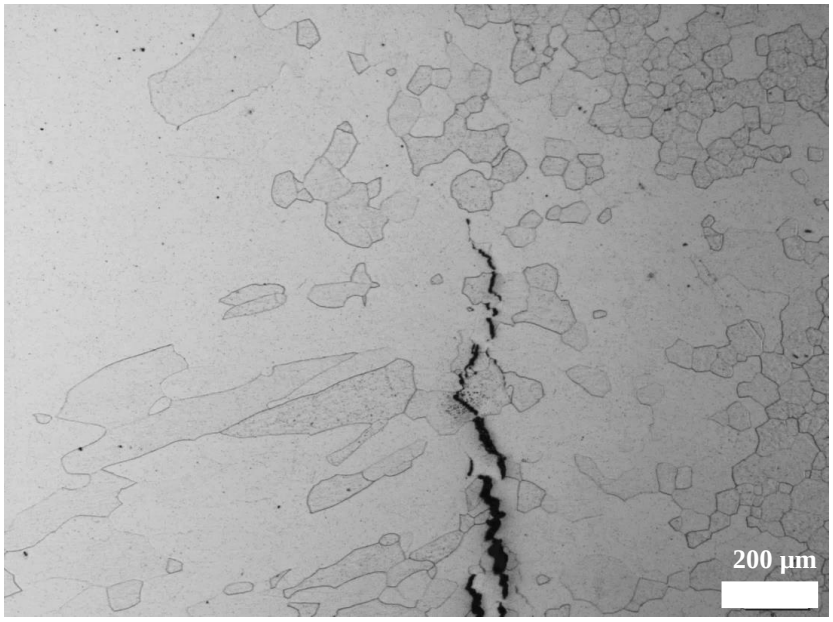

Figure 5.13: The crack at the weld metal interface showing equiaxed and columnar grains of the 0.4Ti + 0.6Nb - stabilized ferritic stainless steel (E:0.4Ti;0.6Nb) during the welding speed 6 mm/s.

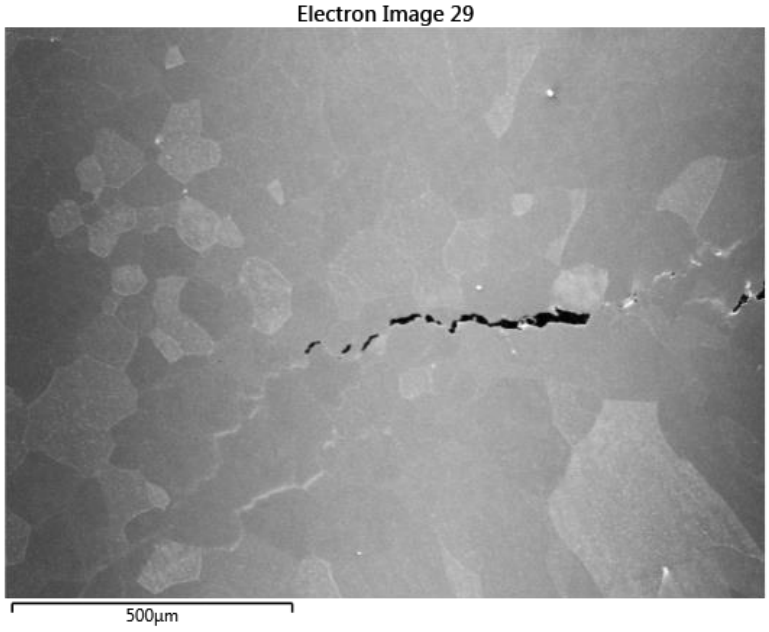

Figure 5.14: Secondary electron micrograph of the 0.4Ti + 0.6Nb - stabilized ferritic stainless steel (E:0.4Ti;0.6Nb) revealing secondary particles and the crack along the grain boundary during the welding speed 6 mm/s.

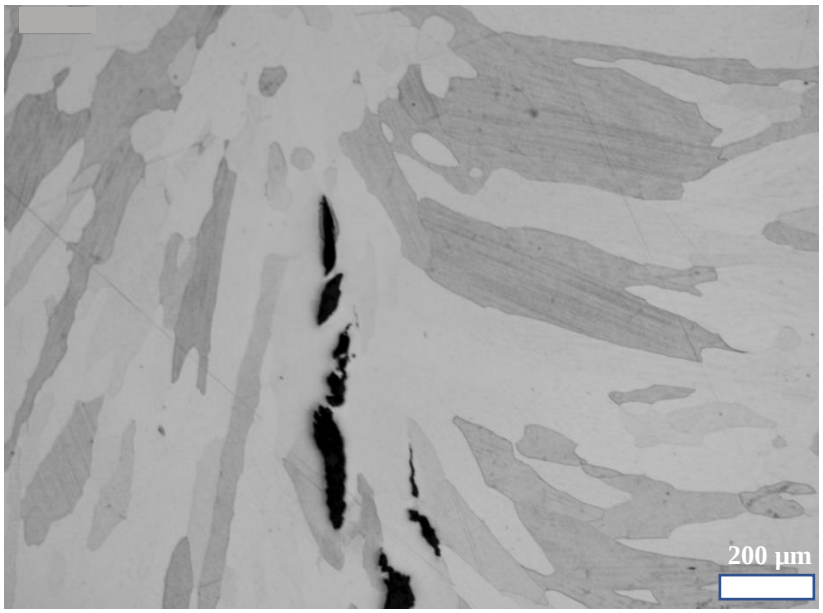

Figure 5.15: The crack at the centerline of the weld metal revealing the columnar grains of the 0.1Ti + 0.4Nb - stabilized ferritic stainless steel (G:0.1Ti;0.4Nb) during the welding speed 6 mm/s.

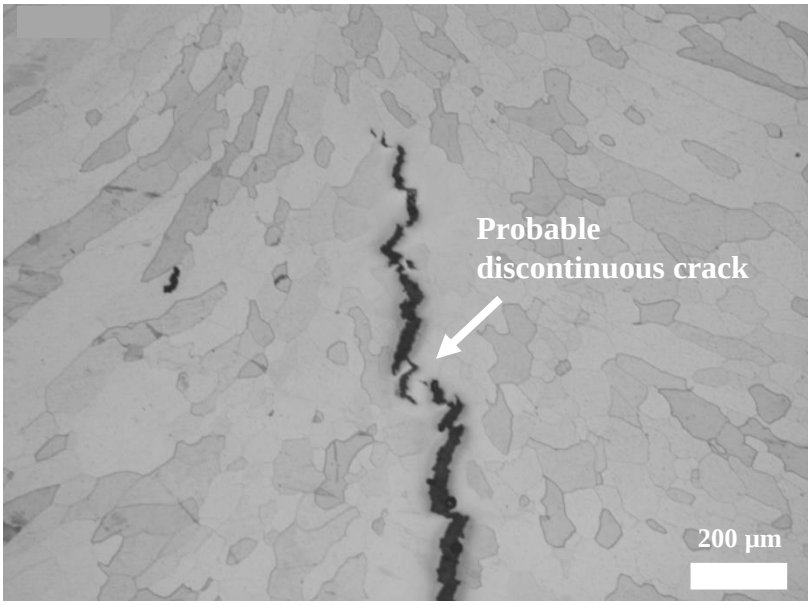

Figure 5.16: Discontinuous crack in the weld centerline and weld metal columnar grains of the 0.4Ti + 0.9Nb - stabilized ferritic stainless steel (F:0.4Ti;0.9Nb) during the welding speed 3 mm/s.

The polished surface transverse to the welding direction showed three different microstructures. Literature on cross-sectional welds exist for the geometry of multi-pass welds, which are used for solidification cracking susceptibility tests studies [5, 16]. In sectioning the specimens, it was not done at the same distance from the start of the weld. The weld bead sizes showed that there was no relationship with the crack lengths (Figure 5.19). The observed grains in the plane perpendicular to the plate surface could not be used to explain solidification cracking mechanism. The contribution of the different grains of the polished surface transverse to the welding direction might have contributed to the different crack lengths of the top and bottom surfaces (Figure 5.17).

The welding at a speed of 6 mm/s resulted in:

- The unstabilized (A:0Ti;0Nb), the mono-stabilized (C:0.7Ti & D:0.6Nb), the experimental dual stabilized F:0.4Ti;0.9Nb, and the commercial dual stabilized (G:0.1Ti;0.4Nb) grades showed mostly columnar grains on the entire thickness of the cross-sectional welds.
- The steel containing E:0.4Ti;0.6Nb grade was seen to contain equiaxed grains in the lower half of the weld thickness and columnar grains at the upper half. This observation was different from the behavior seen in other grades which has been described by Villaret et al. [64] that the grains are either all equiaxed or all columnar.
- The commercial dual stabilized steel containing Mo (I:0.1Ti;0.5Nb;2Mo) revealed equiaxed grains on the top section and columnar grains at the bottom section of the cross-sectional weld.

The welding at a speed of 3 mm/s revealed:

- The unstabilized (A:0Ti;0Nb) and the steels containing C:0.7Ti, E:0.4Ti;0.6Nb, F:0.4Ti;0.9Nb (Figure 5.17), G:0.1Ti;0.4Nb, and I:0.1Ti;0.5Nb;2Mo grades were found to show columnar grains at the bottom of the weld metal and equiaxed grains towards the top.
- The D:0.6Nb steel contained mostly columnar grains.

During the welding speed of 1 mm/s:

- The unstabilized (A:0Ti;0Nb), and the steels containing C:0.7Ti, E:0.4Ti;0.6Nb, F:0.4Ti;0.9Nb, and I:0.1Ti;0.5Nb;2Mo showed columnar grains at the bottom section and equiaxed grains in the top part of the weld.
- The steels containing D:0.6Nb and G:0.1Ti;0.4Nb were found to show columnar grains in the whole thickness of the weld.

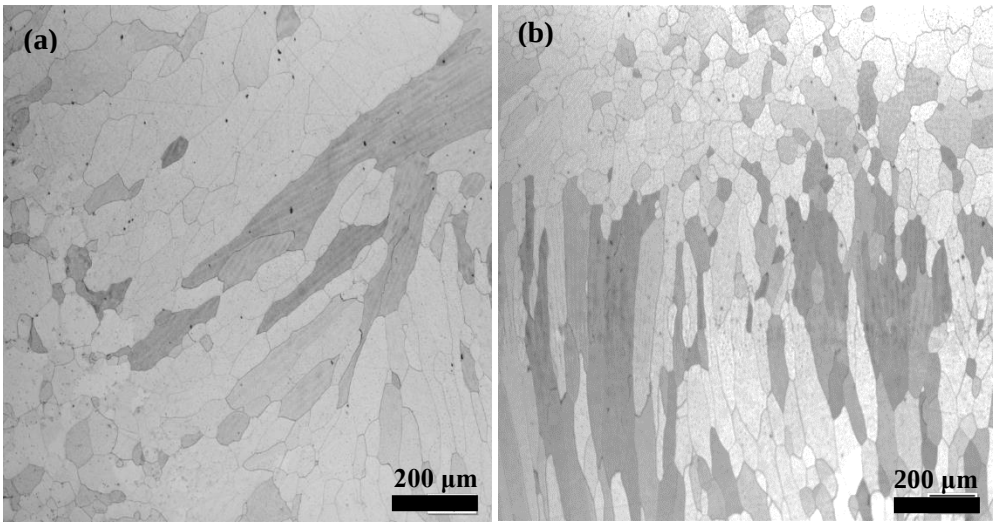

Figure 5.17: Microstructure of the F:0.4Ti;0.9Nb – stabilized ferritic stainless steel showing (a) base, HAZ, and weld region (b) weld centre at a welding speed of 3 mm/s. This showed different grains of equiaxed and columnar through the weld thickness.

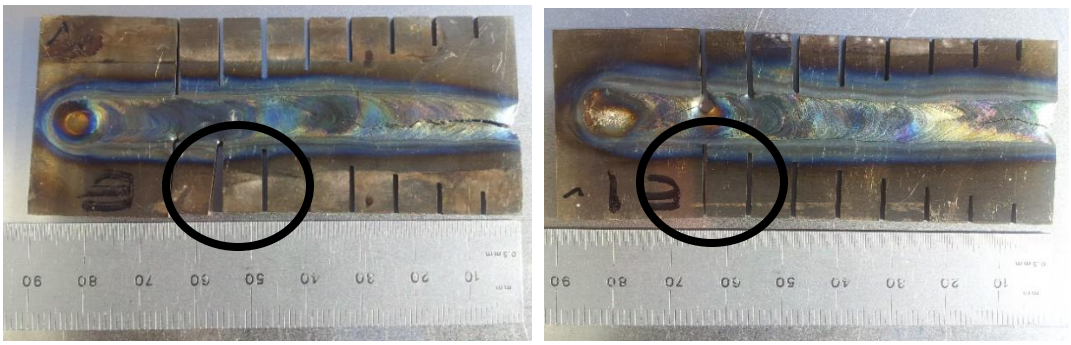

Figure 5.18: The welded sample of cracked E:0.4Ti;0.6Nb stabilized ferritic stainless steel during a welding speed of a) 6 mm/s and b) 3 mm/s showing a slightly rotated slotted material in a) more than in b) which have been circled.

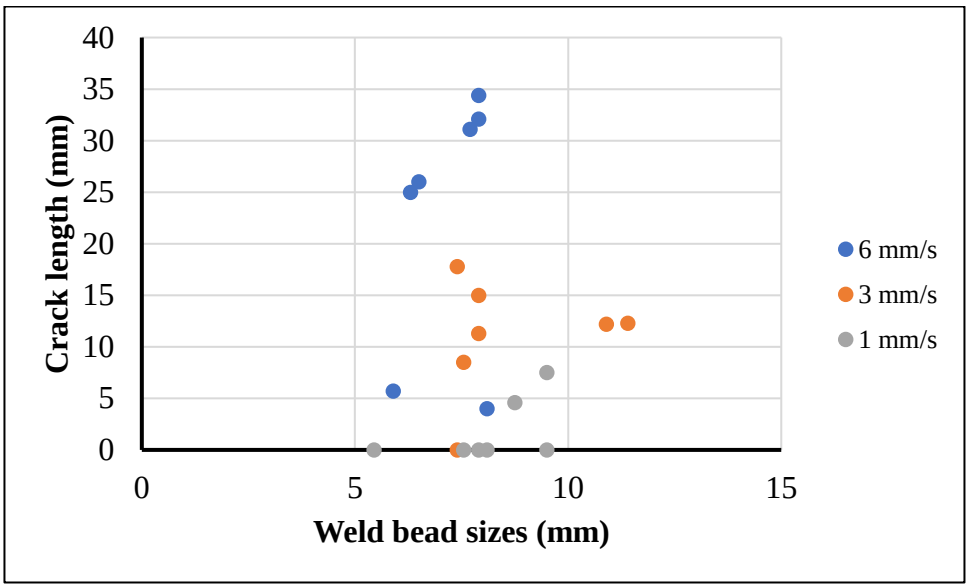

Figure 5.19: The average crack length as a function of the average weld bead sizes.

Fracture surfaces

All the solidification cracks revealed interdendritic structures. Interdendritic structures were found with the steel containing E:0.4Ti;0.6Nb at a welding speed of 6 mm/s being high fraction eutectic liquid (Figure 5.20) and the rest low fraction eutectic liquid (Figures 5.22 & 5.25). The semi-quantitative elemental analyses of the indicated sections have been shown in Figures 5.21, 5.24 and 5.26, with the rest shown in Appendix C.

During interpretation of the fracture morphology, the classification by Lippold [16], as high fraction (Figure 5.20) or low fraction eutectic (Figures 5.22 & 5.25), was used. The low fraction eutectic has been found to have a relatively low fraction (<5%) of eutectic liquid and the fracture surface reveals a very clear dendritic structure. The fracture surface of the high fraction eutectic liquid, on the other hand, is obscured by the backfilling liquid. This liquid coats the dendrites and has been shown to be more than about 10% eutectic liquid [16].

At a welding speed of 3 mm/s (but not at other welding speeds), the fracture surfaces of the D:0.6Nb (Figure 5.22) and E:0.4Ti;0.9Nb alloys contained precipitates between the dendrite arms. From Lippold [16], such precipitates are considered to contribute to solidification cracking (Figure 5.22). Lippold [16] reported the presence of second phase particles on the fracture surface of a Nb-bearing Ni-base alloy due to an eutectic reaction. As solidification began, the solute elements were rejected from the liquid into the mushy zone. At the later stage of solidification, the rejected elements acted as impurities to weaken the boundary layer, thereby resulting in cracking along the grain boundary [3]. SEM-EDX analysis of the precipitates in Figure 5.23 revealed that the particle contained mostly Nb and C (Figure 5.24). It was therefore concluded that the particle in Figure 5.23 was likely to be a NbC particle, consistent with the results of the Thermo-Calc calculations (Table 4.2).

The EDX elemental analysis of the fractured surfaces showed the elements Nb, Ti, O, Mn, Al, Si, Mo, S, and Ni to be associated with the solidification cracks for all welding speeds. These elements were based on the segregation coefficient between the representative elemental composition (Table 5.4 & Figure 5.27) and the fractured surfaces using the SEM-EDX semi-quantitative analysis of the samples. Figure 5.27 shows the analysis used for the representative bulk elemental analysis and Table 5.4 is the semi-quantitative analysis of selected six alloys. See Tables 5.5 – 5.7. (As discussed in more detail in section 7.1.2, the segregation coefficient is a semi-quantitative indicator of the ratio of alloy content on the fracture surface to the bulk alloy content using SEM-EDX). These elements were seen as being ejected to the grain boundary during solidification to form low melting point phases which eventually caused the

solidification cracking. Also, during solidification of weld metals, the solutes are ejected from the solids into the liquids and due to the fast cooling rate, the boundaries are enriched with the solutes causing impurities at the grain boundaries [85]. Not all the elements revealed by the fractured surface were found on the bulk representative elemental composition analyses using SEM-EDX. And such weight percent values of the elements found on the fractured surfaces were used as they were. The elements not revealed on the bulk elemental composition were found in the bulk chemical composition (Table 4.1).

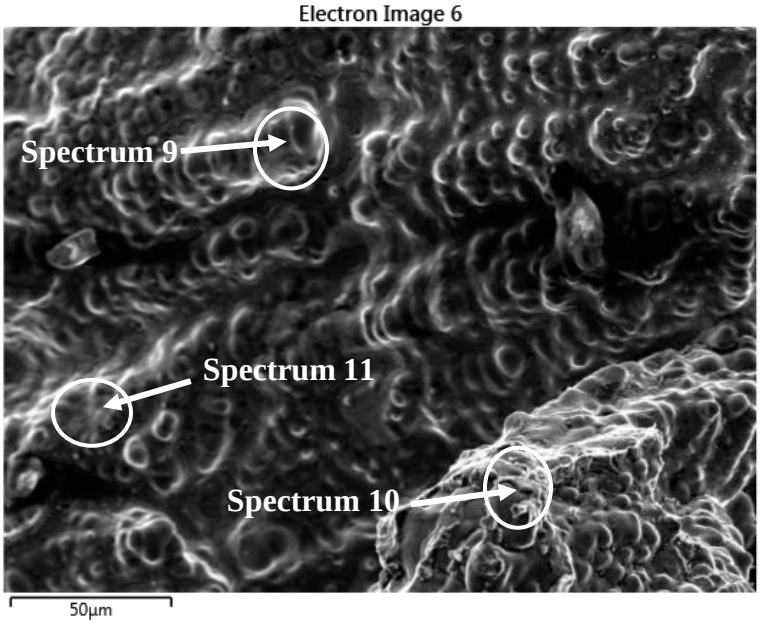

Figure 5.20: Secondary electron image of solidification cracking morphology of the 0.4Ti + 0.6Nb - stabilized ferritic stainless steel (E:0.4Ti;0.6Nb) showing the high fraction eutectic during the welding speed of 6 mm/s.

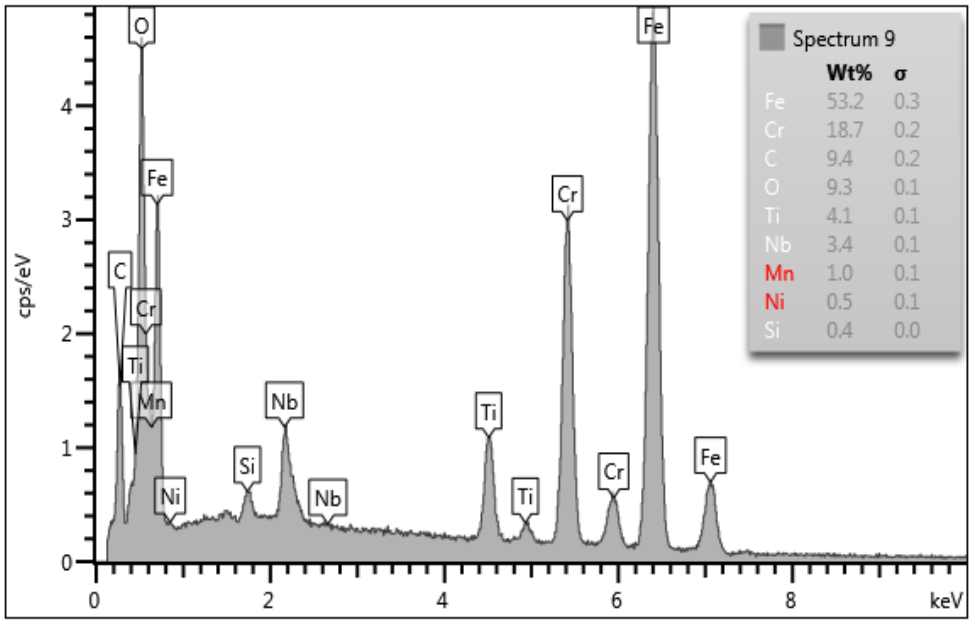

Figure 5.21: EDX semi-quantitative analysis during a welding speed of 6 mm/s for 0.4Ti + 0.6Nb - stabilized ferritic stainless steel (E:0.4Ti;0.6Nb) showing spectrum 9.

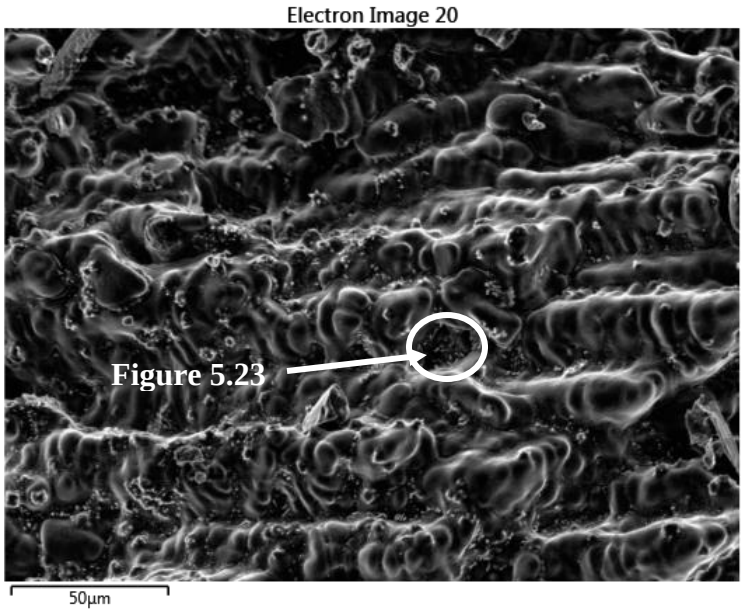

Figure 5.22: Secondary electron image of the solidification cracking morphology of the 0.6Nb - stabilized ferritic stainless steel (D:0.6Nb) showing low fraction eutectic during the welding speed of 3 mm/s.

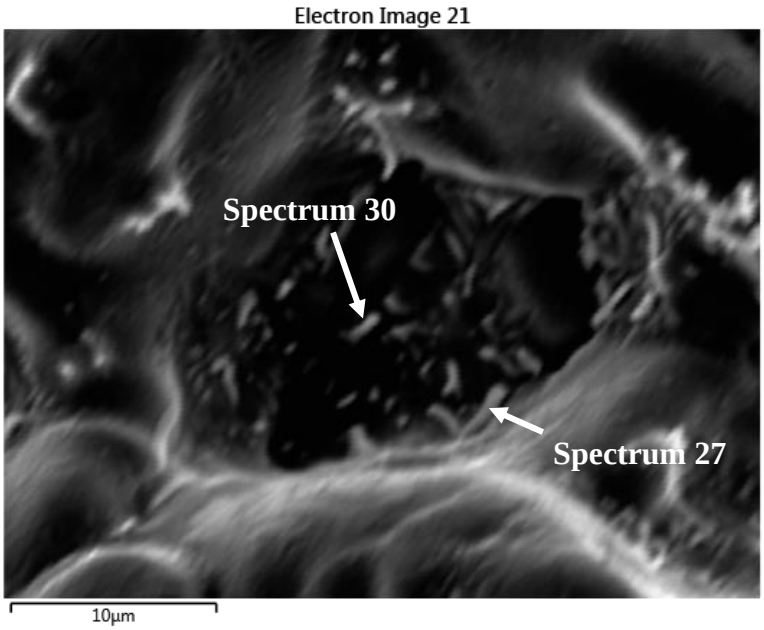

Figure 5.23: SEM fracture solidification cracking morphology of 0.6Nb -stabilized ferritic stainless steel (D:0.6Nb) showing precipitates at a welding speed of 3 mm/s.

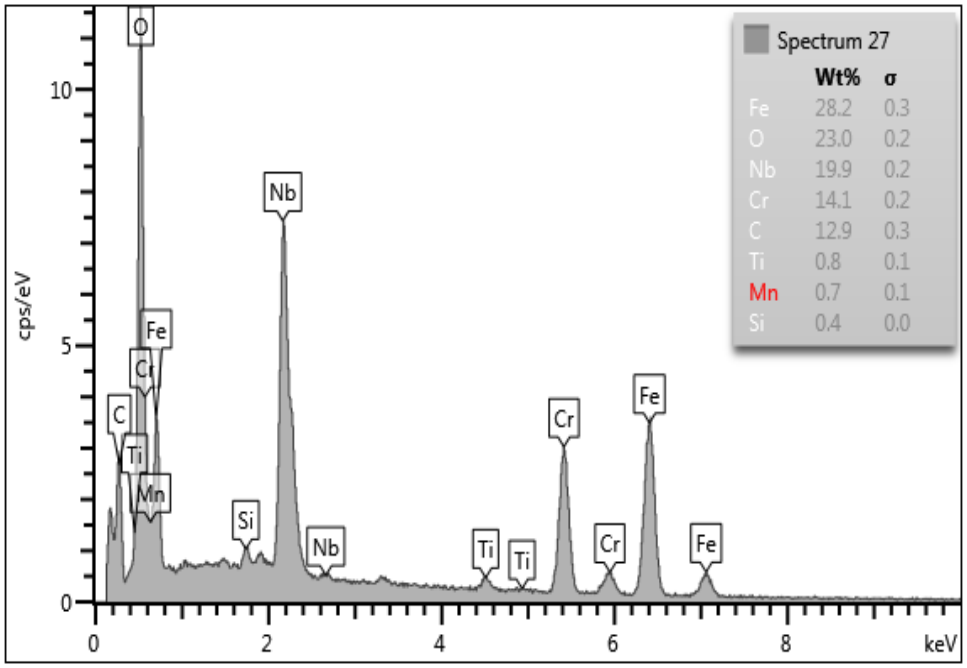

Figure 5.24: EDX semi-quantitative analysis during a welding speed of 6 mm/s for 0.6Nb - stabilized ferritic stainless steel (D: 0.6Nb) showing spectrum 27.

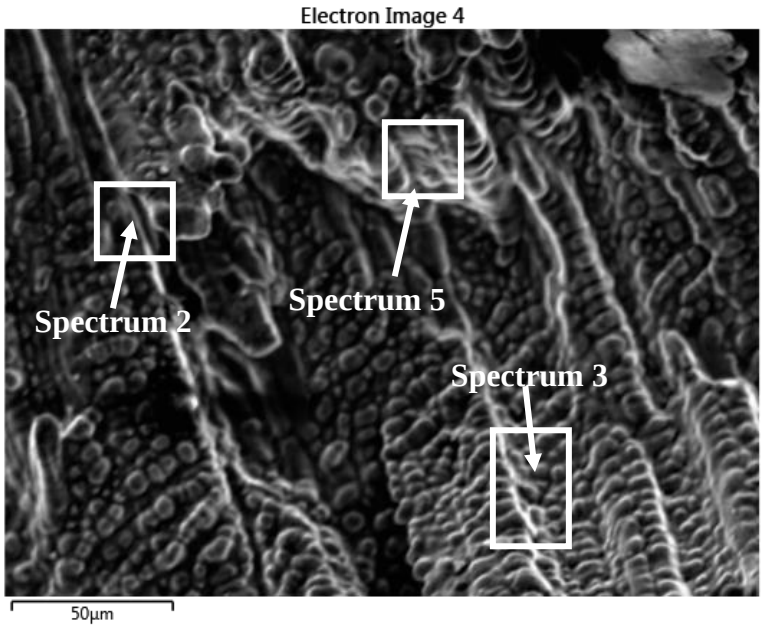

Figure 5.25: Secondary electron image of the solidification cracking morphology of the 0.7Ti - stabilized ferritic stainless steel (C:0.7Ti) showing the low fraction eutectic during the welding speed of 6 mm/s.

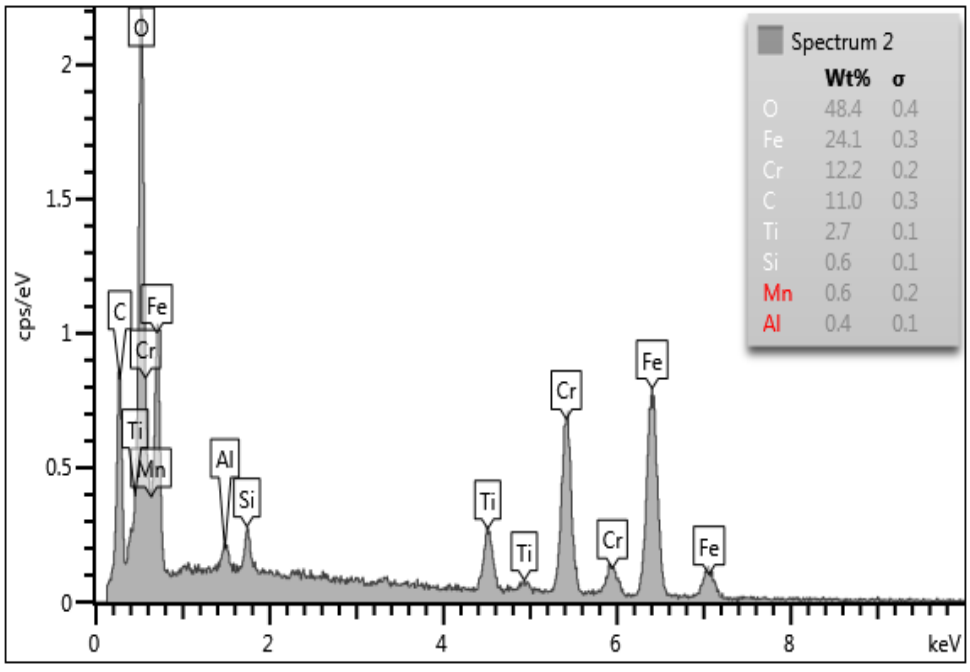

Figure 5.26: EDX semi-quantitative analysis during a welding speed of 6 mm/s for 0.7Ti - stabilized ferritic stainless steel (C:0.7Ti) showing spectrum 2.

Table 5.4: Selected EDX semi-quantitative analysis of five alloys as representative of the bulk composition

Sample ID	Fe	Cr	Nb	Ti	Si	Mn	Mo
C:0.7Ti	79.2	18.9		0.7	0.7	0.6	
D:0.6Nb	78.9	19.8	0.8	0.1	0.4		
E:0.4Ti;0.6Nb	78.4	19.4	0.8	0.4	0.5	0.5	
F:0.4Ti;0.9Nb	78.3	19.3	1.1	0.4	0.5	0.4	
G:0.1;0.4Nb	79.7	19	0.5	0.2	0.6	0.5	
I:0.1Ti;0.5Nb;2Mo	76.3	19.1	0.7	0.2	0.6	0.6	2.5

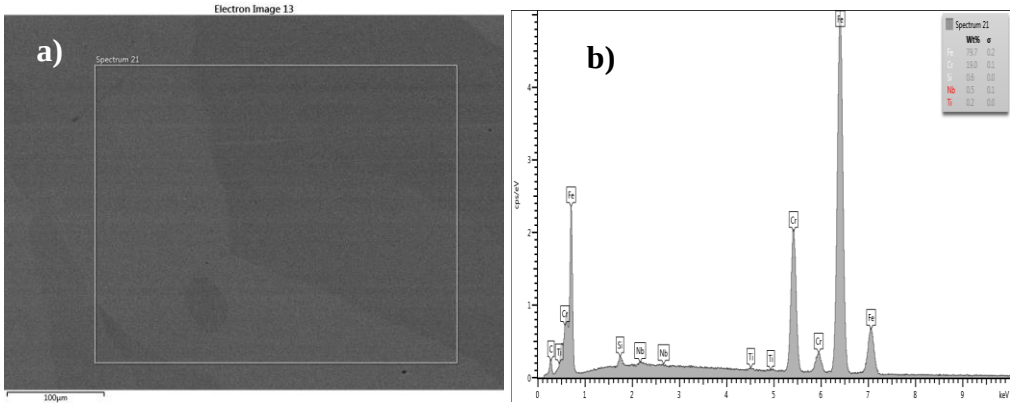

Figure 5.27: a) The image showing the area for the analysis and b) semi-quantitative bulk analysis of the G:0.1Ti;0.4Nb alloy.

Table 5.5: Selected EDX semi-quantitative analysis during a welding speed of 6 mm/s for E:0.4Ti;0.6Nb alloy

Element	Wt% on fracture surface	SEM-EDX bulk elemental composition	Concentration on fracture surface / bulk elemental composition
Nb	5.6	0.8	7
Ti	4.5	0.4	11
Mn	0.9	0.5	2
Si	0.5	0.5	1
Al	0.1	-	0.1
S	0.2	-	0.2

Table 5.6: Selected EDX semi-quantitative analysis during a welding speed of 3 mm/s for F:0.4Ti;0.9Nb alloy

Element	Wt% on fracture surface	SEM-EDX bulk chemical composition	Concentration on fracture surface from / bulk chemical composition
Nb	3.5	1.1	3
Ti	2.1	0.4	5
Mn	1.6	0.4	4
Si	0.5	0.5	1
Al	0.1	-	0.1

Table 5.7: Selected EDX semi-quantitative analysis during a welding speed of 1 mm/s for I:0.1Ti;0.5Nb;2Mo alloy

Element	Mass% on fracture surface	SEM-EDX bulk elemental composition	Concentration on fracture surface / bulk elemental composition
Nb	2.2	0.7	3
Ti	0.9	0.2	5
Mn	0.7	0.6	1
Si	0.6	0.6	1
Mo	1.8	2.5	1

The semi-quantitative analyses were also carried out at the crack tip, on the crack and adjacent to the crack to find the segregation behavior of Nb and Ti and the other elements of some of the alloys.

At the crack tip

From Table 5.8, it is seen that the ejection of Ti and Nb was about one and half times more for the Nb and same for the Ti, showing that the ejection was not as much as on the crack tip compared to the fractured surfaces. This revealed that the ejection of elements occurred at the grain boundaries during solidification. The Si was the same and the Mn was a little low. Generally, the other alloys revealed the same amount of ejection of Nb and Ti compared to the G:0.1;0.4Nb at the crack tip. Figure 5.28 shows the image for the crack tip and the EDX semi-quantitative analysis for the F:0.4Ti;0.9Nb alloy.

Table 5.8: Selected EDX semi-quantitative analysis of the G:0.1Ti;0.4Nb alloy

Element	Mass% on fracture surface	SEM-EDX bulk elemental composition	Concentration at crack tip / bulk elemental composition
Nb	0.7	0.5	1.4
Ti	0.2	0.2	1
Mn	0.5	0.5	1
Si	0.5	0.6	0.8

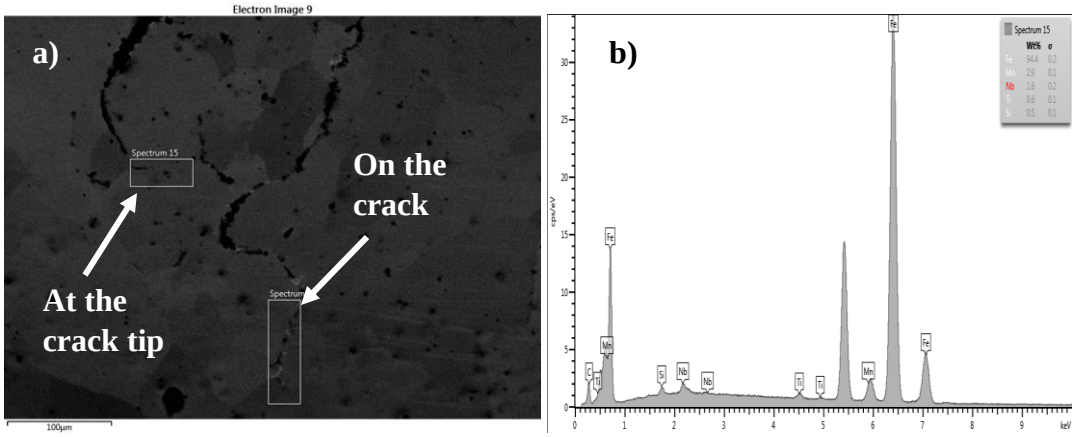

Figure 5.28: a) The image showing the area at the crack tip and on the crack for analysis and b) SEM-EDX semi-quantitative spectrum of the F:0.4Ti;0.9Nb alloy.

On the crack

EDX semi-quantitative analysis done on the crack is shown in Figure 5.28 and Table 5.9, it revealed that the ejection of Nb, Ti, Mn and Si were about the same. This showed that the ejection of elements at the polished crack tip was low.

Table 5.9: Selected EDX semi-quantitative analysis of the F:0.4Ti;0.9Nb alloy

Element	Mass% on fracture surface	SEM-EDX bulk elemental composition	Concentration on the crack / bulk elemental composition
Nb	1.2	1.1	1
Ti	0.4	0.4	1
Mn	0.5	0.4	1
Si	0.4	0.5	1

Adjacent to the crack

The EDX semi-quantitative analysis adjacent to the crack showed that the elements concentration was low for Nb, Ti and Mo, whilst that for Si and Mn were the same. Figure 5.29 shows the image and the EDX semi-quantitative spectrum and Table 5.10 shows the concentration of the elements based on the representative bulk elemental analysis.

Table 5.10: Selected EDX semi-quantitative analysis of the I:0.1Ti;0.5Nb;2Mo alloy

Element	Mass% on fracture surface	SEM-EDX bulk elemental composition	Concentration adjacent to the crack / bulk elemental composition
Nb	0.5	0.7	0.7
Ti	0.1	0.2	0.5
Mn	0.6	0.6	1.0
Si	0.6	0.6	1.0
Mo	2.3	2.5	0.9

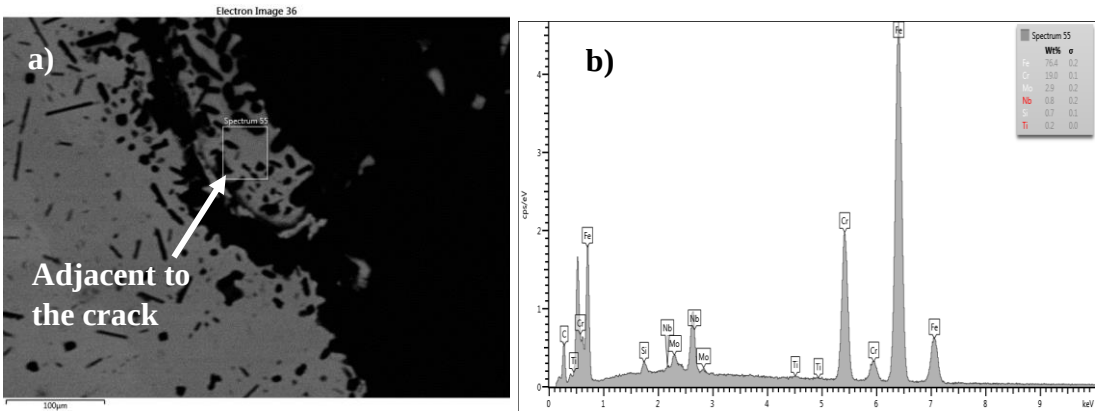

Figure 5.29 a) The image showing the area adjacent to the crack for analysis and b) semi-quantitative bulk analysis of the I:0.1Ti;0.5Nb;2Mo alloy.

Generally, the EDX semi-quantitative analysis of the elements at the crack tip, adjacent to the crack and on the crack was low compared to the fractured surfaces. This showed that, the elements segregated to the grain boundaries and those within the grains were similar to the representative chemical bulk analyses except the elements on the fractured surfaces.

Nb forms an eutectic composition with Fe at 1356°C. In the Fe-Ti phase diagram, an (αFe) - iron titanide (Fe_2Ti) eutectic composition is present at 1289°C. The presence of such eutectic components may increase the brittle temperature range, thereby increasing the risk of solidification cracking [3]. The solidus temperature of the D:0.6Nb steel showed 1387°C (Table 4.2) from the Thermo-Calc simulations, which was very close to the eutectic value reported. The addition of Ti + Nb increased the length of the solidification cracks which agrees with Lippold & Kotecki [4]. It could be argued that both individual eutectic effects acted in synergy to increase the crack lengths, though the solidification structures contained equiaxed grains. This is in agreement with the effect of the dual (Ti + Nb) content (Figure 5.1) compared to the mono stabilized Ti and Nb graphs (Figures 5.3 & 5.5) respectively. A ternary phase of either Fe-Cr-Nb or Fe-Cr-Ti could have been used for the explanation of the work, but these ternary phase diagrams do not exist.

Interim conclusions

The seven alloys investigated to ascertain the susceptibility to solidification cracking of ferritic stainless steels using self-restrained Houldcroft samples revealed the following:

- The unstabilized ferritic stainless steel (A:0Ti;0Nb) was resistant to solidification cracking except at the highest welding speed of 6 mm/s in one of the tests (Table 5.2).
- The addition of Ti slightly increased the susceptibility to solidification cracking, as the samples cracked in welding speeds 6 mm/s and 3 mm/s. The addition of Nb to the ferritic stainless steel resulted in a significant increase in the susceptibility to solidification cracking as there was cracking at all three welding speeds of 6 mm/s, 3 mm/s, and 1 mm/s. The addition of Ti to Nb in the ferritic stainless steels increased the length of the solidification crack. The crack length of the samples of ferritic stainless steels that contained Nb was longer than the crack length of samples of the dual stabilized steels.
- The solidification structure of the unstabilized (A:0Ti;0Nb), C:0.7Ti and D:0.6Nb stabilized and the commercial dual stabilized ferritic stainless (G:0.1Ti;0.4Nb) steels revealed columnar grains. The experimental dual stabilized ferritic stainless steels (E:0.4Ti;0.6Nb & F:0.4Ti;0.9Nb) showed different microstructures on the two sides of the surface of the crack for the welding speed of 6 mm/s. The dual stabilized plus Mo (I:0.1Ti;0.5Nb;2Mo) alloy showed equiaxed grains in the weld region for speeds 6 and 3 mm/s. It seems that the weld solidification structure did not contribute to the susceptibility to cracking as both columnar and equiaxed grains cracked. This was supported by the graph of crack length as a function of fraction equiaxed grains which showed that there was no relationship between the two parameters (Figure 5.7).
- The segregation of elements to grain boundaries during solidification might have contributed to solidification cracking of the alloys.

- Elemental analysis revealed Nb, Ti, Mn, Al, Si, Mo, S, and Ni associated with the fractured surfaces of all the alloys in all the welding speeds.
- The mechanism for solidification cracking is likely to be that eutectic components containing Nb increased the brittle temperature range.

CHAPTER SIX - RESULTS AND DISCUSSION FOR MODIFIED VARESTRAINT-TRANSVARESTRAINT (MVT) TESTS

Generally, the results from BAM revealed that the total crack length increased with increasing bending strain for all the grades, consistent with published behavior [42]. From Figure 6.1, it was noted that all the cracks were seen in the hot crack-resistance sectors with two exceptions.

- The 0.6Nb stabilized ferritic stainless steel (D:0.6Nb) at strain 1, which was in sector 2 at the welding speeds of 6 mm/s and 3 mm/s, indicating that this grade was marginally susceptible to solidification cracking. This could be attributed to the Nb in the ferritic stainless steel which has been found to form a eutectic at 1356°C with Fe. This eutectic increases the brittle temperature range. Moreover, Nb has also been seen to be detrimental to steels by promoting solidification cracking through columnar grain formation [3].
- The 0.4Ti + 0.9Nb steel (F:0.4Ti;0.9Nb) at 1% strain for a welding speed of 3 mm/s. It appeared that the F:0.4Ti;0.9Nb grade was marginally crack sensitive. This could be due to the high Ti + Nb contents in the grade as it has been reported that Ti and Nb in ferritic stainless steels can cause solidification cracking [4].

The two commercial grades did not crack at any strain. The commercial dual stabilized steel had a lower Ti + Nb content and this might have contributed to the solidification crack resistance. From Table 6.1 and Figure 6.1, it was seen that increasing welding speed increased the total crack length for 0.6Nb ferritic stainless steel. The reverse was observed of the F:0.4Ti;0.9Nb grade, in that, decreasing the welding speed from 6 mm/s to 3 mm/s showed an increase in total crack length. The behavior of the F:0.4Ti;0.9Nb grade was inconsistent in that the crack length at 3 mm/s was higher than that at 6 mm/s. Reasons for this anomaly was not clear.

From Figure 6.1, the hot cracking tendencies of the four alloys and their respective welding speeds can be compared without the regions. This comparison is based on the total crack length and their respective bending strains. It can be seen that the

commercial steels H:0.1Ti:0.4Nb and B:0Ti;0Nb at welding speed 3 mm/s showed no cracking in all the bending strains used. The experimental steels D:0.6Nb in welding speeds (6 mm/s and 3 mm/s) and F:0.4Ti;0.9Nb at a welding speed of 3 mm/s cracked in all the bending strains. The F:0.4Ti;0.9Nb at a welding speed of 6 mm/s cracked in two of the bending strains (2 & 4). On this basis and from Figure 6.1 without the regions, the F:0.4Ti;0.9Nb at a welding speed of 3 mm/s had the greatest sensitivity to solidification cracking. The D:0.6Nb at both welding speeds (6 mm/s and 3 mm/s) and F:0.4Ti;0.9Nb at a welding speed of 6 mm/s showed intermediate sensitivity to solidification cracking. The H:0.1Ti:0.4Nb and B:0Ti;0Nb were the least sensitive to solidification cracking [86].

Table 6.1: Total crack length measured at BAM for the welding speeds of 6 mm/s and 3 mm/s

Welding speed (mm/s)	Steel	Number of cracks	Total crack length (mm)
6	D:0.6Nb (1)	2	1.2
	D:0.6Nb (2)	8	2.6
	D:0.6Nb (3)	12	6.6
	F:0.4Ti;0.9Nb (1)	0	0.0
	F:0.4Ti;0.9Nb (2)	6	1.2
	F:0.4Ti;0.9Nb (3)	31	6.6
3	D:0.6Nb (4)	1	0.5
	D:0.6Nb (5)	2	0.7
	D:0.6Nb (6)	12	3.2
	F:0.4Ti;0.9Nb (4)	16	2.9
	F:0.4Ti;0.9Nb (5)	9	1.6
	F:0.4Ti;0.9Nb (6)	30	11.0
	H:0.1Ti;0.4Nb (1)	0	0.0
	H:0.1Ti;0.4Nb (2)	0	0.0
	H:0.1Ti;0.4Nb (3)	0	0.0
	B:0Ti;0Nb (1)	0	0.0
	B:0Ti;0Nb (2)	0	0.0
	B:0Ti;0Nb (3)	0	0.0

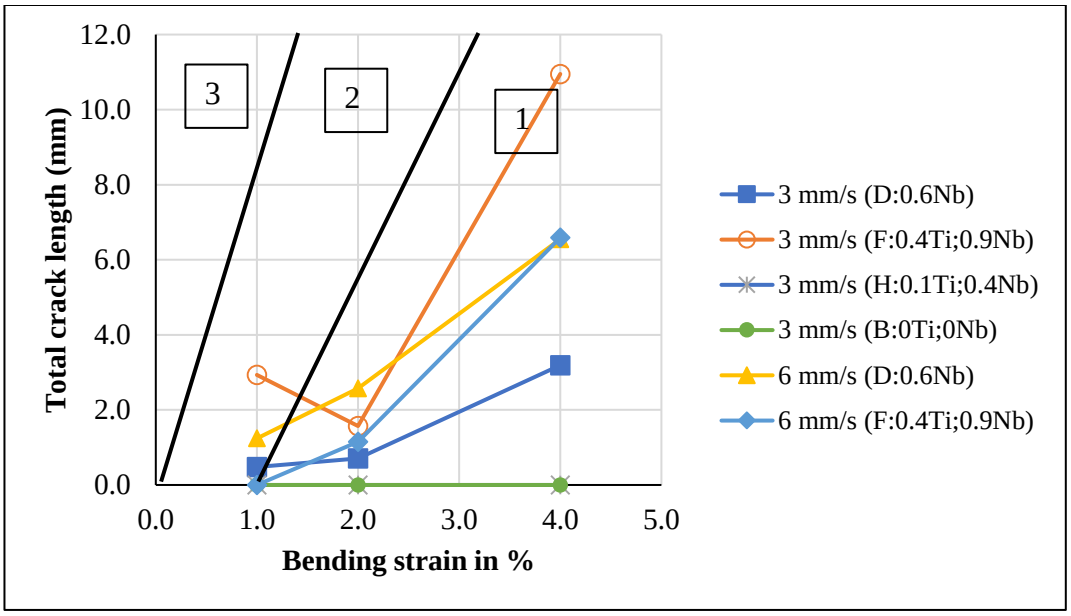

Figure 6.1: Total crack length vs strain for the welding speeds of 6 mm/s and 3 mm/s (BAM). Region 1: hot crack resistant, Region 2: increasing hot cracking susceptibility, Region 3: hot crack-prone.

Figure 6.2 shows the solidification cracking sensitivity of the D:0.6Nb and F:0.4Ti;0.9Nb alloys based on the heat inputs with the same specification [86]. It can be seen that heat 1 was better than heat 2 for D:0.6Nb alloy with respect to the total crack length and the bending strain. This was probably due to the welding speeds, with heat 1 welded at a lower welding speed. It has been shown that high welding speeds can result in high sensitivity to solidification cracking [5, 16, 22]. The reverse behavior was observed of the F:0.4Ti;0.9Nb alloy, in that, heat 2 was less sensitive to solidification cracking than heat 1.

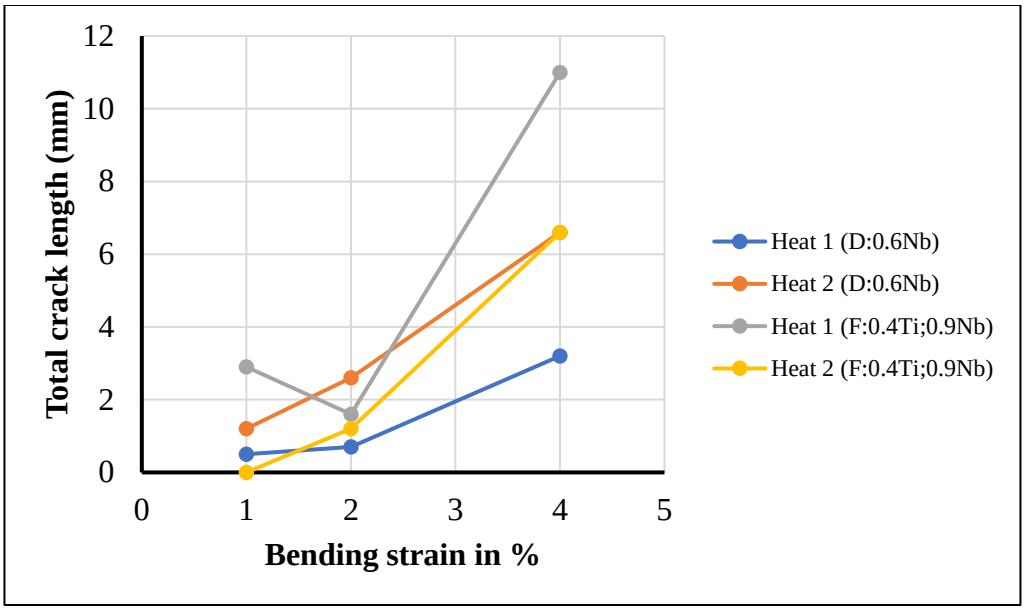

Figure 6.2: Comparison of the heat inputs of the D:0.6Nb alloy.

The University of Pretoria (UP) measurements are in agreement with the BAM total crack length measurements as all the cracks were located in the same sectors for both measurements. During the measurements of the crack lengths by the author, it was found that the total crack lengths were in sector 1 except for the D:0.6Nb grade at 1% strain, which was found in sector 2 during a welding speed of 6 mm/s. For a welding speed of 3 mm/s, it was revealed that the total crack lengths were located in sector 1 at all strains except for the F:0.4Ti;0.9Nb grade at 1% strain (Table 6.2 & Figure 6.3). For the F:0.4Ti;0.9Nb specimen, the total crack length value seemed to be inconsistent, with a longer crack obtained with a welding speed of 3 mm/s than at 6 mm/s, at 4% strain (Table 6.2). A longer crack was expected at a higher welding speed. Furthermore, for the same alloy composition, at a welding speed of 3 mm/s, an increase in strain from 1% to 2% resulted in an unexpected decrease in total crack length (Table 6.2).

Table 6.2: Measurement of the total crack length for both welding speeds (UP). Modified Varestraint Transvarestraint tests done at BAM, crack measurements done at UP

Welding speed (mm/s)	Steel	Number of cracks	Total crack length (mm)
6	D:0.6Nb (1)	2	1.7
	D:0.6Nb (2)	4	2.8
	D:0.6Nb (3)	11	10.1
	F:0.4Ti;0.9Nb (1)	0	0.0
	F:0.4Ti;0.9Nb (2)	0	0.0
	F:0.4Ti;0.9Nb (3)	16	7.8
3	D:0.6Nb (4)	0	0.0
	D:0.6Nb (5)	1	0.2
	D:0.6Nb (6)	7	3.8
	F:0.4Ti;0.9Nb (4)	3	1.9
	F:0.4Ti;0.9Nb (5)	2	0.7
	F:0.4Ti;0.9Nb (6)	15	11.7
	H:0.1Ti;0.4Nb (1)	0	0.0
	H:0.1Ti;0.4Nb (2)	0	0.0
	H:0.1Ti;0.4Nb (3)	0	0.0
	B:0Ti;0Nb (1)	0	0.0
	B:0Ti;0Nb (2)	0	0.0
	B:0Ti;0Nb (3)	0	0.0

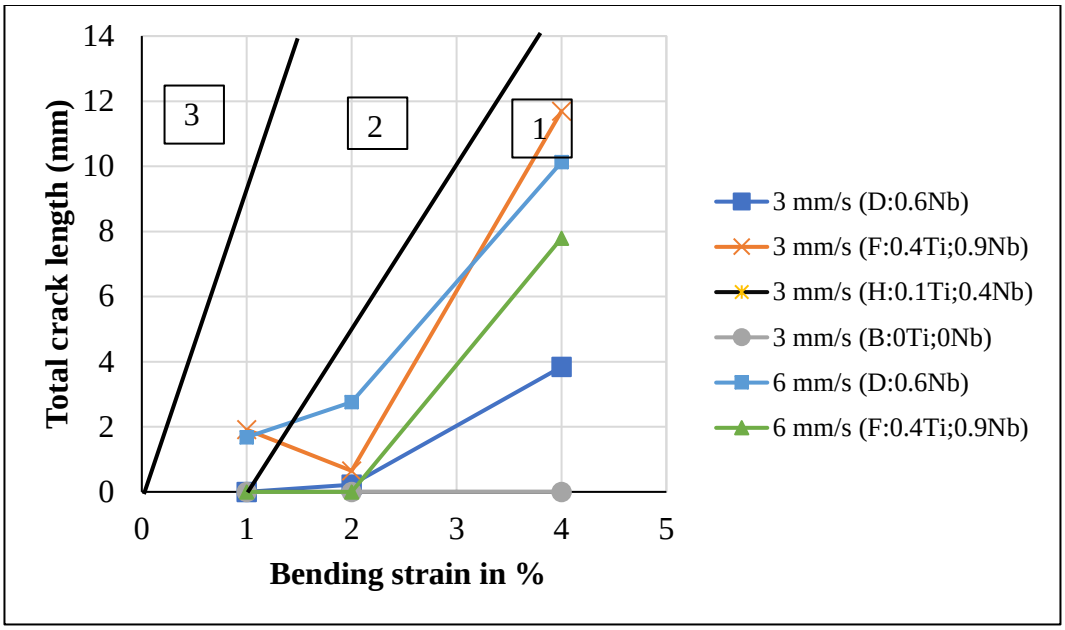

Figure 6.3: Measurement of the total crack length vs strain for both welding speeds (UP). Modified Varestraint Transvarestraint tests done at BAM, crack measurements done at UP.

The total crack length measurements executed in BAM, Germany, and in the University of Pretoria laboratory, are compared in Table 6.3. From the trend line equation, it was seen that the measurements of UP were higher by about 15% (Figure 6.4). This might be due to the fact that different laboratories equipment and procedures are not the same. Generally, by the sectors, there was no significant difference in measurements.

Table 6.3: Comparison of total crack length measurements between BAM and UP

Welding speed (mm/s)	Steel	Total crack length (mm)	
		BAM	UP
6	D:0.6Nb (1)	1.2	1.7
	D:0.6Nb (2)	2.6	2.8
	D:0.6Nb (3)	6.6	10.1
	F:0.4Ti;0.9Nb (1)	0.0	0.0
	F:0.4Ti;0.9Nb (2)	1.2	0.0
	F:0.4Ti;0.9Nb (3)	6.6	7.8
3	D:0.6Nb (4)	0.5	0.0
	D:0.6Nb (5)	0.7	0.2
	D:0.6Nb (6)	3.2	3.8
	F:0.4Ti;0.9Nb (4)	2.9	1.9
	F:0.4Ti;0.9Nb (5)	1.6	0.7
	F:0.4Ti;0.9Nb (6)	11.0	11.7
	H:0.1Ti;0.4Nb (1)	0.0	0.0
	H:0.1Ti;0.4Nb (2)	0.0	0.0
	H:0.1Ti;0.4Nb (3)	0.0	0.0
	B:0Ti;0Nb (1)	0.0	0.0
	B:0Ti;0Nb (2)	0.0	0.0
	B:0Ti;0Nb (3)	0.0	0.0

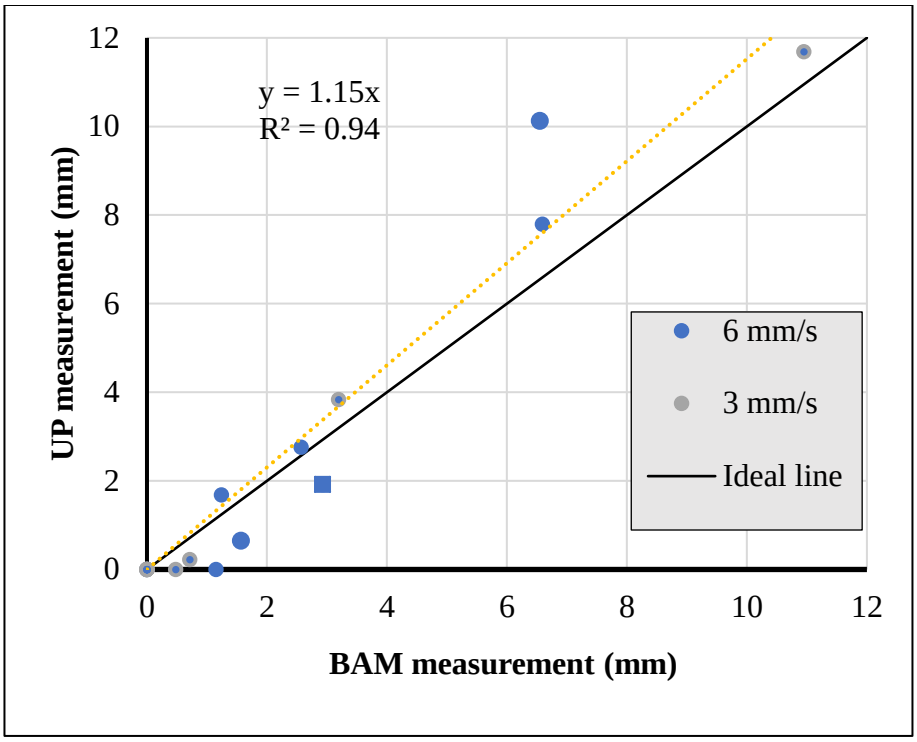

Figure 6.4: Comparison measurement of total crack length between BAM and UP.

The optical microstructure of the plane transverse to the welding direction revealed mostly columnar grains and sub-surface cracks which were not visible as solidification cracks on the parallel plane using the stereoscope. The orientation of the micrograph in respect to the fusion line is presented in Figures 6.5 – 6.7. Figures 6.5 and 6.6 show columnar grains with the sub cracks for the F:0.4Ti;0.9Nb grade in Figure 6.6. Figure 6.7 shows the microstructure of the commercial unstabilized steel as having a small amount of sawteeth martensite at the ferrite grain boundaries. The commercial unstabilized B:0Ti;0Nb grade has a 0.046 wt% C (which is slightly higher than average {Table 4.1}) and some austenite might have formed along the ferrite grain boundaries. The austenite then transformed to martensite when the weld metal cooled to room temperature. This agrees with Lippold & Kotecki as it was reported that 0.05 wt% carbon do form martensite at the ferrite grain boundary [4]. Kah and Dickinson [12] reported of the formation of untampered martensite at the grain boundaries in unstabilized ferritic stainless steel and attributed the martensite formed to the interstitial content. It was further stated that the martensite is a function of interstitial content and

no martensite formed at very low interstitial contents. All these agree with the formation of sawteeth martensite to be due to the carbon content in the B:0Ti;0Nb alloy. It has also been stated that any austenite that forms at elevated temperatures during thermo-mechanical processing transforms to martensite upon cooling. At elevated temperatures, the carbon will partition to the austenite from ferrite since austenite has a higher solubility of carbon in austenite [4].

Thermal contraction and solidification shrinkage occur during solidification of a weld metal. Residual stresses are produced in the weld metal as a result, which can aid solidification cracking [5]. The residual stresses that were set up in the weld metal during cooling might have assisted in the solidification cracking of the samples that were marginally susceptible. Table 6.4 summaries the solidification structure of the microstructures transverse to the welding direction.

Table 6.4: The solidification structure of the cross-sectional welds

Steel grade	Solidification structure
B:0Ti;0Nb (B1 – B3)	Equiaxed grains close to the fusion line; columnar grains at the centreline of the weld (Figure 6.7).
D:0.6Nb (D4 – D6)	Columnar (Figure 6.5).
F:0.4Ti;0.9Nb (F4 – F6)	Mostly columnar grains.
D:0.6Nb (D1 – D3)	Columnar.
F:0.4Ti;0.9Nb (F1 – F3)	Columnar (Figure 6.6).
H:0.1Ti;0.4Nb (H1 – H3)	Mostly columnar grains.

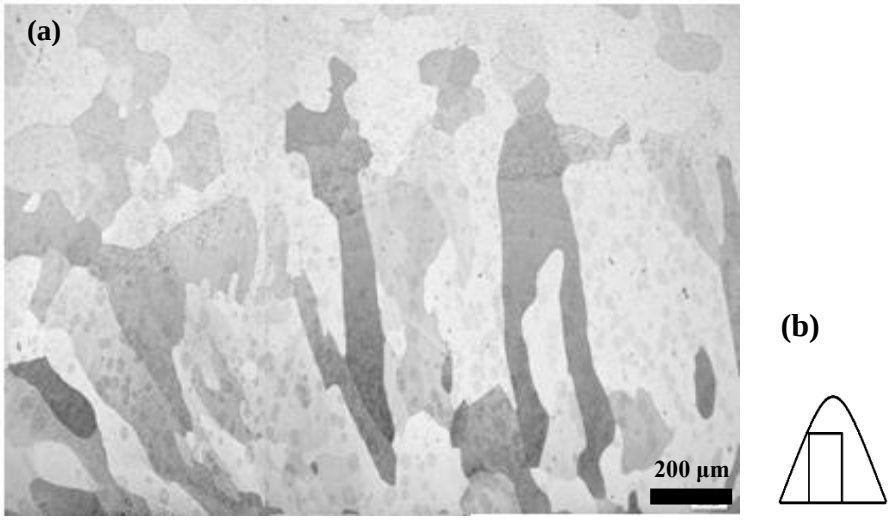

Figure 6.5: Microstructure of the 0.6Nb - stabilized ferritic stainless steel (D:0.6Nb) at 2% strain showing a) the base metal and HAZ region and the weld center at a welding speed of 6 mm/s b) the schematic orientation of the micrographs with respect to the fusion zone.

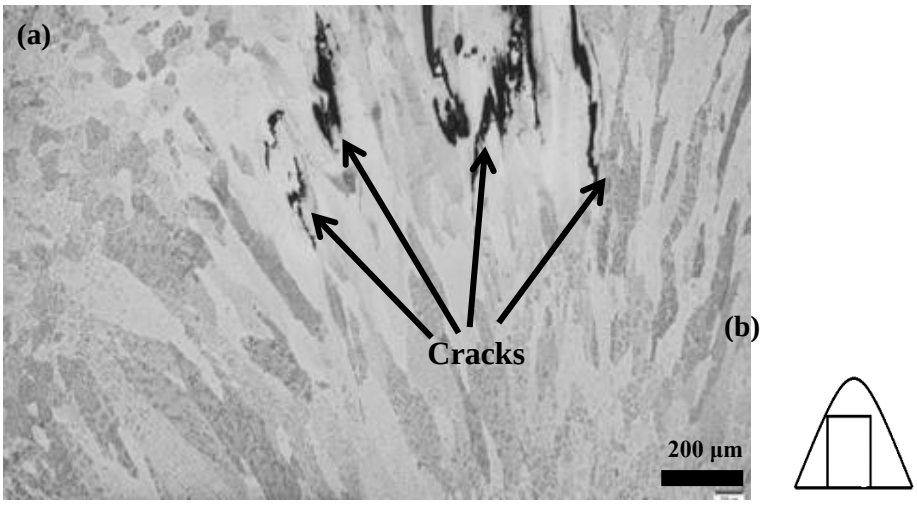

Figure 6.6: Microstructure of the 0.4Ti + 0.9Nb - stabilized ferritic stainless steel (F:0.4Ti;0.9Nb) at 4% strain showing a) the base metal and HAZ region and the weld centre at a welding speed of 3 mm/s b) the schematic orientation of the micrographs with respect to the fusion zone.

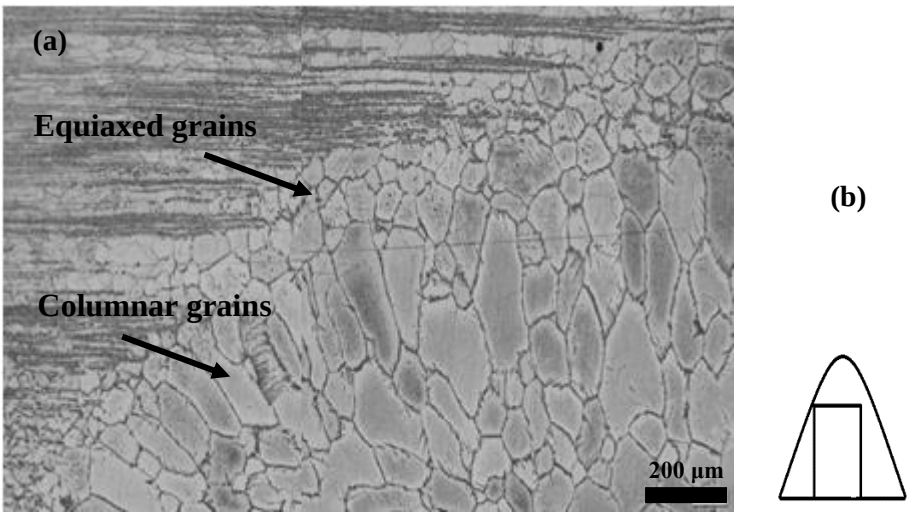

Figure 6.7: Microstructure of the unstabilized ferritic stainless steel (B:0Ti;0Nb) at 2% strain showing a) the base metal and HAZ region and the weld centre at a welding speed of 3 mm/s b) the schematic orientation of the micrographs with respect to the fusion zone.

In conclusion, the unstabilized (B:0Ti;0Nb) ferritic stainless steels was crack resistant. The 0.6%Nb ferritic stainless steel (D:0.6Nb) was observed to be marginally susceptible to solidification cracking in both welding speeds of 6 mm/s and 3 mm/s. Low content of dual stabilization, H:0.1Ti;0.4Nb, showed resistance to solidification cracking. High content dual stabilization, F:0.4Ti;0.9Nb, was found to be resistant and marginally susceptible to solidification cracking at welding speeds of 6 and 3 mm/s respectively. The F:0.4Ti;0.9Nb alloy at a welding speed of 3 mm/s showed the greatest sensitivity to solidification cracking. The F:0.4Ti;0.9Nb at a welding speed of 6 mm/s and the D:0.6Nb at both welding speeds were showed intermediate sensitivity to solidification cracking. The B:0Ti;0Nb and the H:0.1Ti;0.4Nb were the least sensitive to solidification cracking. The solidification structure of the weld metal transverse to the welding direction showed mostly columnar grains in all the steel grades.

CHAPTER SEVEN - RESULTS AND DISCUSSION FOR HOT TENSILE TESTING

7.1 Results

7.1.1 Hot mechanical properties

Engineering stress-strain curve

The engineering stress-strain curves showed that the stress rose to a maximum point with increasing strain for samples machined from C:0.7%Ti and from E:0.4%Ti;0.6%Nb. The peak stress was followed by a steep drop in stress with increasing strain till the stress reached a steady state before subsequent fracture (Figure 7.1). For samples machined from the D:0.6%Nb steel, the peak stress was less clearly defined (Figure 7.1).

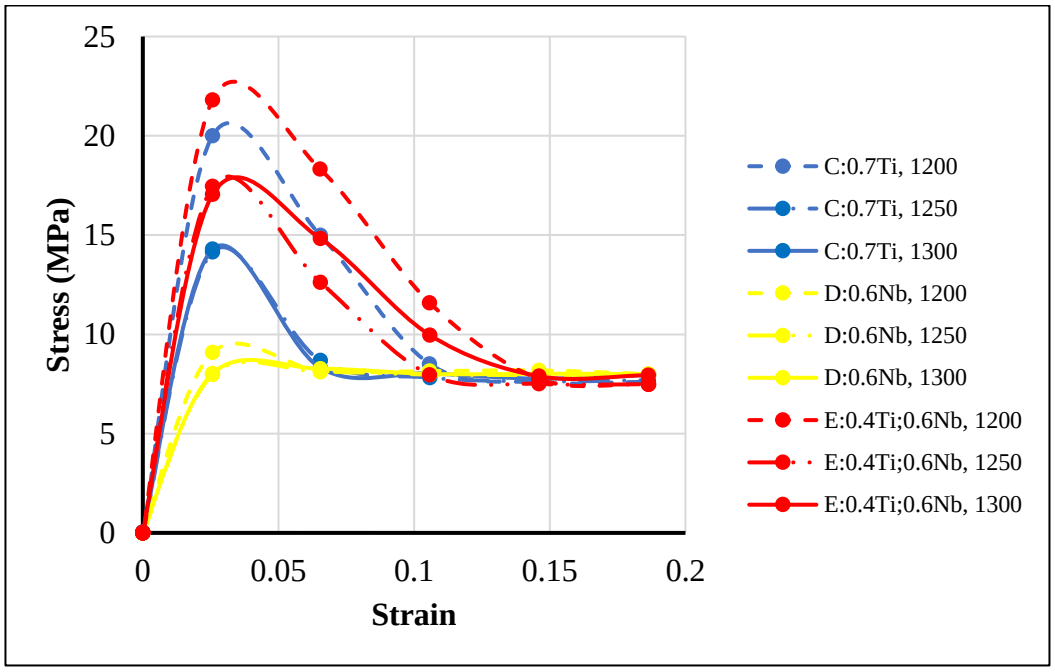

Figure 7.1: Stress – strain curves for steels C:0.7Ti, D:0.6Nb, and E:0.4Ti;0.6Nb at testing temperatures ranging from 1200 to 1300°C. Points indicate measurements (captured at a measurement interval of 1 second). Continuous lines are interpolated between the measured points.

Tensile properties

The C:0.7Ti steel had a slightly lower reduction in area values (varying from 34 to 73% depending on the temperature) compared to the E:0.4Ti;0.6Nb grade (73 to 84%) but much higher than the D:0.6Nb grade (1 to 6%) (Figure 7.2). With increasing testing temperatures, the reduction in area decreased continuously for the C:0.7Ti grade from 74% to 34% (Figure 7.2). It was also observed that testing at the lowest temperature (1200°C) resulted in the highest reduction in area for C:0.7Ti with a value of 74% and E:0.4Ti;0.6Nb grade with 84% (Table 7.1). The true strain at fracture showed the E:0.4Ti;0.6Nb and the C:0.7Ti grades were ductile (Table 7.1). On the other hand, the D:0.6Nb steel grade showed very little strain at fracture for all testing temperatures.

Table 7.1: Reduction in area, highest measured stress, true strain, engineering and true fracture stress of the steel grades at the testing temperatures

Sample ID	Testing temperature (°C)	Reduction in area (%)	Highest measured stress (MPa)	Eng. fracture stress (MPa)	True strain at fracture	True fracture stress (MPa)
C:0.7Ti	1200	74	20.0	7.6	1.35	34
C:0.7Ti	1250	43	14.2	7.7	0.57	15
C:0.7Ti	1300	34	14.3	7.9	0.42	14
D:0.6Nb	1200	1	9.1	8.0	0.007	9
D:0.6Nb	1250	1	8.1	8.0	0.007	9
D:0.6Nb	1300	6	8.3	8.0	0.057	8
E:0.4Ti;0.6Nb	1200	84	21.8	7.5	1.82	49
E:0.4Ti;0.6Nb	1250	73	17.5	7.5	1.30	32
E:0.4Ti;0.6Nb	1300	77	17.1	8.0	1.48	38

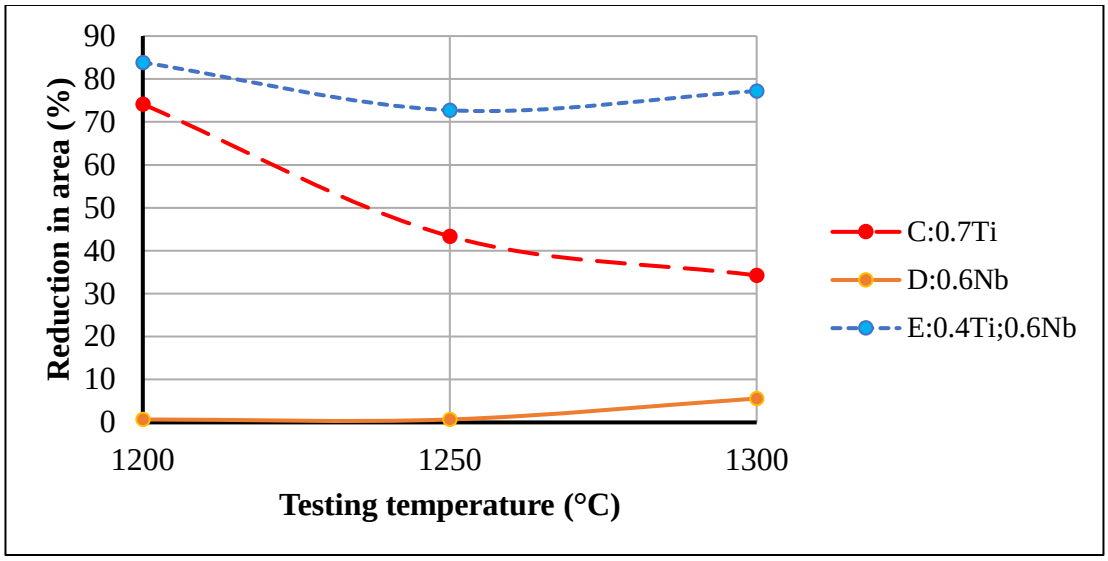

Figure 7.2: Reduction in area during hot tensile testing, as a function of testing temperature and steel grades.

In general, the engineering fracture stress was about the same for all the samples at all temperatures, between 7.6 and 7.9 MPa for the C:0.7Ti. For the D:0.6Nb grade, the fracture stress was about 8.0 MPa (Table 7.1). The E:0.4Ti;0.6Nb samples had fracture stress values between 7.5 and 8.0 MPa (Table 7.1). The true fracture stress showed values of 34 MPa (C:0.7Ti) and 49 MPa (E:0.4Ti;0.6Nb grade) at 1200°C (Table 7.1 & Figure 7.3). The other testing temperatures revealed a consistently lower true fracture stress for the Ti grade compared to the Ti + Nb grade. The D:0.6Nb grade had a consistently low true fracture stress (around 9 MPa) for all testing temperatures; the low true fracture stress was associated with a low reduction in area.

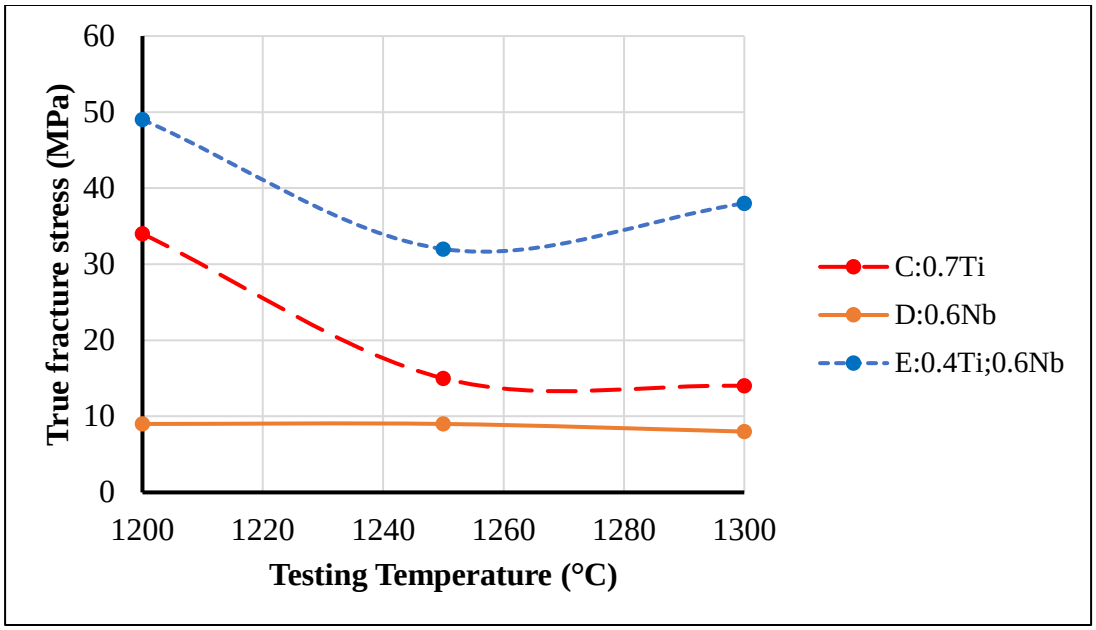

Figure 7.3: True fracture stress during hot tensile testing, as a function of testing temperature and steel grades.

7.1.2 Metallography

Microstructure

In general, the microstructure of all the grades tested at 1200, 1250 and 1300°C showed equiaxed grains in the parent metal.

- For the C:0.7Ti grade, the structure of the part of the sample exposed to high temperatures consisted of elongated grains. The fractured surface of the C:0.7Ti grade also showed very fine equiaxed grains (Figure 7.4a) and equiaxed grains (Figure 7.4b).
- The D:0.6Nb steel revealed the length of the zone exposed to high temperatures microstructures to contain equiaxed grains for all testing temperatures. The microstructure adjacent to the fracture surface was equiaxed, decreasing grain sizes with higher temperatures (Figure 7.4c).
- The E:0.4Ti;0.6Nb grade also revealed equiaxed grains with decreasing grain sizes as testing temperatures increased for the fractured surface microstructure (Figure 7.4d). Different morphologies of mixed equiaxed and elongated grains

were seen in the length of the zone exposed to the testing temperatures for the E:0.4Ti;0.6Nb grade. The equiaxed grains of the E:0.4Ti;0.6Nb grade were observed to be smaller than the grain sizes on the fractured surfaces of the C:0.7Ti and D:0.6Nb grades.

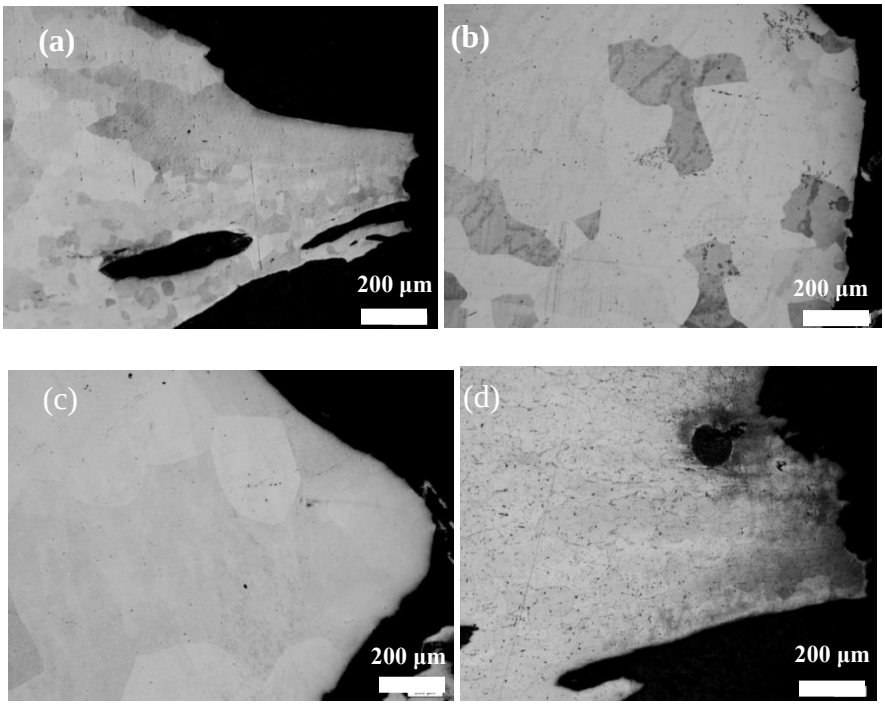

Figure 7.4: Micrograph of the fractured surfaces of a) C:0.7Ti steel at 1200°C showing very fine equiaxed grains, b) C: 0.7Ti steel at 1250°C, c) D:0.6Nb steel at 1250°C, and d) E:0.4Ti;0.6Nb steel at 1250°C showing very fine equiaxed grains.

Precipitates predicted using Thermo-Calc at the various testing temperatures

Thermo-Calc was used to determine the precipitates that were likely to form during the simulations at the testing temperatures. These predictions were reported in section 4.3. The precipitates were (Ti,Nb)(C,N) and $Ti_4C_2S_2$ for the C:0.7Ti grade, NbC and MnS for the D:0.6Nb grade, and Ti[C,N] and $Ti_4C_2S_2$ for the E:0.4Ti;0.6Nb grade. It was observed that the precipitates were essentially similar for all testing temperatures for each grade. Figures B.3b, B.4b, and B.5b show the fraction amount of the precipitates for the alloys used for the hot tensile test. At the testing temperatures used, the calculated precipitate content was invariably low (at most, 0.008 mole fraction). From

the Thermo-calc results, it seemed that the addition of Ti suppressed the formation of NbC.

SEM and EDX analysis

There were either precipitates or inclusions on the fractured surfaces. The precipitates were clustered on the surface (Figure 7.5 & 7.13) and the inclusions were seen to be scattered on the surface (Figure 7.7 & 7.11) (Table 7.2). The clustered precipitates were mostly rectangular in shape (Figure 7.5 & 7.13). The corresponding elemental analysis for either the precipitates or inclusions or the dendrite surfaces are shown in Figures 7.6, 7.8, 7.10, 7.12 and 7.14. The rest of the spectra can be found in Appendix C. EDX elemental analysis revealed that the rectangular particles were high in Ti, C and N and therefore was most likely to be TiC (Figure 7.6) or TiN (Figure 7.14). This seemed to agree with the observed Thermo-Calc calculations that the addition of Ti in ferritic stainless steel suppressed NbC formation. There were needle-like precipitates on the D:0.6Nb grade during testing at 1250°C (Figure 7.9). The elemental analysis of one of the needle-like particles is shown in Figure 7.10, which contained Nb, Ti and C. The other spectra showed similar elemental analysis (Figures C.14-C.16). This probably might be a (Ti,Nb)C particle. The various precipitates observed during the SEM examination are summarized in Table 7.2.

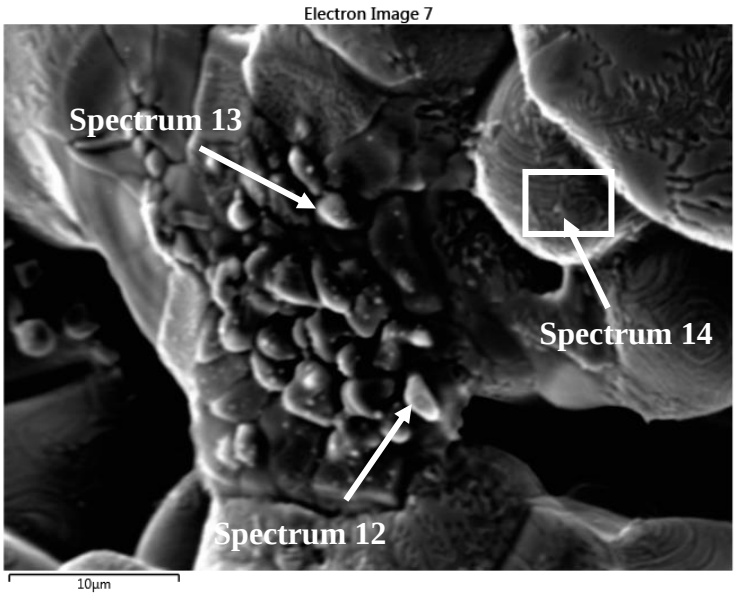

Figure 7.5: Secondary electron image of precipitates on the fracture surface of the dual E:0.4Ti;0.6Nb stabilized ferritic stainless steel. Testing temperature 1300°C and reduction in area is 77%.

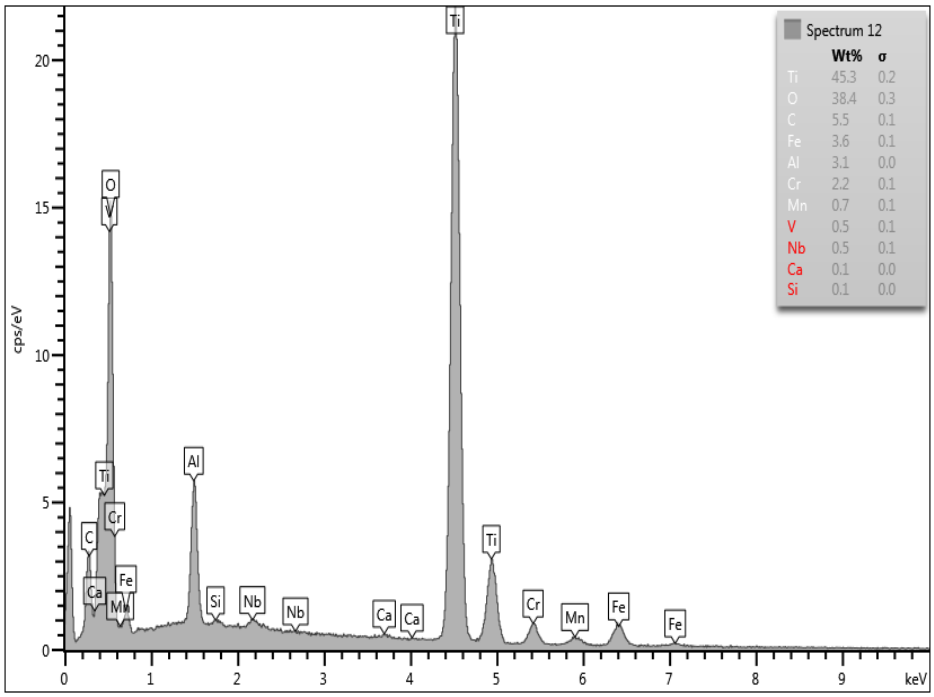

Figure 7.6: EDX semi-quantitative analysis for E:0.4Ti;0.6Nb stabilized ferritic stainless steel at the testing temperature of 1300°C showing spectrum 12.

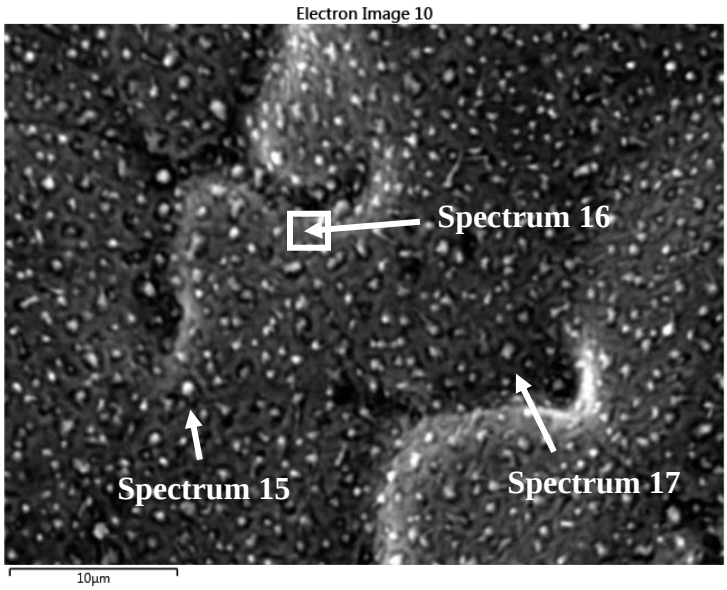

Figure 7.7: Secondary electron image of inclusions on the fracture surface of the simulated C:0.7Ti stabilized ferritic stainless steel. Testing temperature is 1300°C and reduction in area is 34%.

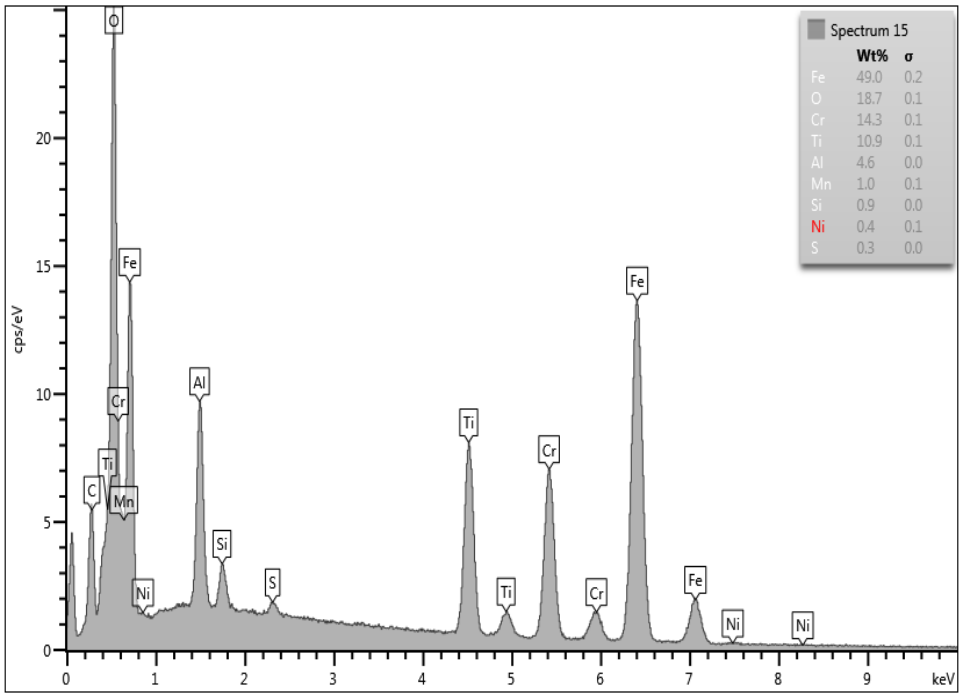

Figure 7.8: EDX semi-quantitative analysis for C:0.7Ti grade at the testing temperature of 1300°C showing spectrum 15.

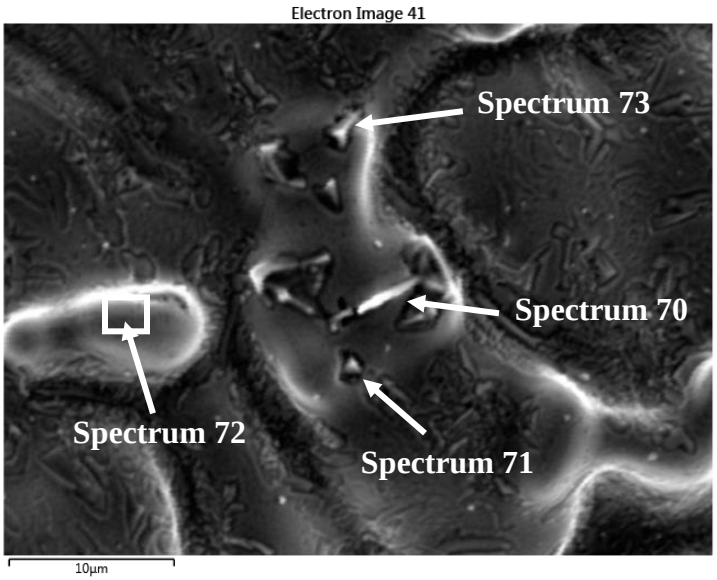

Figure 7.9: Secondary electron image revealing precipitates on the fracture surface of the D:0.6Nb - stabilized ferritic stainless steel. Testing temperature is 1250°C and reduction in area is 1%.

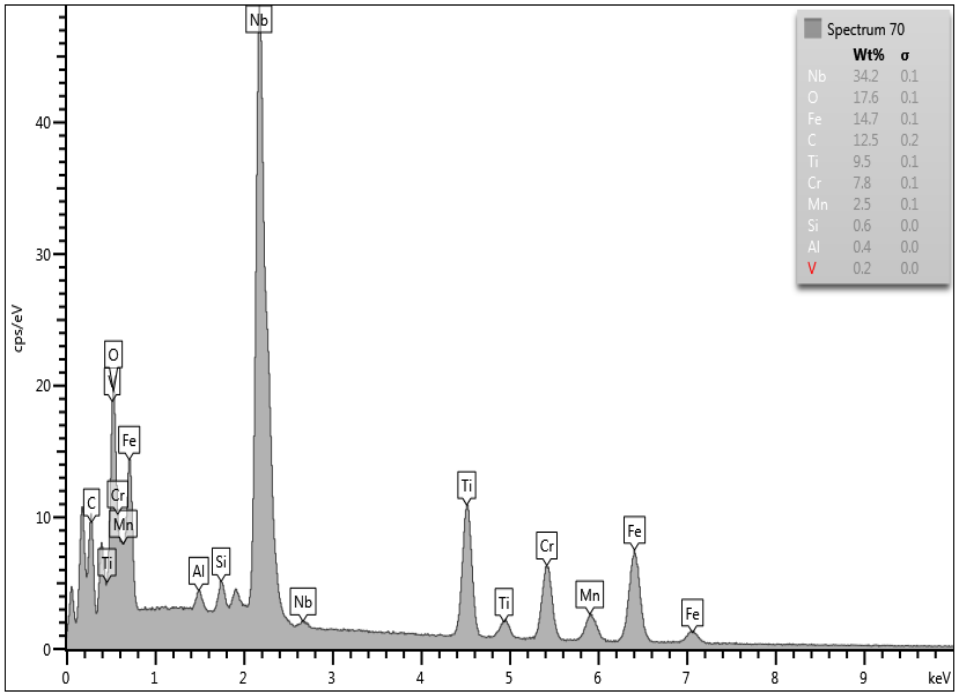

Figure 7.10: EDX semi-quantitative analysis for D:0.6Nb - stabilized ferritic stainless steel at the testing temperature of 1250°C showing spectrum 70.

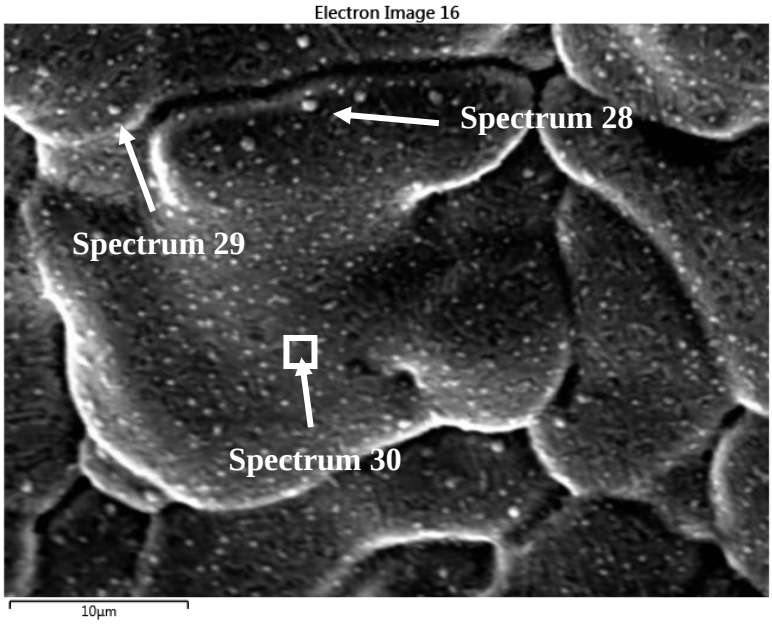

Figure 7.11: Secondary electron image revealing precipitates on the fracture surface of the C:0.7Ti - stabilized ferritic stainless steel. Testing temperature is 1200°C and reduction in area is 74%.

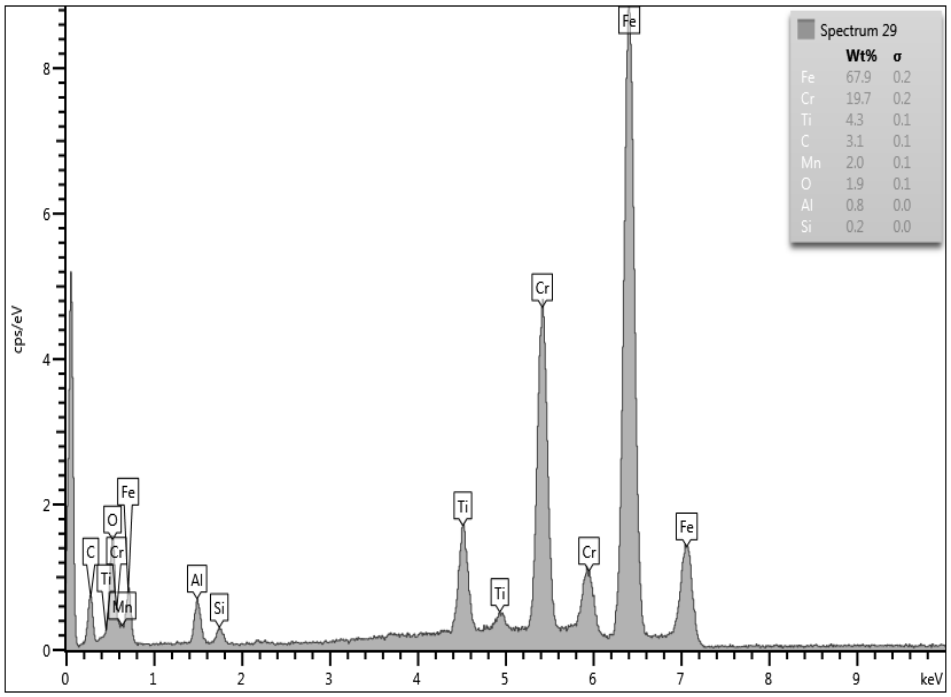

Figure 7.12: EDX semi-quantitative analysis for C:0.7Ti - stabilized ferritic stainless steel at the testing temperature of 1200°C showing spectrum 29.

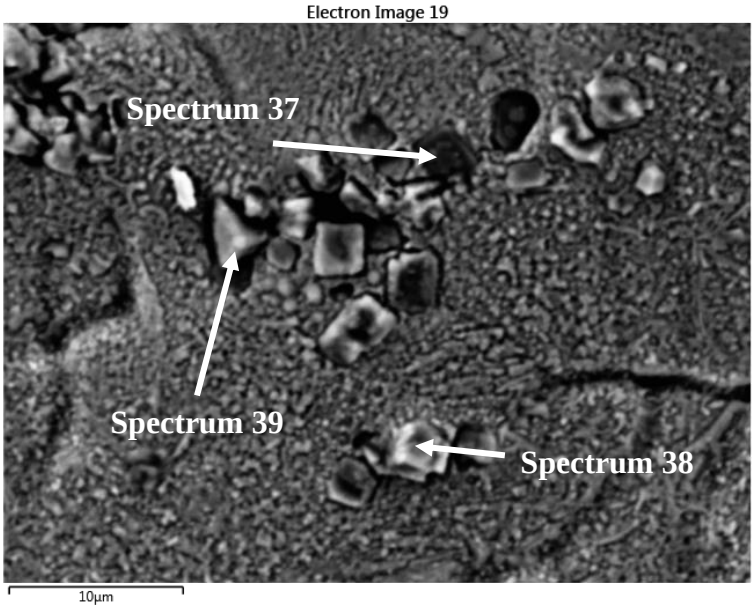

Figure 7.13: Secondary electron image revealing precipitates on the fracture surface of the E:0.4Ti;0.6Nb - stabilized ferritic stainless steel. Testing temperature is 1200°C and reduction in area is 84%.

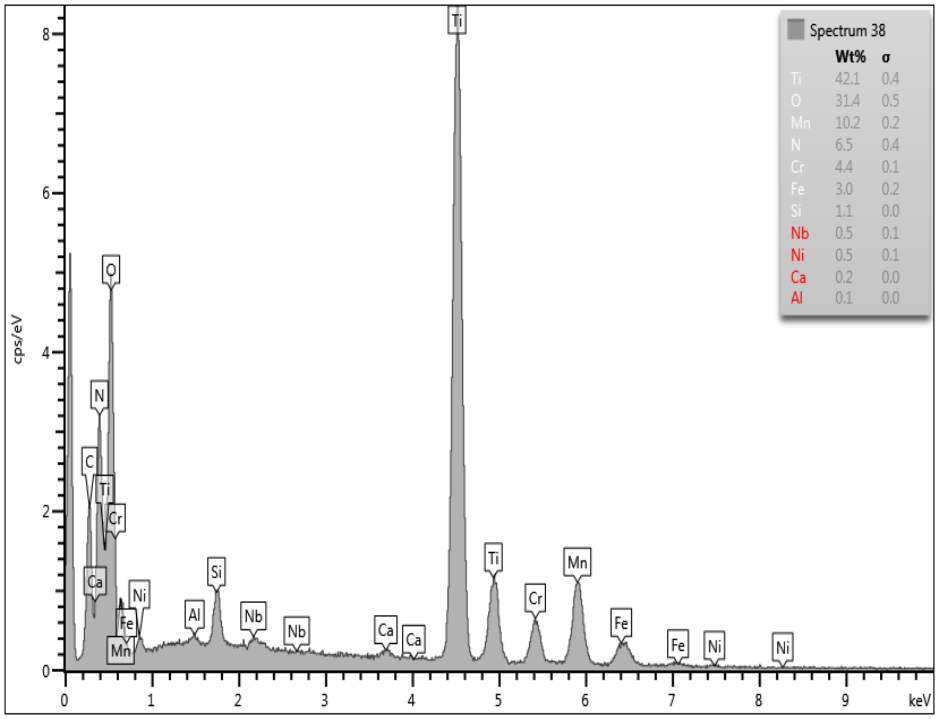

Figure 7.14: EDX semi-quantitative analysis for E:0.4Ti;0.6Nb - stabilized ferritic stainless steel at the testing temperature of 1200°C showing spectrum 38.

Table 7.2: Summary of precipitate morphology observed by scanning electron microscopy

Sample ID	1200°C	1250°C	1300°C
C:0.7Ti	Clustered rectangular precipitates and inclusions	Clustered rectangular precipitates	Inclusions
D:0.6Nb	Inclusions	Needle-like precipitates	Inclusions
E:0.4Ti;0.6Nb	Clustered rectangular precipitates	None	Clustered rectangular precipitates

From EDX elemental analysis, Ti, Nb, Mn, Al, Si, Ni, and S were found to be associated with the fracture surfaces (Tables 7.3 – 7.5). A segregation coefficient was calculated as the chemical composition on fracture surface divided by the bulk elemental composition (all from SEM-EDX analysis). The segregation coefficient is therefore based on the elemental composition on the fracture surface, that is determined using SEM-EDX, a semi-quantitative analytical technique. The bulk elemental composition was determined using the same SEM-EDX. The segregation coefficient is therefore, a semi-quantitative indicator of the difference in chemical composition of the last to solidify liquid and the elemental composition. Not all the elements found on the fracture surface was observed on the bulk elemental composition, but compared with the elemental analysis in Table 4.1, these elements were present in the alloys. The missing elements for EDX analysis were represented with 1 (Tables 7.3 – 7.5).

The segregation coefficient for sulphur was more than twice in the C:0.7Ti at 1200°C and very low in the D:0.6Nb at 1250°C testing temperature respectively. The Al segregation coefficient was averagely twice for the C:0.7Ti and E:0.4Ti;0.6Nb grades at the testing temperatures (Figures 7.15 & 7.17) and was low for the D:0.6Nb grade (Figure 7.16). The Ti segregation coefficient was the highest and it increased and then decreased with increasing testing temperatures for the C:0.7Ti and E:0.4Ti;0.6Nb (Figures 7.15 & 7.17). The element Ti was low in the D:0.6Nb and then increased with

increasing testing temperatures (Figure 7.16). The Mn and Si segregated almost the same weight% in the alloys. Generally, the segregation coefficients of Ti and Nb were high compared to the other solutes (Tables 7.3 – 7.5). The presence of sulphur in C:0.7Ti and D:0.6Nb might have contributed to the cracks as it has been reported that, sulphur segregation to the grain boundaries can cause micro-fissures when these low melting point eutectic phases undergo shrinkage strains during cooling [5].

Table 7.3: Selected EDX semi-quantitative analysis for C:0.7Ti grade at the different testing temperatures

Element	**Bulk elemental composition**	**Alloy content on fracture surface, as determined using SEM-EDX (semi-quantitative analysis, wt%)**			**Segregation (concentration on fracture surface / bulk elemental composition)**		
		1200°C	1250°C	1300°C	1200°C	1250°C	1300°C
Ti	0.7	3.2	3.4	1.7	4.6	4.9	2.4
Mn	0.6	1.5	1.0	0.6	2.5	1.7	1.0
Al	1	2.3	3.6	1.5	2.3	3.6	1.5
Si	0.7	0.6	1.1	1.0	0.9	1.6	1.4
S	1	2.2			2.2		

Table 7.4: Selected EDX semi-quantitative analysis for D:0.6Nb grade at the different testing temperatures

Element	Bulk elemental composition	Alloy content on fracture surface, as determined using SEM-EDX (semi-quantitative analysis, wt%)			Segregation (concentration on fracture surface / bulk elemental composition)		
		1200°C	1250°C	1300°C	1200°C	1250°C	1300°C
Ti	0.1	0.2	0.3	1.45	2	3	14.5
Nb	0.8	2.8	5.8	5.8	3.5	7.3	7.3
Mn	1	0.7	0.7	0.8	0.7	0.7	0.8
Al	1	0.85	0.35	0.25	0.9	0.4	0.3
Si	0.4	1.2	0.8	0.40	3	2	1
Ni	1	0.33			0.3		
S	1	0.1.			0.1		

Table 7.5: Selected EDX semi-quantitative analyses for the E:0.4Ti;0.6Nb grade at the different testing temperatures

Element	Bulk elemental composition	Alloy content on fracture surface, as determined using SEM-EDX (semi-quantitative analysis, wt%)			Segregation (concentration on fracture surface / bulk elemental composition)		
		1200°C	1250°C	1300°C	1200°C	1250°C	1300°C
Ti	0.4	3.2	3.4	1.7	8	8.5	4.3
Nb	0.8	1.6	2.7	0.7	2	3.4	0.9
Mn	0.5	1.5	1.0	0.6	3	2	1.2
Al	-	2.03	3.6	1.5	2.0	3.6	1.5
Si	0.5	0.4	0.6	1.0	0.8	1.2	2
Ni	-	0.5			0.5		

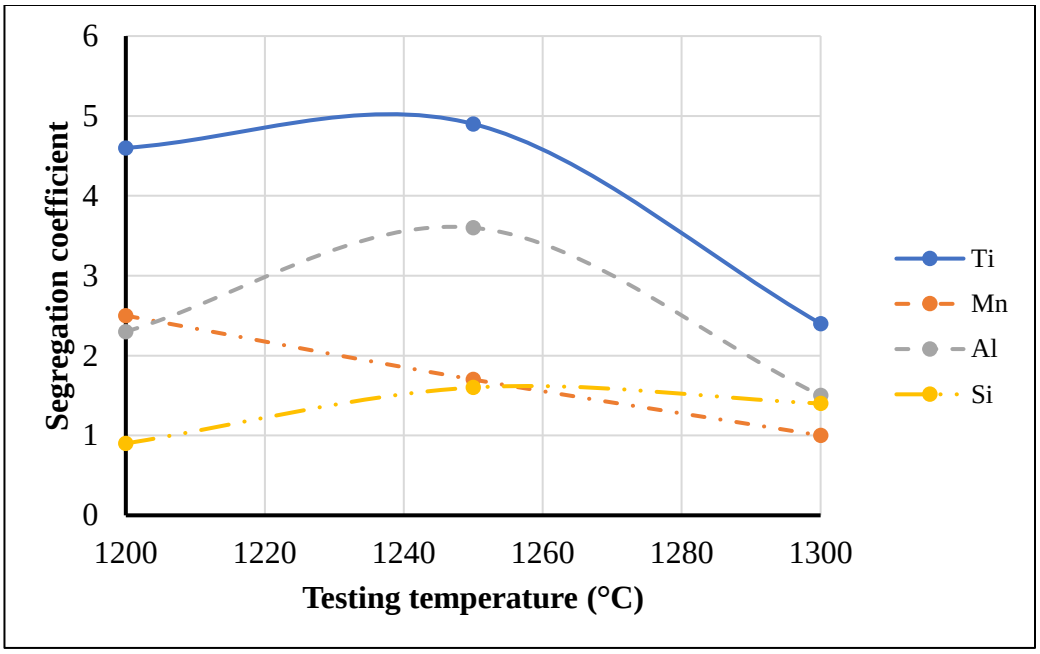

Figure 7.15: Segregation coefficient as a function of temperature for the C:0.7Ti grade.

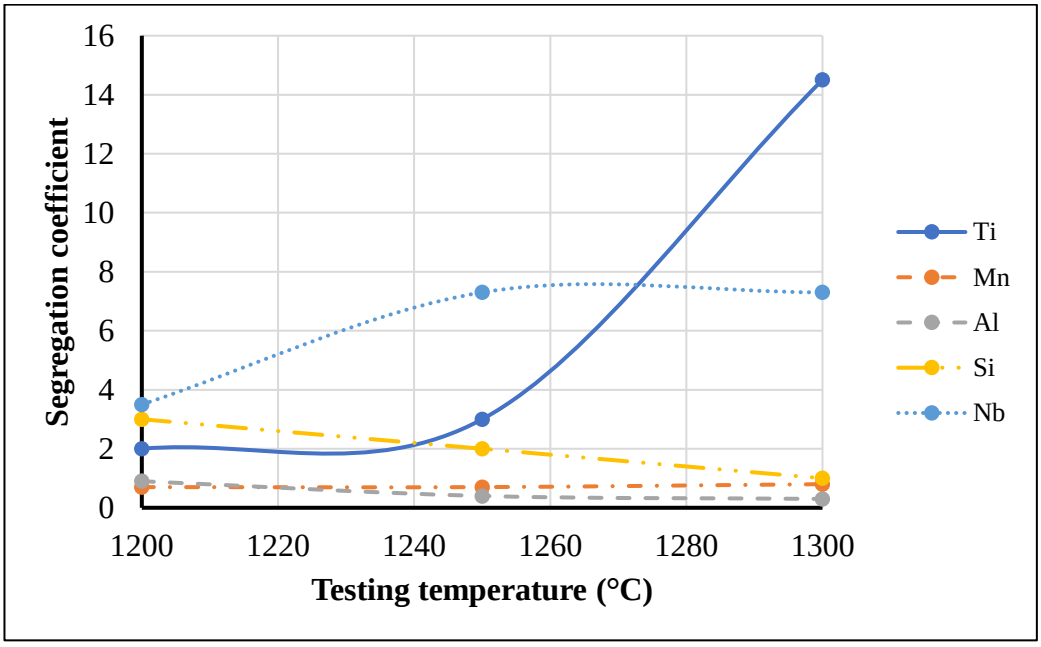

Figure 7.16: Segregation coefficient as a function of temperature for the D:0.6Nb grade.

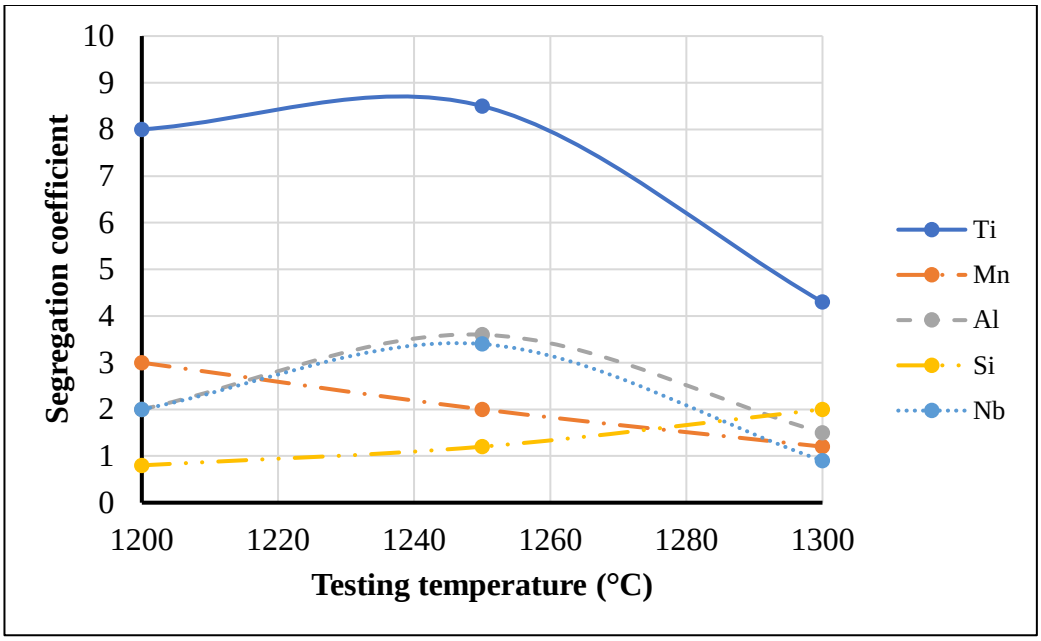

Figure 7.17: Segregation coefficient as a function of temperature for the E:0.4Ti;0.6Nb grade.

7.2 Discussion

The flow stress curves (Figure 7.1) were characterised, for Steel C:0.7Ti and Steel E:0.4Ti;0.6Nb by a rapid increase in flow stress at a low strain (in the order of 0.05), followed by a rapid decline in flow stress. Steel D:0.6Nb did not exhibit a similar increase in flow stress. Such behaviour could be explained in terms of dynamic recrystallization [87–89] or in terms of the onset of necking. Dynamic recrystallization is considered unlikely, given the low strain. Steel C:0.7Ti and Steel E:0.4Ti;0.6Nb showed substantial reduction in area (Figure 7.2), while Steel D:0.6Nb showed very low reduction in area, and it is therefore possible that the shape of the flow curve can be explained by the onset of necking. The low acquisition rate (one measurement per second) made a detailed discussion of the mechanisms likely to be active during the hot tensile test impossible. Comparing the flow stress curves of the different grades, the E:0.4Ti;0.6Nb alloy generally showed the highest measured flow stress. The same steel had a high hot ductility, as measured by the reduction in area values (Figure 7.2).

The low hot ductility of the D:0.6Nb grade could be attributed to the Nb-rich eutectics that are formed with Nb in steels, which is consistent with the low estimated Ts (1387°C – Table 4.2). The E:0.4Ti;0.6Nb steel had a high and fairly constant reduction in area with increasing testing temperatures. This could be attributed to the synergistic effect of Ti and Nb on the ferritic stainless steel. The high fracture stress for the D:0.6Nb steel could be attributed to the presence of Nb in the alloy. Nb is known to be a high temperature solid solution strengthener [48-50].

The grains of the E:0.4Ti;0.6Nb fractured surface microstructure was found to be equiaxed and this might be due to TiN precipitates which have been said to increase the density of nucleation sites in solidification [90]. The E:0.4Ti;0.6Nb grade showed decreasing equiaxed grains with increasing testing temperatures. It is speculated that during the deformation of E:0.4Ti;0.6Nb alloy at high temperatures, the non-metallic inclusions were broken up, others deformed and uniformly distributed throughout the alloy in a more refined form. These non-metallic inclusions caused more nucleation sites and resulted in finer equiaxed grains with increasing testing temperatures [91]. The equiaxed grains of the E:0.4Ti;0.6Nb grade was observed to be smaller than the grains on the other fractured surfaces of the C:0.7Ti and D:0.6Nb grades. Small grains have been found to promote ductility [92] and this might have contributed to the high hot ductility of the E:0.4Ti;0.6Nb grade.

For the C:0.7Ti and E:0.4Ti;0.6Nb grades, there were similar precipitates of rectangular particles at testing temperatures of 1200 and 1300°C. There were no such rectangular precipitates at 1250°C. Both Nb(C,N) and TiN have been shown to be tetragonal/rectangular in shape in ferritic stainless steels [90]. In contrast, Sello & Stumpf [93] proved that the tetragonal/rectangular shape was firstly nucleated as Ti(C,N) and the Nb(C,N) nucleated around the Ti(C,N). Siyasiya et al. [94] reporting on Ti and Nb stabilizers in ferritic stainless steel found the rectangular particle to be $MgO.Al_2O_3$ spinel and TiN nucleating heterogeneously on the spinel and the NbC on the TiN particle in that order. In this work, the particle was probably a TiN as the EDX spectrum revealed Ti and N on some of the major elements that were observed. The

0.6Nb grade showed the needle-like precipitates at 1250°C testing temperature whiles the 1200 and 1300°C temperatures revealed inclusions.

The high hot ductility of the E:0.4Ti;0.6Nb grade seems to be due to the low rejection of solutes apart from Al on the fractured surfaces (Table 7.5 & Figure 7.13). These solutes might have been retained in solid solution to increase the hot ductility of the E:0.4Ti;0.6Nb steel. Sulphur segregated significantly in the C:0.7Ti and this could have formed low melting points compounds (FeS) which widens the solidification temperature range to cause solidification cracking [5, 12]. SEM-EDX is not particularly accurate in determining the composition of small particles and this makes the existence of these solutes in the steels not to be particularly accurate.

The SEM-EDX results must be treated with caution due to the size of the excitation volume, that is likely to be significantly larger than the inclusions or precipitates that were visible on the fracture surface.

The two important properties for hot cracking susceptibility measurement, being the reduction in area and tensile strength, revealed different results for the hot ductility. The hot ductility was found to be low with Nb addition but Ti addition showed an improvement. A much higher hot ductility was observed with the simultaneous addition of Ti and Nb in the alloy.

The main parameters for solidification cracking susceptibility using hot tensile testing are ductility recovery temperature (DRT), the nil ductility temperature range (DTR), and the nil strength temperature (NST). These parameters could not be determined during this study [16, 95]. These parameters are determined during the on-heating and on-cooling measurements [19, 20]. Kuzsella et al. [96] reported that a specific pneumatic system was installed on the Gleeble-3500 before measurements of such parameters were done. The pneumatic system was not found on the Gleeble-1500D for the current project and thus might have limited the data needed to test the susceptibility to solidification cracking of ferritic stainless steels. The difference between DTR and NST could have been used to define the brittle temperature range [BTR] (DIN EN ISO 17641-3:2005).

CHAPTER EIGHT – GENERAL DISCUSSION OF RESULTS, CONCLUSIONS AND RECOMMENDATIONS

8.1 Outline of statistical treatment of welding data

The two sets of data resulting from welding trials (the Houldcroft and the MVT results) were compared.

- From the literature, five parameters were identified that influence the susceptibility to solidification cracking. These parameters were the Ti content, the Nb content, the heat input, the welding speed, and the geometry of the weld bead. The geometry of the weld bead was quantified in terms of the fusion line angle. The schematic diagrams of the fusion line angle for the Houldcroft and MVT tests are shown in Figures 8.1 and 8.2 respectively. This was calculated based on assumptions made as follows;

  Self-restrained Houldcroft

  Since there was complete penetration, the fusion line angle was drawn as shown in Figure 8.1;

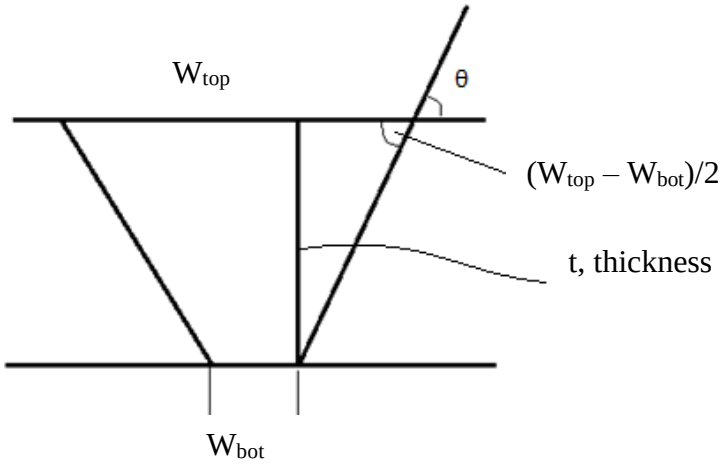

Figure 8.1: Schematic diagram of the self-restrained Houldcroft fusion line angle.

$$\tan\theta = \frac{t}{(W_{top} - W_{bot})/2} = \frac{2t}{W_{top} - W_{bot}} \qquad (8.1)$$

$W_{top} = W_{bot}$ if $\tan\theta \longrightarrow \infty$ (8.2)

then $\theta \longrightarrow 90°$

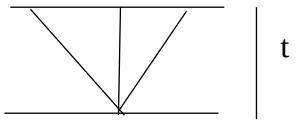

$W_{bot} = \theta$

$$\tan\theta = \frac{2t}{W_{top}} \quad (8.3)$$

MVT

There was no complete penetration of the samples during the MVT tests.

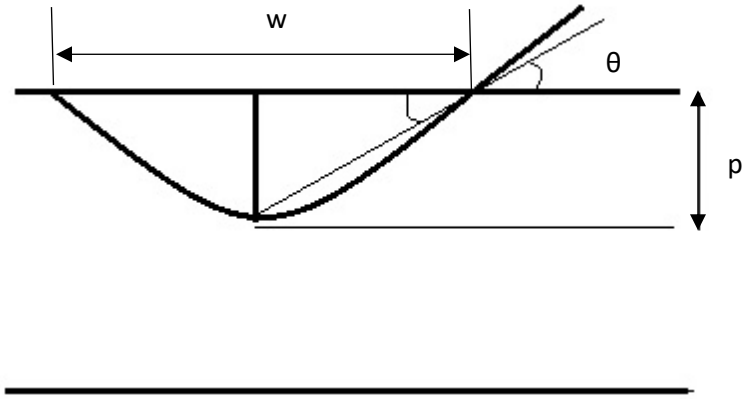

Figure 8.2: Schematic diagram of the MVT fusion line angle.

$$\tan\theta = \frac{p}{w/2} = \frac{2p}{w} \quad (8.4)$$

- The first question that was addressed in the analysis of the data was which of these five parameters were dominant in determining the susceptibility to solidification cracking.
- The second question was whether the Houldcroft and the MVT tests gave a different view on the susceptibility to solidification cracking.

In order to make quantitative comparison of the results of the Houldcroft and the MVT tests possible, a crack index was calculated, as follows:

- For the Houldcroft tests:

Crack index = (total crack length measured for a specific sample) / (average crack length for all Houldcroft samples) (21 observations, with 6 samples with no cracking)

- For the MVT tests:

  Crack index = (total crack length measured for a specific sample) / (average crack length for all samples subjected to the same bending strain, that is, 1%, 2% or 4%). (18 observations, with 7 samples with no cracking).

- The crack index of the self-restrained Houldcroft and Modified Varestraint Transvarestraint (MVT) test methods were compared with the Nb content, Ti content, the welding speed, the heat input and the fusion line angle as already stated. The MVT showed that with increasing Nb content, the crack index increased (Figure 8.3). This might be explained as the D:0.6Nb steel which was marginally susceptible in both welding speeds of 6 mm/s and 3 mm/s. It is also seen that, the F:0.4Ti;0.9Nb steel was the most crack sensitive of the alloys. For the self-restrained Houldcroft, the crack index value ranged between 0 and about 2.2 with no Nb content. With increasing Nb content, the crack index ranged between 0 and 3 till about 0.6Nb content. Then, the range changed between 1 and 2.7 for the crack index as the Nb content increased. This is generally seen that there was no relationship between the crack index and increasing Nb content for the Houldcroft method, though there was some increase in crack index.
- For the MVT test, the crack index generally increased with increasing Ti content but there was a scatter for the Houldcroft method (Figure 8.4). This behavior of Ti content for the MVT test might be due to the stabilized steels, which showed crack resistant for the H:0.1Ti;0.4Nb alloy, but with an increase in Ti from 0.1 to 0.4 in F:0.4Ti;0.9Nb, the steel was the most sensitive alloy of all the alloys.
- Figure 8.5 shows the relationship between the crack index and the welding speed for both MVT and Houldcroft methods. It is clearly seen that, increasing

welding speed increased the crack index for the Houldcroft method. This revealed that the susceptibility to solidification cracking in the Houldcroft method was dominated by the welding speed and not the chemistry of the alloys. This behavior was demonstrated in Figure 5.1 and this is explained as the high welding speed producing longer crack lengths. High welding speed are associated with teardrop shaped weld pools which are more susceptible to solidification cracking. Generally, all the steels cracked during a welding speed of 6 mm/s, six out of the seven steels cracked during a welding speed of 3 mm/s and only two cracked at a welding speed of 1 mm/s. The MVT revealed a higher crack index for the low welding speed compared to the high welding speed. The F:0.4Ti;0.9Nb alloy showed a marginal susceptibility to solidification cracking at a welding speed of 3 mm/s compared to the welding speed of 6 mm/s.

- The crack index and its relationship to the heat input was shown in Figure 8.6. It is seen that the heat input as a function of the welding speed revealed high crack index for the low heat input in the Houldcroft test. The low heat input was as a result of the high welding speed. The high welding speed produced columnar and equiaxed grains which were susceptible to solidification cracking. The MVT seems to show the opposite effect as the high heat input as a function of welding speed revealed high crack index.
- The crack index as a function of the fusion line index revealed a behavior where the MVT fusion line angle was in a sector/region and the Houldcroft fusion line angle was also in a different sector (Figure 8.7). This might be due to the complete penetration in the Houldcroft and the partial penetration in the MVT test. It also showed that there was no relationship between the crack index and the fusion line angle as the graph points were scattered. These different penetrations revealed different fusion line angles. From Figure 8.7, it therefore seemed that the solidification cracking was not particularly sensitive to the depth to width ratio of the weld bead (as quantified using the fusion line angle θ)

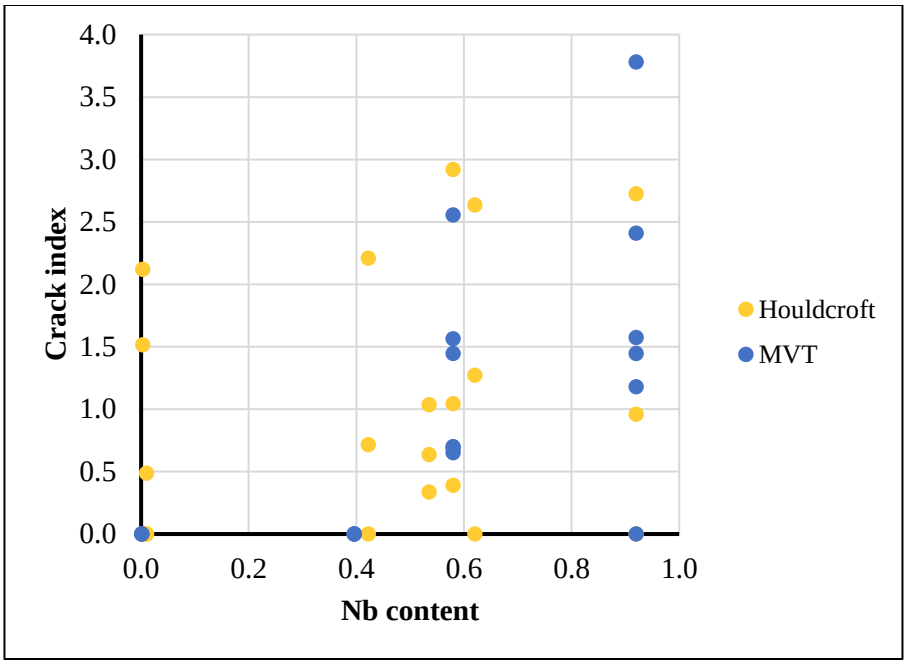

Figure 8.3: The relationship between crack index and Nb content.

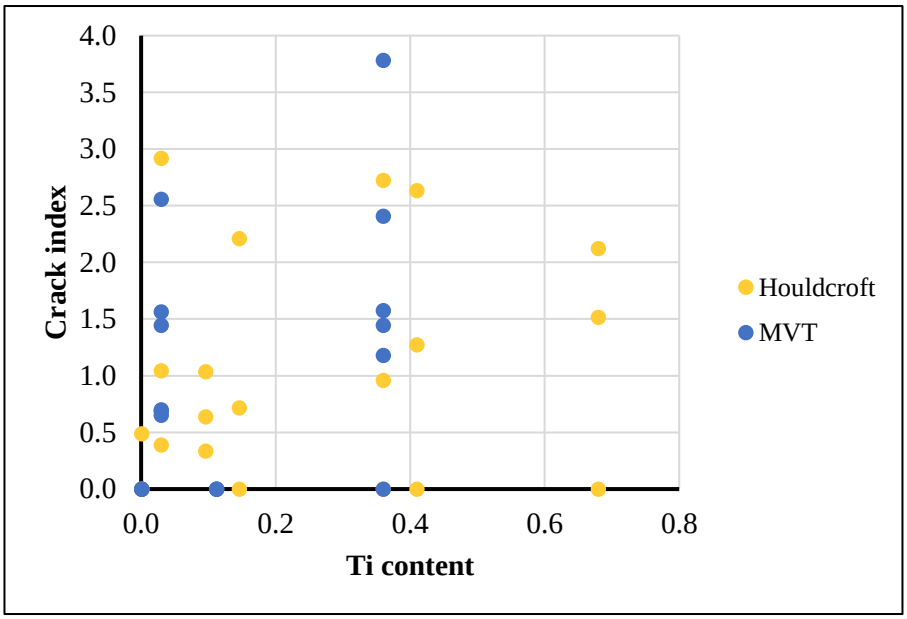

Figure 8.4: The relationship between crack index and Ti content.

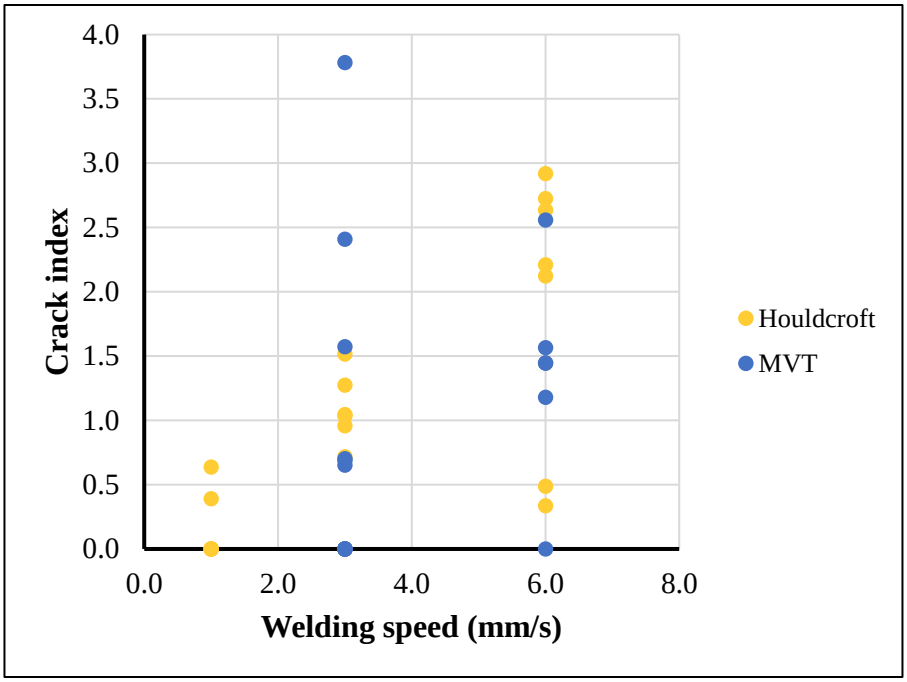

Figure 8.5: The relationship between crack index and welding speed.

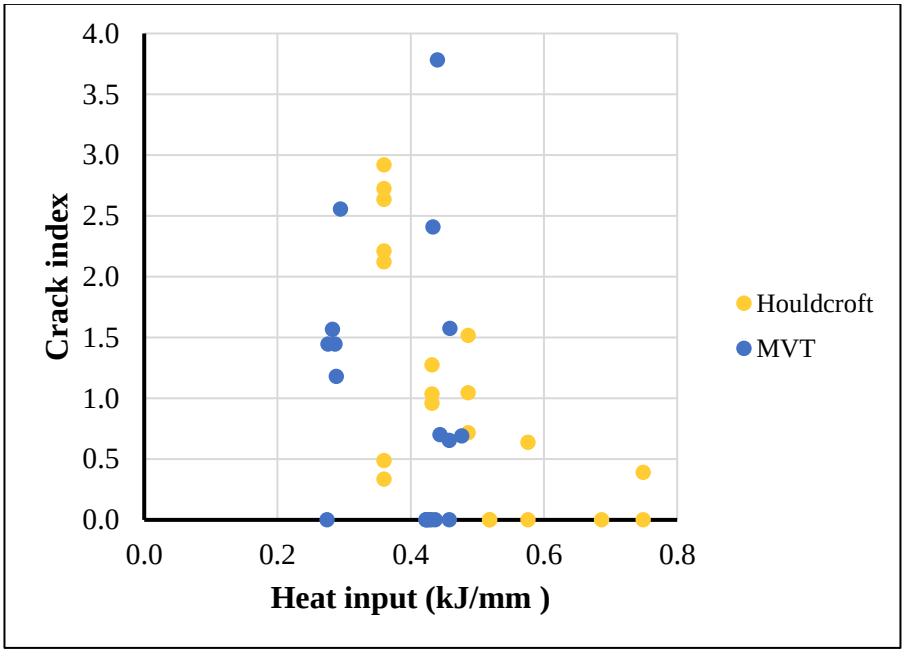

Figure 8.6: The relationship between crack index and heat input.

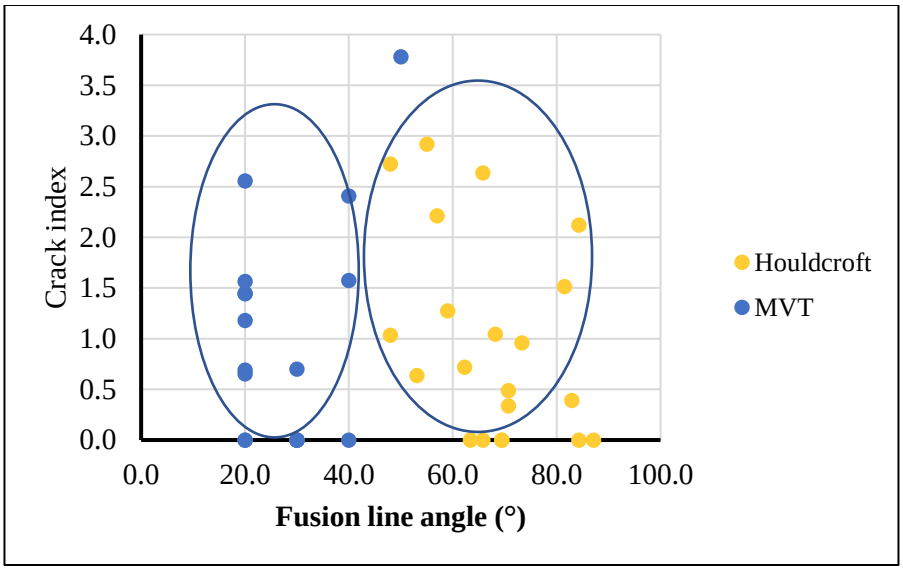

Figure 8.7: The relationship between crack index and fusion line angle, showing the two sectors.

A multiple linear regression model was fitted to the data. The model had the following general form:

(crack index) =

$a_0 + a_1$.(Nb content) + a_2.(Ti content) + a_3.(welding speed) + a_4.(heat input).+ a_5.(fusion line angle) (8.5)

The quality of the fit was judged by considering the following statistical parameters:

- R square, the correlation coefficient;
- The adjusted R square, a parameter that incorporates the degree of freedom;
- For individual coefficients, the p-value. It is generally accepted that a p-value below 0.05 indicates that the specific parameter has a significant effect on the dependent variable.

The linear regression model for the total data was considered, and for the Houldcroft and the MVT data separately. Refer to Tables 8.2 and 8.3 for the details of the linear regression.

Table 8.1: Results of multiple regression model for crack index, using data from Houldcroft and MVT

Independent variable	All data		Houldcroft data only		MVT data only	
	Coefficient	**p-value**	**Coefficient**	**p-value**	**Coefficient**	**p-value**
Intercept	-1.68	0.32	0.13	0.94	-5.35	0.65
Nb	1.03	0.03	0.57	0.27	2.79	0.10
Ti	0.84	0.26	1.13	0.09	-3.42	0.31
Welding speed (mm/s)	0.34	0.04	0.35	0.02	0.41	0.70
Heat input (kJ/mm)	1.22	0.66	0.50	0.83	5.53	0.77
Fusion line angle (°)	0.0043	0.57	-0.0159	0.28	0.0526	0.14
R square		0.44		0.69		0.51
Adjusted R-square		0.36		0.59		0.30
Number of observations		39		21		18

The following general observations could be made on the results of the statistical analysis as stated in Table 8.1:

- No multiple regression model was particularly accurate since the R square values were not close to unity.
- For most independent variables, the p-value is above 0.05, indicating that the variables do not have a significant effect on the Houldcroft and MVT tests (dependent variables).
- For all three models, an increase in Nb content results in a higher cracking index.
- The effect of Ti was not consistent for all the data as it increased cracking susceptibility, it showed high cracking susceptibility in the Houldcroft test and less cracking susceptibility in MVT.

- Higher welding speed results in a higher cracking index. The p-value was significant for the total data and Houldcroft as these dependent variables had values less than 0.05.
- Higher heat input results in a higher cracking index.
- Effect of geometry of weld pool as quantified using the fusion line angle was not consistent.
- To further explore the effect of specific parameters on the susceptibility to solidification cracking, multiple linear regression models were developed, based on the parameters that had a low p-value. The results are summarized in Table 8.2.

Table 8.2: Results of multiple regression model for crack index, using data from Houldcroft and MVT, showing only parameters with a p-value below 0.05

Independent variable	All data		Houldcroft data only		MVT data only	
	Coefficient	**p-value**	**Coefficient**	**p-value**	**Coefficient**	**p-value**
Intercept	-0.46	0.18	-0.17	0.54	-0.19	0.66
Nb	1.04	0.02			2.10	0.01
Welding speed (mm/s)	0.26	0.001	0.35	0.0001		
R square		0.38		0.56		0.39
Adjusted R-square		0.34		0.54		0.35
Number of observations		39		21		18

Observations:

- The cracking response of Houldcroft seems to be dominated by welding speed, and not by Nb content (welding speed was 1, 3 and 6 mm/s).
- Cracking response of MVT test seems to be dominated by Nb content; and it therefore seems that the MVT test was more successful in demonstrating the effect of Nb than Houldcroft.

Additional analysis of response of crack length to changes in base metal composition

From the discussion so far, it is seen that a significant number of samples showed no cracks, resulting in a crack index of zero. These samples might have affected the statistical analyses. A set of statistical analyses were performed ignoring the zero crack length data. This analysis was reasoned based on Figure 8.8, which clearly shows the effect of ignoring the zero crack lengths, revealing a better line fit.

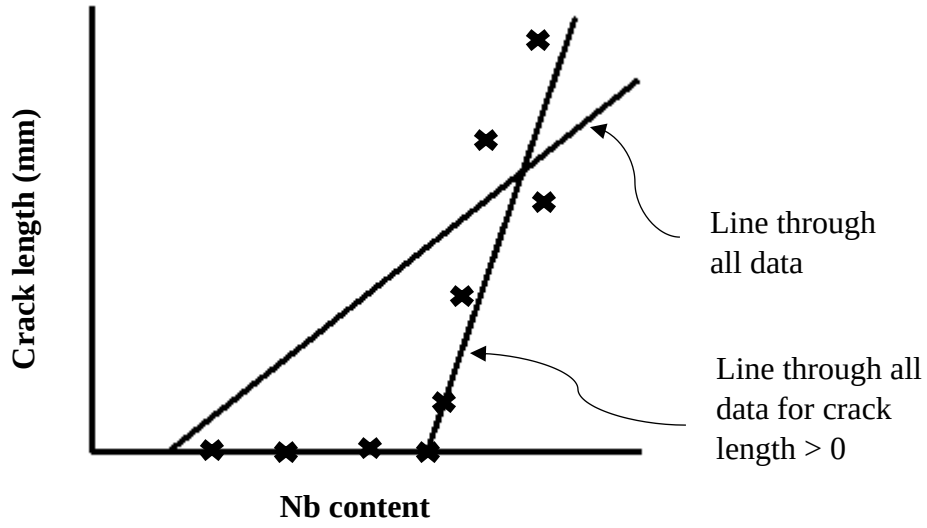

Figure 8.8: Schematic explanation of the reason to exclude the zero crack length measurement.

Table 8.3: Results of multiple regression model for crack index, using data from Houldcroft and MVT ignoring the zero crack lengths

Independent variable	All data		Houldcroft data only		MVT data only	
	Coefficient	p-value	Coefficient	p-value	Coefficient	p-value
Intercept	-0.91	0.75	-1.79	0.44	-8.96	0.54
Nb	1.07	0.15	0.37	0.58	-1.20	0.44
Ti	1.61	0.11	2.66	0.01	0.00	
Welding speed (mm/s)	0.25	0.34	0.56	0.02	1.05	
Heat input (kJ/mm)	0.88	0.85	6.89	0.11	9.62	0.66
Fusion line angle (°)	0.001	0.96	-0.05	0.04	0.12	0.01
R square		0.36		0.73		0.76
Adjusted R-square		0.20		0.58		0.43
Number of observations		26		15		11

From Table 8.3, the same observations as stated earlier are revealed below Tables 8.1 and 8.2. It is clearly seen that the MVT method was successful in determining the effect of Nb on ferritic stainless steels. Cracking of the Houldcroft samples were dependent on Ti, welding parameters and the weld bead geometry, but was insenstive to the Nb content. The reasons for the difference in the success of the MVT and the Houldcroft techniques may be related to the direction of strain and the fact that the MVT weld beads were bead-on-plate, and not full penetration welds. For MVT, the weld bead is strained in tension, transverse to the welding direction, resulting in a high strain in the weld centreline. For Houldcroft, the strain is often parallel to the welding direction as demonstrated in the slightly rotated slotted material (Figure 5.18).

Final remarks

The susceptibility to solidification cracking of ferritic stainless steels was investigated to find the influence of Ti and/or Nb as stabilizers. The self-restrained Houldcroft, Modified Varestraint Transvarestraint (MVT) and hot tensile testing methods were

used. The study considered the research questions, problems and the set aim. Based on the results obtained from the experiment, the following conclusions were made.

- Ferritic stainless steels are not particularly susceptible to solidification cracking. This has been attributed to the primary ferrite phase formation during solidification [4]. This was observed during the self-restrained Houldcroft and MVT tests as the steel (unstabilized) showed resistance to solidification cracking in both techniques. The optical micrograph of the unstabilized steel showed columnar grains in the polished plane parallel to the welding direction during the Houldcroft test. In the MVT, equiaxed grains close to the fusion line and columnar grains at the weld centreline microstructures were observed in the polished plane transverse to the welding direction. These structures were resistant to solidification cracking.
- Ti addition to ferritic stainless steel had a minor increase to susceptibility to solidification cracking. Ti is known to form a eutectic, an iron titanide ($FeTi_2$) with approximately 14% Ti at 1289°C, and this can account for the increased susceptibility to solidification cracking [3, 49]. In the self-restrained Houldcroft test, the Ti stabilized steel cracked at the higher welding speed, but not at the lower speed. The cracking in the Houldcroft was mostly attributed to the welding speed than the chemistry, though the chemistry played a role, which was demonstrated in Figure 5.1. The optical microstructures revealed columnar grains which were susceptible to solidification cracking at the high speeds.
- Nb in ferritic stainless steel increases solidification cracking. Nb is also known to form a eutectic with Fe at 18.6% Nb at a melting point of 1373°C [3, 49]. It has been reported that Nb forms low melting temperatures in Fe-Cr alloy [3, 50]. When the Nb stabilized steels are welded, the ductility of the welded joint is poor at room temperature. This is attributed to columnar grains and epitaxial grain growth from the fusion line [47]. In the self-restrained Houldcroft method, Nb steels cracked in all the welding speeds, showing that the chemistry of the alloy was prominent. Moreover, the D:0.6Nb cracked the highest in the highest welding speed during the same test. In the MVT test, it showed to be marginally

susceptible in both welding speeds of 6 mm/s and 3 mm/s, implying that Nb in ferritic stainless steels increases solidification cracking susceptibility. Columnar grains characterized the weld zone and these structures resulted in the susceptibility to solidification cracking.

- The addition of Ti and Nb in ferritic stainless steels has a lower increasing effect to solidification cracking compared to Nb only. Ti and Nb with high impurity elemental levels in ferritic stainless steels can increase susceptibility to solidification cracking [4]. The crack length value of the Ti + Nb was found to be just lower to the Nb steel crack length value at a welding speed of 6 mm/s in the Houldcroft method (Table 5.2). All the crack length values for steels containing Ti + Nb were found to be between the mono-Nb and -Ti steel crack lengths. In the MVT test, the high Ti and Nb steel was marginally susceptible to solidification cracking during the welding speed of 3 mm/s, but was resistant to solidification cracking during the welding speed of 6 mm/s. The low Ti and Nb steel was resistant to solidification cracking in both welding speeds. The microstructures showed both columnar and equiaxed grains, but none were able to resist solidification cracking in the self-restrained Houldcroft test. In the MVT, the low Ti and Nb showed columnar grains which was resistant to solidification cracking. The high Ti and Nb revealed columnar grains but were marginally susceptible to solidification cracking.
- The brittle temperature range (BTR), which is approximated by the difference between the liquidus and solidus temperatures of the material can be used to explain some observations [5, 17]. The BTR as estimated from the Thermo-Calc estimates for liquidus and solidus temperatures seem to contribute to the susceptibility to solidification cracking. From Table 4.2, the unstabilized steels showed high BTR values, but the addition of Ti reduced it from 70 to 52. This meant that the unstabilized steels should be susceptible to solidification cracking. This was not the behavior in both the self-restrained Houldcroft and the MVT methods, as the unstabilized steels were resistant to solidification cracking compared to the Ti stabilized steels. The addition of Nb increased the

BTR values significantly and thus the alloy containing Nb should be susceptible to solidification cracking. Nb in ferritic stainless steel decreases the solidus temperature thereby increasing the solidification temperature range and eventually, increases the susceptibility to solidification cracking [73]. The same authors [73] also stated that Nb contributed more than Ti in the solidification temperature range for the ferritic stainless steels [73].

- MVT test is better than the self-restrained Houldcroft, and the self-restrained Houldcroft is better than the hot tensile tests. It is found that the MVT and Houldcroft are both based on actual welding, similar to the type of welding done in practice (autogenous GTAW). The MVT involves deformation of the weld metal as it solidifies, higher than that encountered in practice, the weld metal is more likely to crack. In executing the tests, MVT welds are away from an edge and this gives practical results. The Houldcroft sample starts to crack at the edge. Cracking in the Houldcroft test may therefore be more unreliable. In this specific study, the hot tensile test work was done poorly as a result of the small number of samples and poor choice of measurement interval.
- In self-restraint tests, two phenomena are used to evaluation the susceptibility to solidification cracking: whether cracking occurred or not, and the total crack length. The total crack length is often used to quantify the susceptibility to solidification cracking. Comparison of different materials is difficult to make as numerous examples of materials were crack resistant under self-restraint tests, but during actual fabrication conditions were found to be crack susceptible. Moreover, there are more than 140 solidification cracking susceptibility tests which have been developed and only some are standardized internationally [97]. This does not give same results for a particular material.
- The Thermo-Calc simulations revealed the various precipitates that occurred during solidification of the ferritic stainless steels. The DSC experiment revealed only the δ and α ferrite phase formations without showing any arrestments for these precipitates. The experiments using the self-restrained Houldcroft and hot tensile testing methods also revealed some precipitates. The

BTR values of the DSC experiment showed the unstabilized steels as having the highest values but the Thermo-Calc revealed Nb stabilized steels as the highest and the solidus temperature value was close to reports in literature. It is a known fact that Nb in steels are detrimental due to the formation of low melting phases. The Thermo-Calc simulations is probably more reliable under these circumstances than the DSC experimental values.

- All the SEM morphologies were found to be interdendritic confirming solidification cracking as the dominant cracking mechanism. The self-restraint Houldcroft method revealed low and high fraction eutectic. There were precipitates and inclusions on the surfaces in both methods. Generally, the EDX elemental analysis revealed Nb, Ti, Mn, Al, Si, Mo, S, and Ni for the self-restraint Houldcroft method and the hot tensile testing showed Al, Mn, Ti, Si, S, Nb, and Ni. This showed that the same elements were ejected during the solidification process.

Table 8.5 presented the summary of the susceptibility to solidification cracking of the ferritic stainless steels

Table 8.4: Summary of results of evaluation of susceptibility to solidification cracking

Type of stabilization	Steel ID	Self-restraint Houldcroft			MVT-test		Hot tensile testing
		1 mm/s	3 mm/s	6 mm/s	3 mm/s	6 mm/s	
None	A:0Ti;0Nb	Resistant	Resistant	Susceptible			
	B:0Ti;0Nb				Not susceptible	Not susceptible	
Ti	C:0.7Ti	Resistant	Susceptible	Susceptible			Ductile
Nb	D:0.6Nb	Susceptible	Susceptible	Susceptible	Marginally resistant	Marginally resistant	Low ductility
Ti + Nb	E:0.4Ti;0.6Nb	Resistant	Susceptible	Susceptible			Ductile
	F:0.4Ti;0.9Nb	Resistant	Susceptible	Susceptible	Marginally resistant	Not susceptible	
	G:0.1Ti;0.4Nb	Resistant	Susceptible	Susceptible			
	H:0.1Ti;0.4Nb				Not susceptible	Not susceptible	
	I:0.1Ti;0.5Nb	Susceptible	Susceptible	Susceptible			

- Solidification cracking susceptibility tests should be economical, simple to conduct and evaluate, and should show a direct correlation between test and service conditions. The applied stresses tests equipment are expensive. The self-restrained Houldcroft does not use any equipment. It has already been stated that there is no clear, consistent relationship between the results of self-restraint tests and service conditions. Production of Houldcroft samples require an equipment which can wire cut the samples to the correct dimensions without induced stresses. Measurement of parameters like BTR which aid in research of susceptibility to solidification cracking is not possible. As a consequence, the self-restraint tests are considered inadequate for fundamental studies of the susceptibility to solidification cracking. The hot tensile tests measure the on-heating and on-cooling temperatures to determine BTR which is the difference between nil strength temperature (NST) and the ductility recovery temperature (DRT).
- MVT test is simple to conduct of all the three methods. The samples of MVT are rectangular and have dimensions of 100 × 40 × 10 mm and can be produced easily. The MVT uses the total crack length and the applied strain to plot a graph which has three sectors and the same graph can be used without the sectors to investigate the susceptibility to solidification cracking. It does not measure any other parameters but it has been proven by Bundesanstalt für Materialforschung und – prüfung, Berlin (BAM) which carried out many thousand research results on a huge field of experiences, that MVT tests correlate well with practical knowledge [21]. Though there is little information for research investigations using MVT test, the fact that it relates well in practice makes it the best of the three susceptibility methods used for this study. All these laboratory susceptibility tests are aimed at using the material under investigations to meet the service conditions. Moreover, none of the three susceptibility tests was able to measure the BTR for this study. The best estimate for the BTR remains the difference between the liquidus and solidus. For steels that contain Nb, a higher

Nb content consistently resulted in a larger difference between the liquidus and the solidus temperatures.

8.2 Conclusions

The effect of Nb

The addition of Nb results in a larger increase in the difference between the liquidus and the solidus than a similar addition of Ti. Furthermore, the presence of Nb does not affect the weld metal solidification structure [64]. In the solid if the Nb content is below a certain value (that depends on the carbon and nitrogen content), Nb is present as Nb(CN) [49]. The presence of Nb carbonitrides may limit grain growth in the HAZ and this will affect the grain size in the weld metal that grows epitaxially from the fusion line.

From the current investigation, Thermo-Calc simulation and DSC experiments showed that a higher Nb content results in an increase in the difference between the liquidus and solidus temperatures. The addition of Nb resulted in, for the MVT test, a significant increase in susceptibility to solidification cracking and segregation of Nb to surface of solidification cracks. Hot tensile tests, although problematic, showed Nb steels to have a very low reduction in area.

These observations are consistent with the that fact that Nb segregates strongly during solidification (low k value). A higher Nb content results in a significant increase in the difference between the liquidus and the solidus. This difference increased the brittle temperature range results in a higher susceptibility to solidification cracking.

The effect of Ti

If the Fe-Ti and Fe-Nb phase diagrams are compared, the addition of Ti results in a smaller increase in the difference between the liquidus and the solidus than a similar addition of Nb. The presence of Ti affects the weld metal solidification structure. Specifically, a low Ti content of less than 0.1 resulted in a columnar solidification structure. Equiaxed structure was obtained if the steel contained more than 0.15% Ti [64].

Thermo-Calc simulation in particular (Table 4.2) and DSC experiments showed that a higher Ti content results in an increase in the difference between the liquidus and solidus temperatures. The addition of Ti resulted in a general increase in the susceptibility to solidification crack in the MVT. Hot tensile tests showed Ti steels to have a very high reduction in area. Ti (high k value) segregates less than Nb during solidification and there is a smaller increase in the difference between the liquidus and the solidus due to the addition of Ti than for a similar addition of Nb.

8.3 Recommendations

- It is recommended that welding at higher speeds be avoided, to reduce the risk of solidification cracking of ferritic stainless steels, irrespective of stabilization content.
- The Ti and Nb stabilizers are used for prevention of sensitization but welding these alloys results in solidification cracking. It is therefore recommended that the stabilizers (Ti & Nb) should not be used except for high temperature tensile strength. On the other hand, low levels of carbon and nitrogen may be used for the control of sensitization and also to prevent or reduce solidification cracking.
- Of the two welding-based techniques used to evaluate the susceptibility to solidification cracking the Varestraint method is statistically more reliable in demonstrating the deleterious effect of Nb than the self-restrained Houldcroft method. For this reason, the use of the Varestraint method is to be recommended in similar studies.
- The Varestraint or Trans-Varestraint method which is able to measure the brittle temperature range (BTR), should be used to measure this parameter for ferritic stainless steel.

References

[1] R. L. O'brien, *Jefferson's Welding Encyclopedia*, 18th ed. Miami USA: American Welding Society, 1997.

[2] K. G. Schofield, "A Literature Survey of Strain and Restrain Measurements in Welded Joints," *Int. J. Pres. Ves. Pip.*, vol. 4, pp. 1–28, 1976.

[3] E. Folkhard, *Welding Metallurgy of Stainless Steels*, 1st ed. Vienna: Springer Vienna, 1988.

[4] J. C. Lippold and D. J. Kotecki, *Welding Metallurgy and Weldability of Stainless Steels*, 1st ed. New Jersey: John Wiley and Sons, 2005.

[5] S. Kou, *Welding Metallurgy*, 2nd ed. New Jersey: John Wiley & Sons, 2003.

[6] G. Aggen, F. W. Akstens, C. M. Allen, H. S. Avery, and Etc, *ASM Handbook Volume 1*. United States of America: ASM International, 1993.

[7] V. Shankar, T. P. S. Gill, S. L. Mannan, and S. Sundaresan, "Solidification Cracking in Austenitic Stainless Steel Welds," *Sadhana*, vol. 28, no. 3–4, pp. 359–382, 2003.

[8] Z. Sun, "A Study of Solidification Crack Susceptibility using the Solidification Cycle Hot-tension Test," *Mater. Sci. Eng. A*, vol. 154, pp. 85–92, 1992.

[9] I. Varol, W. A. Baeslack III, and J. C. Lippold, "Characterization of Weld Solidification Cracking in a Duplex Stainless Steel," *Metallography*, vol. 23, pp. 1–19, 1989.

[10] A. Lakshminarayanan, K. Shanmugam, and V. Balasubramanian, "Effect of Welding Processes on Tensile and Impact Properties, Hardness and Microstructure of AISI 409M Ferritic Stainless Joints Fabricated by Duplex Stainless Steel Filler Metal," *J. Iron Steel Res. Int.*, vol. 16, no. 5, pp. 66–72, 2009.

[11] A. Lakshminarayanan, K. Shanmugam, and V. Balasubramanian, "Effect of Autogenous Arc Welding Processes on Tensile and Impact Properties of Ferritic Stainless Steel Joints," *J. Iron Steel Res. Int.*, vol. 16, no. 1, pp. 62–16, 2009.

[12] D. H. Kah and D. W. Dickinson, "Weldability of Ferritic Stainless Steels," *Weld. J.*, vol. 64, no. 16, pp. 135-s-142-s, 1981.

[13] Y. Nisho, T. Ohmae, Y. Yoshida, and Y. Miura, “Weld Cracking and Mechanical Properties of 17 % Chromium Steel Weldment,” *Weld. J.*, vol. 50, no. 1, pp. 9-s-18-s, 1971.

[14] D. E. Nelson, W. A. Baeslack III, and J. C. Lippold, “An Investigation of Weld Hot Cracking in Duplex Stainless Steels,” *Weld. J.*, vol. 66, no. 8, pp. 241s-250s, 1987.

[15] R. M. Nunes, B. L. Alia, R. L. Alley, W. R. Apblett Jr, W. A. Baeslack III, and Etc, *ASM Handbook Volume 6 Welding, Brazing and Soldering*. USA: ASM International, 1993.

[16] J. C. Lippold, *Welding Metallurgy and Weldability*, 1st ed. Hoboken, New Jersey: John Wiley & Sons, 2015.

[17] C. E. Cross, “On the Origin of Weld Solidification Cracking,” in *Hot Cracking Phenomena in Welds*, Berlin Heidelberg: Springer Berlin Heidelberg, 2005, pp. 1–397.

[18] J. C. Borland, “Generalized Theory of Super-solidus Cracking in Welds and Castingse,” *Br. Weld. J.*, vol. 7, no. 8, pp. 508–512, 1960.

[19] S. T. Mandziej, “Testing for Susceptibility to Hot Cracking on Gleeble Physical Simulator.” pp. 1–10, 2004.

[20] G. Srinivasan *et al.*, “Weldability Studies on Borated Stainless Steels using Varestraint and Gleeble Test,” *Weld World*, vol. 59, pp. 119–126, 2015.

[21] T. Böllinghaus and H. Herold, *Hot Cracking Phenomena in Welds*. Berlin Heidelberg: Springer Vienna, 2005.

[22] J. F. Lancaster, *Metallurgy of Welding*, 6th ed. Abington, Cambridge England: Woodhead Publishing Limited, 1999.

[23] R. D. Campbell and D. W. Walsh, “Weldability Testing,” in *ASM Handbook Volume 6*, D. L. Olson, T. A. Siewert, S. Liu, and G. R. Edwards, Eds. 1993, pp. 603–613.

[24] C. D. Lundin, W. T. Delong, and D. F. Spond, “The Fissure Bend Test,” *Weld. J.*, vol. 55, no. 6, pp. 145-s-151-s, 1976.

[25] K. F. Krysiak, J. F. Grubb, B. Pollard, and R. D. Campbell, “Selection of Wrought Ferritic Stainless Steels,” in *ASM Handbook, Volume 6: Welding,*

Brazing, and Soldering, 1993, pp. 443–455.

[26] F. Matsuda, H. Nakagawa, S. Ogata, and S. Katayama, "Fractographic Investigation on Solidification Crack in the Varestraint Test of Fully Austenitic Stainless Steel," *Trans. JWRI*, vol. 7, no. 1, pp. 59–70, 1978.

[27] G. Madhusudhan Reddy, A. K. Mukhopadhyay, and A. Sambasiva Rao, "Influence of Scandium on Weldability of 7010 Aluminium Alloy," *Sci. Technol. Weld. Join.*, vol. 10, no. 4, pp. 432–441, 2005.

[28] J. Adamiec, "The Influence of Construction Factors in the Weldability of AZ91E Alloy," *Arch. Metall. Mater.*, vol. 56, no. 3, pp. 769–778, 2011.

[29] A. R. Safari, M. R. Forouzan, and M. Shamanian, "Hot Cracking in Stainless Steel 310s, Numerical Study and Experimental Verification," *Comput. Mater. Sci.*, vol. 63, pp. 182–190, 2012.

[30] S. Lampman, *Weld Integrity and Performance*, 1st ed. ASM International, 1997.

[31] Messler Jr., R. W., *Principles of Welding*, 1st ed. Weinheim: WILEY-VCH Verlag GmbH & Co., 2004.

[32] S. H. Cho, K. B. Kang, and J. J. Jonas, "The Dynamic, Static and Metadynamic Recrystallization of a Nb-microalloyed Steel," *ISIJ Int.*, vol. 41, no. 1, pp. 63–69, 2001.

[33] F. J. Humphreys and M. Hatherly, *Recrystallization and Related Annealing phenomena*. Elsevier Oxford, 2004.

[34] I. A. DeArdo, "Mechanical Behavior of IF 409 Ferritic Stainless Steel," McGill University Montreal, Quebec, Canada, 1998.

[35] W. F. Savage and G. D. Lundin, "The Varestraint Test," *Weld. J.*, vol. 44, no. 10, pp. 433–442, 1965.

[36] V. Shankar, T. P. S. Gill, A. L. E. Terrance, S. L. Mannan, and S. Sundaresan, "Relation between Microstructure , Composition , and Hot Cracking in Ti-Stabilized Austenitic Stainless Steel Weldments," *Metall. Mater. Trans. A*, vol. 31, no. A, pp. 3109–3122, 2000.

[37] H. T. Kim and S. W. Nam, "Solidification Cracking Susceptibility of High Strength Aluminum Alloy Weldment," *Scr. Mater.*, vol. 34, no. 7, pp. 1139–1145, 1996.

[38] C.-M. Lin, “Relationships between Microstructures and Properties of Buffer Layer with Inconel 52M Clad on AISI 316L Stainless Steel by GTAW Processing,” *Surf. Coatings Technol.*, vol. 228, pp. 234–241, 2013.

[39] J. C. Lippold, T. Bollinghaus, and C. E. Cross, *Hot Cracking Phenomena in Welds III*. New York: Springer, 2011.

[40] J. C. Lippold, “Recent Developments in Weldability Testing for Advanced Materials,” in *International Conference on Joining of Advances and Specialty Materials VII*, 2005, pp. 1–16.

[41] B. Thomas, H. Herold, C. E. Cross, and J. C. Lippold, *Hot Cracking Phenomena in Welds II*, 1st ed. Berlin Heidelberg: Springer, 2008.

[42] A. Ankara and H. B. Ari, “Determination of Hot Crack Susceptibility of Various Kinds of Steels,” *Mater. Des.*, vol. 17, no. 5, pp. 261–265, 1997.

[43] A. C. Davies, *The Science and Practice of welding Volume 2*, 10th ed. Cambridge, United Kingdom: Cambridge University Press, 2002.

[44] J. Norrish, *Advanced welding Processes, Technology and Process Control*, 2nd ed. Cambridge: Woodhead Publishing Limited, 2006.

[45] W. D. Callister Jr and D. G. Rethwisch, *Materials Science and Engineering, An Introduction*, 8th ed. United States of America: John Wiley and Sons, 2008.

[46] T. Mohandas, G. Madhusudhan Reddy, and M. Naveed, “A Comparative Evaluation of Gas Tungsten and Shielded Metal Arc Welds of a Ferritic Stainless Steel,” *J. Mater. Process. Technol.*, vol. 94, no. 2–3, pp. 133–140, 1999.

[47] W. Gordon and A. van Bennekom, “Review of Stabilisation of Ferritic Stainless Steels,” *Mater. Sci. Technol.*, vol. 12, pp. 126–131, 1996.

[48] N. O. Fujita, K. Kikuchi, T. Suzuki, S. Funaki, and L. Hiroshige, “Effect of Niobium on High Temperature Properties for Ferritic Stainless Steel,” *Scr. Mater.*, vol. 35, pp. 705–710, 1996.

[49] N. Fujita, K. Ohmura, and A. Yamamoto, “Changes of Microstructures and High Temperature Properties during High Temperature Service of Niobium Added Ferritic Stainless Steels,” *Mater. Sci. Eng. A*, vol. 351, no. 1–2, pp. 272–281, 2003.

[50] G. M. Sim, J. C. Ahn, S. C. Hong, K. J. Lee, and K. S. Lee, “Effect of Nb

Precipitate Coarsening on the High Temperature Strength in Nb Containing Ferritic Stainless Steels," *Mater. Sci. Eng. A*, vol. 396, no. 1–2, pp. 159–165, 2005.

[51] R. M. Notis, N. A. Gjostein, N. C. Jessen Jr., E. C. Kendall, and Etc, *ASM Handbook Volume 3 Alloys Phase Diagrams*. 1992.

[52] J. Shu, H. Bi, X. Li, and Z. Xu, "Effect of Ti Addition on Forming Limit Diagrams of Nb-bearing Ferritic Stainless Steel," *J. Mater. Process. Technol.*, vol. 212, pp. 59–65, 2012.

[53] H. Yan, H. Bi, X. Li, and Z. Xu, "Precipitation and Mechanical Properties of Nb-modified Ferritic Stainless Steel during Isothermal Aging," *Mater. Charact.*, vol. 60, no. 3, pp. 204–209, 2009.

[54] V. Kuzucu, M. Aksoy, M. H. Korkut, and M. M. Ylldlrlm, "The Effect of Niobium on the Microstructure of Ferritic Stainless Steel," *Mater. Sci. Eng. A*, vol. 230, pp. 75–80, 1997.

[55] H. Yan, H. Bi, X. Li, and Z. Xu, "Microstructure and Texture of Nb+Ti Stabilized Ferritic Stainless Steel," *Mater. Charact.*, vol. 59, no. 12, pp. 1741–1746, 2008.

[56] W. Du, L. Jiang, Q. Sun, Z. Liu, and X. Zhang, "Microstructure, Texture, and Formability of Nb+Ti Stabilized High Purity Ferritic Stainless Steel," *J. Iron Steel Res. Int.*, vol. 17, no. 6, pp. 47–52, 2010.

[57] R. E. Smallman and R. J. Bishop, *Modern Physical Metallurgy and Materials Engineering*, 6th ed. New York: Butterworth-Heinemann, 2002.

[58] L. Yang, *Materials Characterisation - Introduction to Microscope and Spectroscopty*. Singapore: John Wiley & Sons (Asia) Pte Ltd, 2008.

[59] B. J. Ganesh *et al.*, "Differential Scanning Calorimetry Study of Diffusional and Martensitic Phase Transformations in Some 9 wt- % Cr Low Carbon Ferritic Steels," *Mater. Sci. Technol.*, vol. 27, no. 2, pp. 500–512, 2011.

[60] D. Steiner Petrovič, G. Klančnik, M. Pirnat, and J. Medved, "Differential Scanning Calorimetry Study of the Solidification Sequence of Austenitic Stainless Steel," *J. Therm. Anal. Calorim.*, vol. 105, no. 1, pp. 251–257, 2011.

[61] R. S. Parmar, *Welding Processes and Technology*, 1st ed. New Delhi, India:

Khanna Publishers, 2003.

[62] C. C. Silva, J. P. Farias, H. C. Miranda, R. F. Guimarães, J. W. A. Menezes, and M. A. M. Neto, "Microstructural Characterization of the HAZ in AISI 444 Ferritic Stainless Steel Welds," *Mater. Charact.*, vol. 59, no. 5, pp. 528–533, 2008.

[63] A. K. Lakshminarayanan and V. Balasubramanian, "Assessment of Sensitization Resistance of AISI 409M Grade Ferritic Stainless Steel Joints using Modified Strauss Test," *Mater. Des.*, vol. 39, pp. 175–185, 2012.

[64] V. Villaret *et al.*, "Characterization of Gas Metal Arc Welding Welds obtained with New High Cr–Mo Ferritic Stainless Steel Filler Wires," *Mater. Des.*, vol. 51, pp. 474–483, 2013.

[65] G. B. Hunter and T. W. Eager, "Ductility of Stabilized Ferritic Stainless Steel Welds," *Metall. Trans. A*, vol. 11A, pp. 1–6, 1980.

[66] O. Daehee, K. Han, S. Hong, and C. Lee, "Effects of Alloying Elements on the Thermal Fatigue Properties of the 15wt% Cr Ferritic Stainless Steel Weld HAZ," *Mater. Sci. Eng. A*, vol. 555, pp. 44–51, 2012.

[67] V. Villaret, F. Deschaux-Beaume, C. Bordreuil, S. Rouquette, and C. Chovet, "Influence of Filler Wire Composition on Weld Microstructures of a 444 Ferritic Stainless Steel Grade," *J. Mater. Process. Technol.*, vol. 213, no. 9, pp. 1538–1547, 2013.

[68] J. C. Villafuerte, H. W. Kerr, and S. A. David, "Mechanisms of Equiaxed Grain Formation in Ferritic Stainless Steel Gas Tungsten Arc Welds," *Mater. Sci. Eng. A*, vol. 194, no. 2, pp. 187–191, 1995.

[69] M. Tullmin, F. P. A. Robinson, C. A. O. Henningt, A. Strausst, and J. Le Grange, "Properties of Laser-welded and Electron-beam-welded Ferritic Stainless Steel," *J. South African Inst. Min. Metall.*, vol. 89, no. 8, pp. 243–249, 1989.

[70] M. O. H. Amuda and S. Mridha, "Grain Refinement in Ferritic Stainless Steel Welds: The Journey so Far," *Adv. Mater. Res.*, vol. 83–86, pp. 1165–1172, 2009.

[71] J. C. Villafuerte, E. Pardo, and H. W. Kerr, "The Effect of Alloy Composition and Welding Conditions on Columnar-Equiaxed Transitions in Ferritic Stainless Steel Gas-Tungsten Arc Welds," *Metall. Trans. A*, vol. 21A, pp. 2009–2019,

1990.

[72] G. M. Reddy and T. Mohandas, “Explorative Studies on Grain Refinement of Ferritic Stainless Steel Welds,” *J. Mater. Sci. Lett.*, vol. 20, pp. 721–723, 2001.

[73] Y. Shan, X. Luo, X. Hu, and S. Liu, “Mechanisms of Solidification Structure Improvement of Ultra Pure 17 wt % Cr Ferritic Stainless Steel by Ti , Nb Addition,” *J. Mater. Sci. Technol.*, vol. 27, no. 4, pp. 352–358, 2011.

[74] H. Tripathy, S. Raju, A. Kumar, G. Panneerselvam, and T. Jayakumar, “Thermal Stability and Thermal Property Characterisation of Fe–14.4Cr–15.4Ni–2.4Mo–2.36Mn–0.25Ti–1.02Si–0.042C–0.04P–0.005B (mass%) Austenitic Stainless Steel (Alloy D9I),” *Nucl. Eng. Des.*, vol. 255, pp. 86–96, 2013.

[75] O. Martinik *et al.*, “Prediction and Measurement of Selected Phase Transformation Temperatures of Steels,” *J. Min. Metall. Sect. B Metall.*, vol. 53, no. 3, pp. 391–398, 2017.

[76] C. J. van Niekerk and M. du Toit, “Sensitization Behaviour of 11 — 12 % Cr AISI 409 Stainless Steel during Low Heat Input Welding,” *J. South. African Inst. Min. Metall.*, vol. 111, pp. 243–256, 2011.

[77] H. Fourie, “African NDT Centre,” Pretoria, South Africa, 2015.

[78] C. Lundin, C. Qiao, T. Gill, and G. Goodwin, “Hot Ductility and Hot Cracking Behavior of Modified 316 Stainless Steels Designed for High-temperature Service,” *Weld. Res. Suppl.*, pp. 189-s-200-s, 1993.

[79] G. F. Vander Voort, *Metallography Principles and Practices*, 4th ed. New York: ASM International, 2007.

[80] M. Wolf, H. Schobbert, and T. Böllinghaus, “Influence of the Weld Pool Geometry on Solidification Crack Formation,” in *Hot Cracking Phenomena in Welds*, Berlin Heidelberg: Springer Berlin Heidelberg, 2005, pp. 245–270.

[81] S. Kou, “Solidification and Liquation Cracking Issues in Welding,” *JOM*, pp. 37–42, 2003.

[82] S. A. David, S. S. Babu, J. M. Vitek, S. A. David, S. S. Babu, and J. M. Vitek, “Recent Advances in Modelling and Characterisation of Weld Microstructures,” *Sci. Technol. Weld. Join.*, vol. 6, no. 6, pp. 341–346, 2001.

[83] S. Kou and Y. Le, “Welding Parameters and the Grain Structure of Weld Metal-

A Thermodynamic Consideration," *Metall. A*, vol. 19A, pp. 1075–1082, 1988.

[84] A. Mirzaee-Sisan and G. Wu, "Residual Stress in Pipeline Girth Welds- A Review of Recent Data and Modelling," *Int. J. Press. Vessel. Pip.*, vol. 169, pp. 142–152, 2019.

[85] S. D. Harvey, "Fundamentals of Weld Solidification," in *ASM Handbook Vol 6, Welding, Brazing and Soldering*, United States of America: ASM International, 1993, pp. 111–136.

[86] W. F. Savage and C. D. Lundin, "Application of the Varestraint Technique to the Study of Weldability," *Weld. J.*, vol. 45, no. 11, pp. 496-s-503-s, 1966.

[87] A. M. Alshahrani, "The effects of Niobium and Dynamic Recrystallisation on Microstructural Homogeneity of Microalloyed Steels," 2013.

[88] L. Cheng, X. Xue, B. Tang, H. Kou, and J. Li, "Flow Characteristics and Constitutive Modeling for Elevated Temperature Deformation of a Nb containing TiAl alloy," *Intermetallics*, vol. 49, pp. 23–28, 2014.

[89] I. Mejia, A. E. Salas-Reyes, J. Calvo, and J. M. Cabrera, "Effect of Ti and B Microadditions on the Hot Ductility Behaviour of a High-Mn austenitic Fe-23Mn-1.5Al-1.3Si-0.5C TWIP Steel," *Mater. Sci. Eng. A*, vol. 648, pp. 311–329, 2015.

[90] Y. Kang, W. M. Mao, Y. J. Chen, J. Jing, and M. Cheng, "Effect of Ti Content on Grain Size and Mechanical Properties of UNS S44100 Ferritic Stainless Steel," *Mater. Sci. Eng. A*, vol. 677, pp. 211–221, 2016.

[91] H. K. D. H. Bhadeshia and S. R. Honeycombe, *Steels, Microstructure and Properties*, 3rd ed. Cambridge: Butterworths-Heinemann (Elsevier), 2006.

[92] S. E. Kang, "Hot Ductility of TWIP Steels," 2014.

[93] M. P. Sello and W. E. Stumpf, "Laves Phase Embrittlement of the Ferritic Stainless Steel Type AISI 441," *Mater. Sci. Eng. A*, vol. 527, no. 20, pp. 5194–5202, 2010.

[94] C. W. Siyasiya, M. G. Maruma, and W. E. Stumpf, "Influence of Chemical Composition on the Evolution of Texture in 441 Ferritic Stainless Steel," in *17th International Conference on Textures of Materials*, 2015, pp. 1–4.

[95] K. Han, J. Yoo, B. Lee, I. Han, and C. Lee, "Effect of Ni on the Hot Ductility

and Hot Cracking Susceptibility of High Mn Austenitic Cast Steel," *Mater. Sci. Eng. A*, vol. 618, pp. 295–304, 2014.

[96] K. Kuzsella, J. Lukaes, and K. Szues, "Nil-Strength Temperature and Hot Tensile Tests on SQ60QL High-Strength Low-Alloy Steel," *Prod. Process. Syst.*, vol. 6, no. 1, pp. 67–78, 2013.

[97] T. Kannengiesser and T. Boellinghaus, "Hot Cracking Tests - An Overview of Present Technologies and Applications," *Weld. World*, vol. 57, no. 1, pp. 3–37, 2014.

APPENDICES

Appendix A

Thermo-Calc stable phases – Sample A:0Ti;0Nb
Table A.1: MnS phase in sample A:0Ti;0Nb

	Moles	Mass	Volume Fraction
MNS#1	0.0001	0.0050	0.0001
Composition			
Component	Mole Fraction	Mass Fraction	
Mn	0.5000	0.6314	
S	0.5000	0.3686	
Fe	4.15E-05	5.32E-05	
Cr	0	0	
Si	0	0	
P	0	0	
V	0	0	
N	0	0	
C	0	0	
Ti	0	0	
Nb	0	0	
Ni	0	0	

Thermo-Calc stable phases – Sample B:0Ti;0Nb
Table A.2: MnS phase in sample B:0Ti;0Nb

	Moles	Mass	Volume Fraction
MNS#1	0.0004	0.0194	0.0004
Composition			
Component	Mole Fraction	Mass Fraction	
Mn	0.5	0.631442	
S	0.5	0.368558	
Fe	2.36E-07	3.03E-07	
Cr	0	0	
Si	0	0	
P	0	0	
V	0	0	
N	0	0	
C	0	0	
Ti	0	0	
Nb	0	0	
Ni	0	0	

Thermo-Calc stable phases – Sample C:0.7Ti
Table A.3: TiN phase in sample C:0.7Ti

	Moles	Mass	Volume Fraction
FCC_A1#2	0.0057	0.1776	0.0046
Composition			
Component	Mole Fraction	Mass Fraction	
Ti	0.5080	0.7803	
N	0.4692	0.2108	
C	0.0227	0.0088	
Cr	7.77E-05	0.0001	
V	1.06E-05	1.73E-05	
Nb	5.42E-06	1.62E-05	
Fe	4.12E-07	7.38E-07	
Mn	6.72E-08	1.18E-07	
Mo	1.29E-08	3.98E-08	
Ni	1.27E-10	2.39E-10	
Si	1.39E-11	1.26E-11	
Al	9.43E-12	8.16E-12	
S	5.08E-13	5.23E-13	
P	5.08E-13	5.05E-13	

Table A.4: Laves phase in sample C:0.7Ti

	Moles	Mass	Volume Fraction
LAVES_PHASE_C14	0.0081	0.4241	0.0091
Composition			
Component	Mole Fraction	Mass Fraction	
Fe	0.5812	0.6197	
Ti	0.3301	0.3017	
Ni	0.0450	0.0504	
Si	0.0391	0.0210	
Nb	0.0019	0.0034	
Mo	0.0012	0.0022	
Cr	0.0015	0.0015	
Mn	3.91E-05	4.1E-05	
Al	3.09E-09	1.59E-09	
S	0	0	
P	0	0	
V	0	0	
N	0	0	
C	0	0	

Table A.5: Sigma phase in sample C:0.7Ti

	Moles	Mass	Volume Fraction
SIGMA	0.0998	0.5334	0.0983
Composition			
Component	Mole Fraction	Mass Fraction	
Fe	0.5549	0.5795	
Cr	0.4036	0.3924	
Si	0.0290	0.0152	
Mn	0.0117	0.0120	
Ni	0.0006	0.0007	
V	0.0002	0.0002	
Mo	4.24E-05	7.6E-05	
Ti	5.48E-06	4.91E-06	
Nb	3.72E-07	6.46E-07	
Al	2.82E-09	1.42E-09	
S	0	0	
P	0	0	
N	0	0	
C	0	0	

Thermo-Calc stable phases – Sample D:0.6Nb
Table A.6: NbC in sample D:0.6Nb

	Moles	Mass	Volume Fraction
FCC_A1#2	0.0013	0.0725	0.0013
Composition			
Component	Mole Fraction	Mass Fraction	
Nb	0.5259	0.8911	
C	0.3965	0.0869	
N	0.0741	0.0189	
Ti	0.0024	0.0022	
Cr	0.0008	0.0007	
V	0.0002	0.0002	
Fe	4.19E-06	4.27E-06	
Mn	9.75E-08	9.77E-08	
Mo	1.84E-09	3.21E-09	
Ni	8.93E-11	9.55E-11	
S	5.29E-13	3.1E-13	
P	5.29E-13	2.99E-13	
Si	5.29E-13	2.71E-13	
Al	5.29E-13	2.6E-13	

Table A.7: MnS phase in sample D:0.6Nb

	Moles	Mass	Volume Fraction
MNS	0.0002	0.0104	0.0002
Composition			
Component	Mole Fraction	Mass Fraction	
Mn	0.5000	0.6314	
S	0.5000	0.3686	
Fe	2.76E-06	3.54E-06	
Cr	0	0	
Si	0	0	
P	0	0	
V	0	0	
N	0	0	
C	0	0	
Ti	0	0	
Nb	0	0	
Al	0	0	
Ni	0	0	
Mo	0	0	

Table A.8: Z - phase in sample D:0.6Nb

	Moles	Mass	Volume Fraction
Z_PHASE	0.0075	0.4018	0.0072
Composition			
Component	Mole Fraction	Mass Fraction	
Nb	0.3267	0.5646	
Cr	0.2810	0.2716	
N	0.3106	0.0809	
Fe	0.0637	0.0662	
V	0.0177	0.0168	
Mo	1.72E-05	3.06E-05	
Si	0	0	
S	0	0	
P	0	0	
C	0	0	
Ti	0	0	
Al	0	0	
Ni	0	0	
Mn	0	0	

Thermo-Calc stable phases – Sample E:0.4Ti;0.6Nb
Table A.9: Ti(C,N) phase in sample E:0.4Ti;0.6Nb

	Moles	Mass	Volume Fraction
FCC_A1#2	0.0071	0.2205	0.0058
Composition			
Component	Mole Fraction	Mass Fraction	
Ti	0.5097	0.7849	
N	0.3809	0.1716	
C	0.1089	0.0421	
Nb	0.0005	0.0014	
Cr	1.51E-05	2.53E-05	
V	6.71E-06	1.1E-05	
Fe	6.23E-09	1.12E-08	
Mo	2.97E-09	9.15E-09	
Mn	3.48E-09	6.15E-09	
Ni	4.05E-12	7.65E-12	
S	5.1E-13	5.26E-13	
P	5.1E-13	5.08E-13	
Si	5.1E-13	4.61E-13	
Al	5.1E-13	4.43E-13	

Table A.10: Laves phase in sample E:0.4Ti;0.6Nb

	Moles	Mass	Volume Fraction
LAVES_PHASE_C14	0.0005	0.0339	0.0006
Composition			
Component	Mole Fraction	Mass Fraction	
Fe	0.5535	0.4736	
Nb	0.3231	0.4599	
Si	0.0855	0.0368	
Cr	0.0272	0.0217	
Ti	0.0099	0.0073	
Ni	0.0006	0.0005	
Mo	0.0002	0.0003	
Mn	1.57E-05	1.32E-05	
Al	4.37E-08	1.81E-08	
S	0	0	
P	0	0	
V	0	0	
N	0	0	
C	0	0	

Thermo-Calc stable phases – Sample F:0.4Ti;0.9Nb
Table A.11: TiN phase in sample F:0.4Ti;0.9Nb

	Moles	Mass	Volume Fraction
FCC_A1#2	0.0064	0.1971	0.0052
Composition			
Component	Mole Fraction	Mass Fraction	
Ti	0.5074	0.7827	
N	0.4135	0.1866	
C	0.0792	0.0306	
Nb	6.4E-08	1.92E-07	
V	7.84E-09	1.29E-08	
Cr	5.1E-10	8.55E-10	
Mo	5.07E-13	1.57E-12	
Ni	5.07E-13	9.59E-13	
Fe	5.07E-13	9.13E-13	
Mn	5.07E-13	8.98E-13	
S	5.07E-13	5.24E-13	
P	5.07E-13	5.06E-13	
Si	5.07E-13	4.59E-13	
Al	5.07E-13	4.41E-13	

Table A.12: Laves phase in sample F:0.4Ti;0.9Nb

	Moles	Mass	Volume Fraction
LAVES_PHASE_C14	0.0182	1.1723	0.0218
Composition			
Component	Mole Fraction	Mass Fraction	
Fe	0.5744	0.5003	
Nb	0.2943	0.4264	
Si	0.0846	0.0370	
Ti	0.0378	0.0282	
Cr	0.0069	0.0056	
Mo	0.0011	0.0017	
Ni	0.0008	0.0007	
Mn	9.69E-07	8.3E-07	
Al	1.09E-11	4.57E-12	
S	0	0	
P	0	0	
V	0	0	
N	0	0	
C	0	0	

Table A.13: MnS phase in sample F:0.4Ti;0.9Nb

	Moles	Mass	Volume Fraction
MNS	0.0001	0.0060	0.0001
Composition			
Component	Mole Fraction	Mass Fraction	
Mn	0.5000	0.6314	
S	0.5000	0.3686	
Fe	5.07E-05	6.51E-05	
Cr	0	0	
Si	0	0	
P	0	0	
V	0	0	
N	0	0	
C	0	0	
Ti	0	0	
Nb	0	0	
Al	0	0	
Ni	0	0	
Mo	0	0	

Table A.14: $Ti_4C_2S_2$ phase in sample F:0.4Ti;0.9Nb

	Moles	Mass	Volume Fraction
$TI4C_2S_2$	0.0003	0.0095	0.0003
Composition			
Component	Mole Fraction	Mass Fraction	
Ti	0.5000	0.6848	
S	0.2500	0.2293	
C	0.2500	0.0859	
Cr	0	0	
Si	0	0	
P	0	0	
V	0	0	
N	0	0	
Nb	0	0	
Al	0	0	
Ni	0	0	
Mo	0	0	
Mn	0	0	
Fe	0	0	

Thermo-Calc stable phases – Sample G:0.1Ti;0.4Nb
Table A.15: Ti(C,N) phase in sample G:0.1Ti;0.4Nb

	Moles	Mass	Volume Fraction
FCC_A1#2	0.0023	0.0720	0.0020
Composition			
Component	Mole Fraction	Mass Fraction	
Ti	0.5223	0.8019	
N	0.2205	0.0990	
C	0.2571	0.0990	
Nb	2.64E-06	7.86E-06	
V	8.26E-08	1.35E-07	
Cr	3.85E-08	6.42E-08	
Mn	3.96E-12	6.97E-12	
Ni	5.22E-13	9.83E-13	
Fe	5.22E-13	9.35E-13	
S	5.22E-13	5.37E-13	
P	5.22E-13	5.19E-13	
Si	5.22E-13	4.7E-13	

Table A.16: MnS phase in sample G:0.1Ti;0.4Nb

	Moles	Mass	Volume Fraction
MNS	0.0004	0.0194	0.0004
Composition			
Component	Mole Fraction	Mass Fraction	
Mn	0.5000	0.6314	
S	0.5000	0.3686	
Fe	2.36E-07	3.03E-07	
Cr	0	0	
Si	0	0	
P	0	0	
V	0	0	
N	0	0	
C	0	0	
Ti	0	0	
Nb	0	0	
Ni	0	0	

Table A.17: $Ti_4C_2S_2$ phase in sample G:0.1Ti;0.4Nb

	Moles	Mass	Volume Fraction
$TI4C_2S_2$	4.19E-05	0.0015	4.07E-05
Composition			
Component	Mole Fraction	Mass Fraction	
Ti	0.5000	0.6848	
S	0.2500	0.2293	
C	0.2500	0.0859	
Cr	0	0	
Si	0	0	
P	0	0	
V	0	0	
N	0	0	
Nb	0	0	
Ni	0	0	
Mn	0	0	
Fe	0	0	

Thermo-Calc stable phases – Sample H:0.1Ti;0.4Nb
Table A.18: $Ti_4C_2S_2$ phase in sample H:0.1Ti;0.4Nb

	Moles	Mass	Volume Fraction
TI4C2S2#1	0.0009	0.0310	0.0009
Composition			
Component	Mole Fraction	Mass Fraction	
Ti	0.5000	0.6848	
S	0.2500	0.2293	
C	0.2500	0.0859	
Cr	0	0	
Si	0	0	
P	0	0	
V	0	0	
N	0	0	
Nb	0	0	
Ni	0	0	
Mn	0	0	
Fe	0	0	

Table A.19: Ti(C,N) phase in sample H:0.1Ti;0.4Nb

	Moles	Mass	Volume Fraction
FCC_A1#2	0.0018	0.0564	0.0015
Composition			
Component	Mole Fraction	Mass Fraction	
Ti	0.5138	0.7904	
N	0.2803	0.1261	
C	0.2043	0.0788	
Nb	0.0015	0.0044	
Cr	9.83E-05	0.0002	
V	2.19E-05	3.59E-05	
Fe	3.65E-08	6.54E-08	
Mn	2.84E-08	5.02E-08	
Ni	3.73E-11	7.03E-11	
S	5.15E-13	5.31E-13	
P	5.15E-13	5.13E-13	
Si	5.15E-13	4.65E-13	

Thermo-Calc stable phases – Sample I:0.1Ti;0.5Nb;2Mo

Table A.20: Ti(C,N) phase in sample I:0.1Ti;0.5Nb;2Mo

	Moles	Mass	Volume Fraction
FCC_A1#2	0.0021	0.0635	0.0017
Composition			
Component	Mole Fraction	Mass Fraction	
Ti	0.5005	0.7823	
N	0.3332	0.1524	
C	0.1663	0.0652	
Nb	2.44E-05	7.41E-05	
Cr	1.01E-06	1.71E-06	
Mo	1.71E-09	5.35E-09	
Mn	1.28E-11	2.3E-11	
Ni	5.01E-13	9.59E-13	
Fe	5.01E-13	9.13E-13	
S	5.01E-13	5.24E-13	
P	5.01E-13	5.06E-13	
Si	5.01E-13	4.59E-13	

Table A.21: MnS phase in sample I:0.1Ti;0.5Nb;2Mo

	Moles	Mass	Volume Fraction
MNS	0.0001	0.0050	0.0001
Composition			
Component	Mole Fraction	Mass Fraction	
Mn	0.5000	0.6314	
S	0.5000	0.3686	
Fe	2.37E-07	3.04E-07	
Cr	0	0	
Si	0	0	
P	0	0	
N	0	0	
C	0	0	
Ti	0	0	
Nb	0	0	
Ni	0	0	
Mo	0	0	

Table A.22: $Ti_4C_2S_2$ phase in sample I:0.1Ti;0.5Nb;2Mo

	Moles	Mass	Volume Fraction
$TI4C_2S_2$	0.0002	0.0077	0.0002
Composition			
Component	Mole Fraction	Mass Fraction	
Ti	0.5000	0.6848	
S	0.2500	0.2293	
C	0.2500	0.0859	
Cr	0	0	
Si	0	0	
P	0	0	
N	0	0	
Nb	0	0	
Ni	0	0	
Mo	0	0	
Mn	0	0	
Fe	0	0	

Appendix B

Possible precipitates from Thermo-Calc calculations

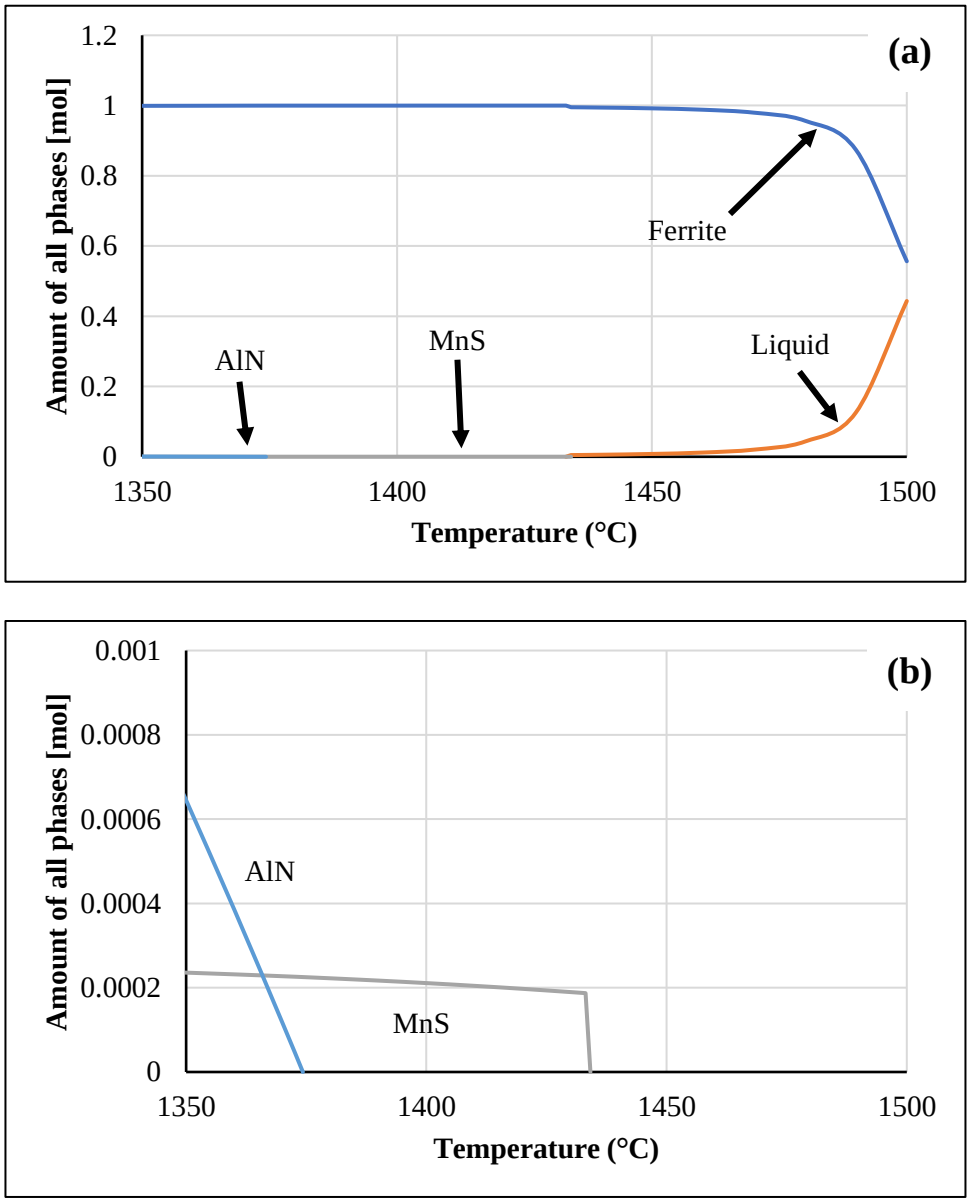

Figure B.1:a) The possible precipitates from Thermo-Calc between 1350°C and 1500°C for sample A:0Ti;0Nb, and b) the molar fraction precipitate.

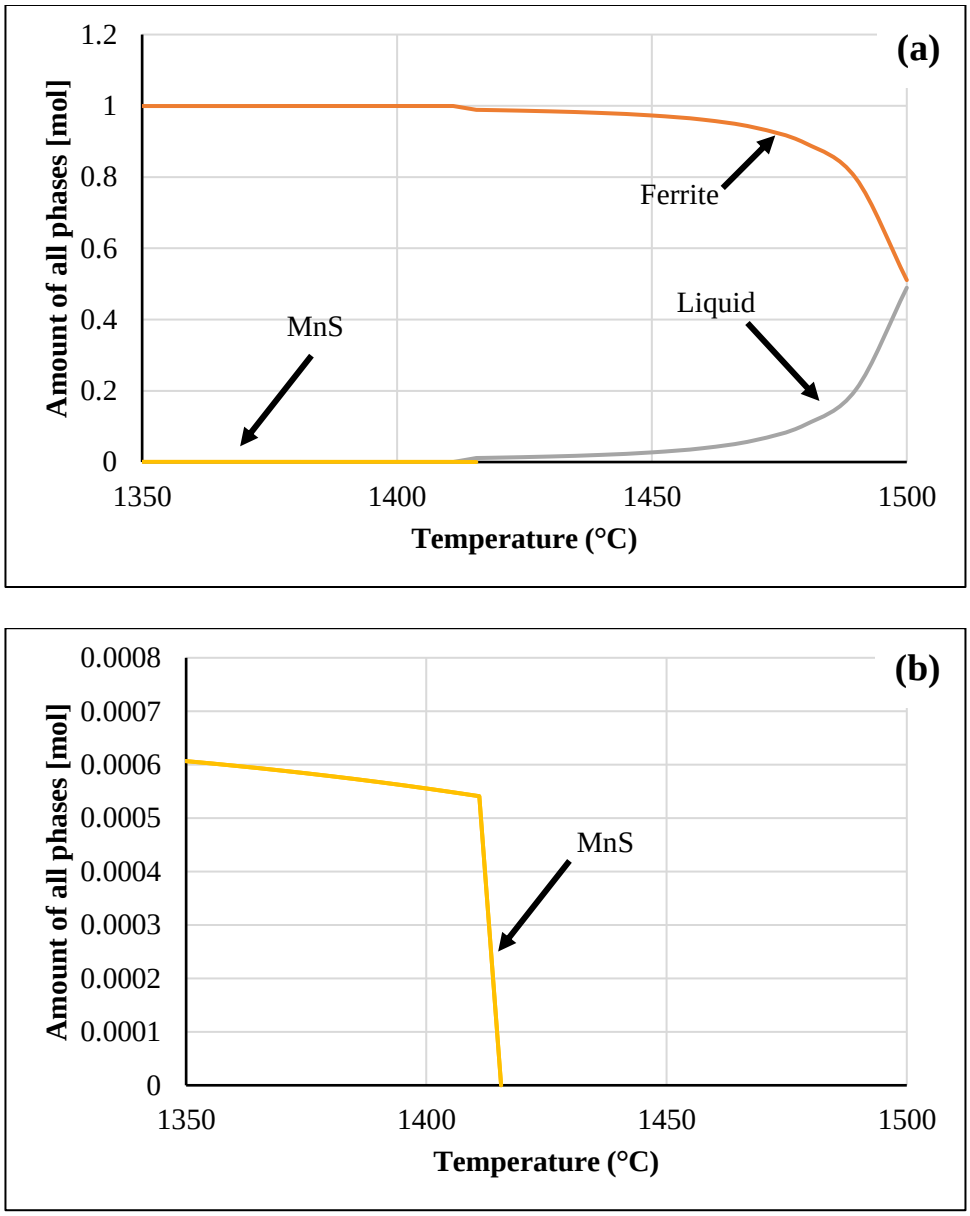

Figure B.2: a) The possible precipitates from Thermo-Calc between 1350°C and 1500°C for sample B:0Ti;0Nb, and b) the molar fraction precipitate.

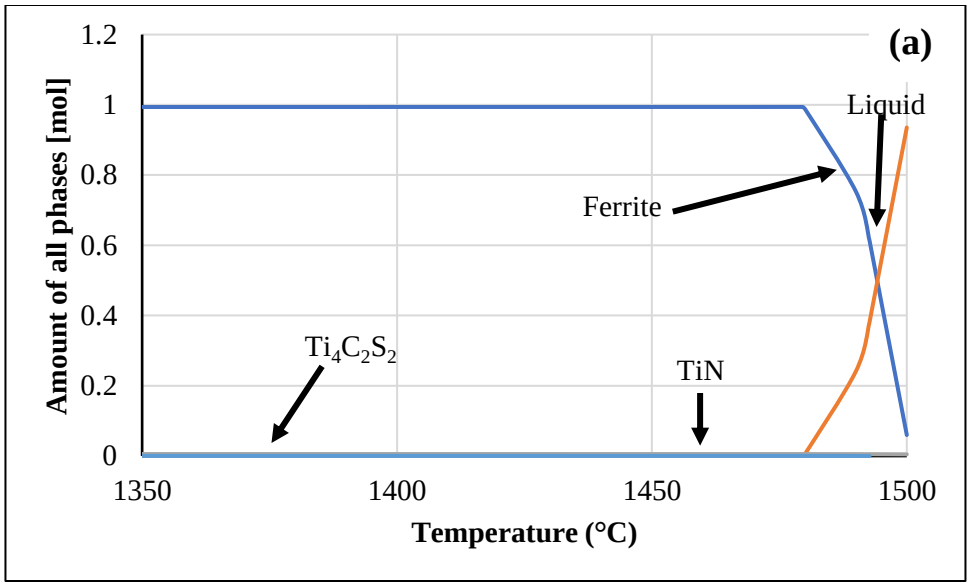

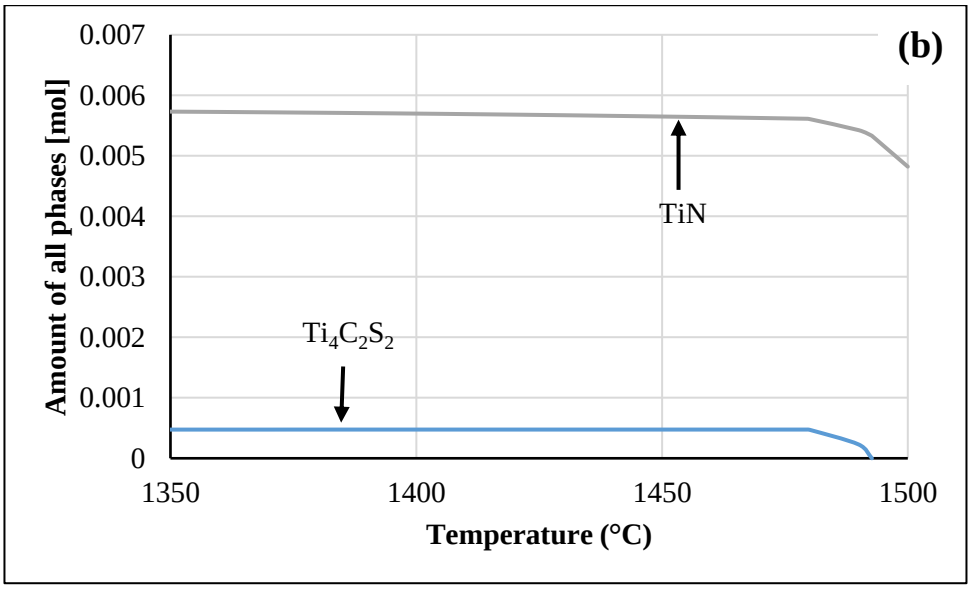

Figure B.3: a) The possible precipitates from Thermo-Calc between 1350°C and 1500°C for sample C:0.7Ti, and b) the molar fraction precipitate.

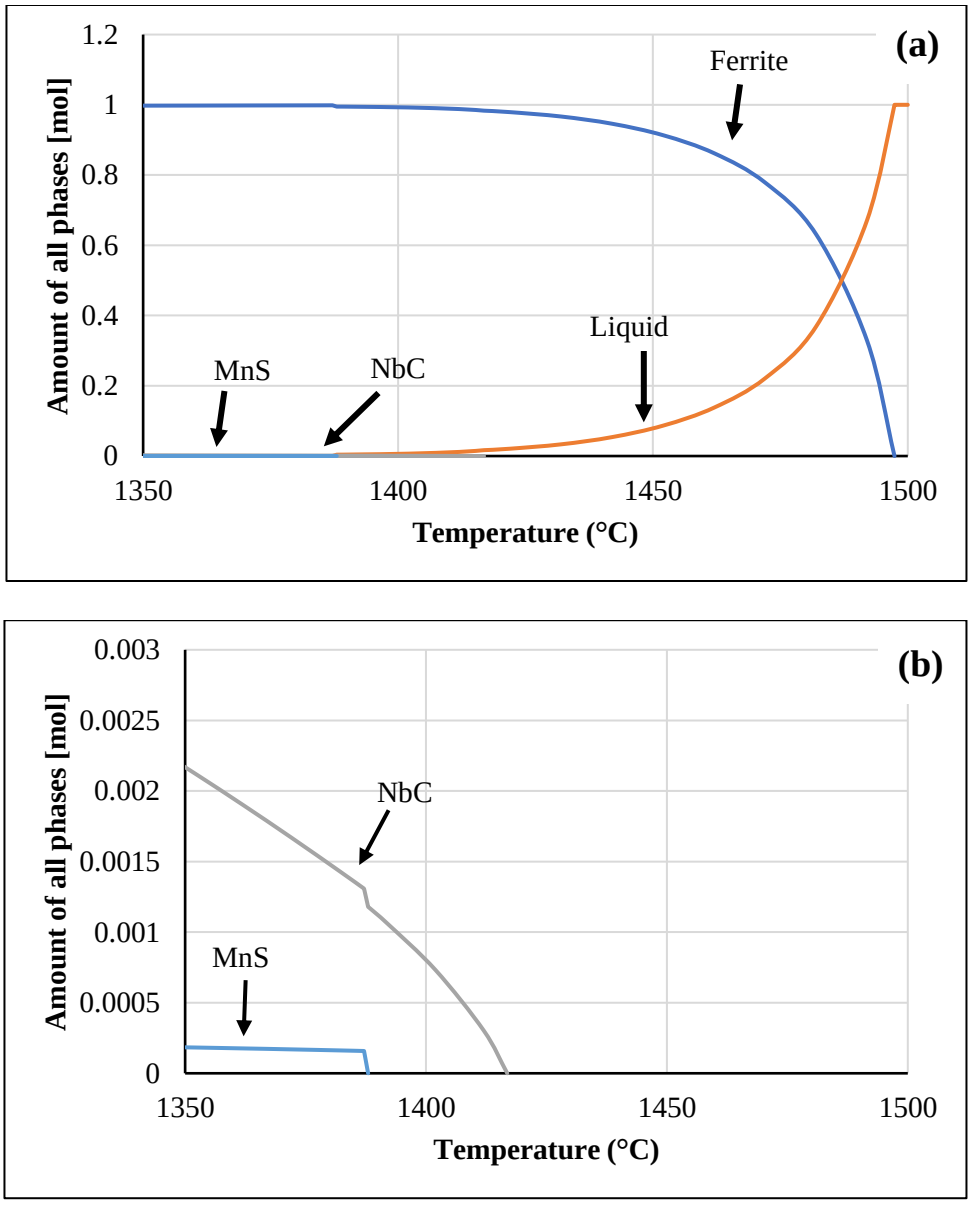

Figure B.4: a) The possible precipitates from Thermo-Calc between 1350°C and 1500°C for sample D:0.6Nb, and b) the molar fraction precipitate.

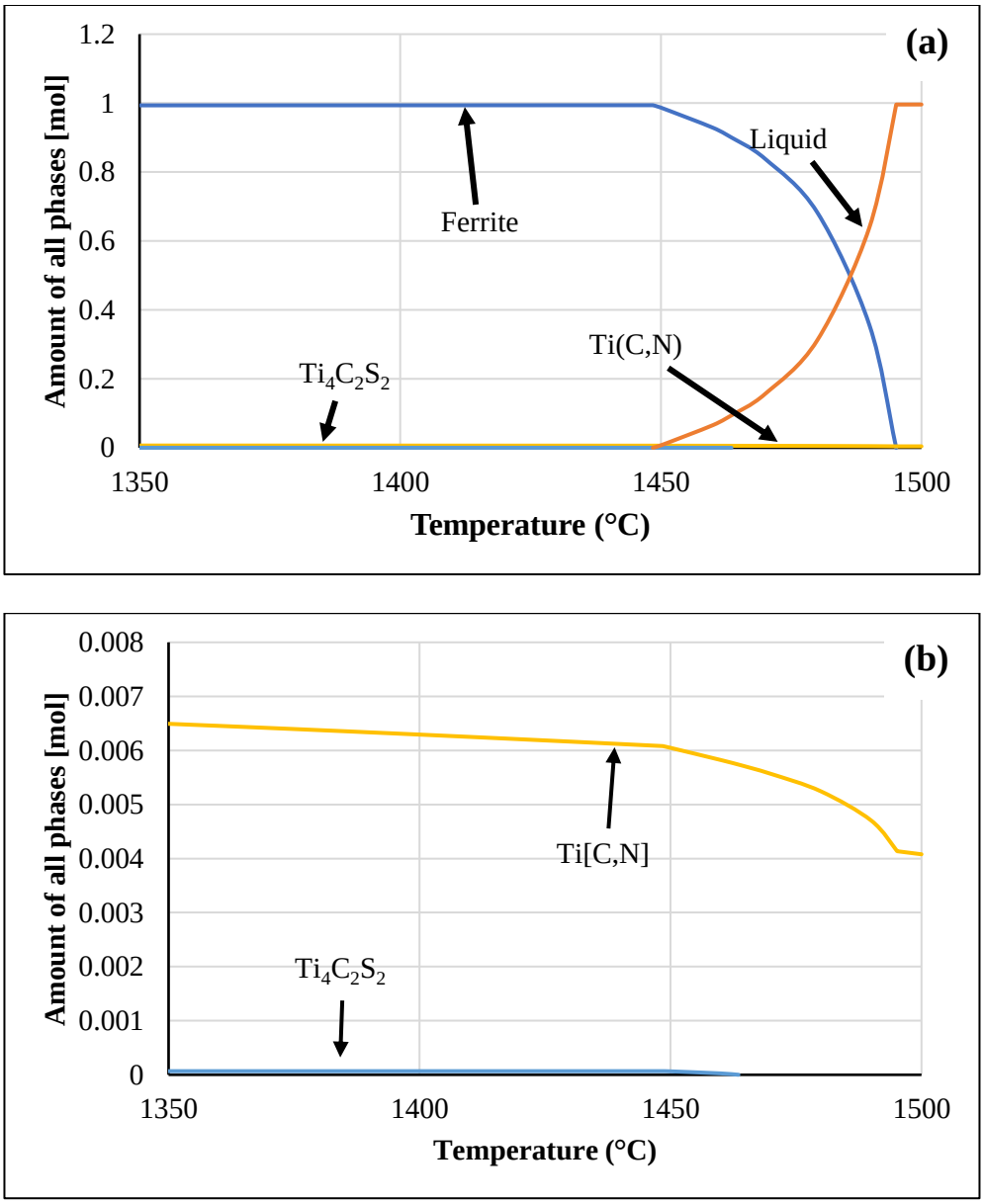

Figure B.5: a) The possible precipitates from Thermo-Calc between 1350°C and 1500°C for sample E:0.4Ti;0.6Nb, and b) the molar fraction precipitate.

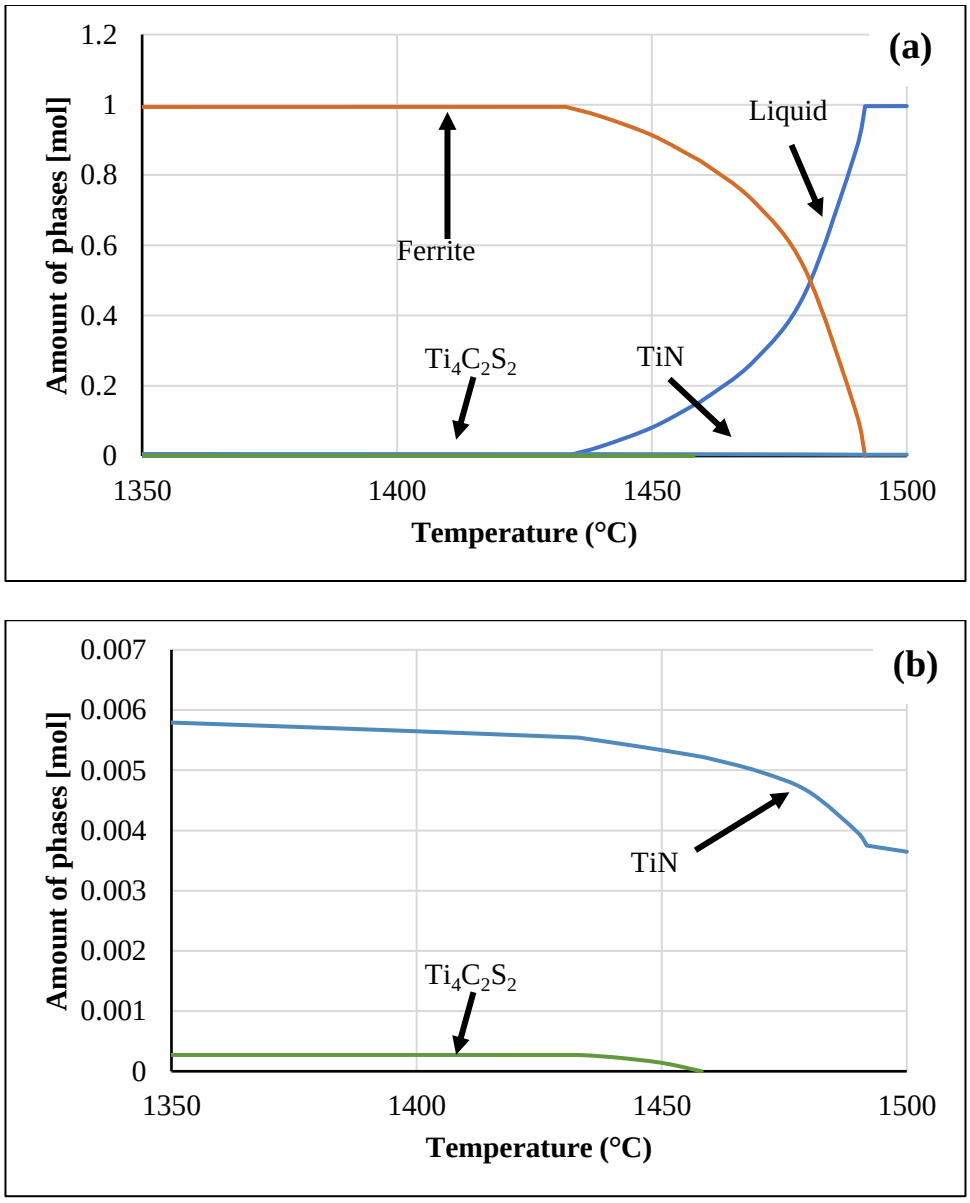

Figure B.6: a) The possible precipitates from Thermo-Calc between 1350°C and 1500°C for sample F:0.4Ti;0.9Nb, and b) the molar fraction precipitate.

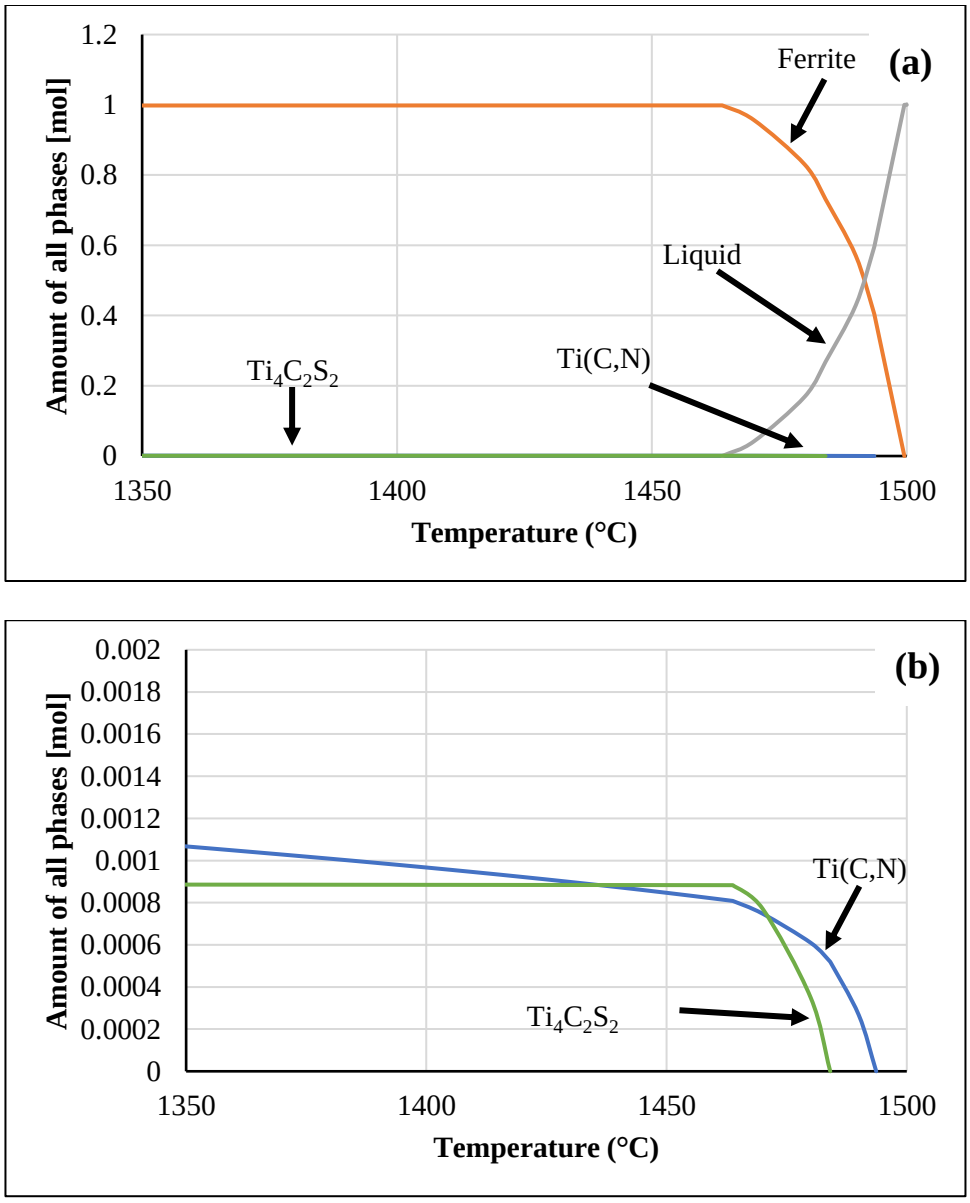

Figure B.7: a) The possible precipitates from Thermo-Calc between 1350°C and 1500°C for sample G:0.1Ti;0.4Nb, and b) the molar fraction precipitate.

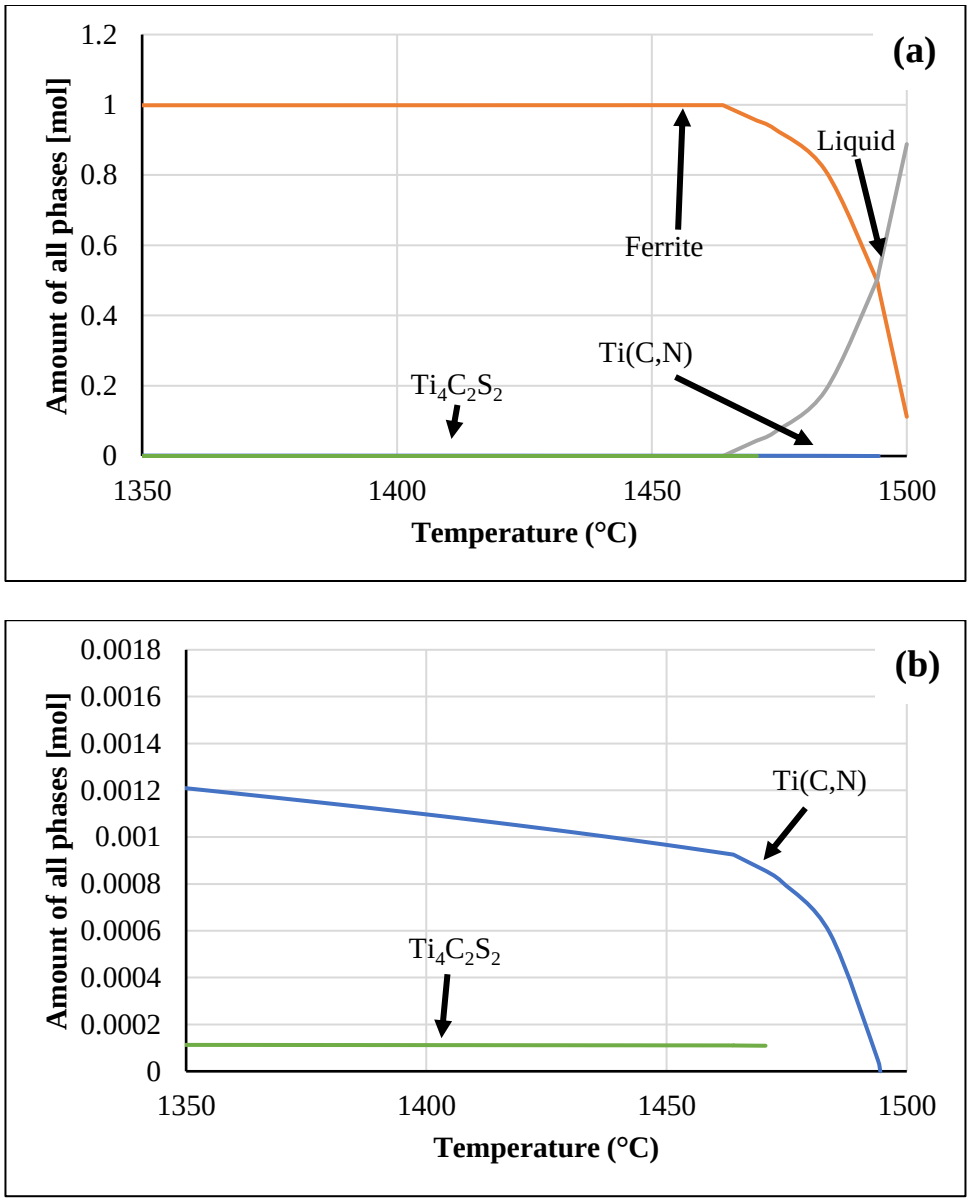

Figure B.8: a) The possible precipitates from Thermo-Calc between 1350°C and 1500°C for sample H:0.1Ti;0.4Nb, and b) the molar fraction precipitate.

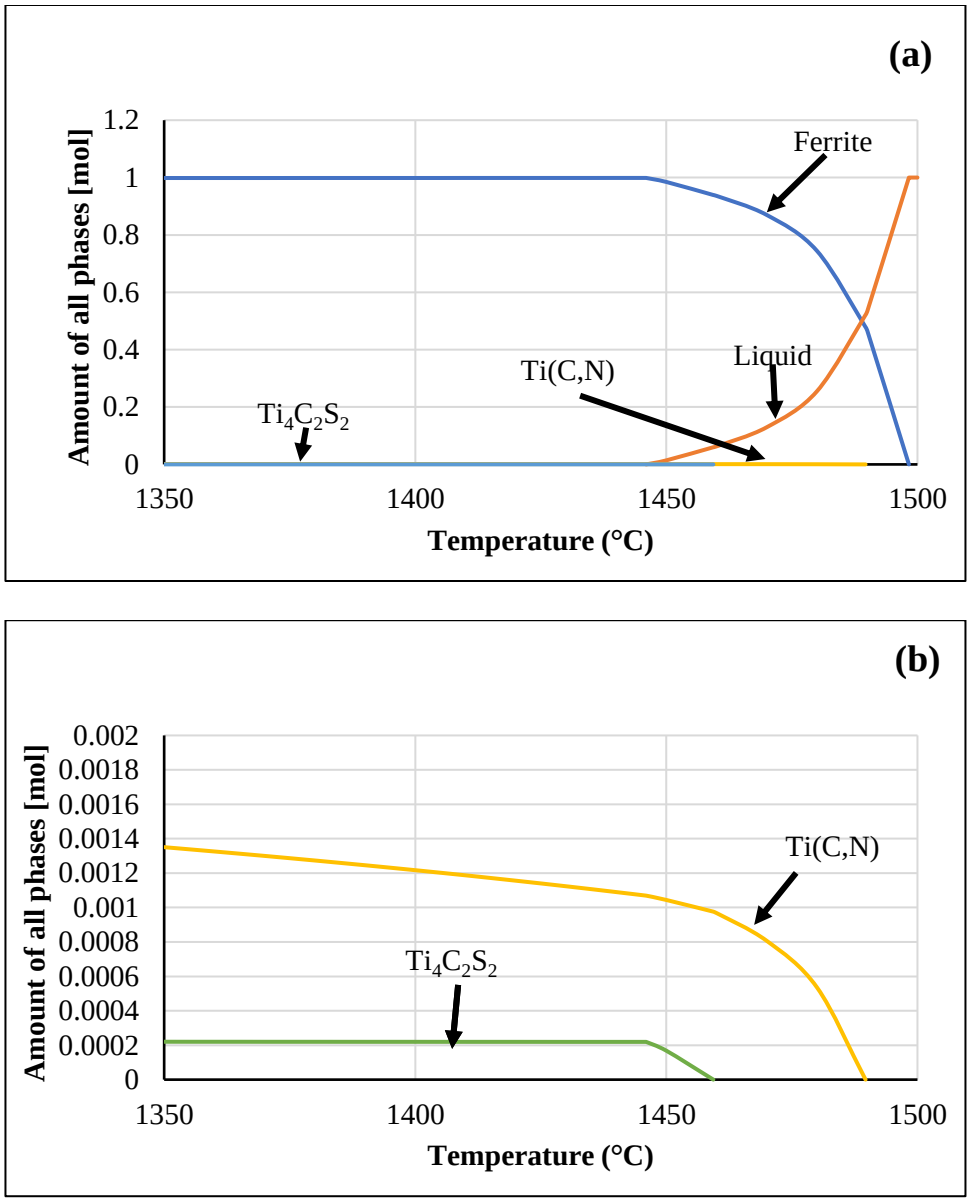

Figure B.9: a) The possible precipitates from Thermo-Calc between 1350°C and 1500°C for sample I:0.1Ti;0.5Nb;2Mo, and b) the molar fraction precipitate.

Appendix C

Houldcroft test semi-quantitative analysis

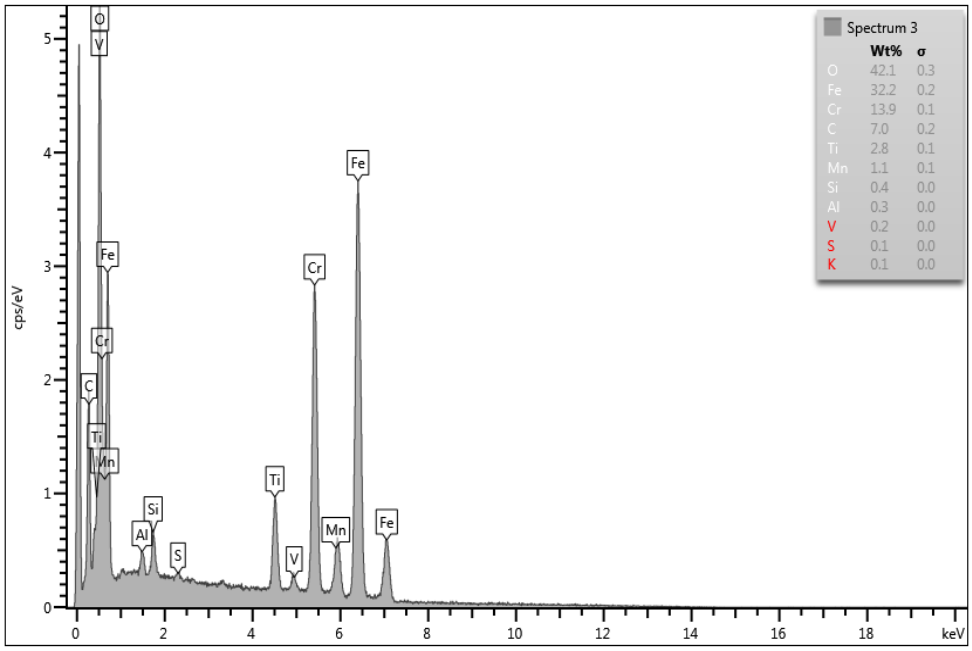

Figure C.1: EDX semi-quantitative analysis during a welding speed of 6 mm/s for 0.7Ti - stabilized ferritic stainless steel (C:0.7Ti) showing spectrum 3.

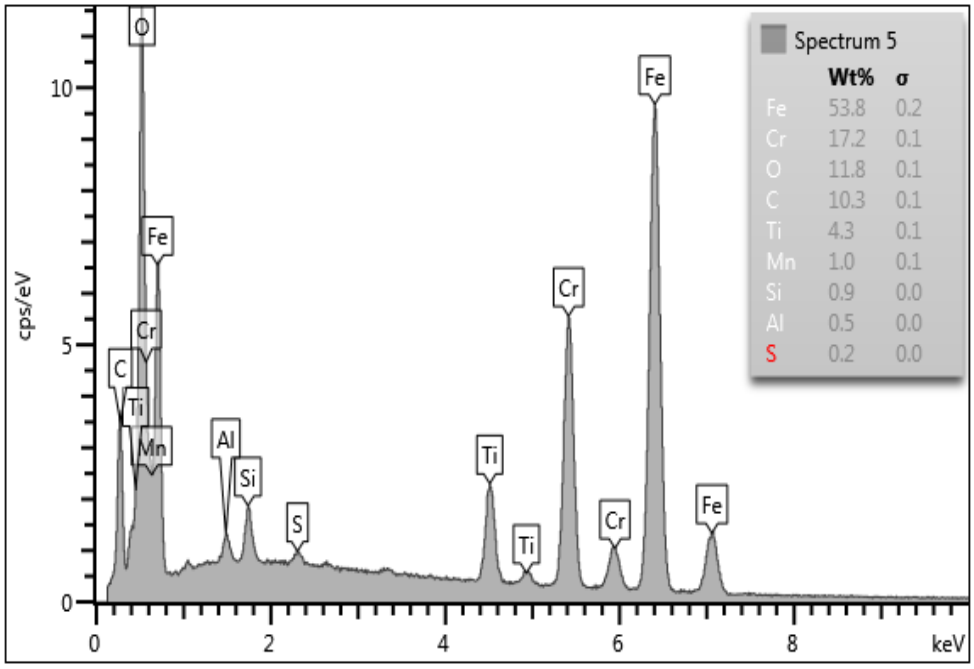

Figure C.2: EDX semi-quantitative analysis during a welding speed of 6 mm/s for 0.7Ti - stabilized ferritic stainless steel (C:0.7Ti) showing spectrum 5.

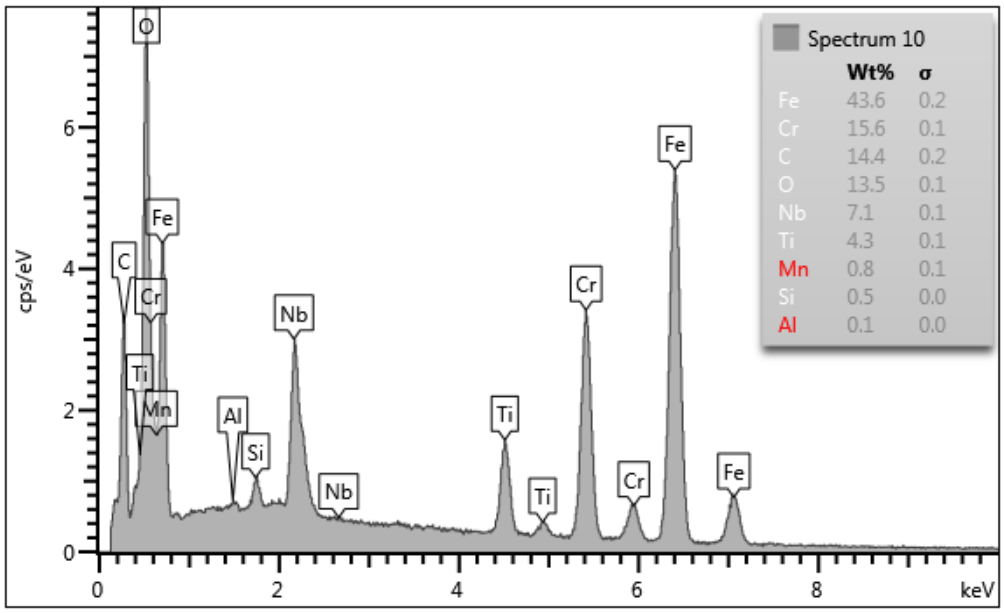

Figure C.3: EDX semi-quantitative analysis during a welding speed of 6 mm/s for E:0.4Ti;0.6Nb alloy showing spectrum 10.

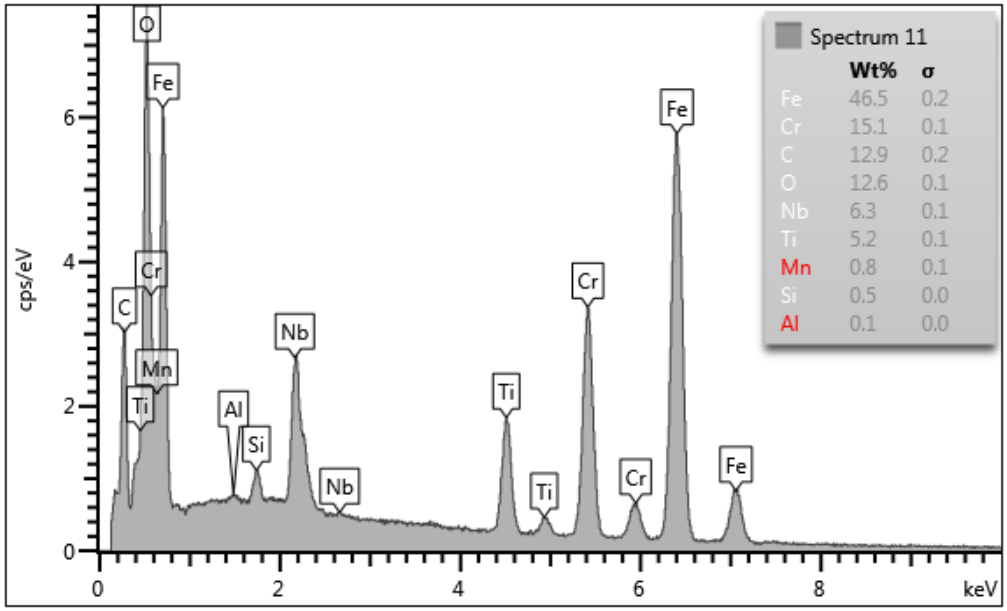

Figure C.4: EDX semi-quantitative analysis during a welding speed of 6 mm/s for E:0.4Ti;0.6Nb alloy showing spectrum 11.

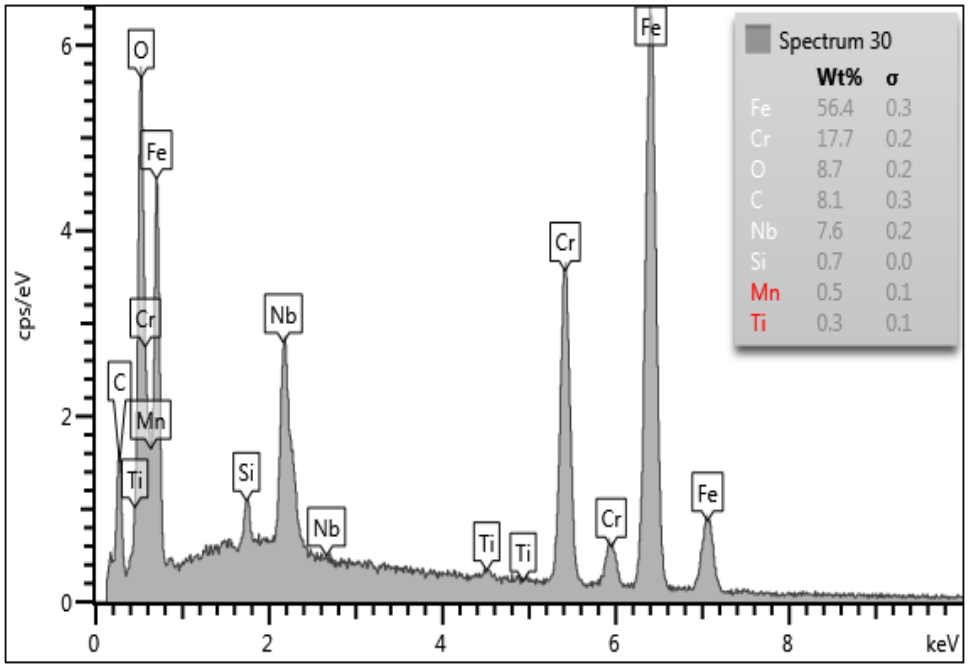

Figure C.5: EDX semi-quantitative analysis during a welding speed of 3 mm/s for 0.6Nb - stabilized ferritic stainless steel (D:0.6Nb) showing spectrum 30.

Hot tensile test semi-quantitative analysis

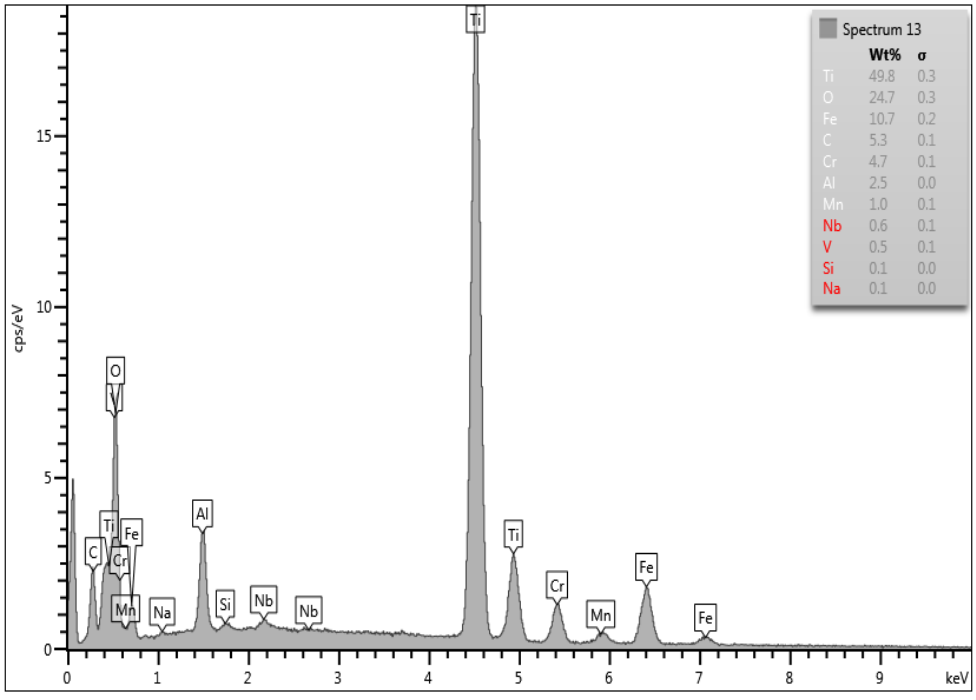

Figure C.6: EDX semi-quantitative analysis for E:0.4Ti;0.6Nb stabilized ferritic stainless steel at the testing temperature of 1300°C showing spectrum 13.

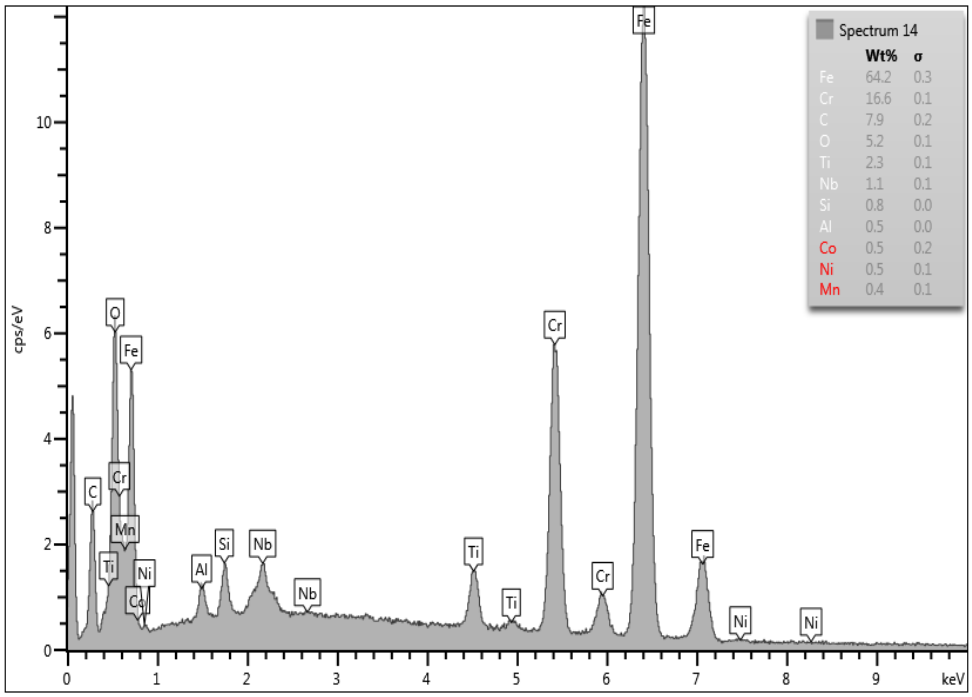

Figure C.7: EDX semi-quantitative analysis for E:0.4Ti;0.6Nb stabilized ferritic stainless steel at the testing temperature of 1300°C showing spectrum 14.

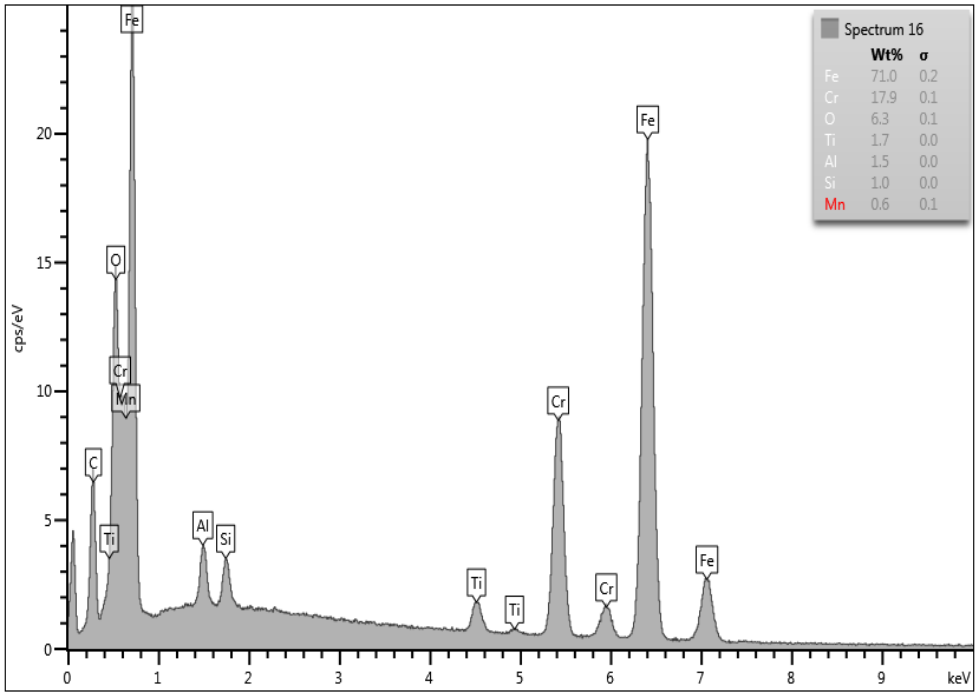

Figure C.8: EDX semi-quantitative analysis for C:0.7Ti grade at the testing temperature of 1300°C showing spectrum 16.

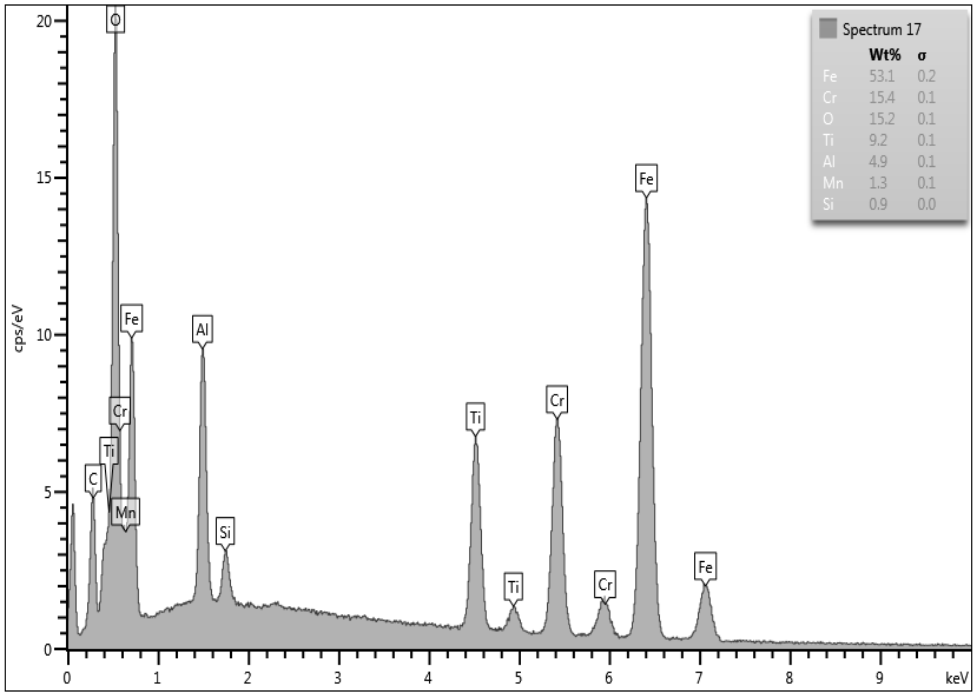

Figure C.9: EDX semi-quantitative analysis for C:0.7Ti grade at the testing temperature of 1300°C showing spectrum 17.

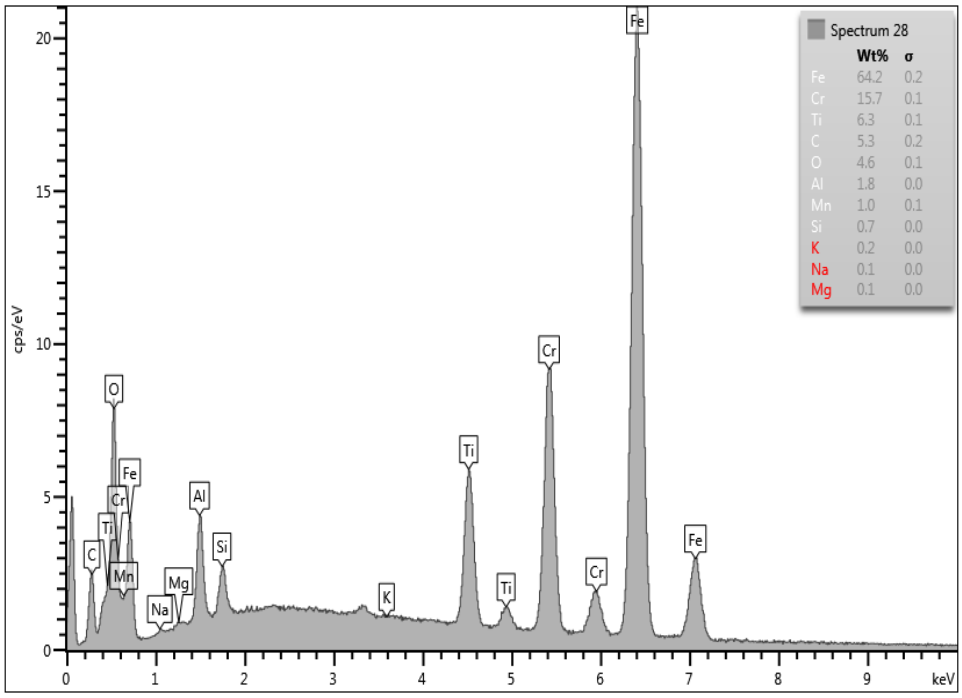

Figure C.10: EDX semi-quantitative analysis for C:0.7Ti - stabilized ferritic stainless steel at the testing temperature of 1200°C showing spectrum 28.

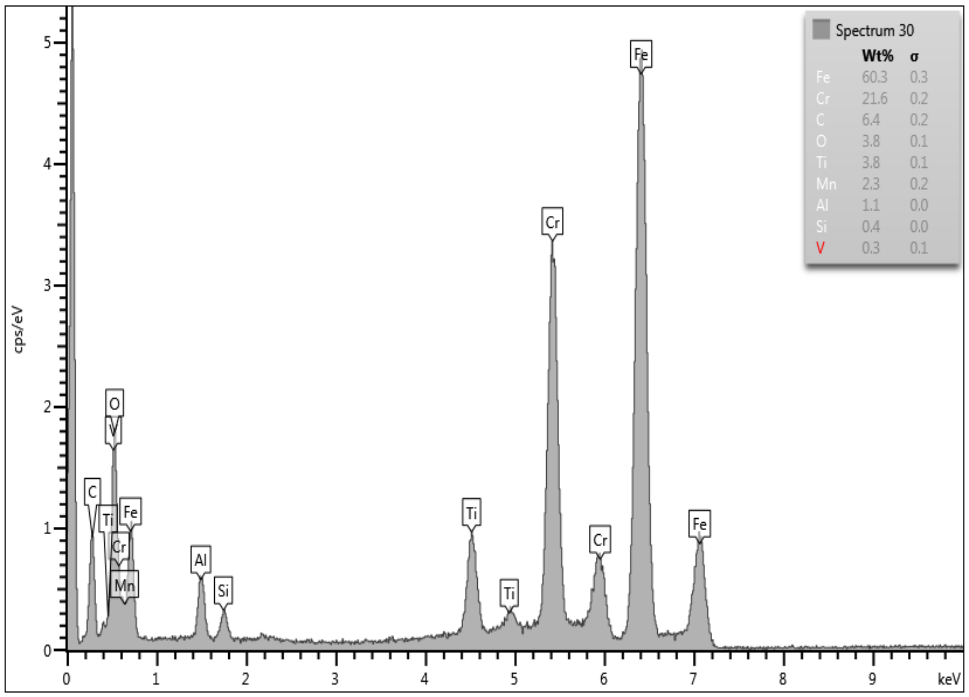

Figure C.11: EDX semi-quantitative analysis for C:0.7Ti - stabilized ferritic stainless steel at the testing temperature of 1200°C showing spectrum 30.

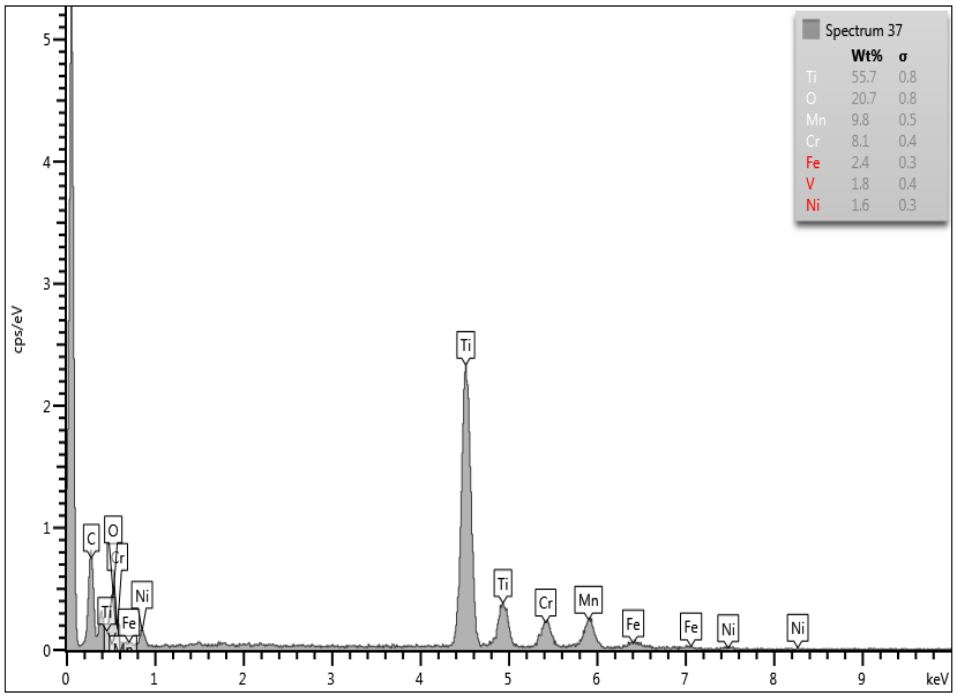

Figure C.12: EDX semi-quantitative analysis for E:0.4Ti;0.6Nb - stabilized ferritic stainless steel at the testing temperature of 1200°C showing spectrum 37.

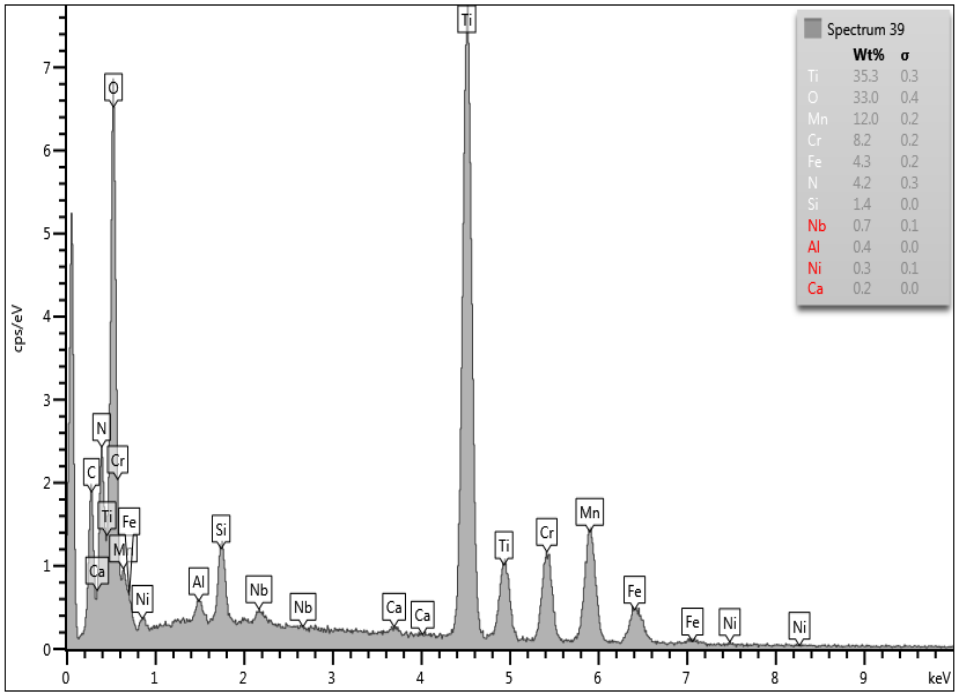

Figure C.13: EDX semi-quantitative analysis for E:0.4Ti;0.6Nb - stabilized ferritic stainless steel at the testing temperature of 1200°C showing spectrum 39.

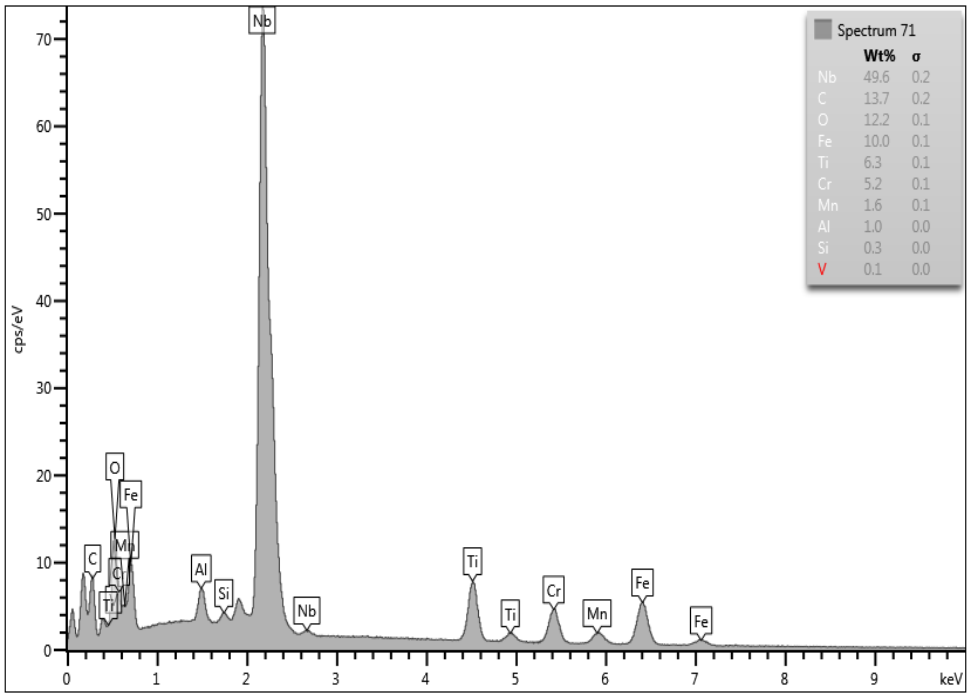

Figure C.14:EDX semi-quantitative analysis for D:0.6Nb - stabilized ferritic stainless steel at the testing temperature of 1250°C showing spectrum 71.

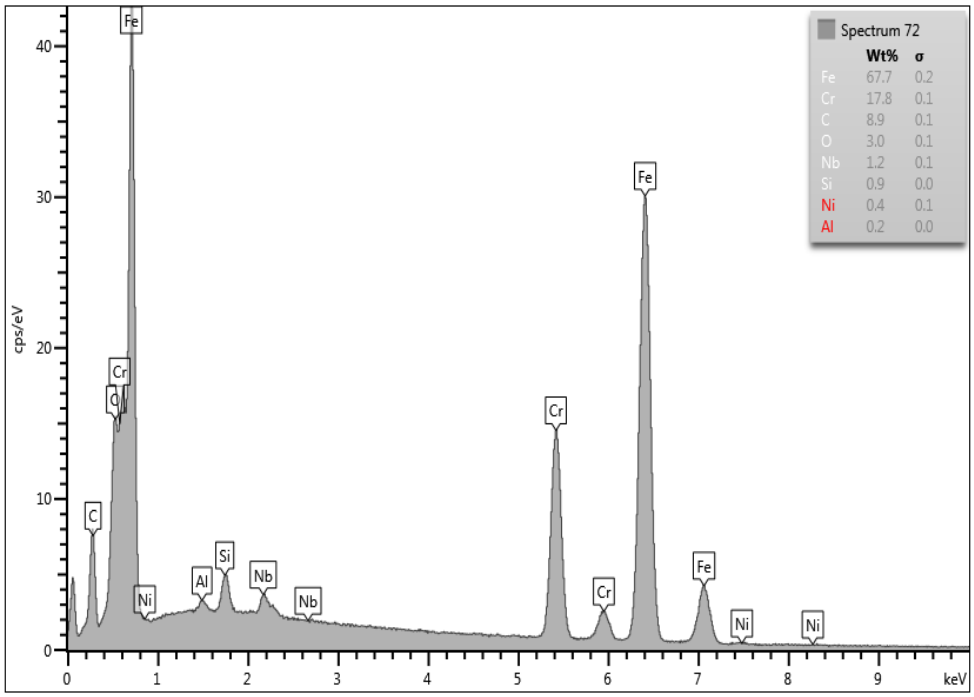

Figure C.15: EDX semi-quantitative analysis for D:0.6Nb - stabilized ferritic stainless steel at the testing temperature of 1250°C showing spectrum 72.

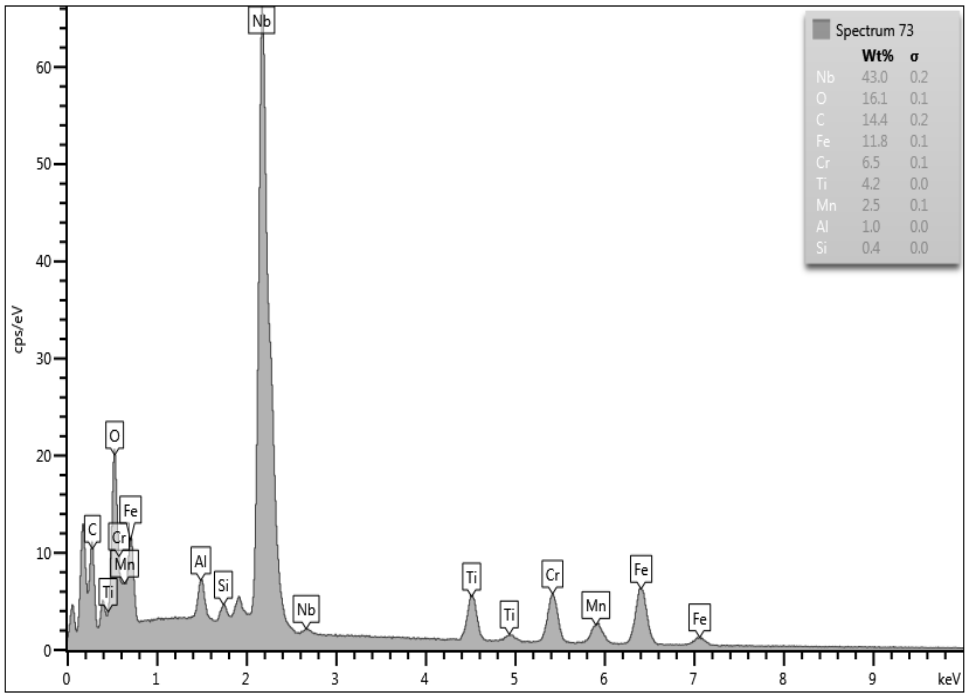

Figure C.16: EDX semi-quantitative analysis for D:0.6Nb - stabilized ferritic stainless steel at the testing temperature of 1250°C showing spectrum 73.

Appendix D

DSC thermograms of the alloys

Sample A:0Ti;0Nb

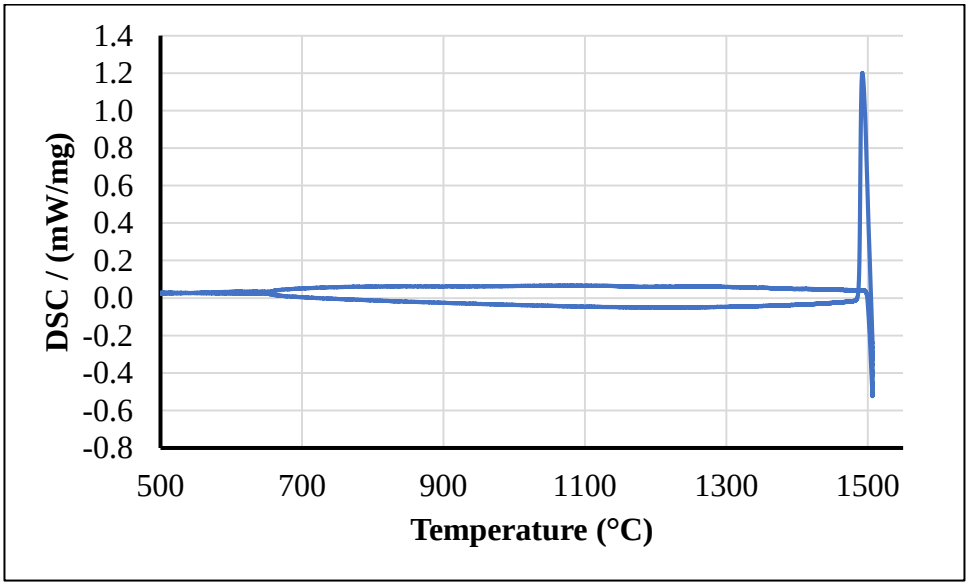

Figure D.1: DSC thermogram for the sample A:0Ti:0Nb during heating and cooling.

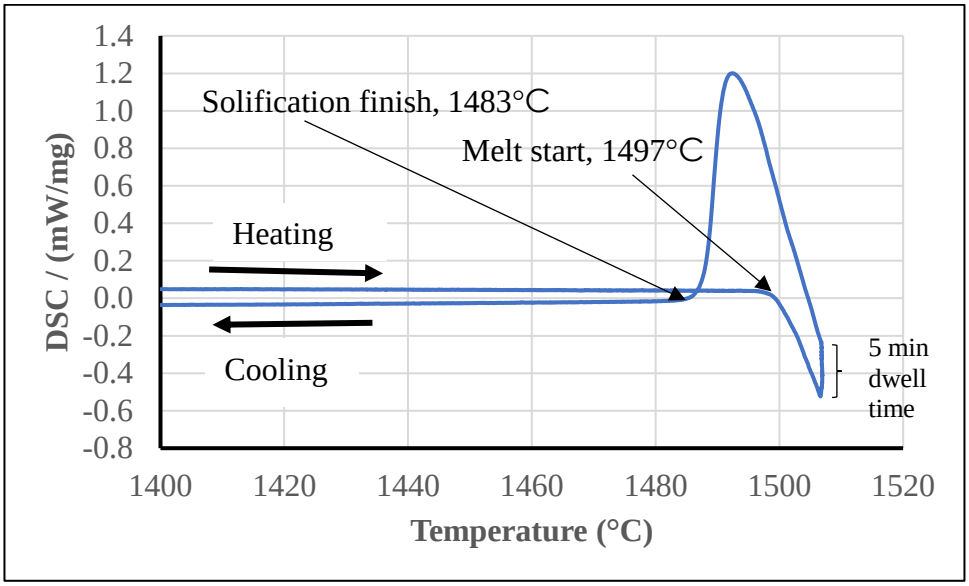

Figure D.2: Expanded thermogram for alloy A:0Ti;0Nb showing the solidus and liquidus temperatures.

Sample B:0Ti;0Nb

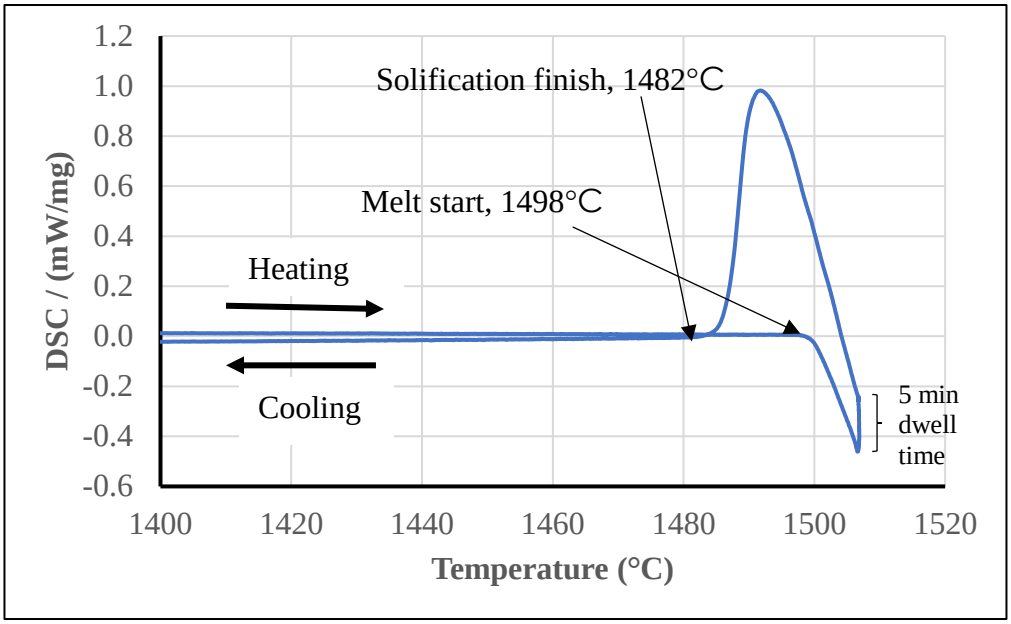

Figure D.3: Expanded thermogram for alloy B:0Ti;0Nb showing the solidus and liquidus temperatures.

Sample C:0.7Ti

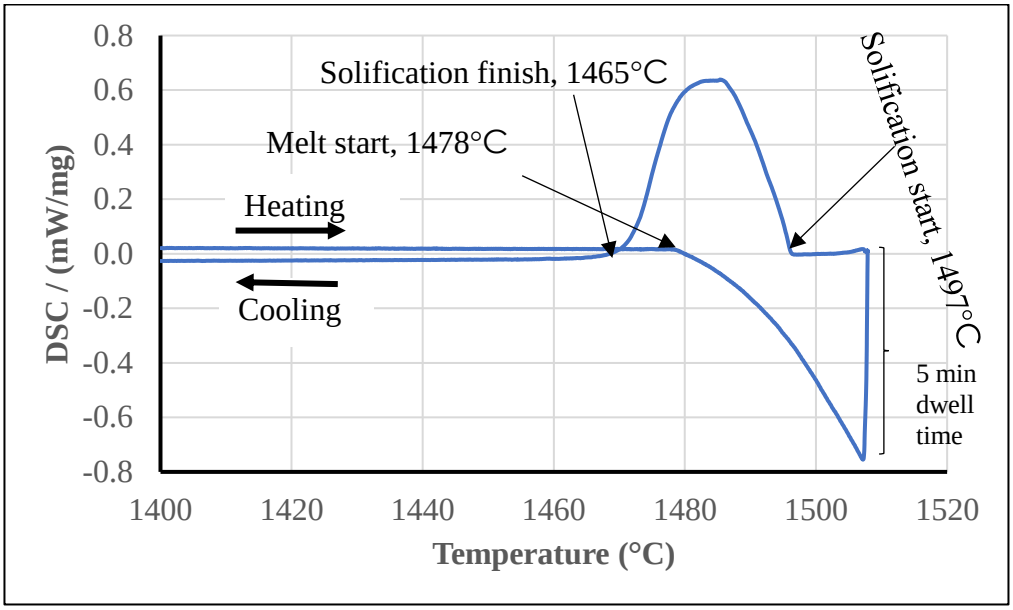

Figure D.4: Expanded thermogram for alloy C:0.7Ti showing the solidus and liquidus temperatures.

Sample D:0.6Nb

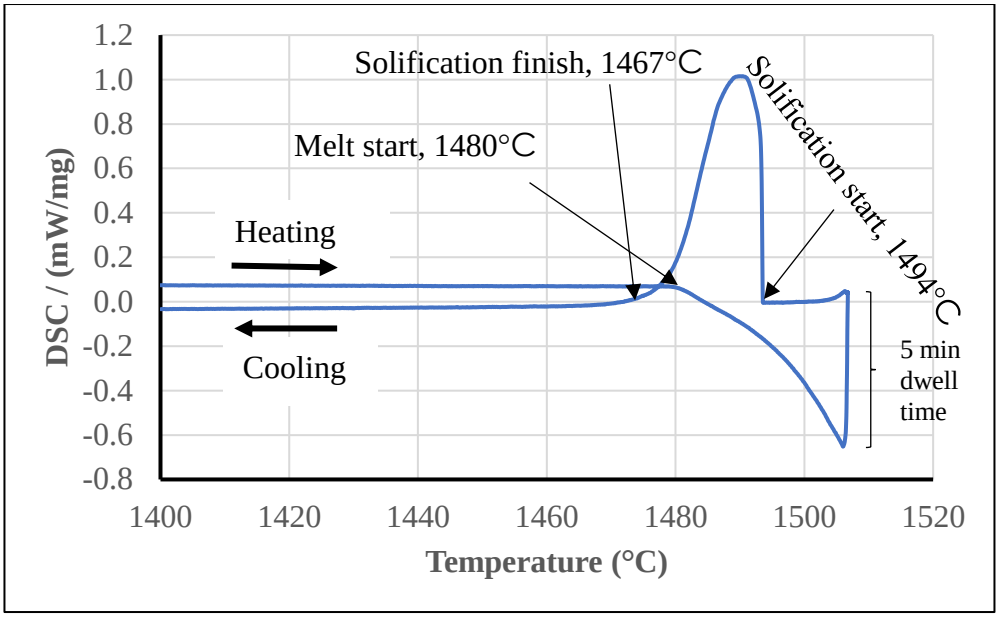

Figure D.5: Expanded thermogram for alloy D:0.6Nb showing the solidus and liquidus temperatures.

Sample F:0.4Ti;0.9Nb

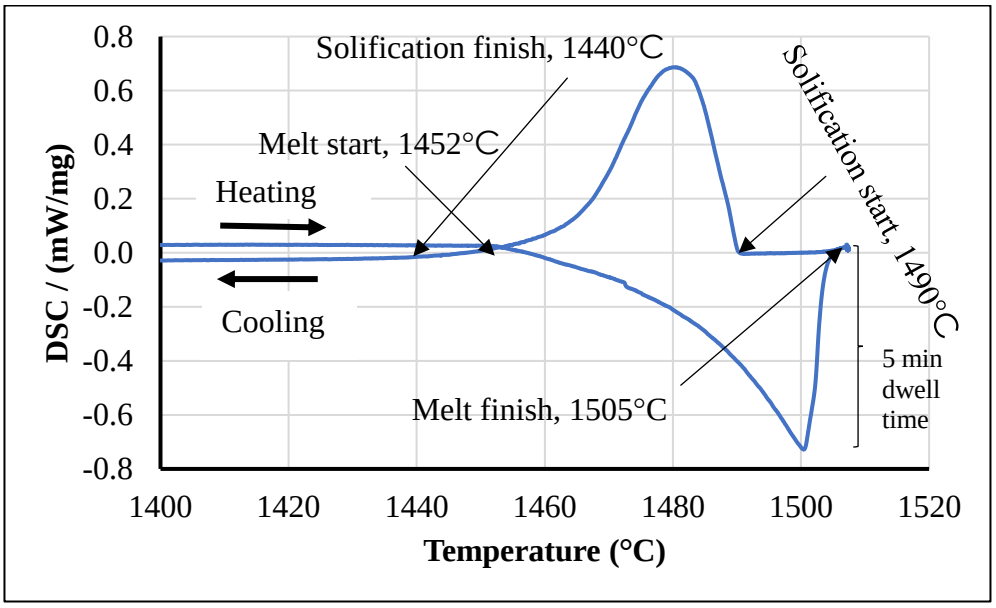

Figure D.6: Expanded spectra for alloy F:0.4Ti;0.9Nb showing the solidus and liquidus temperatures.

Sample H:0.1Ti;0.4Nb

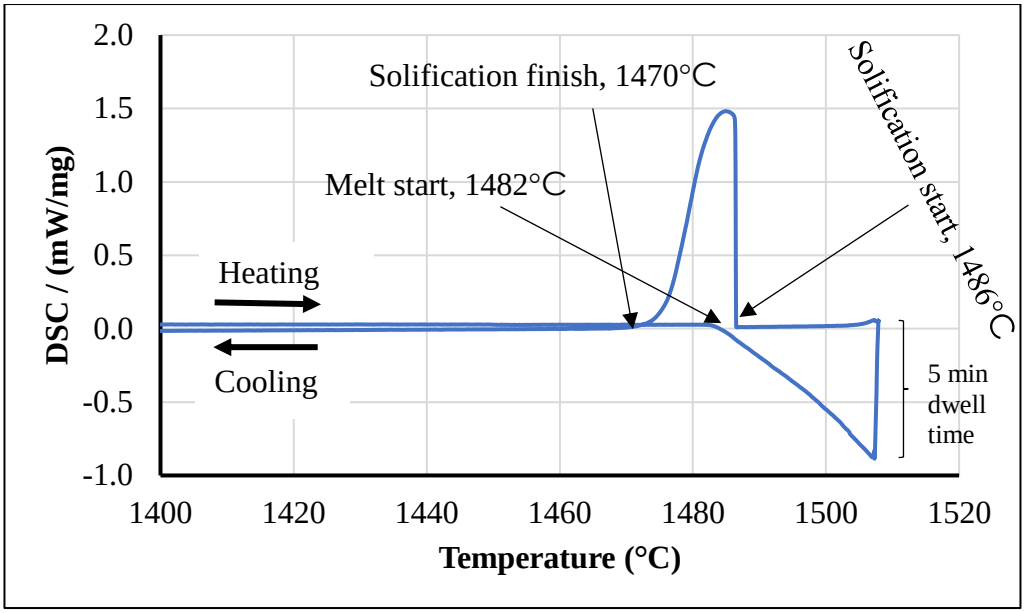

Figure D.7: Expanded thermogram for alloy H:0.1Ti;0.4Nb showing the solidus and liquidus temperatures.

Sample I:0.1Ti;0.5Nb;2Mo

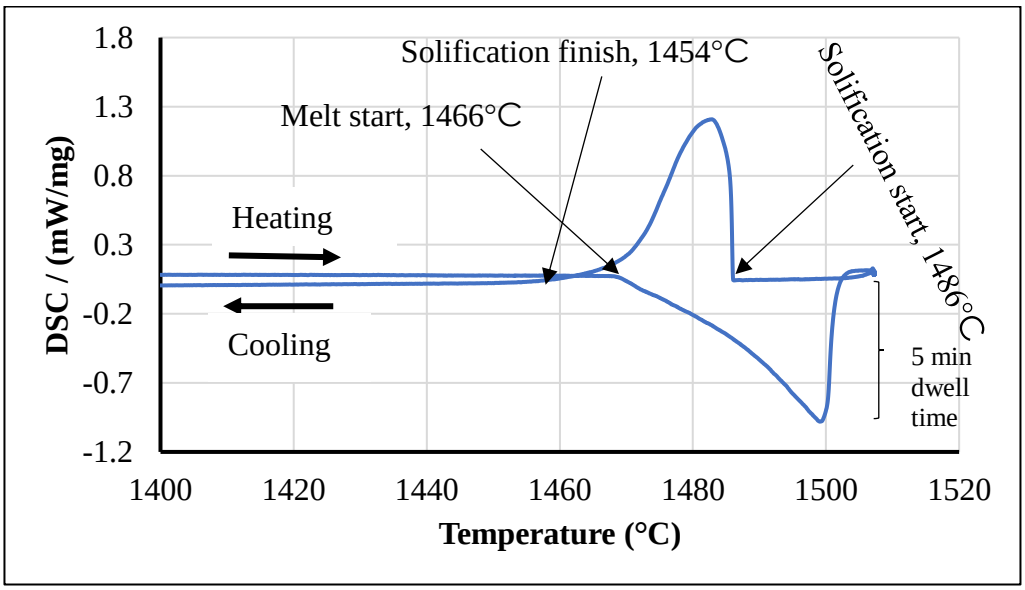

Figure D.8: Thermogram for alloy I:0.1Ti;0.5Nb;2Mo showing the solidus and liquidus temperatures.